

**SEPARATING CONTRIBUTIONS OF SMALL-SCALE
TURBULENCE, LARGE-SCALE TURBULENCE, AND CORE
NOISE FROM FAR-FIELD EXHAUST NOISE MEASUREMENTS**

A Dissertation
Presented to
The Academic Faculty

by

Donald Kirby Nance

In Partial Fulfillment
of the Requirements for the Degree
Doctor of Philosophy in the
School of Aerospace Engineering

Georgia Institute of Technology
December 2007

**SEPARATING CONTRIBUTIONS OF SMALL-SCALE
TURBULENCE, LARGE-SCALE TURBULENCE, AND CORE
NOISE FROM FAR-FIELD EXHAUST NOISE MEASUREMENTS**

Approved by:

Dr. Krishan K. Ahuja, Advisor
School of Aerospace Engineering
Georgia Institute of Technology

Dr. Kenneth Cunefare
School of Mechanical Engineering
Georgia Institute of Technology

Dr. Tim C. Lieuwen
School of Aerospace Engineering
Georgia Institute of Technology

Dr. Jeff Mendoza
Honeywell Aerospace
Phoenix, Arizona

Dr. Lakshmi Sankar
School of Aerospace Engineering
Georgia Institute of Technology

Date Approved: August 22, 2007

To my wife and family

“I will praise you, O Lord, with all my heart; I will tell of all your wonders.”

Psalm 9:1 (NIV)

ACKNOWLEDGEMENTS

My sincerest thanks go to my advisor, Dr. Krishan K. Ahuja, for his guidance and support during my research. His endless enthusiasm and dedication toward his students and their work is greatly appreciated.

I also would like to thank Dr. Jeff Mendoza for serving on my committee and all the time and energy he has spent with Dr. Ahuja and me discussing this research. Thanks also to Dr. Tim C. Lieuwen, Dr. Lakshmi Sankar, and Dr. Kenneth Cunefare for serving on my committee. Thanks also to Dr. Richard Gaeta, Dr. Robert Funk, and Dr. Kevin Massey for their advice and assistance. Also, I would like to acknowledge the students that I was privileged to work with during my time at GTRI/ATAS for their help, friendship, and support. I would also like to thank the GTRI/ATAS administrative staff for their help and understanding.

The financial support of the Robert G. Shackleford Graduate Fellowship and the NASA/Honeywell Aerospace EVNERT program is gratefully acknowledged. Portions of this work were sponsored by the NASA Vehicle Systems Program and the Department of Defense Research and Engineering (DDR&E) under the scope of the Aeropropulsion University Research Engineering Technology Institute (URETI).

Finally, I am grateful to my wife, Kristin, for her patience, understanding, and encouragement.

TABLE OF CONTENTS

ACKNOWLEDGEMENTS	iv
TABLE OF CONTENTS	iv
LIST OF TABLES	viii
LIST OF FIGURES	ix
NOMENCLATURE.....	xvii
SUMMARY	xviii
CHAPTER 1.....	1
INTRODUCTION.....	1
CHAPTER 2.....	8
PREVIOUS WORK.....	8
2.1 The Two-Noise Source Model.....	9
2.2 Universal Similarity Spectra	15
2.3 Direct Evidence of the Two Noise Sources	18
2.4 Signal Enhancement Techniques	20
2.4.1 Coherent Output Power Spectrum	20
2.4.2 The Three-Microphone Signal Enhancement Technique	22
2.4.3 Partial Coherence Method.....	26
2.4.4 The Five-Microphone Method.....	28
2.5 Summary.....	32
CHAPTER 3.....	34
EXPERIMENTAL PROGRAM.....	34
3.1 Anechoic Facilities.....	35
3.2 Investigating the Role of the Turbulence Scales.....	37
3.2.1 Cross-Correlation and Coherence Measurements.....	37
3.2.2 Implementation of the Three-Microphone Method	41

3.3	Investigating the Applicability of the Jet Noise Incoherence Assumption.....	42
3.4	Experimentally Identifying the Limitations of the Three-Microphone Method	43
3.5	Model-Scale Acoustic Experimentation	44
3.6	Full-Scale Engine Noise Diagnostics.....	47
CHAPTER 4.....		49
SMALL-SCALE VERSUS LARGE-SCALE CONTRIBUTIONS		49
4.1	Cross-Correlation and Coherence Measurements.....	50
4.1.1	Subsonic Jets.....	51
4.1.2	Effect of Nozzle Geometry in Subsonic Jets	69
4.1.2.1	Effect of Nozzle Diameter	71
4.1.2.2	Axisymmetric Jet v. Non-Axisymmetric Jet.....	73
4.1.2.3	Jets with Enhanced Mixing.....	76
4.1.3	A Fully-Expanded Supersonic Jet.....	78
4.2	Separation of the Turbulence Scale Contributions in the Far-Field	83
CHAPTER 5.....		94
JET NOISE INCOHERENCE APPLICABILITY.....		94
5.1	Establishment of a Coherence Threshold	95
5.2	Some Questions Answered	98
5.3	Far-Field Coherence Measurements	101
5.3.1	Microphone Arrangement: Polar v. Linear.....	101
5.3.2	Radial Microphone Arc Positioning	105
5.3.3	Microphone Separation.....	106
5.3.4	Nozzle Geometry	111
5.3.5	Supersonic Jet Mach Numbers.....	117
CHAPTER 6.....		124
LIMITATIONS OF THE THREE-MICROPHONE METHOD.....		124
6.1	Verification of the Minami/Ahuja Three-Microphone Method Error	125
6.2	Numerical Simulations.....	130
6.2.1	Effect of Multiple Correlated Sources	131
6.2.2	Effect of Microphone Spacing.....	137
6.3	Verification via Proof-of-Concept Testing.....	142
CHAPTER 7.....		149

APPLICATION OF FINDINGS	149
7.1 Model-Scale Application	150
7.1.1 External-Source Configuration Results	151
7.1.1.1 Three-Microphone Method Results	152
7.1.1.2 Coherent Output Power Spectrum Results	154
7.1.1.3 Partial Coherence Method Results	157
7.1.2 Internal-Source Configuration	158
7.1.2.1 Three-Microphone Method Results	159
7.1.2.2 Coherent Output Power Spectrum Results	160
7.2 Application of the Lessons Learned to Full-Scale Engine Noise Measurements 165	
7.2.1 Far-field Microphone Layout.....	165
7.2.2 Internal Sensors.....	166
7.2.3 Data Acquisition Requirements	166
7.2.4 Coherence Threshold	167
7.2.5 Full-Scale Engine Results	168
 CHAPTER 8.....	 173
SOLVING THE FIVE-MICROPHONE PROBLEM	173
8.1 Minami and Ahuja Solution Routine	173
8.2 Physics-Based Initial Guess/Bounds.....	174
8.3 Numerical Schemes Employed.....	175
8.3.1 Using the Netwon-Rhapon Based Polymath 6.0	177
8.3.2 Using MATLAB <i>fminsearch</i>	177
8.3.3 Using MATLAB <i>fminsearch</i> and <i>ga</i>	179
8.3.3.1 Solving the Minami and Ahuja Simulation	179
8.3.3.2 Solving the Five-Microphone Problem for Model-Scale Testing.....	179
 CHAPTER 9.....	 182
UNCERTAINTY ANALYSIS.....	182
9.1 Uncertainty Involved in Coherence-Based Signal Enhancement Techniques	184
9.1.1 Auto-Power Spectrum Uncertainty.....	185
9.1.2 Cross-Power Spectrum Magnitude Uncertainty	186
9.1.3 Cross-Power Spectrum Phase Uncertainty	187
9.1.4 Coherence Estimation Uncertainty	188
9.2 Three-Microphone Method Uncertainty	190
9.2.1 Effect of Relative Coherence Levels	196
9.2.2 Effect of Relative Sound Pressure Levels.....	200

9.2.3	Uncertainty Applied to Three-Microphone Method Experiments.....	202
9.3	Coherent Output Power Spectrum	204
9.4	Partial Coherence Method.....	209
CHAPTER 10	211
CONCLUSION	211
REFERENCES	214
VITA	220

LIST OF TABLES

Table 8.1 Summary of five-microphone problem solution routines.....	176
Table 9.1 Uncertainty involved in using coherence-based techniques.....	184

LIST OF FIGURES

Figure 1.1 Ideal single-input/single-output system.....	5
Figure 1.2 Single-input/single-output system with additional input $n(t)$	6
Figure 2.1 PIV image of jet from a rectangular nozzle (20.32 x 3.05 mm) operated at Mach 0.9.	10
Figure 2.2 The sound field from the fine-scale turbulence and the Mach wave radiation from the large-scale turbulence structures.	12
Figure 2.3 Similarity spectra for the two components of turbulence within a jet.....	17
Figure 2.4 Schematic diagram of coherent output power spectrum application.....	21
Figure 2.5 Schematic diagram for the application of the three-microphone method.	23
Figure 2.6 Schematic diagram for applying partial coherence based conditional spectral analysis to signal enhancement technique.	26
Figure 2.7 Range of error of auto-spectrum when the three-microphone technique is applied to a system that contains two correlated sources (from Minami and Ahuja).	29
Figure 2.8 Schematic diagram for applying the five-microphone technique.....	30
Figure 3.1 GTRI/CCRF state-jet anechoic facility interior.	35
Figure 3.2 GTRI/CCRF flight simulation facility interior and tunnel schematic.	36
Figure 3.3 Schematic diagram of test setup for coherence and two-correlation measurements.....	39
Figure 3.4 Conical round nozzle with exit diameter of 1.6 inches.	39
Figure 3.5 Conical round nozzle configurations with tabs with exit diameter of 1.6 inches and tab dimension schematic.	40
Figure 3.6 Conical round nozzle with exit diameter of 0.75 inches.	40
Figure 3.7 Rectangular nozzle of aspect ratio eight with equivalent exit diameter of 1.6 inches.	41

Figure 3.8 Converging-diverging round nozzle with design Mach number of 1.67 and exit diameter of 2.0 inches.	41
Figure 3.9 Schematic diagram of the test setup used in separating the turbulence scales.	42
Figure 3.10 Schematic diagram of test setup for investigating the spatial characteristics of jet noise.	43
Figure 3.11 Schematic diagram of the test configuration used in investigating the limitations of the three-microphone method.	44
Figure 3.12 Schematic diagram of “external-source” configuration.	45
Figure 3.13 Schematic diagram of “internal-source” configuration.	46
Figure 4.1 Cross-correlation with a fixed reference microphone at $\theta = 30^\circ$, Mach 0.9 jet.	52
Figure 4.2 Coherence spectra with a fixed reference microphone at $\theta = 30^\circ$, Mach 0.9 jet.	53
Figure 4.3 Maximum cross-correlation R_{mn} for a Mach 0.9 jet.	55
Figure 4.4 Overall coherence $OACF_{mn}$ for a Mach 0.9 jet.	58
Figure 4.5 Maximum cross-correlation R_{mn} for a Mach 0.2 jet.	60
Figure 4.6 Maximum cross-correlation R_{mn} for a Mach 0.4 jet.	61
Figure 4.7 Maximum cross-correlation R_{mn} for a Mach 0.6 jet.	62
Figure 4.8 Maximum cross-correlation R_{mn} for a Mach 0.8 jet.	63
Figure 4.9 Overall coherence $OACF_{mn}$ for a Mach 0.2 jet.	64
Figure 4.10 Overall coherence $OACF_{mn}$ for a Mach 0.4 jet.	65
Figure 4.11 Overall coherence $OACF_{mn}$ for a Mach 0.6 jet.	66
Figure 4.12 Overall coherence $OACF_{mn}$ for a Mach 0.8 jet.	67
Figure 4.13 Maximum cross-correlation as a function of Mach number and position.	69
Figure 4.14 Overall coherence $OACF_{(30^\circ, n)}$ for nozzle geometries operated at Mach 0.9.	72
Figure 4.15 Overall coherence $OACF_{(60^\circ, n)}$ for nozzle geometries operated at Mach 0.9.	72
Figure 4.16 Overall coherence $OACF_{(90^\circ, n)}$ for nozzle geometries operated at Mach 0.9.	73

Figure 4.17 Overall coherence $OACF_{(30^\circ, n)}$ for nozzle geometries operated at Mach 0.9.	74
Figure 4.18 Overall coherence $OACF_{(60^\circ, n)}$ for nozzle geometries operated at Mach 0.9.	75
Figure 4.19 Overall coherence $OACF_{(90^\circ, n)}$ for nozzle geometries operated at Mach 0.9.	75
Figure 4.20 Overall coherence $OACF_{(30^\circ, n)}$ for nozzle geometries operated at Mach 0.9.	76
Figure 4.21 Overall coherence $OACF_{(60^\circ, n)}$ for nozzle geometries operated at Mach 0.9.	77
Figure 4.22 Overall coherence $OACF_{(90^\circ, n)}$ for nozzle geometries operated at Mach 0.9.	77
Figure 4.23 Cross-correlation with reference microphone at $\theta = 30^\circ$, fully-expanded Mach 1.67 jet.	79
Figure 4.24 Coherence spectra with reference microphone at $\theta = 30^\circ$, fully-expanded Mach 1.67 jet.	80
Figure 4.25 Maximum cross-correlation R_{mm} for a fully-expanded Mach 1.67 jet.	81
Figure 4.26 Overall coherence $OACF_{mm}$ for a fully-expanded Mach 1.67 jet.	82
Figure 4.27 Three-microphone method (using microphones at 30, 35, and 40 degrees) findings at $\theta = 30^\circ$, Mach 0.9 jet exhausting from a 1.6-inch diameter conical round nozzle.	84
Figure 4.28 Three-microphone method (using microphones at 30, 40, and 50 degrees) findings at $\theta = 50^\circ$, Mach 0.9 jet exhausting from a 1.6-inch diameter conical round nozzle.	85
Figure 4.29 Three-microphone method (using microphones at 70, 80, and 90 degrees) findings at $\theta = 70^\circ$, Mach 0.9 jet exhausting from a 1.6-inch diameter conical round nozzle.	85
Figure 4.30 Three-microphone method (using microphones at 70, 80, and 90 degrees) findings at $\theta = 90^\circ$, Mach 0.9 jet exhausting from a 1.6-inch diameter conical round nozzle.	86
Figure 4.31 Three-microphone method results for the 0.75-inch diameter conical round nozzle at $\theta = 30^\circ, 50^\circ, 70^\circ$ and 90° , Mach 0.9 jet.	90
Figure 4.32 Three-microphone method results for the 1.6-inch diameter conical round nozzle with two tabs at $\theta = 30^\circ, 50^\circ, 70^\circ$ and 90° , Mach 0.9 jet.	90
Figure 4.33 Three-microphone method results for the 1.6-inch diameter conical round nozzle with four tabs at $\theta = 30^\circ, 50^\circ, 70^\circ$ and 90° , Mach 0.9 jet.	91

Figure 4.34 Three-microphone method results for the 8:1 rectangular nozzle at $\theta = 30^\circ$, 50° , 70° and 90° , Mach 0.9 jet.....	91
Figure 5.1 Measured coherence values between two completely independent signals. ...	97
Figure 5.2 Percent of measured coherence values between two completely independent signals across all frequencies below a given coherence level.....	97
Figure 5.3 Reduction in coherence of jet noise between two far-field microphones with increasing separation between them (reference microphone positioned at 90° relative to the jet exit).	98
Figure 5.4 Effect of number of averages on coherence values: (a) 128 averages, (b) 512 averages, (c) 1024 averages, and (d) 8195 averages, Mach 0.8 jet, 25% Overlap. ...	100
Figure 5.5 Measured jet noise coherence as function of distance from nozzle centerline, fixed linear separation of 22.5 diameters, 1.6-inch nozzle, Mach 0.8 jet.	102
Figure 5.6 Measured jet noise coherence as function of linear microphone spacing, fixed distance from nozzle centerline of 22.5 diameters, 1.6-inch nozzle, Mach 0.8 jet. ...	103
Figure 5.7 Measured jet noise coherence as function of radial distance from nozzle exit, fixed angular separation of 10 degrees, 1.6-inch nozzle, Mach 0.8 jet.....	106
Figure 5.8 Coherence spectra for microphone pairs spaced at 10 degrees, 1.6-inch nozzle, Mach 0.8 jet.	109
Figure 5.9 Coherence spectra for microphone pairs spaced at 20 degrees, 1.6-inch nozzle, Mach 0.8 jet.	110
Figure 5.10 Coherence spectra for microphone pairs spaced at 30 degrees, 1.6-inch nozzle, Mach 0.8 jet.	110
Figure 5.11 Coherence spectra for microphone pairs spaced at 10 degrees; 1.6-inch round, 0.75-inch round, and 8:1 rectangular nozzles; Mach 0.8 jet.....	112
Figure 5.12 Coherence spectra for microphone pairs spaced at 10 degrees; 1.6-inch nozzle with no, two, and four tabs; Mach 0.8 jet.	113
Figure 5.13 Overall coherence $OACF_{(m, m+20^\circ)}$, for multiple nozzle geometries operated at Mach 0.8.	115
Figure 5.14 Overall coherence $OACF_{(m, m+20^\circ)}$, for multiple nozzle geometries operated at Mach 0.8.	115
Figure 5.15 Overall coherence $OACF_{(m, m+30^\circ)}$, for multiple nozzle geometries operated at Mach 0.8.	116

Figure 5.16 Coherence spectra for microphone pairs spaced at 10 degrees, Mach 1.67 CD nozzle with exit diameter of 2.0 inches, Mach 1.67 jet.	118
Figure 5.17 Coherence spectra for microphone pairs spaced at 10 degrees, Mach 1.67 CD nozzle with exit diameter of 2.0 inches, Mach 1.4 jet.	119
Figure 5.18 Coherence spectra for microphone pairs spaced at 10 degrees, Mach 1.67 CD nozzle with exit diameter of 2.0 inches, Mach 1.9 jet.	120
Figure 5.19 Bar chart showing the overall coherence $OACF_{(m, m+20^\circ)}$ for fully-expanded and non-fully-expanded cases, Mach 1.67 CD nozzle.	121
Figure 5.20 Bar chart showing the overall coherence $OACF_{(m, m+30^\circ)}$ for fully-expanded and non-fully-expanded cases, Mach 1.67 CD nozzle.	122
Figure 6.1 Range of error of auto-spectrum when the three-microphone technique is applied to a system that contains two correlated sources (from Minami and Ahuja).	125
Figure 6.2 Photograph collage and top-view sketch of experimental setup used in the Minami/Ahuja three-microphone method error verification.	127
Figure 6.3 Three-microphone method results at the 60-degree microphone for drivers A and B with relative levels of (a) 20 dB, (b) 10 dB, (c) 5 dB and (d) 0 dB.	128
Figure 6.4 Comparison of the Minami and Ahuja ⁷ prediction to experimental results. .	129
Figure 6.5 Schematic of the numerical simulation.	131
Figure 6.6 Auto-spectra of microphone 2 with one active correlated source buried in uncorrelated noise ($d = 1"$, $\Delta f = 200$ Hz).	132
Figure 6.7 Auto-spectra of microphone 2 with two active correlated sources buried in uncorrelated noise ($d = 1"$, $\Delta f = 200$ Hz).	133
Figure 6.8 Auto-spectra of microphone 2 with three active correlated sources buried in uncorrelated noise ($d = 1"$, $\Delta f = 200$ Hz).	135
Figure 6.9 Auto-spectra of microphone 2 with four active correlated sources buried in uncorrelated noise ($d = 1"$, $\Delta f = 200$ Hz).	136
Figure 6.10 Auto-spectra of microphone 2 with two active correlated sources buried in uncorrelated noise with two-inch microphone spacing ($d = 2"$, $\Delta f = 200$ Hz).	138
Figure 6.11 Auto-spectra of microphone 2 with two active correlated sources buried in uncorrelated noise with four-inch microphone spacing ($d = 4"$, $\Delta f = 200$ Hz).	138

Figure 6.12 Auto-spectra of microphone 2 with two active correlated sources buried in uncorrelated noise with eight-inch microphone spacing ($d = 8''$, $\Delta f = 200$ Hz).	139
Figure 6.13 Auto-spectra of microphone 2 with two active correlated sources buried in uncorrelated noise with 16-inch microphone spacing ($d = 16''$, $\Delta f = 200$ Hz).	139
Figure 6.14 Wave front propagation.....	141
Figure 6.15 Three microphone method results at the 60-degree microphone for (a) source <i>A</i> and (b) source <i>B</i> buried in uncorrelated jet noise.	144
Figure 6.16 Three microphone method results at the 60-degree microphone with two correlated sources buried in uncorrelated jet noise.....	145
Figure 6.17 Three-microphone method results at the 60-degree microphone for sources <i>A</i> and <i>B</i> buried in uncorrelated jet noise with microphone spacing of (a) 10° , (b) 20° , (c) 30° and (d) 40°	147
Figure 7.1 Schematic diagram of (a) external- and (b) internal-source configurations..	151
Figure 7.2 Three-microphone method results for tests where drivers were operated individually and collectively, (a) Mach 0.68 jet + <i>A</i> , (b) Mach 0.68 jet + <i>B</i> , (c) Mach 0.68 jet + <i>A</i> + <i>B</i> (external-source configuration).	153
Figure 7.3 Coherent output power method results for tests where drivers were operated individually and collectively, (a) Mach 0.68 jet + <i>A</i> , (b) Mach 0.68 jet + <i>B</i> , (c) Mach 0.68 jet + <i>A</i> + <i>B</i> (external-source configuration).	155
Figure 7.4 Measured coherence for a single driver (<i>A</i> : $\gamma^2_{(60^\circ, \#1)}$ and <i>B</i> : $\gamma^2_{(60^\circ, \#3)}$, external-source configuration).	157
Figure 7.5 Partial coherence method results, Mach 0.5 jet + <i>A</i> + <i>B</i> (external-source configuration).....	158
Figure 7.6 Three-microphone method results for tests where drivers were operated individually and collectively, (a) Mach 0.46 jet + <i>A</i> , (b) Mach 0.46 jet + <i>B</i> , (c) Mach 0.46 jet + <i>A</i> + <i>B</i> (internal-source configuration).	160
Figure 7.7 Coherent output power method results for tests where drivers were operated individually and collectively, (a) Mach 0.46 jet + <i>A</i> , (b) Mach 0.46 jet + <i>B</i> , (c) Mach 0.46 jet + <i>A</i> + <i>B</i> (internal-source configuration).	162
Figure 7.8 Comparison of three-microphone and coherent output power spectrum findings for (a) Mach 0.46 jet + <i>A</i> , (b) Mach 0.46 jet + <i>B</i> (internal-source configuration).....	164
Figure 7.9 Measured coherence for a single driver (<i>A</i> : $\gamma^2_{(60^\circ, \#1)}$ and <i>B</i> : $\gamma^2_{(60^\circ, \#2)}$, internal-source configuration).	164

Figure 7.10 Far-field microphone arc used in the full-scale engine tests.	166
Figure 7.11 Typical results from full-scale engine (a) aligned versus (b) unaligned coherence study, 60% power.	168
Figure 7.12 Educated results—(a) full frequency span and (b) concentrated frequency span below 1 kHz—via the three-microphone and coherent output power spectrum methods at the 50-degree far-field microphone, 60% power.....	170
Figure 7.13 Educated results—(a) full frequency span and (b) concentrated frequency span below 1 kHz—via the three-microphone and partial coherence methods at the 50-degree far-field microphone, 60% power.	170
Figure 9.1 Normalized uncertainty of auto-power spectra estimates versus number of averages.....	185
Figure 9.2 Normalized systematic uncertainty of cross-power spectra magnitude estimates versus number of averages.....	186
Figure 9.3 Normalized random uncertainty of cross-power spectra magnitude estimates versus number of averages.....	187
Figure 9.4 Random uncertainty of cross-power spectra phase estimates versus number of averages.....	188
Figure 9.5 Normalized systematic uncertainty of coherence function estimates versus number of averages.	189
Figure 9.6 Normalized random uncertainty of coherence function estimates versus number of averages.	189
Figure 9.7 Uncertainty in the calculated correlated results obtained using the three-microphone method at (a) microphones 1 and 3 and (b) microphone 2 and uncertainty in the calculated uncorrelated results at (c) microphones 1 and 3 and (d) microphone 2 relative to $\gamma^2_{(1,3)}$	197
Figure 9.8 Calculated uncorrelated uncertainty at (a) microphones 1 and 3 and (b) microphone 2 relative to $\gamma^2_{(1,3)}$	200
Figure 9.9 Typical three-microphone method results (a single correlated source) with 95% confidence interval uncertainty bars applied.	203
Figure 9.10 Typical three-microphone method results (two correlated sources) with 95% confidence interval uncertainty bars applied.	204
Figure 9.11 Coherent output power uncertainty versus number of averages.	206

Figure 9.12 Typical coherent output power spectrum results (a single correlated source) with 95% confidence interval uncertainty bars applied.	208
Figure 9.13 Typical coherent output power spectrum results (two correlated sources) with 95% confidence interval uncertainty bars applied.	208
Figure 9.14 Typical partial coherence method results with 95% confidence interval uncertainty bars applied.	210

NOMENCLATURE

G	= spectral density function
G_{ii}	= auto-spectral density function for microphone i
G_{jj}	= auto-spectral density function for microphone j
G_{ij}	= cross-spectral density function between microphones i and j
n	= received signal of uncorrelated noise
u	= received signal of correlated noise source
v	= received signal of correlated noise source
y	= sum of received signals
ϕ_{ij}	= phase angle of cross-spectrum of y_i and y_j
α_{ij}	= phase angle of cross-spectrum of u_i and u_j
β_{ij}	= phase angle of cross-spectrum of v_i and v_j
γ_{ij}^2	= coherence function between microphones i and j
H	= transfer function
COP	= coherent output power
R_{mn}	= normalized cross-correlation coefficient between the m th and n th microphones
$p_m(t)$	= pressure time signal of the m th microphone
$p_n(t)$	= pressure time signal of the n th microphone
$\langle x \rangle$	= time average of argument x
$OACF_{mn}$	= overall coherence function between the m th and n th microphones
SPL	= Sound pressure level
U_r	= normalized uncertainty in result r
B_r	= systematic uncertainty in result r
R_r	= random uncertainty in result r
n_d	= number of ensemble averages

SUMMARY

Lighthill's acoustic analogy has long been thought of as the gold standard for predicting jet noise. More recently a new model called the "two-noise source model for jet noise" has emerged. This new model claims that the radiated jet noise is composed of two distinct sources—one associated with the small-scale turbulence and another associated with the large-scale turbulence. The former source is claimed to radiate noise predominantly at larger angles with respect to the downstream jet axis, whereas the large-scale turbulence radiates predominantly at the shallower angles. A key objective of this effort is to experimentally validate this model using two-point space-time correlation and coherence measurements. Upon the successful validation of the two-noise source model for jets exhausting from multiple nozzle geometries driven at Mach numbers ranging from subsonic to supersonic, a three-microphone signal enhancement technique is employed to separate the contribution of the small-scale turbulence from that of the large-scale turbulence in the far-field. This is the first-ever quantitative separation of the contributions of the two turbulence scales in far-field jet noise measurements. Furthermore, by suitable selection of far-field microphone positions, the separation of the contribution of any internal or core noise from that of the jet-mixing noise is achieved. Using coherence-based techniques to separate the contributions of the small-scale turbulence, large-scale turbulence, and any internal or core noise from far-field exhaust noise measurements forms the backbone of this effort.

In the application of coherence-based multiple-microphone signal processing techniques to separate the contributions of the small-scale turbulence, large-scale turbulence, and any internal or core noise in the far-field, research efforts focus on three techniques (1) the coherent output power spectrum method using two microphones, (2) an ordinary coherence method using the three-microphone technique, and (3) the partial-coherence method using five microphones. The assumption of jet noise incoherence between correlating microphone is included in each of these methods. In light of the noise radiation mechanisms described within the framework of the two-noise source model and their spatial characteristics as experimentally determined in the far-field, the assumption of jet noise incoherence is evaluated through a series of experiments designed to study jet noise coherence across a variety of nozzle geometries and jet Mach numbers ranging from subsonic to supersonic. Guidelines for the suitable selection of far-field microphone locations are established.

An additional coherence-based signal enhancement technique that claims to utilize only far-field microphones to separate multiple internal noise sources from jet mixing noise, is investigated for its potential use in future engine noise diagnostics. Specifically, the five-microphone problem associated with the implementation the so-called multi-microphone signal enhancement technique is examined. Extensive work has been done in an attempt to solve the five-microphone problem. Major difficulties in the solving the non-linear system of algebraic equations resulting from its implementation arose. These difficulties are discussed, and the attempted solution routines are documented for the use of future researchers.

CHAPTER 1

INTRODUCTION

The two-noise source model^{1,2} claims that radiated jet noise is composed of two distinct sources—one related to fine-scale turbulence and another associated with large-scale turbulence. Moreover, the model predicts that the directivities of the sound generated by the two turbulence scales are distinctly different. The large-scale structures are claimed to radiate predominately in the downstream on-jet-axis direction; while the small-scale turbulence radiates nearly omni-directional. These directivity characteristics lead to radiated sound fields that are dominated by the large-scale turbulence in the downstream direction and the fine-scale turbulence in the sideline off-jet-axis direction. A key objective of this effort is to investigate the two-noise source model using multi-microphone, coherence-based signal processing techniques. A survey of the spatial characteristics of the sound field has been completed via cross-correlation and coherence techniques. These experiments have provided significant experimental evidence in support of the two-noise source model. Upon the successful validation of the two-noise source model for jets exhausting from multiple nozzle geometries driven at Mach numbers ranging from subsonic to supersonic, three-microphone signal enhancement technique³ has been employed to separate the contribution of the small-scale turbulence from that of the large-scale turbulence in the far-field. This is the first-ever quantitative separation of the contributions of the two turbulence scales in far-field jet noise measurements.

A second objective of this work is to investigate the applicability of coherence-based, multi-microphone techniques when separating internal or core noise buried in jet-mixing noise as measured in the far-field. Specifically, the focus has centered on the use of the signal enhancement techniques described in Halverson and Bendat⁴, Chung³, and Hsu and Ahuja⁵. With the goal of either educing a buried signal or eliminating signal contamination, the aforementioned signal enhancement techniques rely on the measured coherence within the radiated sound field. Specifically, when applied during this work, the methods rely on the assumption that far-field jet noise measured at microphones spaced some distance apart can be considered incoherent due to its distributed nature at most frequencies. Furthermore, they assume that all far-field microphones measure to some degree the self-coherent perfectly correlated signal(s) of interest and mutually independent (i.e., fully incoherent or uncorrelated) jet-mixing noise. Even though Hsu and Ahuja⁵ and Ahuja⁶ have used the assumption that jet noise is incoherent at microphones spaced some distance apart, the jet operating conditions, nozzle geometries, and microphone arrangement for which this assumption holds have never been studied. The present work is intended to fill this gap.

By way of the two-noise source model, the noise generation mechanisms of jet noise that radiate sound in the downstream and sideline directions are physically different; hence, the jet noise coherence measured at microphone pairs in the downstream direction should differ from that measured at microphone pairs in the sideline direction. According to the model, the random small-scale turbulence radiates incoherently in all directions while the coherent large-scale structures radiate sound primarily in the downstream direction. Thus, one would expect the measured coherence between two microphones positioned in

the downstream direction to be more significant than that measured between a pair of equally-spaced microphones positioned in the sideline direction. If this is in fact true, the implementation of coherence-based signal enhancement techniques would require larger microphone spacing in the downstream direction (relative to that in the sideline direction) to ensure jet noise incoherence at all microphones. The coherent nature of jet noise has been examined through a series of experiments designed to study jet noise coherence across a variety of nozzle geometries and jet Mach numbers ranging from subsonic to supersonic. For the first time, extensive coherence data measured for subsonic jet Mach numbers as well as fully-expanded and non-fully-expanded supersonic jet Mach numbers are presented. This data has provided further understanding of the coherent nature of jet noise and valuable insight for developing the functional envelope of coherence-based signal enhancement techniques used in model-scale aeroacoustic experimentation and full-scale engine noise diagnostics. Utilizing this knowledge to suitably select far-field microphones, the contributions of correlated internal or core noise and jet-mixing noise have been separated in proof-of-concept testing in anechoic facilities and in full-scale engine testing.

A third objective of the present investigation is to examine the usefulness of a multiple-microphone signal enhancement technique that claims to utilize only the far-field microphones to separate individual core noise components from jet-mixing noise. The potential usefulness of the so-called multi-microphone method of Minami and Ahuja⁷ in full-scale engine noise diagnostics is immense. Through its successful implementation, the separation of individual core noise sources can be achieved through the use of far-field microphones only; no internal sensors will be necessary. This will allow researchers

to focus noise mitigation efforts on individual core components without the need for mechanical modifications to the engine. Extensive work has been done by the author in an attempt to solve the five-microphone problem of Minami and Ahuja. Major difficulties arose while developing the algorithms to solve the large number of non-linear algebraic equations associated with the five-microphone method. These difficulties are discussed, and the attempted solution routines are documented for the use of future researchers. It has been concluded that the solution of this problem will require a dedicated effort by an expert in the field of numerical methods used to solve large systems of non-linear algebraic equations.

Much of the work mentioned above involves the measurement of coherence and/or use of measured coherence. The significant role that coherence has played in this work lends itself to an explanation of what exactly is meant when referring to coherence and/or—as described below—correlation throughout a sound field. Interference within a signal field is characterized by the interaction of at least two processes. Depending upon the phase relationship between these processes, they combine either constructively or destructively. The characteristic of such interference is defined by the coherence between the two signals. In acoustics, the coherence of two sound waves follows from how well correlated the waves are as quantified by the cross-correlation function, which is a measure of their similarity. Furthermore, the second wave need not be a separate entity; it could be the first wave at a different position within the temporal or spatial domain. This is referred to as self-coherence. Two sound waves are considered fully coherent if they have exactly the domain of definition (i.e., the same spectral content or range of wavelengths) and the same phase relationship within this domain of definition.

Consider the single-input/single-output system shown in Figure 1.1, for any value of frequency, f , the ordinary coherence function between an input $x(t)$ and an output $y(t)$ can be defined in terms of the magnitude of the cross-spectral density function and the auto-spectral density functions of $x(t)$ and $y(t)$.

$$\gamma_{xy}^2(f) = \frac{|G_{xy}(f)|^2}{G_{xx}(f) G_{yy}(f)} \quad (1.1)$$

The cross-spectrum inequality (see Bendat and Piersol⁸ for proof of this inequality) requires that

$$0 \leq \gamma_{xy}^2(f) \leq 1 \quad (1.2)$$

The quantity $\gamma_{xy}^2(f)$ is used to assess the degree of linear dependence between any two random processes. If these random processes are completely linearly correlated, then the coherence function will be equal to one—fully coherent. If they are unrelated (i.e., uncorrelated), the coherence function will be zero—incoherent. The terms coherent and correlated and the terms incoherent and uncorrelated will be used interchangeably throughout the remainder of this work.

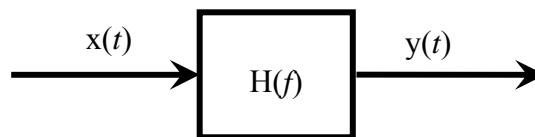


Figure 1.1 Ideal single-input/single-output system.

Bendat and Piersol⁸ considered the single-input/single-output system shown in Figure 1.1. They concluded that if the ordinary coherence function between input $x(t)$ and output $y(t)$, as defined previously, is greater than zero but less than unity, one or more of the following physical conditions must exist.

- (a) Extraneous noise is present in the measurements.
- (b) The system relating $x(t)$ and $y(t)$ is not linear.
- (c) The output $y(t)$ is due to additional inputs other than $x(t)$.

Both cases (a) and (c) can be modeled by the system-block diagram shown in Figure 1.2.

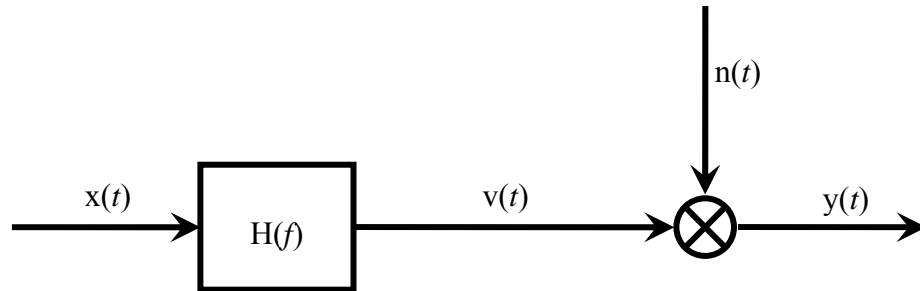


Figure 1.2 Single-input/single-output system with additional input $n(t)$.

Cases (a) and (c) above are representative of physical systems in most aeroacoustic testing. The noise of interest in such experimentation is almost always contaminated by some other noise source. This is especially true in the case of engine noise measurements for both model-scale and full-scale problems. In the case of jet-mixing noise studies in model-scale anechoic facilities, the sources of this contamination noise can range from valve noise to combustion noise to pipe bends upstream of the nozzle exit. For full-scale

engine tests, the far-field acoustic signatures may be contaminated by core noise (e.g., combustor noise, turbine noise, noise due to engine vibration and stability bleed, etc.).

In summary, experimental evidence in support of the two-noise source model^{1,2} has been established through a series of experiments designed to study jet noise coherence across a range of nozzle configurations and jet Mach numbers. The successful separation of the far-field contributions of the turbulence scales has been achieved via the three-microphone method. Based on the coherence results, conclusions concerning the range of applicability of jet noise incoherence in multi-microphone signal enhancement techniques have been drawn and confirmed through the implementation of these techniques in proof-of-concept testing. This knowledge is new to the aeroacoustic community and beneficial to those performing engine noise diagnostics using coherence-based signal enhancement techniques. In fact utilizing this knowledge, the contribution of correlated internal or core noise and jet-mixing noise have been separated in proof-of-concept testing in anechoic facilities and in full-scale engine testing. Lastly, the effort of the author in solving the non-linear system of equations resulting from the implementation of the five-microphone method⁷ has been documented for the use of future researchers.

CHAPTER 2

PREVIOUS WORK

The theoretical work of Lighthill^{9,10} has dominated the study of aerodynamic noise production since its formulation in the early nineteen-fifties. Lighthill introduced an acoustic analogy, in which the unsteady fluid flow is replaced by a volume distribution of equivalent acoustic sources throughout the entire flow field. These sources are embedded in a uniform medium at rest, in which the sources may move. All actual flow dynamics, including the generation of noise within the flow and its interaction with the flow, are included in the strength and distribution of the equivalent acoustic source field. It is in this sense that Lighthill's theory of aerodynamic noise is exact.

Over past 50 years, this theory—commonly referred to as Lighthill's acoustic analogy—has been, unquestionably, the jet noise theory of choice for aero-acousticians. Within its framework, the sources of jet noise are quadrupoles. Many variants of the basic theory (e.g., Proudman¹¹, Ffowcs-Williams¹², Lilley¹³, Phillips¹⁴, Ribner¹⁵, Doak¹⁶, and Goldstein and Rosenbaum¹⁷) have been developed over the years. The source terms of the various modified acoustic analogy theories are not the same, but they are all loosely referred to as quadrupoles. Lilley's approach seems to be the most widely accepted variant of the basic theory with followers including: Tester and Morfey¹⁸, Kharavan et al.¹⁹, Hunter et al.²⁰, Morris and Farassat²¹, and Goldstein²².

Laufer et al.²³ and Schlinker²⁴ appear to be the first to propose an alternative jet noise source model. Their proposed model, consisting of two sources, is based on their own experimental observations. A spherical reflector directional microphone capable of focusing on and measuring the noise radiated from a localized region of a jet was developed to measure the location of jet noise sources. The researchers observed that for high supersonic jets, the locations and distributions of the noise sources radiated in the sideline direction (i.e., 90° relative the nozzle exit) and that radiated in the downstream direction (i.e., 30° relative to the nozzle exit) were distinctly different. Differences in the omni-directional microphone real-time pressure signals at 90° and 30° were also observed. The real-time signal in the 90° direction was found to be very similar to that of a subsonic jet—random but smooth. However, in the 30° direction, numerous shock-like spikes were present throughout the real-time pressure signature. With measured differences between the sideline and downstream directions, Laufer et al.²³ concluded that these differences could only be a direct result of two separate noise sources. As discussed below, the sources of jet noise within the framework of the Laufer et al. model are quite different from those proposed by Tam and Chen¹ and Tam².

2.1 The Two-Noise Source Model

The universal agreement among the aeroacoustic community is that jet-mixing noise is generated by the turbulence of the jet flow. Prior to the nineteen-seventies, jet turbulence was conceived as consisting of numerous small eddies distributed throughout the jet. The presence of large-scale structures (in addition to the classical small-scale structures) of the turbulence in the mixing region of a jet was first reported in the early nineteen-seventies by Crow and Champagne²⁵ and Brown and Roshko²⁶. Since their work, there

has been an abundance of papers in the literature devoted to the measurement, analysis, and numerical simulation of these large-scale structures. A typical optical observation of large-scale turbulence in the mixing layer of turbulent jet flow is depicted in Figure 2.1.

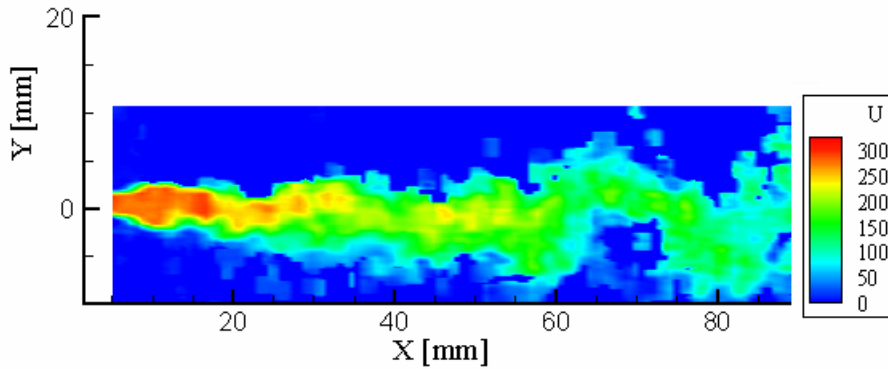


Figure 2.1 PIV image of jet from a rectangular nozzle (20.32 x 3.05 mm) operated at Mach 0.9.²⁷

Large-scale structures are generated near the nozzle, and they tend to grow quickly as they are convected downstream. They are coherent over distances comparable to and often longer than the diameter of the jet in the axial direction. Tam et al.²⁸ indicate that, as sources of jet noise, the small-scale structures are compact whereas the large-scale structures are non-compact.

Optical observations of turbulent jet flows indicate that the large-scale structures are the dominant dynamical entities within the mixing layer of a jet in a region extending from the nozzle exit to some distance downstream of the potential core. The large-scale turbulence structures tend to decay further downstream of the potential core. The most turbulent and, subsequently, most dynamically energetic region of a jet lies within a region extending through the first one and a half potential core lengths of the jet. Optical

observations within this region do not indicate a single monotonic spectrum of turbulence scales. In fact, according to Tam et al.²⁸, there is a distinct separation of turbulence scales—small turbulent eddies with dimensions much smaller than the jet diameter and large-scale structures with dimensions equal to or larger than the jet diameter. Tam et al. further concluded that the physical phenomena that bring about turbulence energy transfer from large to small scales has only a limited duration to act due to the brief fluid residence time within this region; thus, a smooth monotonic turbulence spectrum exists only in the extreme downstream decaying region of the jet.

Based on the work of the early pioneers in the study of turbulence structures—both the small-scale and large-scale structures—and work of Tam and Burton^{29,30} in reference to the description of the physical phenomena by which supersonic instability waves can generate radiated sound, Tam and Chen¹ and Tam² proposed a two-noise source model for the production of jet noise. Figure 2.2 is an illustration of the two noise sources and their radiated sound fields. In this model, the two noise sources are the small-scale turbulence and the large-scale turbulence structures of the jet flow.

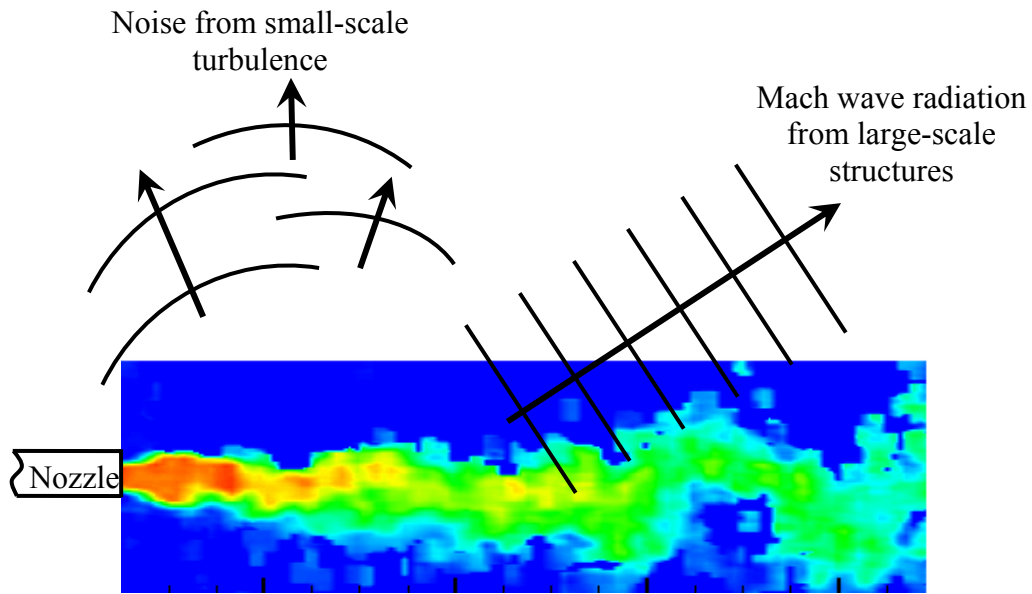


Figure 2.2 The sound field from the fine-scale turbulence and the Mach wave radiation from the large-scale turbulence structures.

The small-scale turbulence is distributed throughout the mixing layer of the jet. According to Tam and Auriault³¹, small-scale turbulence exerts an effective turbulence pressure on its surroundings that is equal to two-thirds of the turbulence kinetic energy. Radiated noise is generated when there are fluctuations in the turbulence pressure arising from fluctuations in turbulence kinetic energy. An envelope of small-scale turbulence is small, and according to Tam et al.²⁸, the noise radiated by this envelope of small-scale turbulence is statistically isotropic. Hence, one would expect the noise from the small-scale turbulence of the jet to be nearly omni-directional. However, due to the downstream convective transport of the small-scale turbulence, the radiated noise is slightly biased toward the downstream direction. In addition, the radiated noise must pass through the jet shear layer to reach the outside; thus, the radiated sound will undergo refraction due to velocity and density gradients in the jet mixing layer. Small-scale

turbulence noise is thus slightly stronger in the downstream direction except in the cone of relative silence created due to the bending of waves away from the jet flow direction via refraction. This effect is said to be especially strong for high-speed heated jets.²⁸

Along with the random small-scale turbulence structures are the large-scale turbulence structures that are spatially coherent in the jet axial direction. The coherent nature of the large-scale turbulence results in interference of the noise radiated from different spatial locations within the jet. This interference—whether it is constructive or destructive—results in highly directional noise radiation. Tam et al.²⁸ postulated that for high-speed jets a simple way to view this noise generation mechanism is to regard the large-scale turbulence structures as a wavy wall moving supersonically (relative to the ambient gas) downstream. Hence, the presence of the highly directional Mach waves depicted in Figure 2.2. Tam and Chen³² stated that, “statistically, the large-scale turbulence structures could be mathematically represented by a stochastic instability-wave model” (i.e., statistically speaking, the large-scale turbulence structures and instability waves of a jet have similar characteristics). The large-scale turbulence structures grow rapidly as they propagate downstream. Beyond the position where the large-scale structures reach their maximum amplitude, the wave becomes a damped wave and its amplitude decreases as the wave further propagates downstream. Tam and Burton^{29,30} pointed out that the growth and decay of the amplitude of the large-scale turbulence structures is important in noise generation.

In order to demonstrate the significance of wave amplitude growth and decay, Tam and Burton^{29,30} considered a constant amplitude wave that behaves like a wavy wall. Mach

wave radiation will only take place if the phase velocity of such a wave is supersonic relative to the ambient speed of sound. Furthermore, Tam et al.²⁸ considered that this wave undergoes amplitude growth and decay. They described such a wave with a broadband of wave numbers (and hence a broadband of phase velocities) rather than a single one. The broadband wave will radiate sound from any region that displays supersonic phase velocity relative to the ambient speed of sound, while no radiation will evolve from the subsonic portion of the wave (just as if it were a subsonic constant amplitude wave). This is the mechanism by which large-scale turbulence structures of high subsonic jets radiate sound to the far-field as first suggested by Tam and Burton^{29,30}.

The two-noise source model^{1,2} claims that both the large-scale and the small-scale turbulence of a jet radiate noise to the far-field in the downstream direction. However, for high-speed jets, the two-noise source model indicates that the noise generated by the large-scale turbulence structures is far more intense. As for the sideline direction, the noise generated by the large-scale structures is less intense and the noise originating from the small-scale turbulence eddies has more influence on the far-field spectra according to the model. The two-noise source model also predicts that the measured data has a well-defined peaky spectrum (due to the large-scale structures) in the downstream direction and a smooth broad spectrum (due to the small-scale turbulence) in the sideline direction. Tam et al.³³ have since verified this prediction and developed two general similarity spectra for jet noise. These universal similarity spectra are the topic of the next section.

2.2 Universal Similarity Spectra

After a thorough analysis of an extensive collection of jet noise data, Tam et al.³³ empirically found two seemingly universal spectra that were able to fit all jet noise spectra, regardless of jet Mach number and temperature. The semi-empirical spectrum functions derived by Tam et al. are listed below. In equations (2.1) and (2.2), the frequency, f , is scaled by f_L , and f_F , respectively. The frequency at the peak of the large-scale turbulence structures noise spectrum is denoted by f_L , and the frequency at the peak of the small-scale turbulence noise spectrum is represented by f_F . Tam et al. deemed this scaling necessary in the absence of an intrinsic time of frequency scale.

$$10 \log F \text{ (dB)} = \left\{ \begin{array}{ll} 5.64174 - 27.7472 \log\left(\frac{f}{f_L}\right); & \frac{f}{f_L} \geq 2.5 \\ \left[1.06617 - 45.29940 \log\left(\frac{f}{f_L}\right) + 21.40972 \left(\log\left(\frac{f}{f_L}\right)\right)^2 \right] \log\left(\frac{f}{f_L}\right); & 2.5 \geq \frac{f}{f_L} \geq 1 \\ -38.19338 \left(\log\left(\frac{f}{f_L}\right)\right)^2 - 16.91175 \left(\log\left(\frac{f}{f_L}\right)\right)^3; & 1 \geq \frac{f}{f_L} \geq 0.5 \\ 2.53895 + 18.4 \log\left(\frac{f}{f_L}\right); & 0.5 \geq \frac{f}{f_L} \end{array} \right. \quad (2.1)$$

$$10 \log G \text{ (dB)} = \left. \begin{array}{l}
29.77786 - 38.16739 \log\left(\frac{f}{f_F}\right); \quad \frac{f}{f_F} \geq 30 \\
-11.8 - \left[\begin{array}{l} 27.2523 \\ + 0.8091863 \log\left(\frac{f}{f_F}\right) \\ + 14.851694 \left(\log\left(\frac{f}{f_F}\right)\right)^2 \end{array} \right] \log\left(\frac{f}{f_F}\right); \quad 30 \geq \frac{f}{f_F} \geq 10 \\
- \left[\begin{array}{l} 8.1476823 \\ + 3.6523177 \log\left(\frac{f}{f_F}\right) \end{array} \right] \left(\log\left(\frac{f}{f_F}\right)\right)^2; \quad 10 \geq \frac{f}{f_F} \geq 1.0 \\
\left[\begin{array}{l} -1.0550362 \\ + 4.9774046 \log\left(\frac{f}{f_F}\right) \end{array} \right] \left(\log\left(\frac{f}{f_F}\right)\right)^2; \quad 1.0 \geq \frac{f}{f_F} \geq 0.15 \\
-3.5 + \left[\begin{array}{l} 11.874876 \\ + 2.1202444 \log\left(\frac{20f}{3f_F}\right) \\ + 7.5211814 \left(\log\left(\frac{20f}{3f_F}\right)\right)^2 \end{array} \right] \log\left(\frac{20f}{3f_F}\right); \quad 0.15 \geq \frac{f}{f_F} \geq 0.05 \\
9.9 + 14.91126 \log\left(\frac{f}{f_F}\right); \quad 0.05 \geq \frac{f}{f_F}
\end{array} \right\} \quad (2.2)$$

Figure 2.3 shows the two similarity spectra plotted as functions of f/f_{peak} , where f is the frequency and f_{peak} is the frequency at the peak of the spectrum (f_L for the large-scale turbulence spectrum and f_F for the small-scale turbulence spectrum).

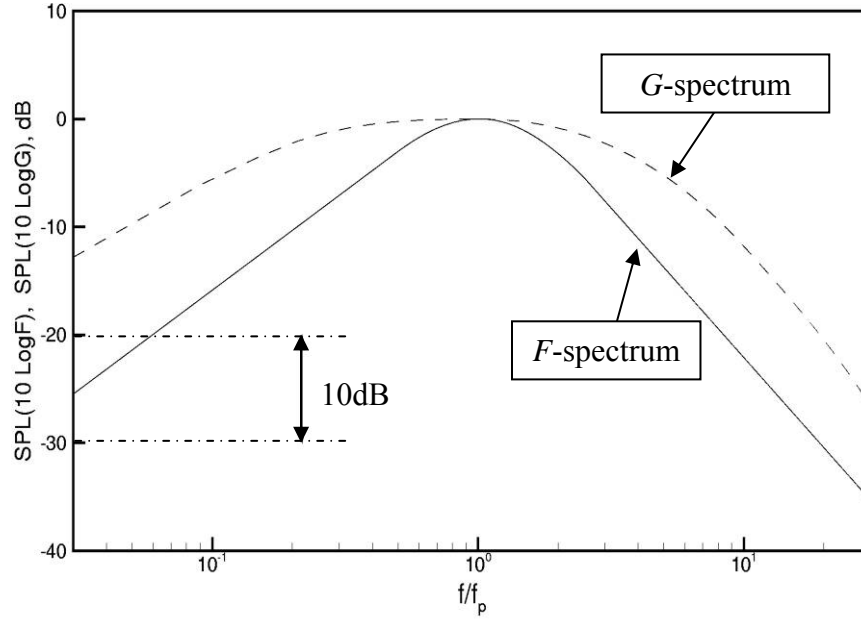


Figure 2.3 Similarity spectra for the two components of turbulence within a jet.³³

The F -spectrum or the peaky spectrum fits a majority of the noise spectra measured in the downstream direction within a cone around the jet axis (i.e., the Mach wave radiation cone as discussed in Tam and Chen¹, Tam², and Tam and Burton²⁹). According to Tam and Burton²⁹, the Mach wave radiation cone angle is a function of the phase velocity of any given region of the large-scale structures, which is in turn a function of the jet Mach number; thus the Mach wave radiation cone angle is a function of the jet Mach number. Tam and Burton define the Mach wave radiation angle as

$$\mu = \arcsin \left(\frac{1 + \frac{a_\infty}{a_j}}{M_j + 1} \right) \quad (2.3)$$

where $\frac{a_\infty}{a_j}$ is the ambient to jet sound speed ratio and M_j is jet Mach number.

The G -spectrum or the broad spectrum fits all noise spectra radiated in the upstream and sideline directions. A superposition of the contributions from the two spectra is required to fit the measured spectra in the transitional directions (i.e., the region where the observation angle transitions from the downstream direction to the sideline direction).

In the literature, many have reported good agreement between the similarity spectra and experimental data. Among these are comparisons with experimental data where coaxial jets (Dahl and Papamoschou³⁴) and converging-diverging, convergent plug, converging-diverging plug, and suppressor nozzles (Tam³⁵) were under examination. Viswanathan^{36,37} provided extensive comparisons between the similarity spectra and measurements over a large range of subsonic Mach numbers and temperature ratios. Tam and Zaman³⁸ compared the similarity spectra with subsonic jet noise data from elliptic, rectangular, tabbed, and six-lobed nozzles. Munro and Ahuja³⁹ showed good agreement for high aspect ratio rectangular nozzles. The existence of two seemingly universal similarity spectra offers strong experimental support for two-noise source model^{1,2}.

2.3 Direct Evidence of the Two Noise Sources

To date the most direct evidence in support of the existence of two noise sources within a jet was presented by Panda et al.^{40,41} in a series of two-point space-time correlation experiments. By correlating the acoustic pressure signal measured by a far-field microphone with the turbulent velocity and density fluctuations measured in an extremely

localized volume (almost point-like measurements) inside a jet utilizing a Rayleigh-scattering-based technique, Panda et al. measured substantial correlation when correlating the localized measurement with a far-field microphone position at 30° relative to the downstream jet axis. The normalized correlation levels between the localized measurement and the 30-degree far-field microphone reached values of 0.22, 0.19, and 0.07 for Mach numbers of 1.8, 1.4, and 0.95, respectively. These correlation levels remained consistent as the measurement point inside the jet was moved radially over the half-width of the jet and axially over a distance of a few jet diameters. However, little correlation was measured when the far-field microphone was moved to the 90° position. These results, along with the observations of Hurdle et al.⁴² and Schaffar⁴³, provide meaningful evidence in support of the proposition that there are two noise sources in a high-speed jet. Since the findings of Panda et al. indicate significant correlation between far-field acoustic pressure measured in the downstream direction (e.g., 30°) and the measured localized turbulence fluctuations, one might conclude that (as postulated by the two-noise source model) the coherence large-scale structures are indeed the dominant noise radiation entity in the downstream direction within the Mach wave radiation cone. Moreover, their results show seemingly insignificant correlation between the far-field pressure measured in the sideline direction (e.g., 90°) and the measured localized turbulence fluctuations. This result can also be considered consistent with the two-noise source model as the dominant source in the sideline direction is the random incoherent small-scale turbulence.

The framework of the two-noise source model and evidence in support of this model gathered to date has been discussed. The previous work concerning the coherence-based,

multiple-microphone signal enhancement techniques considered in this work is focus of the remaining sections within this chapter.

2.4 Signal Enhancement Techniques

As stated earlier this work required the study and/or implementation of four coherence-based signal processing techniques: (1) the coherent output power spectrum method, (2) the three-microphone signal enhancement technique, (3) the partial coherence method, and (4) the five-microphone method. The methodology of each is outlined in the following sections. Some instances of their previous implementation are also discussed.

2.4.1 Coherent Output Power Spectrum

Halvorsen and Bendat⁴ discussed the theory and application of the ordinary coherence function and its associated coherent output power spectrum for acoustic noise measurements. They proposed using the coherent output power spectrum for noise source identification and discussed errors and limitations associated with this technique. The technique requires the source of interest to be instrumented with the fewest number of near-field microphones that adequately represent the source—to minimize the chance of adding extraneous noise—and other microphones be placed in the far-field. The coherent output power spectrum is then computed; thus, the contribution of the source of interest to the far-field acoustic signature can be determined. The use of the ordinary coherence function limits the application of the coherent output power spectrum technique to problems with fully self-coherent, independent (i.e., incoherent with other signals) sources. A diagram of a typical system is shown in Figure 2.4.

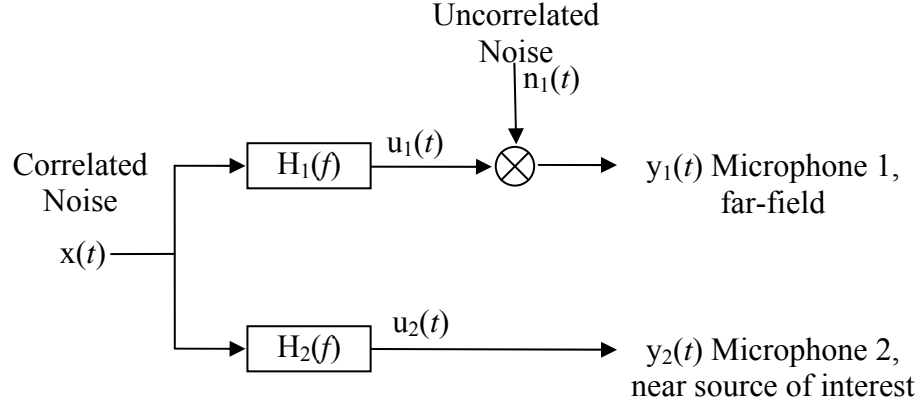


Figure 2.4 Schematic diagram of coherent output power spectrum application.

The coherent output power spectrum at the far-field microphone is given by

$$COP_1 = G_{y_1 y_1} \gamma_{12}^2 \quad (2.4)$$

where $G_{y_1 y_1}$ is the measured auto-power spectrum at microphone 1 and γ_{12}^2 is measured coherence between microphones 1 and 2.

Halvorsen and Bendat⁴ showed that errors associated with propagation time delay can be reduced by time shifting the signals received at the microphones or ensuring that the sampling time is much greater than the propagation delay of the longest path. They also emphasized that significant errors in the calculation of the coherent power output spectrum can result from the presence of periodic components in the data and improper microphone placements. Any periodic components must be removed from the data, because such components will be coherent (i.e., not independent of other sources) regardless of delay. The microphones near the source must be arranged to monitor only sound radiated directly to the far-field measurement position to ensure that any indirectly-

radiated sound will not act as extraneous noise at the measurement location and result in an erroneous estimation of the coherent output power spectrum. Halvorsen and Bendat's technique was later applied to separate core noise from jet noise using an internal-to-far-field coherence function. Karchmer et al.^{44,45} used the ordinary coherence function between internal and far-field microphones and derived the core noise at the far-field locations by calculating the coherent output power. Brooks and Hodgson⁴⁶ used the coherent output power method to remove the effect of open-jet noise from surface pressure measurements to obtain the trailing edge noise.

2.4.2 The Three-Microphone Signal Enhancement Technique

In most aeroacoustic applications, inaccuracies in the coherent output power method due to the presence of uncorrelated extraneous noise are unavoidable. During the experiments of Karchmer et al.⁴⁵, extraneous noise contamination at the internal microphone location caused the derived core noise at the far-field location to be significantly lower than the true level. To overcome this problem, Chung³ developed a three-microphone signal enhancement technique for rejecting transducer flow-noise interference. The three-microphone signal enhancement technique makes use of coherence-function relations between simultaneous pressure measurements at three microphones positioned in the acoustic field and educes from the flow-noise background the power spectrum of the signal in question—whether it be periodic or stationary random—as received at each microphone. The theory allows for an arbitrary arrangement of the microphones within the acoustic field when a single source or a group of completely coherent sources is buried in extraneous flow noise. Regardless of the

signal in question, the extraneous flow noise experienced by each microphone must be mutually independent (i.e., uncorrelated).

The development of the three-microphone method led to six linear equations that can be solved directly using the measured spectral density function at each microphone and the measured coherence function between each pair of microphones. The system representation is shown in Figure 2.5. Here microphones 1, 2, and 3 are assumed to be located within the radiated sound field of a single correlated source buried in uncorrelated noise. The measured signal at each microphone is thus assumed to be the sum of the correlated source and the uncorrelated noise at that microphone.

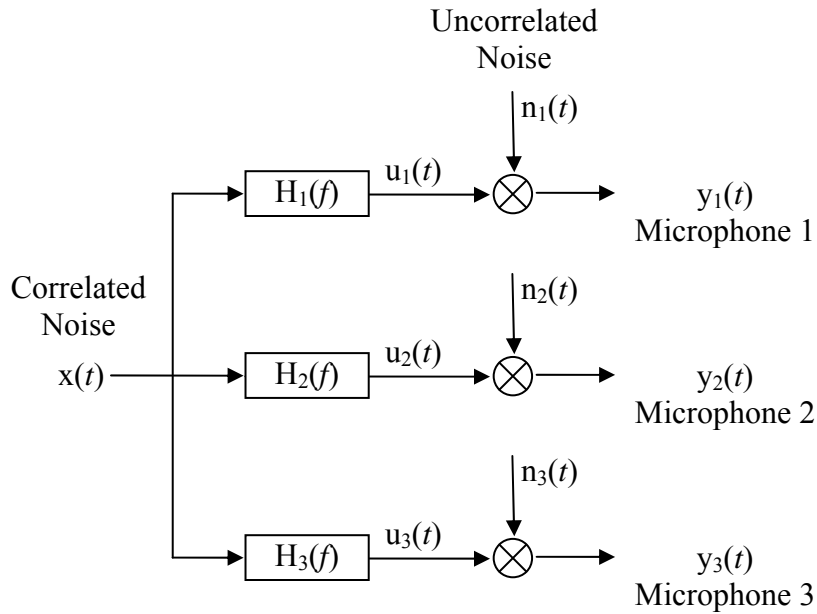


Figure 2.5 Schematic diagram for the application of the three-microphone method.

Given below are the spectral density functions of the correlated signal at each microphone as defined by the three-microphone method.

$$G_{u_1 u_1} = G_{y_1 y_1} \frac{\gamma_{12} \gamma_{13}}{\gamma_{23}} \quad (2.5)$$

$$G_{u_2 u_2} = G_{y_2 y_2} \frac{\gamma_{12} \gamma_{23}}{\gamma_{13}} \quad (2.6)$$

$$G_{u_3 u_3} = G_{y_3 y_3} \frac{\gamma_{13} \gamma_{23}}{\gamma_{12}} \quad (2.7)$$

The following are the spectral density functions of the uncorrelated signal at each microphone.

$$G_{n_1 n_1} = G_{y_1 y_1} - G_{u_1 u_1} \quad (2.8)$$

$$G_{n_2 n_2} = G_{y_2 y_2} - G_{u_2 u_2} \quad (2.9)$$

$$G_{n_3 n_3} = G_{y_3 y_3} - G_{u_3 u_3} \quad (2.10)$$

Chung's signal enhancement technique has been applied in a number of research programs. A few notable studies include Shivashankara⁴⁷, Stoker et al.⁴⁸, and Hsu and Ahuja⁵. Shivashankara⁴⁷ applied Chung's signal enhancement technique to separate aft fan, core, and jet noise components of a large high-bypass ratio engine. In applying Chung's signal enhancement technique, Shivashankara utilized signals gathered from internal and far-field microphones. The use of the internal-to-far-field coherence was shown to be useful for component separation even when the in-duct microphone signals were contaminated by extraneous noise. When separating the core noise, he implemented the signal enhancement technique with two in-duct sensors (positioned such that they were dominated by the core noise) and one far-field sensor (which was assumed to

measure the combined signals). Similarly, for the separation of the fan noise component, he utilized signals from two internal sensors that were dominated by the fan noise and one far-field sensor. The three-microphone signal enhancement technique was also used to reduce the sum of the core plus fan noise from jet-mixing noise received at far-field microphone locations, and the results were compared with those from the use of the internal-to-far-field coherence function and its resulting coherent output power spectrum. Shivashankara showed that with the use of the three-microphone signal enhancement technique and far-field microphones alone, it is possible to separate the sum of the core- and fan-noise components from the jet-mixing noise. However, this technique fails when the separation of multiple individual core noise components from jet-mixing noise is desired.

Stoker et al.⁴⁸ used the three-microphone signal enhancement technique to separate wind-tunnel background noise and boundary layer noise in measurements made in the interior of an automobile tested in a subsonic wind tunnel. They showed that the wind tunnel background noise consisting of motor noise and other dipole sources was mutually coherent between microphone positions. Furthermore they showed that all other noise sources were incoherent; thus, fully validating the assumptions needed to use the three-microphone technique. The three-microphone technique was successfully used to extract known background noise from measured interior noise using two different microphone arrangements: (1) two in-flow microphones and one interior microphone and (2) two flush-mounted (on the surface of the test vehicle) microphones and one interior microphone.

2.4.3 Partial Coherence Method

Hsu and Ahuja⁵ extended Chung's technique to develop a partial-coherence based technique that utilizes five microphones to separate ejector internal mixing noise from far-field acoustic signatures assumed to contain the ejector internal mixing noise, externally generated jet-mixing noise, and another correlated noise presumably from the ejector inlet. The system representation is illustrated in Figure 2.6.

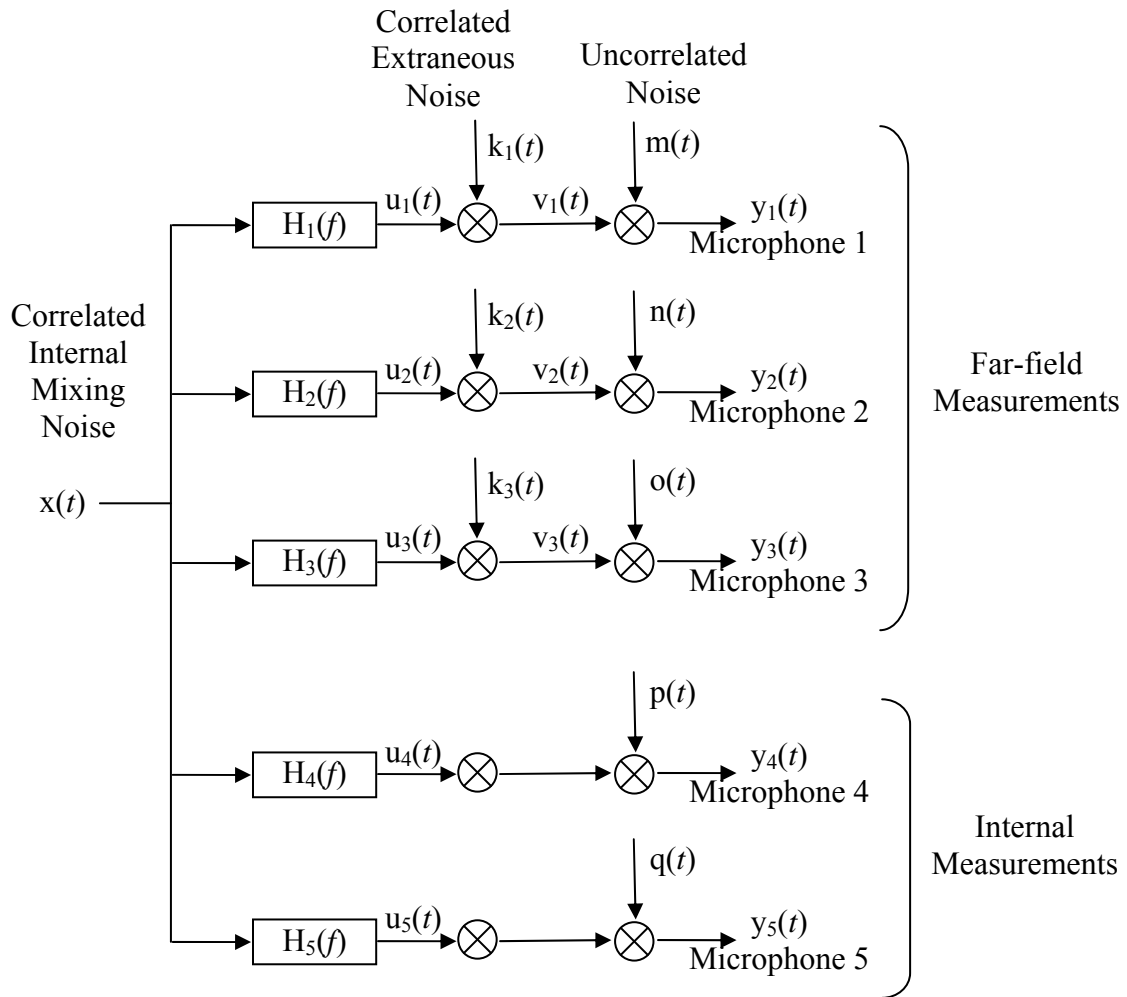


Figure 2.6 Schematic diagram for applying partial coherence based conditional spectral analysis to signal enhancement technique.

The microphones labeled 1, 2, and 3 represent microphones placed in the far-field, and microphones 4 and 5 represent those placed internally. The far-field microphone signals are assumed to measure the sum of the correlated internal noise, the uncorrelated noise, and the noise produced by an extraneous correlated source, while the internally positioned microphones are assumed to measure the correlated internal noise and uncorrelated noise.

Hsu and Ahuja showed that the contribution of the correlated internal mixing noise without the influence of the correlated extraneous noise at the far-field microphones can be calculated as follows:

$$G_{u_1u_1} = \frac{|G_{14}||G_{15}|}{|G_{45}|} \quad (2.11)$$

$$G_{u_2u_2} = \frac{|G_{24}||G_{25}|}{|G_{45}|} \quad (2.12)$$

$$G_{u_3u_3} = \frac{|G_{34}||G_{35}|}{|G_{45}|} \quad (2.13)$$

The correlated extraneous noise can be calculated as follows:

$$G_{k_1k_1} = \frac{\left| G_{12} - \frac{G_{14}G_{52}}{G_{54}} \right| \left| G_{13} - \frac{G_{14}G_{53}}{G_{54}} \right|}{\left| G_{23} - \frac{G_{24}G_{53}}{G_{54}} \right|} \quad (2.14)$$

$$G_{k_2k_2} = \frac{\left| G_{12} - \frac{G_{14}G_{52}}{G_{54}} \right| \left| G_{23} - \frac{G_{24}G_{53}}{G_{54}} \right|}{\left| G_{13} - \frac{G_{14}G_{53}}{G_{54}} \right|} \quad (2.15)$$

$$G_{k_3k_3} = \frac{\left| G_{13} - \frac{G_{14}G_{53}}{G_{54}} \right| \left| G_{23} - \frac{G_{24}G_{53}}{G_{54}} \right|}{\left| G_{12} - \frac{G_{14}G_{52}}{G_{54}} \right|} \quad (2.16)$$

Hsu and Ahuja conducted controlled experiments and successfully compared results from their partial-coherence based five-microphone signal enhancement technique using conditional spectral analysis to results from the coherent output power spectrum method and the three-microphone signal enhancement technique. The methodology assumes that two of the five microphones are dominated by a single correlated source; thus requiring the placement of two microphones adjacent to one of the correlated signals (e.g., if one suspects that one of the correlated signals is produced by the combustor, then two of the five microphones must be placed near the combustor). This requirement clearly restricts the application of this partial-coherence technique when the sources of the correlated signals are unknown.

2.4.4 The Five-Microphone Method

Minami and Ahuja⁷ demonstrated that the errors in the use of the Chung's three-microphone signal enhancement technique can be significant if multiple correlated sources are present at the far-field microphone locations. The error introduced when the three-microphone technique is applied to a system that consisting of two self-correlated

sources (A and B) buried under extraneous noise is shown in Figure 2.7. The error is a function of the relative amplitude of the sound pressure level from the two correlated sources at a given observation position. The error grows infinitely large as the relative level of the two correlated sources approaches zero; conversely, for large values of the relative strength of the two correlated sources, the error is minimized. The latter occurs when one of the sources dominates the other. This discovery led, in part, to the development of the five-microphone methodology.

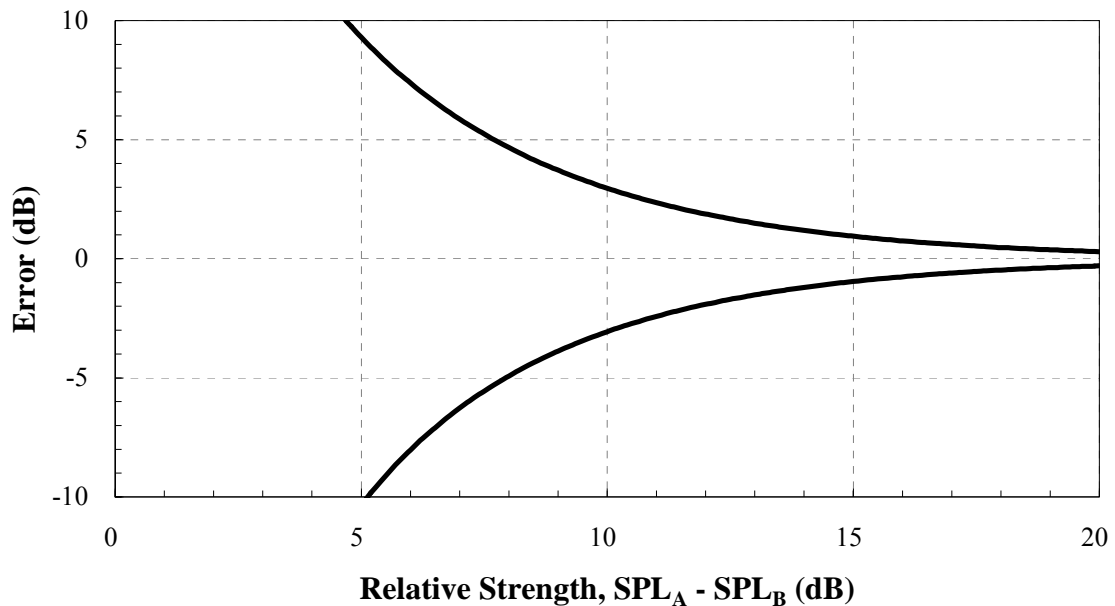


Figure 2.7 Range of error of auto-spectrum when the three-microphone technique is applied to a system that contains two correlated sources (from Minami and Ahuja⁷).

Minami and Ahuja⁷ developed a five-microphone technique for separating two different correlated acoustic sources buried in uncorrelated extraneous noise. The method assumes that all five far-field microphones measure (to some degree) the sum of the two correlated signals and the extraneous noise that is uncorrelated at all far-field microphones across all

frequencies. A schematic representation of the five-microphone system is shown in Figure 2.8.

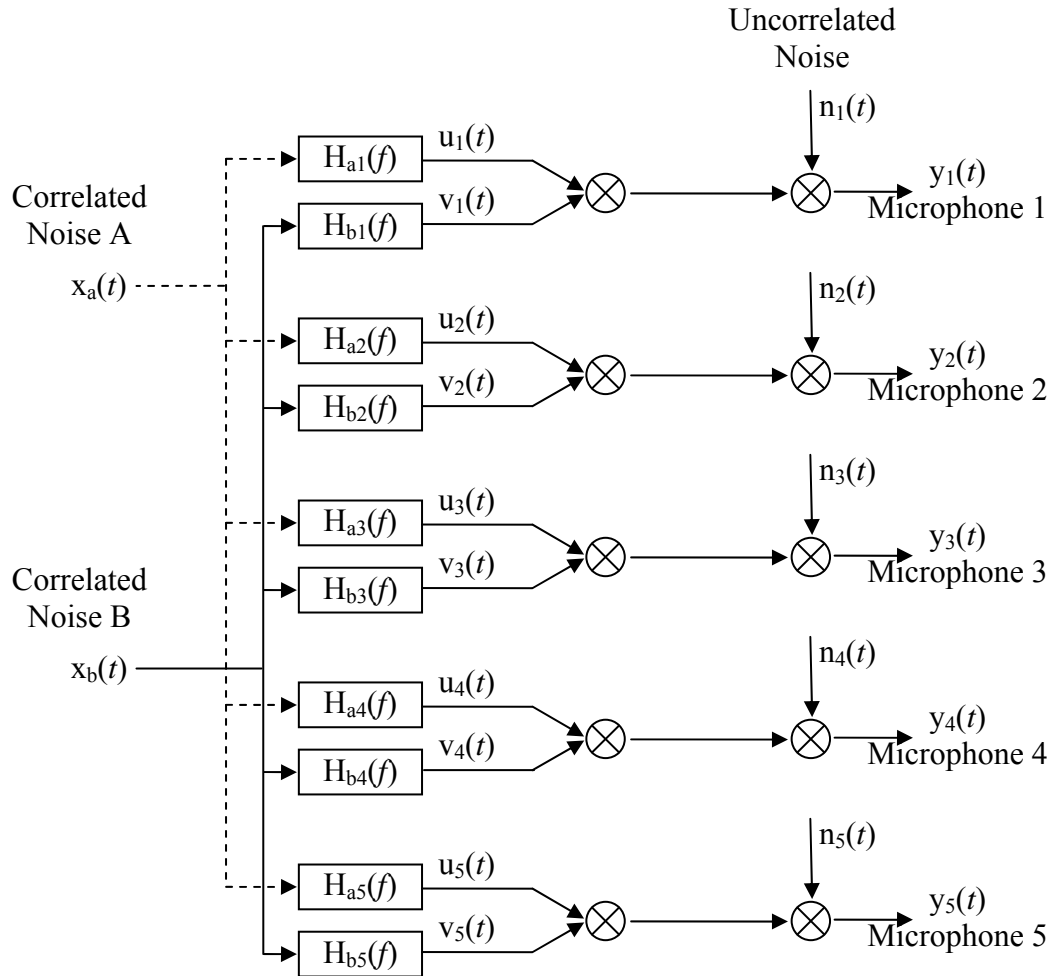


Figure 2.8 Schematic diagram for applying the five-microphone technique.

Figure 2.8 can best be described by considering a typical static jet engine test. In such testing, microphones 1 – 5 would be located in far-field of the radiated sound field produced by a jet engine on a static test-bed. Correlated sources A and B represent some internal sources (say combustor noise and turbine noise). The uncorrelated noise represents any uncorrelated extraneous noise that might be present, such as, jet-mixing

noise. Each microphone is assumed to measure the sum of the correlated two sources and the uncorrelated noise— $u(t) + v(t) + n(t)$. The five microphone-method is used to calculate the contribution of each source— $u(t)$, $v(t)$, and $n(t)$ —at each of the far-field microphones.

Minami and Ahuja identified a set of 55 nonlinear equations that must be solved simultaneously to provide values for 55 unknowns. The nonlinear system of equations is shown below.

$$G_{y_i y_i} = G_{u_i u_i} + G_{v_i v_i} + G_{n_i n_i} \quad (i = 1, 2, \dots, 5) \quad (2.17)$$

$$\begin{aligned} |G_{y_i y_j}| \cos \phi_{ij} &= |G_{u_i u_j}| \cos \alpha_{ij} + |G_{v_i v_j}| \cos \beta_{ij} \\ (i < j; i, j = 1, 2, \dots, 5) \end{aligned} \quad (2.18)$$

$$\begin{aligned} |G_{y_i y_j}| \sin \phi_{ij} &= |G_{u_i u_j}| \sin \alpha_{ij} + |G_{v_i v_j}| \sin \beta_{ij} \\ (i < j; i, j = 1, 2, \dots, 5) \end{aligned} \quad (2.19)$$

$$|G_{u_i u_j}|^2 = G_{u_i u_i} G_{u_j u_j} \quad (i < j; i, j = 1, 2, \dots, 5) \quad (2.20)$$

$$|G_{v_i v_j}|^2 = G_{v_i v_i} G_{v_j v_j} \quad (i < j; i, j = 1, 2, \dots, 5) \quad (2.21)$$

$$\alpha_{12} + \alpha_{23} = \alpha_{13} \quad (2.22)$$

$$\alpha_{12} + \alpha_{24} = \alpha_{14} \quad (2.23)$$

$$\alpha_{12} + \alpha_{25} = \alpha_{15} \quad (2.24)$$

$$\alpha_{23} + \alpha_{34} = \alpha_{24} \quad (2.25)$$

$$\alpha_{23} + \alpha_{35} = \alpha_{25} \quad (2.26)$$

$$\beta_{12} + \beta_{23} = \beta_{13} \quad (2.27)$$

$$\beta_{12} + \beta_{24} = \beta_{14} \quad (2.28)$$

$$\beta_{12} + \beta_{25} = \beta_{15} \quad (2.29)$$

$$\beta_{23} + \beta_{34} = \beta_{24} \quad (2.30)$$

$$\beta_{23} + \beta_{35} = \beta_{25} \quad (2.31)$$

The quantities indicated by y and ϕ are known; while the 55 unknown quantities include:

$$G_{u_i u_i}, G_{v_i v_i}, G_{n_i n_i} \quad (i = 1, 2, \dots, 5)$$

$$|G_{u_i u_j}|, |G_{v_i v_j}|, \alpha_{ij}, \beta_{ij} \quad (i < j; i, j = 1, 2, \dots, 5)$$

The nonlinear system of equations resulting from the implementation of the five-microphone technique must be solved numerically. Validation of this signal enhancement technique was carried out via simple numerical simulations. Also note that, in the development of the five-microphone method, Minami and Ahuja⁷ derived an expression for the auto-spectrum of a single correlated signal buried in extraneous noise identical to that of Chung³; however, the mathematical derivation of these acoustic signal separation methods are quite different.

2.5 Summary

In summary, Lighthill pioneered jet noise research with his acoustic analogy approach. This model has long been thought of as the gold standard in the area, but since the advancement of the two-noise source model^{1,2}, there is increasing evidence that this model may be more correct and thus better. Tam et al.³³ have provided extensive

comparison of the measured data with the predictions of the two-noise source model for limited Mach numbers and nozzle geometries. Also, many coherence-based techniques have been utilized in separating upstream noise from jet-mixing noise. Methods of note are those developed by Halverson and Bendat⁴, Chung³, Hsu and Ahuja⁵. In addition, Minami and Ahuja⁷ have developed and verified numerically the so-called five-microphone technique, which in theory allows for the separation of two correlated sources buried in uncorrelated noise.

CHAPTER 3

EXPERIMENTAL PROGRAM

The experimental program employed in this work consisted of two-point correlation, coherence, auto-spectra, and cross-spectra measurements made in the anechoic facilities located at the Georgia Tech Research Institute/Cobb County Research Facility (GTRI/CCRF). These measurements were made in order to examine the role of the turbulence scales present in jet flow in the generation of jet-mixing noise. They also helped in determining the alignment and separation of microphones to ensure jet noise incoherence when implementing the coherence-based signal enhancement techniques. The findings of these experiments were applied in proof-of-concept testing in the GTRI/CCRF anechoic facilities where electro-acoustic drivers were used to generate correlated noise and a jet was used to produce uncorrelated noise. This experimental data helped identify the limitations of the three-microphone method for separating any internal or core noise from jet-mixing noise in model-scale and full-scale experimentation. The application of the coherent output spectrum, the three-microphone, and the partial coherence methods required the acquisition of coherence, auto-spectra, and cross-spectra data. Such data was gathered in the GTRI/CCRF anechoic chamber and on a Honeywell static engine test bed. The facilities and experimental setups used in during this work are discussed below.

3.1 Anechoic Facilities

The GTRI/CCRF static-jet and flight simulation anechoic facilities were utilized during all model-scale testing. The static-jet anechoic facility is shown in Figure 3.1. The interior surfaces of the 22 x 20 x 28 feet chamber are lined with 15-inch polyurethane foam wedges, rendering the facility 99 percent echo free at frequencies above 200 Hz (for broadband or pure tone signals). Two independently controlled air supply ducts allow single and co-annular jet noise measurements to be made. Primary and secondary flows may each be heated to approximately 1500°F. In-line duct mufflers minimize the propagation of unwanted noise generated upstream into the anechoic chamber. A 300-psi compressor supplies clean, dry air to the facility. A cherry-picker crane is used to gain access to instrumentation and test installations mounted throughout the chamber. The crane is stowed by remote control, under an anechoic cover during all acoustic testing operations. Microphones may be placed anywhere in the room so long as they are positioned more than 15 inches from the wedge tips, in order to avoid any wedge near-field effects.

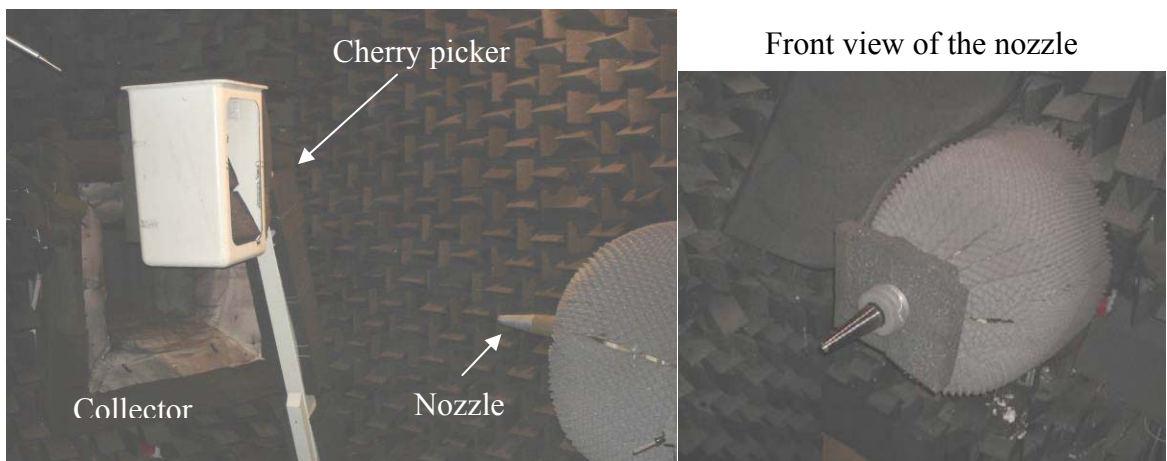


Figure 3.1 GTRI/CCRF static-jet anechoic facility interior.

The second facility, the flight simulation facility, was used sparingly during the early stages of this work and is shown in Figure 3.2. The flight simulation facility is an open jet wind tunnel in an anechoic chamber. The surfaces of the 14 x 14 x 20 feet chamber surrounding the free-jet test section are lined with 15-inch polyurethane foam wedges, rendering the facility 99 percent echo free at frequencies above 200 Hz (for broadband or pure tone signals). The chamber is mounted on colloquial springs to isolate it from the rest of the acoustics laboratory. A spring-tensioned cable floor, suspended from the walls, provides easy access to the interior of the chamber for instrumentation and hardware changes. Like the static-jet anechoic facility, the flight simulation jet supply originates from the main compressor and microphones may be placed anywhere in the room as long as they positioned more 15 inches from the wedge tips.

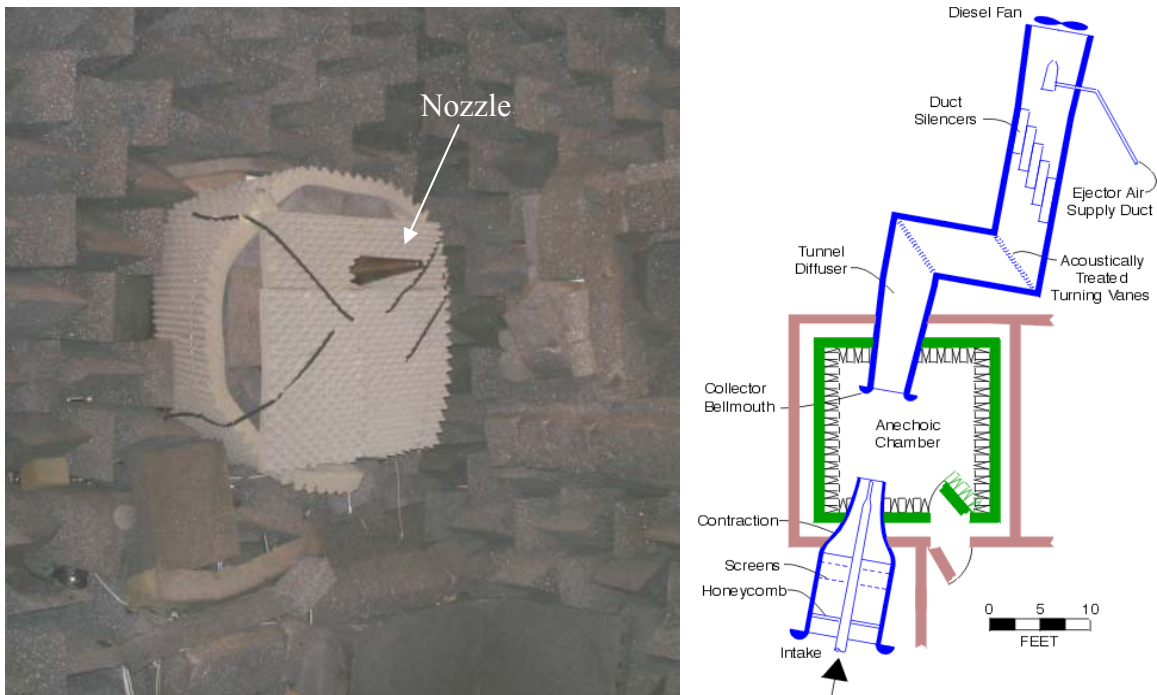


Figure 3.2 GTRI/CCRF flight simulation facility interior and tunnel schematic.

3.2 Investigating the Role of the Turbulence Scales

The role of the small-scale and large-scale turbulence in the generation of jet noise was investigated via cross-correlation and coherence measurements. Additionally, the contributions of each to the far-field were separated through the use of the three-microphone signal enhancement technique. The experiments conducted during this investigation are outlined below, and the findings of this investigation are discussed in Chapter 4.

3.2.1 Cross-Correlation and Coherence Measurements

Coherence and two-point correlation measurements were made with microphones positioned in the far-field of jets exhausting from multiple nozzle geometries operated at a range of Mach numbers. In each experiment, a single jet was monitored by nine microphones spaced equally apart in 10-degree increments ranging from 20° to 100° relative to downstream jet axis. The microphones were positioned along a polar arc located 10 feet radially from the nozzle exit. A schematic diagram of the setup is shown in Figure 3.3. Data was obtained for jet exit Mach numbers ranging from 0.2 to 0.9 exhausting from multiple nozzles. A fully-expanded Mach 1.67 jet exhausting from a converging-diverging nozzle was also observed. All nozzle geometries are listed below:

- Two conical round nozzles
- A two tabbed conical round nozzle configuration
- A four tabbed conical round nozzle configuration
- A rectangular nozzle with aspect ratio of 8

- A Mach 1.67 converging-diverging nozzle

The nozzles are pictured in Figure 3.4 – Figure 3.8. The conical round nozzles have exit diameters measuring 1.6 and 0.75 inches. The pair of tabbed configurations included a two-tabbed and a four-tabbed configuration. The tabs are equally spaced along the circumference of the exit plane of the 1.6-inch round nozzle. In the two tab case, the tabs were placed 180° apart on opposite faces of the exit. In the four tab case, tabs were placed 90° apart along the circumference. The rectangular nozzle has an equivalent exit diameter of 1.6 inches. The exit diameter of the Mach 1.67 CD nozzle is 2.0 inches. The use of multiple nozzle geometries was intended to investigate the role of the turbulence scales in instances where the physical characteristics of the jet (i.e., boundary layer thickness, mixing enhancement, and symmetry) are different. As compared to the 1.6-inch conical round nozzle with no tabs, the 0.75-inch round nozzle is expected to produce a thinner boundary layer, the rectangular nozzle with equivalent exit diameter is expected to produce an axisymmetric flapping instability and a thinner boundary layer, and the tabbed configurations are expected to enhance the mixing within the jet. The expected impact of each nozzle is discussed in more detail in Chapter 4, and the subsequent findings from the use of each nozzle are discussed in Chapter 4.

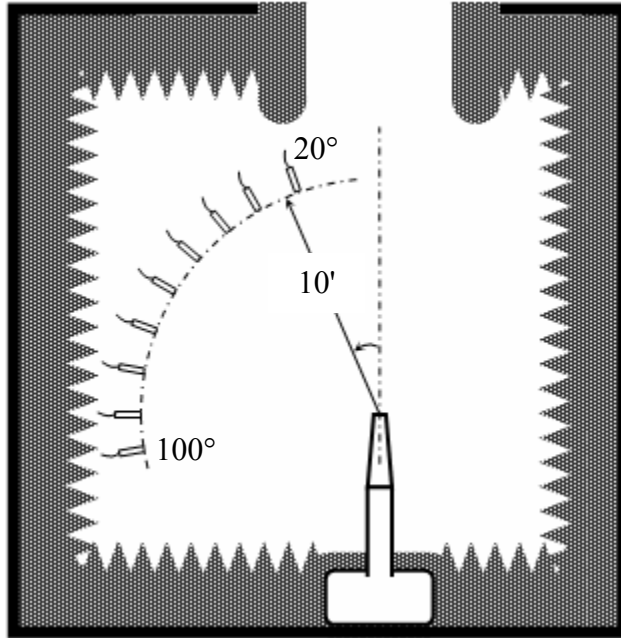


Figure 3.3 Schematic diagram of test setup for coherence and two-correlation measurements.

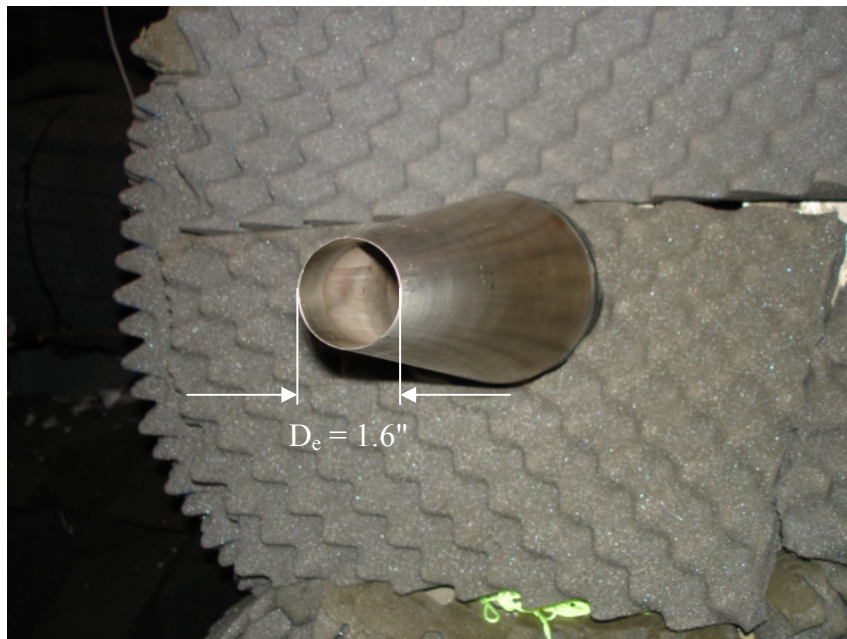
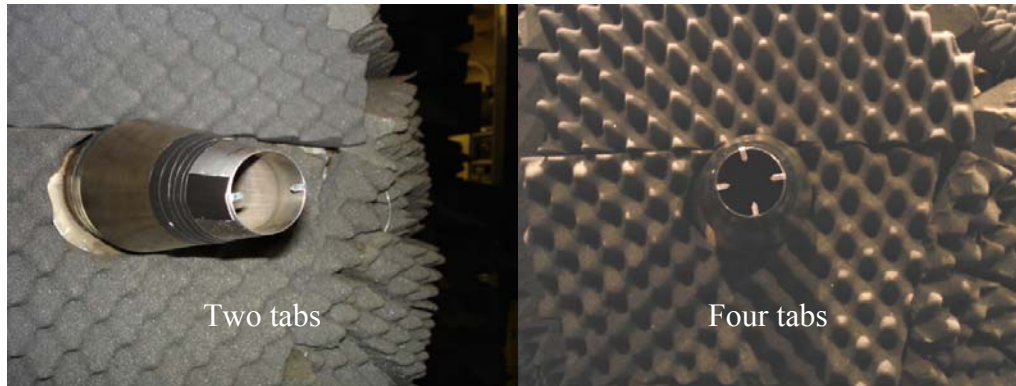


Figure 3.4 Conical round nozzle with exit diameter of 1.6 inches.



Tab Dimensions:

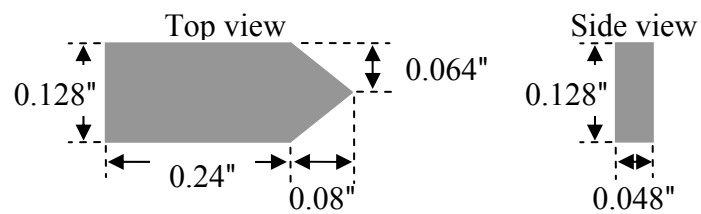


Figure 3.5 Conical round nozzle configurations with tabs with exit diameter of 1.6 inches and tab dimension schematic⁴⁹.

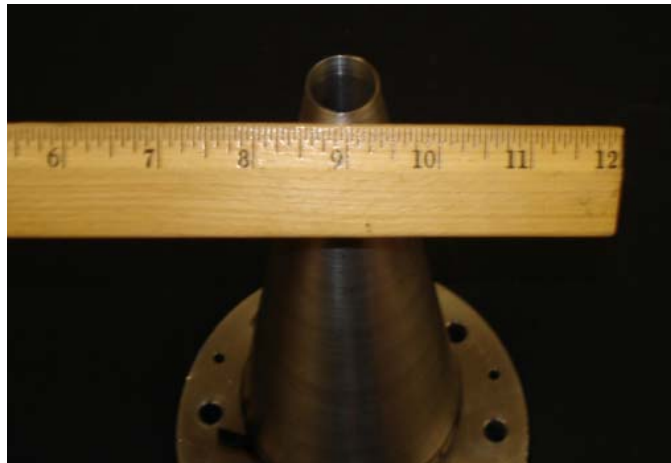


Figure 3.6 Conical round nozzle with exit diameter of 0.75 inches.

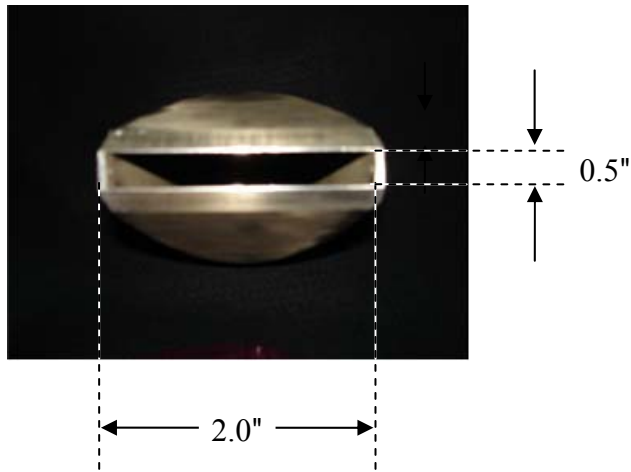


Figure 3.7 Rectangular nozzle of aspect ratio eight with equivalent exit diameter of 1.6 inches.

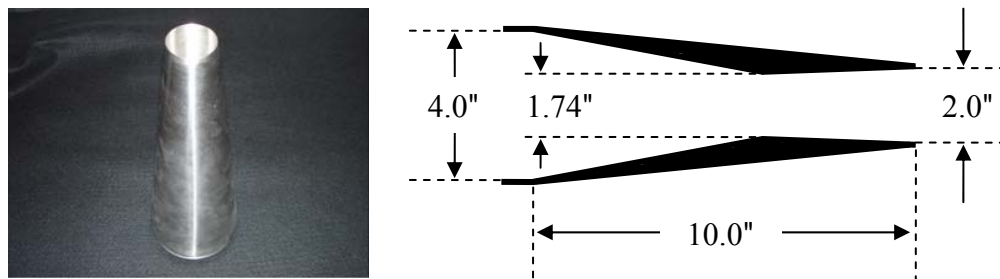


Figure 3.8 Converging-diverging round nozzle with design Mach number of 1.67 and exit diameter of 2.0 inches.

3.2.2 Implementation of the Three-Microphone Method

The three-microphone method was implemented to separate the contribution of the small-scale turbulence from that of the large-scale turbulence in the far-field. Such implementation required the measurement of coherence and auto-spectra data with microphones positioned in the far-field. Nozzles tested include the 1.6-inch and 0.75-inch round nozzles, the tabbed nozzles configurations, and the rectangular nozzle described to above (e.g., those shown in Figure 3.4 – Figure 3.7). All nozzles were

operated at a jet exit Mach number of 0.9. The experimental setup is shown in Figure 3.9.

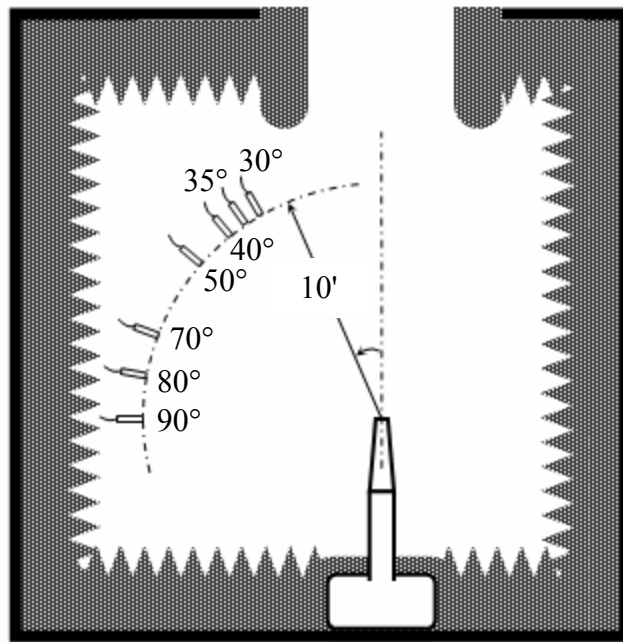


Figure 3.9 Schematic diagram of the test setup used in separating the turbulence scales.

3.3 Investigating the Applicability of the Jet Noise Incoherence Assumption

In order to gather information concerning the spatial nature of radiated jet noise, coherence data were measured as a function of microphone alignment (polar vs. linear), observation distance from the nozzle exit, microphone separation, nozzle geometry, and jet exit Mach number. The nozzle geometries tested are identical to those discussed in Section 3.2.1. Subsonic Mach numbers ranging from 0.2 to 0.9 were studied. Mach numbers in the supersonic regime ranged from 1.0 to 2.0. The basic test setup is shown in Figure 3.10. The polar microphone arc is shown on the left and, linear microphone array is shown on the right. The distance from the surface of the microphones located

within the polar arc to the nozzle exit is indicated by R_c ; while the distance from the nozzle exit to the microphones positioned in the linear array is represented by R_l . The spacing within the linear array is denoted as S . Findings from this experimentation are discussed in Chapter 5.

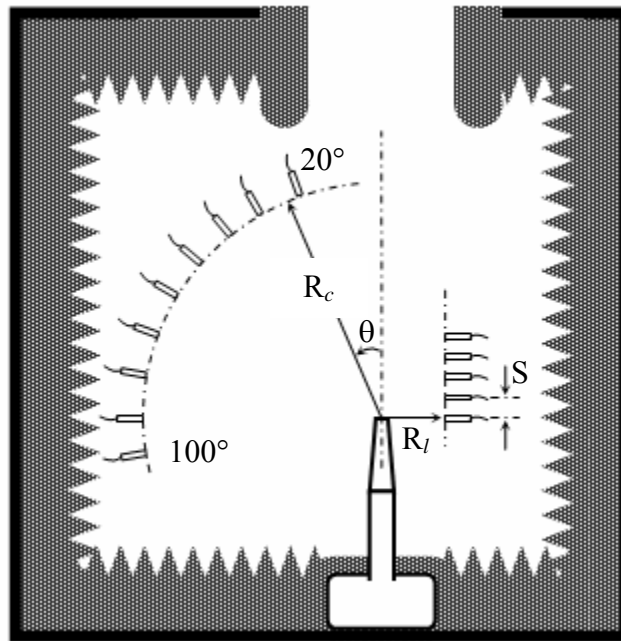


Figure 3.10 Schematic diagram of test setup for investigating the spatial characteristics of jet noise.

3.4 Experimentally Identifying the Limitations of the Three-Microphone Method

In this portion of the experimental program, auto-spectra and coherence data have been measured in the static-jet anechoic facility for analysis via the three-microphone method. The basic test configuration is depicted in Figure 3.11 and consisted of a single jet and two self-correlated but mutually uncorrelated electro-acoustic noise sources (i.e., the drivers are driven in such a way the each is correlated with itself at any two measurements positions in the far-field and they are uncorrelated with each other

throughout the radiated sound field; this term is synonymous with “self-coherent but mutually incoherent sources”). The spacing of the drivers varied throughout these tests. The microphones were spaced from 20° to 100° (relative to the downstream jet axis) at 10-degree intervals along a polar arc positioned 10 feet from the nozzle exit plane. The details of and the findings from this experimentation are discussed in the Chapter 6.

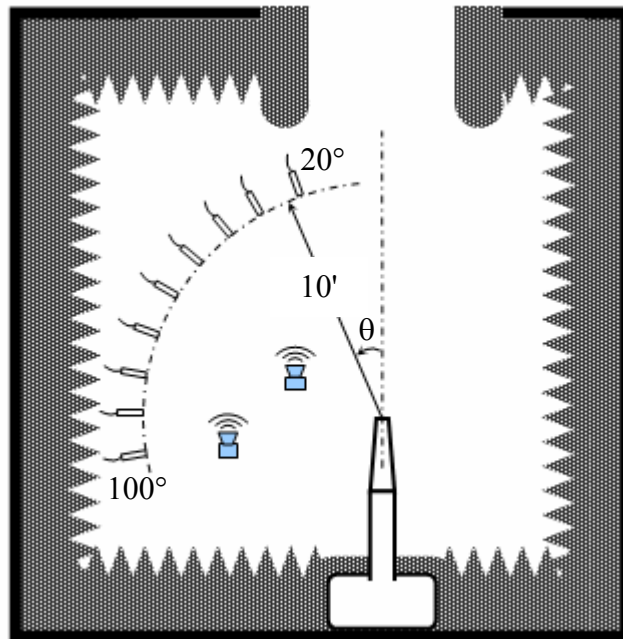


Figure 3.11 Schematic diagram of the test configuration used in investigating the limitations of the three-microphone method.

3.5 Model-Scale Acoustic Experimentation

The model-scale acoustic noise experimentation portion of this program consisted of proof-of-concept testing in model-scale anechoic facilities. The proof-of-concept testing was conducted with two configurations. The first configuration consisted of two independently correlated sources mounted outside the jet nozzle (with the option of the introduction of uncorrelated jet-mixing noise). The second configuration consisted of

two independently correlated sources mounted within a jet-supply duct. The former is referred to as the “external-source” configuration (see Figure 3.12), and the latter is termed the “internal-source” configuration (see Figure 3.13). Each configuration relies on strategically placed far-field microphones to educe the acoustic driver signals buried in jet-mixing noise.

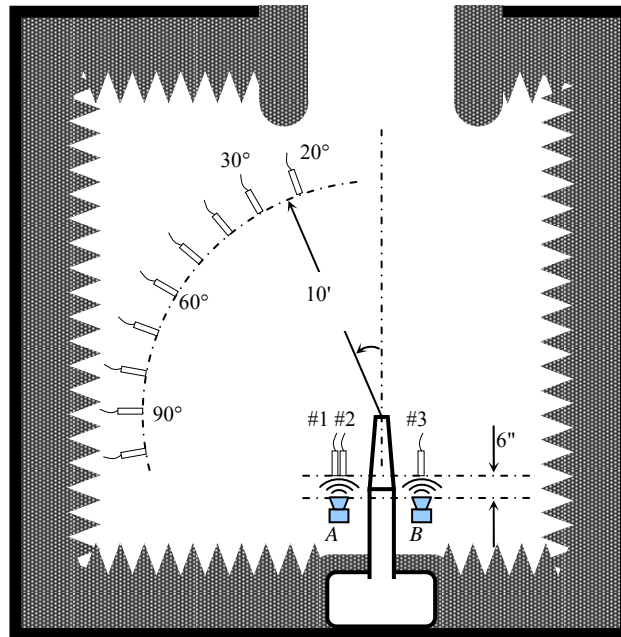


Figure 3.12 Schematic diagram of “external-source” configuration.

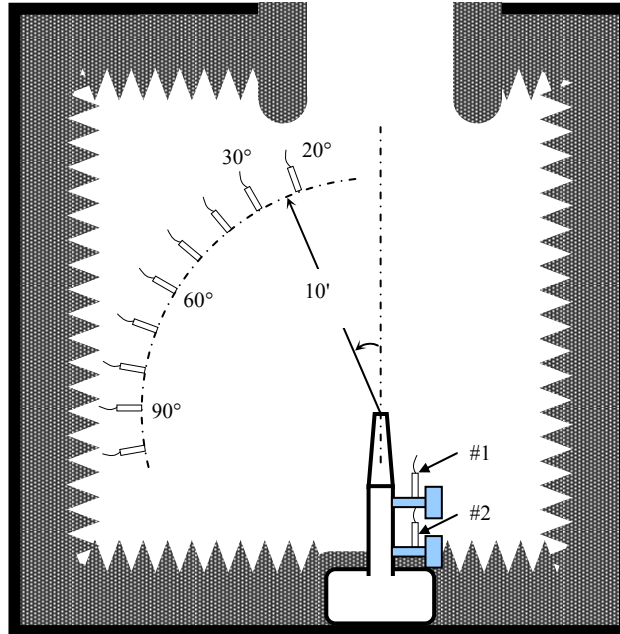


Figure 3.13 Schematic diagram of “internal-source” configuration.

In the external-source configuration, the two self-coherent electro-acoustic driver sources were mounted outside the jet-supply duct. A schematic of the external-source configuration test setup is shown in Figure 3.12. These sources were independently driven by separate signal generators (capable of producing both pure tone and broadband signals) and amplifiers to ensure that the sources were self-coherent, yet uncorrelated with each other and the jet-mixing noise. In this test, first only the acoustic drivers were operational (both individually and collectively). These operating conditions provided the spectra due to each acoustic driver alone and the pair of acoustic drivers at the far-field microphones. The jet was then turned on (along with each individual driver and the pair) to provide uncorrelated extraneous noise. Finally, the jet was operated alone. With both the jet and the acoustic driver(s) operating simultaneously, it was not always possible to distinguish the contribution of the acoustic driver(s) to the far-field spectrum by direct visual observation of the measured far-field spectrum. The contributions of the driver(s)

were determined using the previously discussed multi-microphone signal enhancement techniques. These calculated acoustic driver spectra are compared with the measured spectra from the tests where only the drivers were operational.

The internal-source configuration consisted of two coherent electro-acoustic driver sources mounted upstream within a jet-supply duct to simulate internal or core noise. A schematic of the internal-source configuration test setup is shown in Figure 3.13. The sources were independently driven to ensure self-coherence and incoherence with each other and also with the jet-mixing noise. Operating conditions again included: (1) a single acoustic driver, (2) both drivers collectively, (3) a single acoustic driver plus jet, and (4) two acoustic drivers plus the jet. The aforementioned multi-microphone signal enhancement techniques were utilized to separate the contributions of the driver(s) and the jet from the noise spectra measured by the far-field microphones. Once again, the validity of the calculated results was determined through the comparison with the measured spectra obtained with the jet off.

3.6 Full-Scale Engine Noise Diagnostics

During the involvement of the author and his advisor (Dr. K. K. Ahuja) in the NASA/Honeywell sponsored Engine Validation Noise Reduction Technologies (EVNERT) program, full-scale engine test data were gathered on an industry standard static engine test bed with acoustic measurement capabilities. The details of the testing are not yet fully available for public release. The experimental procedures and the setup configuration recommended by the author and his advisor during their involvement in the EVNERT program are discussed briefly in Chapter 7. The data analysis was done

through the utilization of multi-microphone techniques. Both internal and external sensors were used in order to validate the results from the far-field microphone measurements. Typical findings from this experimentation are discussed (without full disclosure) in Chapter 7. Full disclosure of the results from this portion of the program requires the consent of NASA/Honeywell. The author, Dr. Ahuja, and Dr. Jeff Mendoza (Honeywell Aerospace) are in the process of submitting an abstract for a paper discussing the results of the full-scale engine testing for the 14th AIAA/CEAS Aeroacoustics Conference to be held in Vancouver, Canada in May 2008.

CHAPTER 4

SMALL-SCALE VERSUS LARGE-SCALE CONTRIBUTIONS

The primary focus of this chapter is the determination of the contributions—both qualitatively and quantitatively—of the small-scale and large-scale turbulence structures as applied to the generation of radiated jet noise. As stated earlier, the two-noise source model predicts that the noise generation mechanisms of jet noise that dominate the sound field in downstream and sideline directions are physically different. The spatially coherent large-scale turbulence structures are said to radiate primarily in the downstream direction, while the random incoherent small-scale turbulence structures dominate the sound pressure signal in the sideline direction. To obtain information about the nature of the radiated sound field of a jet in the polar plane, microphone cross-correlation and coherence measurements were made for a series of nozzle geometries and jet Mach numbers. Additionally, the three-microphone method has been implemented to separate the contributions of the turbulence scales at microphones positioned in the far-field. This information is vital to the declaration of the validity of the two-noise source model. Furthermore, this study provides the first-ever quantitative separation of the contributions of the small-scale and the large-scale turbulence to measured total jet noise in the far-field.

4.1 Cross-Correlation and Coherence Measurements

The two-noise source model implies that jet noise exhibits greater coherence within the region where large-scale turbulence structures are dominant. This region lies within the Mach wave radiation cone as indicated in Figure 2.2. Moreover, due to the random incoherent nature of the small-scale turbulence, which (according to the two-noise source model) is the dominant noise radiation entity outside of the Mach wave radiation cone, very little coherence is predicted outside of this region. A series of cross-correlation and coherence measurements were made for both subsonic and supersonic jets in order to investigate these predictions. Sampling parameters of 1024 averages, 25% overlap, 24 Hz bandwidth, and a span of 76.8 kHz were utilized during the data acquisition. The degree of correlation within the radiated sound field has been quantified through the use of the two-point cross-correlations between microphone pairs positioned within the sound field. The two-point cross-correlation results are reported in the form of the normalized cross-correlation coefficient, $R_{mn}(\tau)$, which is defined by

$$R_{mn}(\tau) = \frac{\langle p_m(t)p_n(t+\tau) \rangle}{\langle p_m^2(t) \rangle^{\frac{1}{2}} \langle p_n^2(t) \rangle^{\frac{1}{2}}} \quad (4.1)$$

where $p_m(t)$ is the pressure time signal of the m th microphone, $p_n(t)$ is that of the n th microphone, and $\langle \rangle$ indicates a time-averaged quantity. The correlations have also been accessed in the frequency domain via the use of measured ordinary coherence, γ_{mn}^2 , which is defined by

$$\gamma_{mn}^2(f) = \frac{|G_{mn}(f)|^2}{G_{mm}(f) G_{nn}(f)} \quad (4.2)$$

where $G_{mn}(f)$ is the measured cross-spectral density between the m th and n th microphones, and $G_{mm}(f)$ and $G_{nn}(f)$ are the measured auto-spectral density at the m th and n th microphones, respectively.

4.1.1 Subsonic Jets

Measured normalized cross-correlation $R_{(30^\circ, n)}$, $n = 20^\circ, 40^\circ, 50^\circ, \dots, 100^\circ$ as a function of delay time τ for a Mach 0.9 jet exhausting from a 1.6-inch diameter conical round nozzle is shown in Figure 4.1. The 30-degree microphone is the fixed reference; thus, all delays are relative to the 30-degree microphone. The characteristic shape of the cross-correlation curve is shown here. Furthermore, the results indicate the lack correlation when the second microphone is outside the Mach wave radiation cone depicted in Figure 2.2. This is indicated the extreme low level correlation depicted in Figure 4.1 for those plots where the correlating microphone is positioned beyond 50° relative to the downstream jet axis. These observations are further confirmed by analyzing the correlations between the 30-degree microphone and the other microphones in the frequency domain. Coherence spectra for such measurements are shown in Figure 4.2. This figure clearly shows that as the second microphone is moved away from the 30-degree microphone, increasing the angular separation, the coherence becomes almost non-existent. Qualitatively similar results were obtained for subsonic Mach numbers ranging from 0.2 – 0.8.

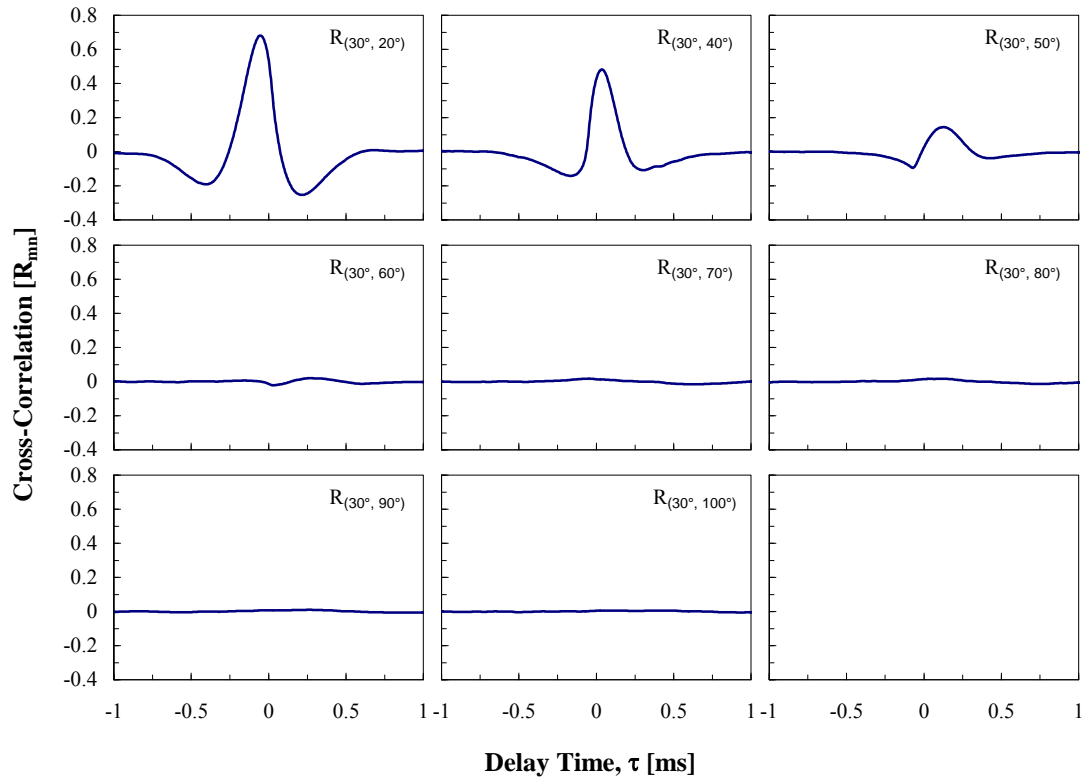


Figure 4.1 Cross-correlation with a fixed reference microphone at $\theta = 30^\circ$, Mach 0.9 jet.

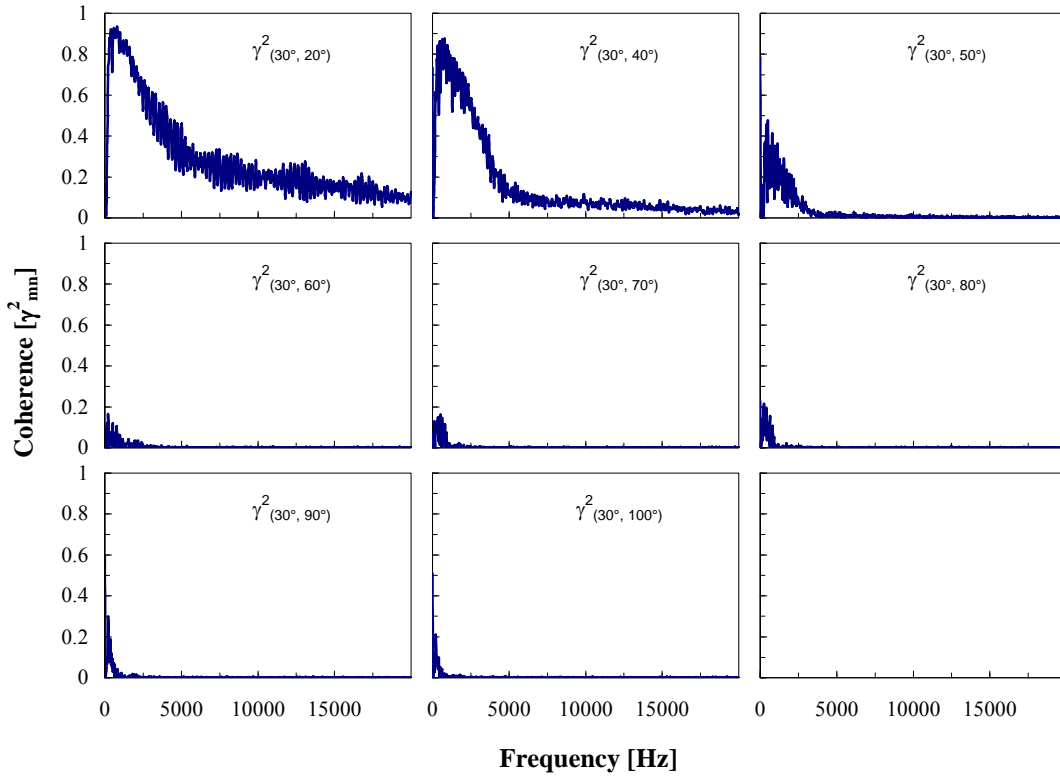


Figure 4.2 Coherence spectra with a fixed reference microphone at $\theta = 30^\circ$, Mach 0.9 jet.

Further observation of Figure 4.1 and Figure 4.2 leads to additional information concerning the propagation characteristics of the noise generated by the large-scale turbulence structures. Focusing only on the data for microphone pairs located in the extreme downstream direction (i.e., 20° , 30° , and 40°), it is seen that the signal is more coherent for microphone pair $(30^\circ, 20^\circ)$ than pair $(30^\circ, 40^\circ)$, which in turn is more coherent than pair $(30^\circ, 50^\circ)$. In fact, the coherence between the 30-degree microphone and the microphones located at angles larger than 50° is negligible at most frequencies. This indicates that within the Mach wave radiation cone the radiated noise generated by the large-scale turbulence structures is highly directional with a tendency toward the extreme downstream on-axis direction. Furthermore, this result is consistent with

prediction of the two-noise source model concerning the generation of noise by the large-scale turbulence structures.

According to Tam et al.²⁸, the maximum value of the normalized cross-correlation coefficient can be used as an indicator of the spatial coherence of the radiated signal between the two microphone positions. Values of the maximum cross-correlation measured by the microphone array shown in Figure 3.3 are plotted via bar charts in Figure 4.3 for simple comparison. Upon examining the plots, it can be said that when both microphones are positioned within the region where the large-scale turbulence structures dominate the radiated signal, the maximum normalized cross-correlation is as high as 0.7. Outside of this region, the cross-correlation—even at the smallest interval of 10° —is generally very low. The values are typically less than 0.15. In fact, when correlating with microphones other than the immediate adjacent neighbor, the cross-correlation is extremely low. In most instances, this cross-correlation value is within the noise level of the facility, which is roughly 0.008. These results indicate that the radiated sound field within the Mach wave radiation cone is reasonably coherent, as predicted by the two-noise source model. Moreover, outside of this region the sound field is poorly correlated. This is also in agreement with the two-noise source model. The region of fair correlation is due to the noise radiated from the large turbulence structures, while the weakly correlated sound field outside this region is due primarily to the fine-scale turbulence structures.

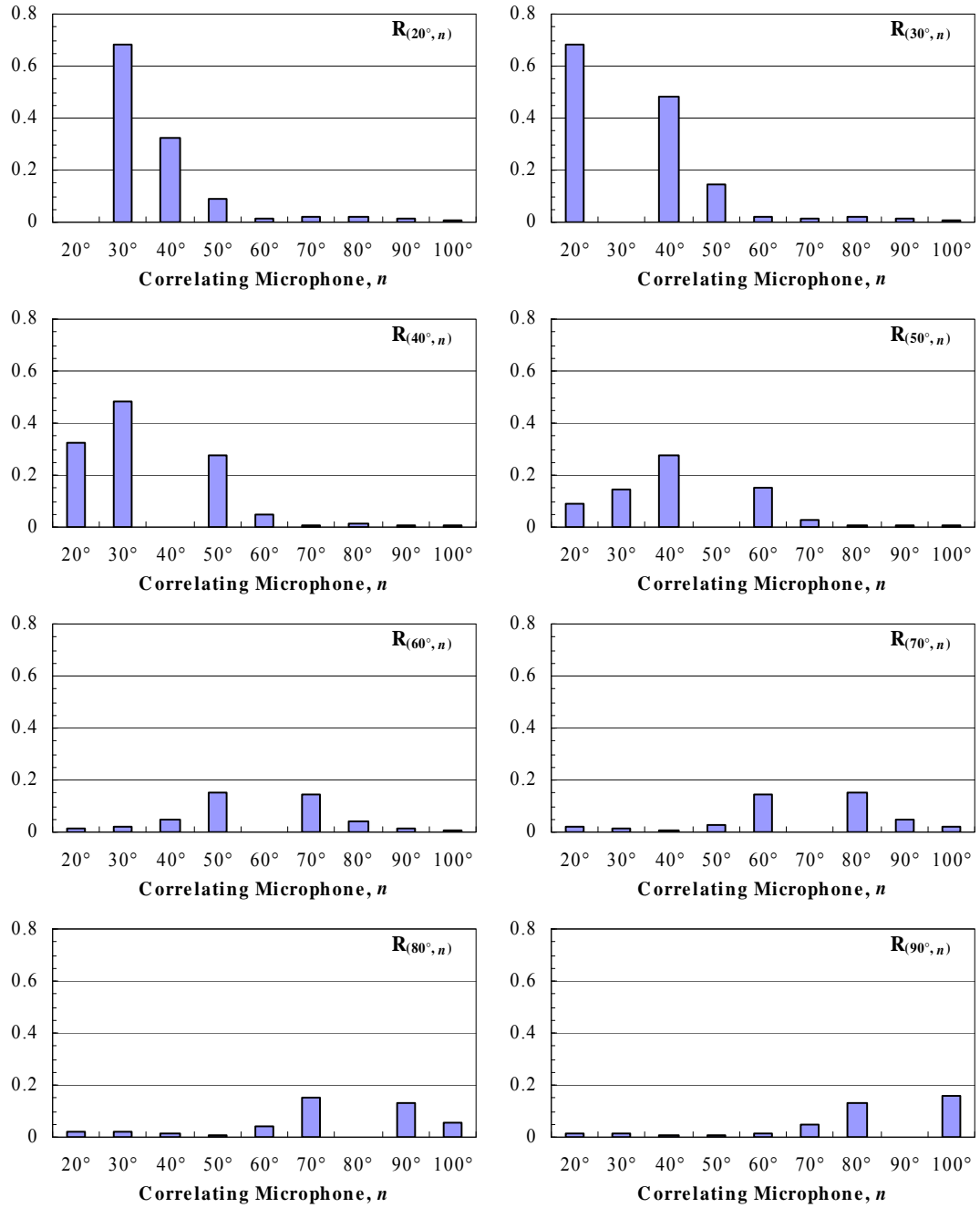


Figure 4.3 Maximum cross-correlation R_{mm} for a Mach 0.9 jet.

A new way of ascertaining the level of correlation throughout the radiated sound field is formed via further manipulation of the coherence spectra shown in Figure 4.2. By normalizing the frequency and discretely integrating—via the trapezoid method of

numerical integration—to find the sum of the area under the spectra greater than the noise floor of the facility, a metric for the level of coherence of the radiated sound field across all frequencies is established. The resulting function will be termed the overall coherence and is calculated as follows:

$$OACF_{mn} = \sum_{i=1}^{N-1} \left(\frac{\gamma_{mn}^2(i+1) + \gamma_{mn}^2(i)}{2} \right) \left(\frac{f(i+1) - f(i)}{f_{span}} \right) \quad (4.3)$$

where N is the total number of discrete frequencies and f_{span} is value of the maximum frequency within the span. The overall coherence is defined in such a way that if the signals m and n are fully coherent over entire frequency spectra then $OACF_{mn} = 1$, and if the signals are completely incoherent $OACF_{mn} = 0$. For $OACF_{mn}$ values between 0 and 1, some other relationship exists between m and n . Hence the following inequality is true of $OACF_{mn}$.

$$0 \leq OACF_{mn} \leq 1 \quad (4.4)$$

The overall coherence values reported in this work are very small (i.e., $0 < OACF_{mn} \leq 0.2$). The implications of this can be explained by considering the typical coherence signatures shown in Figure 4.2. The most significantly correlated signal, $\gamma_{(20^\circ, 30^\circ)}^2$, has an OACF of roughly 0.09. This is due the manner in which the overall coherence is determined and nature of jet noise coherence signatures. Jet noise coherence signatures tend to be most coherent at lower frequencies. Furthermore, typically jet noise coherence decreases with increasing frequency (e.g., see Figure 4.2 and any other jet noise

coherence signature within this work—Chapters 4 and 5). Not only does jet noise coherence decrease with increasing frequency, in most instances, the coherence is negligible beyond roughly 10 kHz. Since the overall coherence is calculated over the entire frequency span (76.8 kHz for the results reported in this work) and jet noise coherence signatures show limited correlation beyond 10 kHz (i.e., jet noise is significantly coherent over only approximately 13% of the frequency span), the small values of overall coherence reported here are to be expected. Nonetheless, the interest in using this metric in the present work is not to determine the absolute levels of the overall coherence but rather as a metric of frequency domain comparison for correlations between multiple pairs of microphones positioned throughout the radiated sound field. As shown below, the overall coherence function as defined above serves as a suitable comparative metric within the frequency domain.

Figure 4.4 illustrates the results from overall coherence manipulations of the coherence spectra shown in Figure 4.2. Much like the maximum normalized cross-correlation results, the overall coherence is largest for microphone pairs positioned within the Mach wave radiation cone. It reaches nearly 0.09 in the extreme downstream direction. Outside of this region the overall coherence is generally low. In fact, when correlating with widely spaced microphones the overall coherence is typically very near or within the noise floor of the facility (which is 0.005).

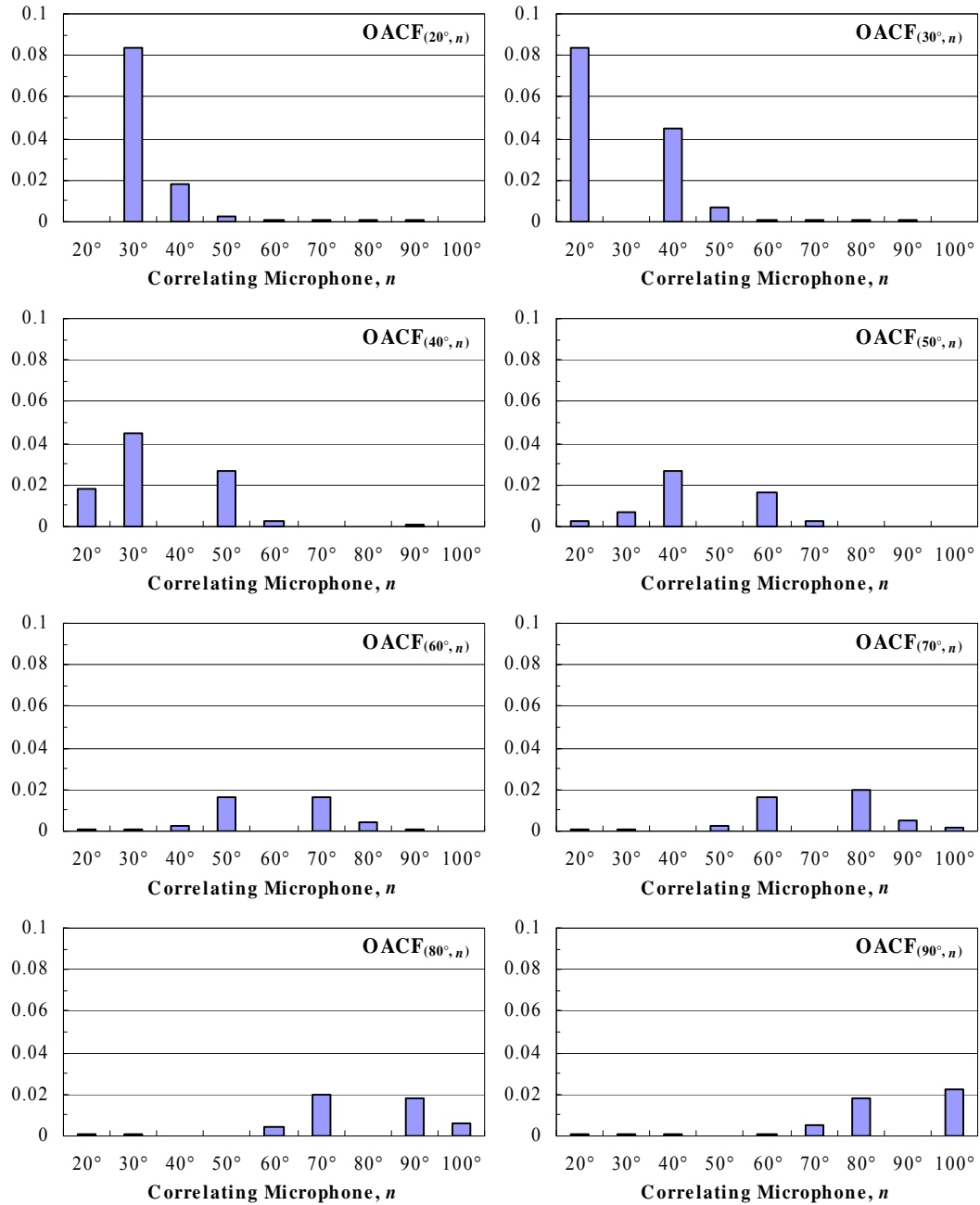


Figure 4.4 Overall coherence $OACF_{mn}$ for a Mach 0.9 jet.

Additional maximum normalized cross-correlation and overall coherence results for a 1.6-inch diameter conical round nozzle operated at Mach numbers ranging from 0.2 – 0.8 are plotted in Figure 4.5 – Figure 4.12 below. Qualitatively the results are the same for

all Mach numbers 0.4 and larger. When correlating microphones are located within the Mach wave radiation cone for the specified jet the maximum cross-correlation and the overall coherence are at their respective highest levels. In fact, the maximum cross-correlation is as high as 0.7 and the overall coherence reaches nearly 0.07 for the Mach 0.4 case and roughly 0.09 for Mach numbers 0.6 and larger. Outside of the Mach wave radiation cone, the levels are greatly reduced even at the smallest microphones spacing intervals. Thus, it can be said that the radiated sound field is most coherent within the Mach wave radiation cone. The random small-scale turbulence structures are said to dominate the sound field outside of the Mach wave radiation cone; thus the relative low level correlation and coherence results shown in the figures below for such microphone pairs is expected.

As for the Mach 0.2 jet (Figure 4.5 and Figure 4.9), the maximum correlation value and overall coherence remains relatively constant throughout the polar arc when comparing correlations of equally-spaced microphone pairs. While the largest overall coherence is observed at the smallest spacing interval and the lowest overall coherence is present when the microphones are spaced the greatest distance, the difference in these levels are not nearly as much as in the cases where the Mach number is 0.4 or larger. These results do not support the two-noise source model. A likely explanation of this phenomenon is that essentially no region of the large-scale turbulence structures are moving with phase velocities that are supersonic relative to the ambient speed of sound within the medium. Hence, the mechanism by which highly directional coherent noise is radiated to the far-field is likely not activated and very little (if any) coherent noise is radiated from the large-scale turbulence structures.

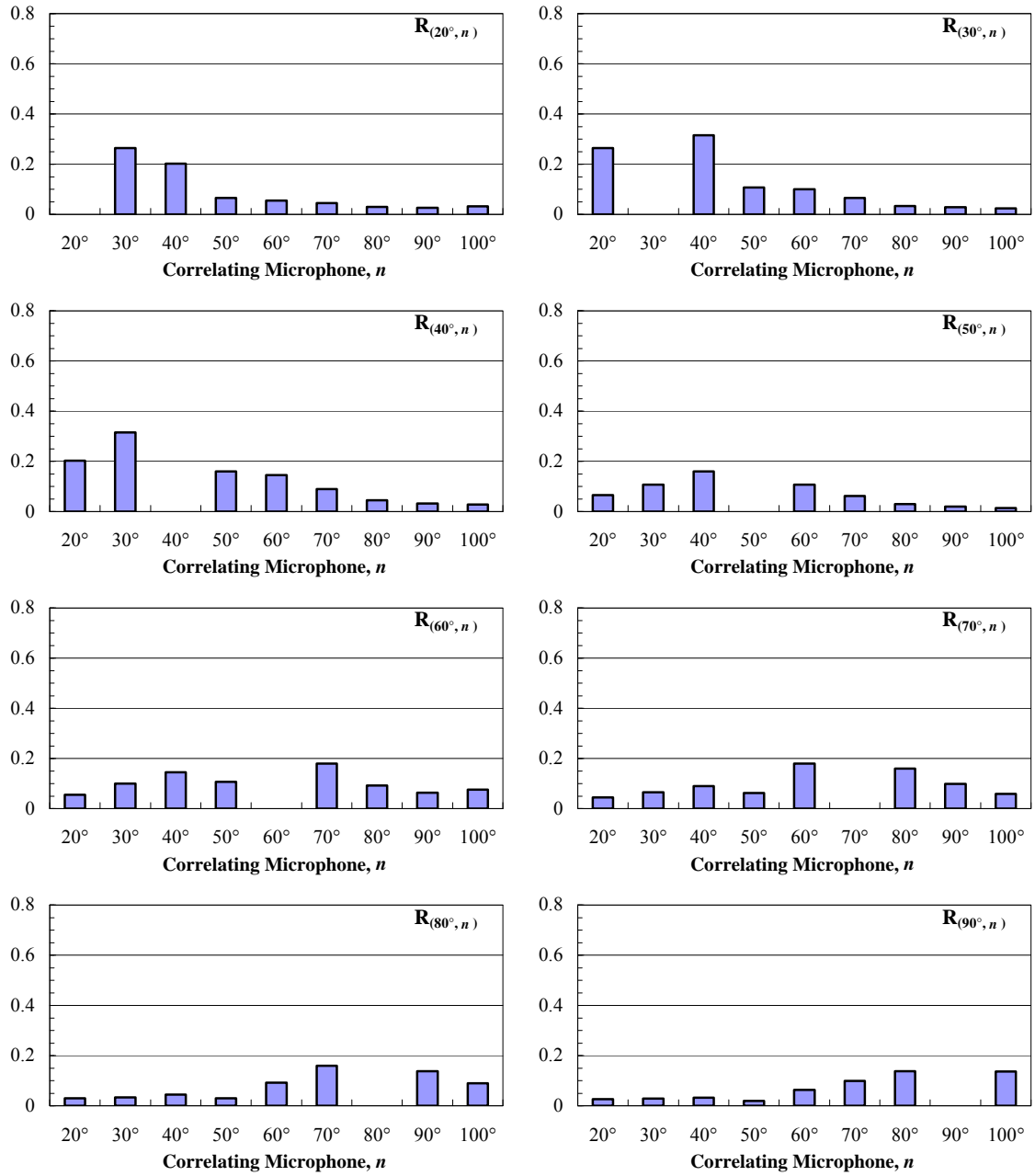


Figure 4.5 Maximum cross-correlation R_{mn} for a Mach 0.2 jet.

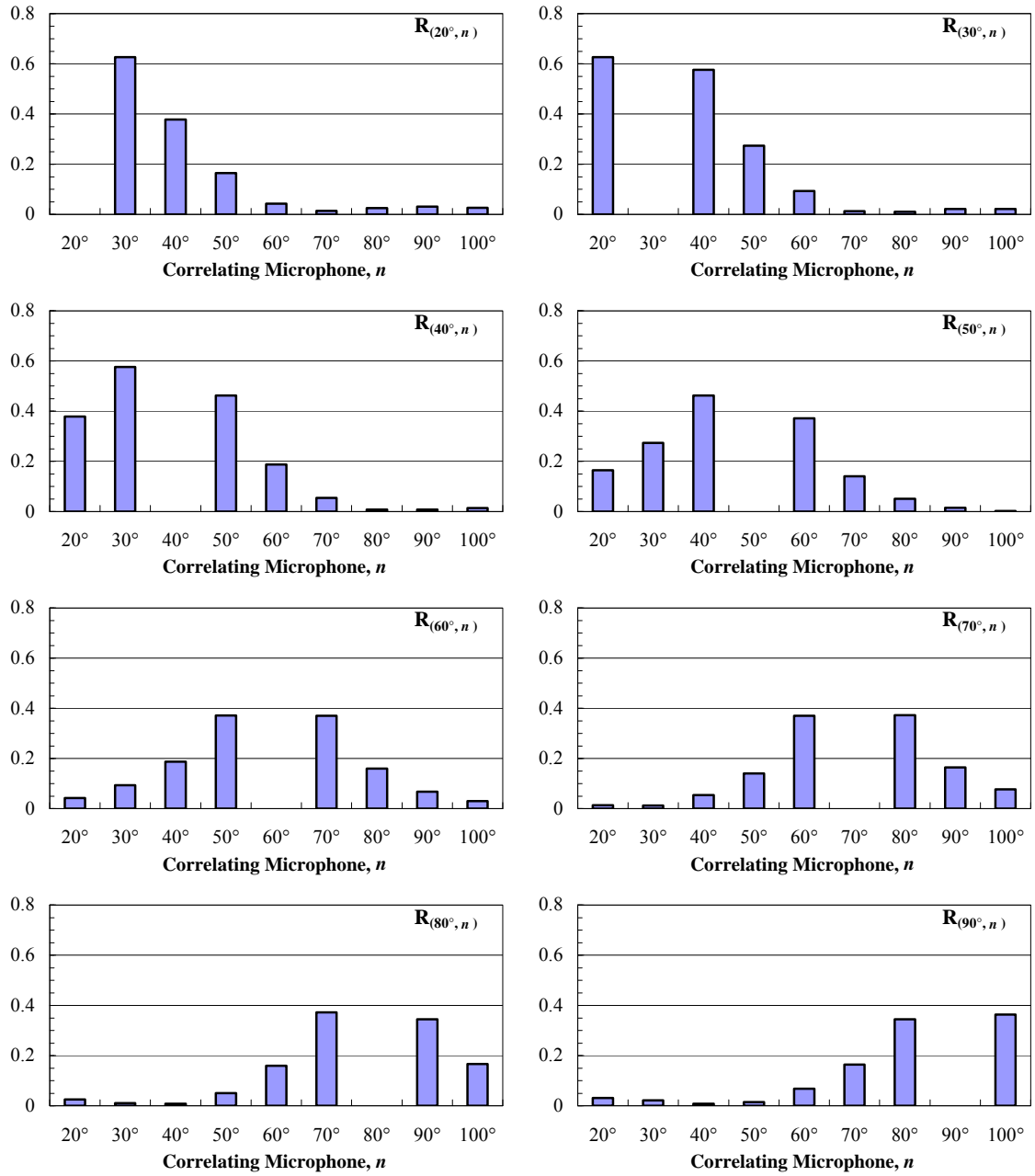


Figure 4.6 Maximum cross-correlation R_{mn} for a Mach 0.4 jet.

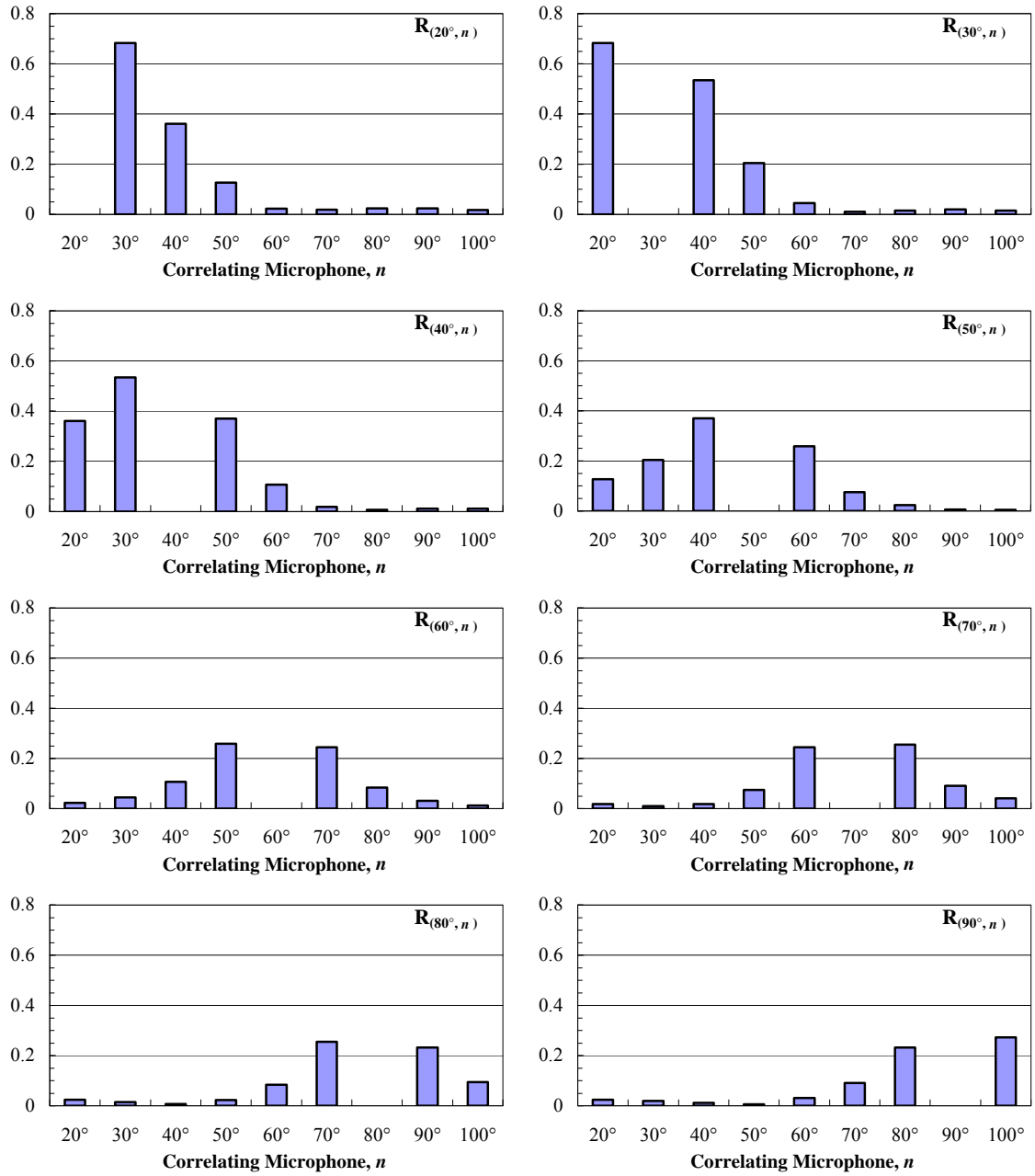


Figure 4.7 Maximum cross-correlation R_{mn} for a Mach 0.6 jet.

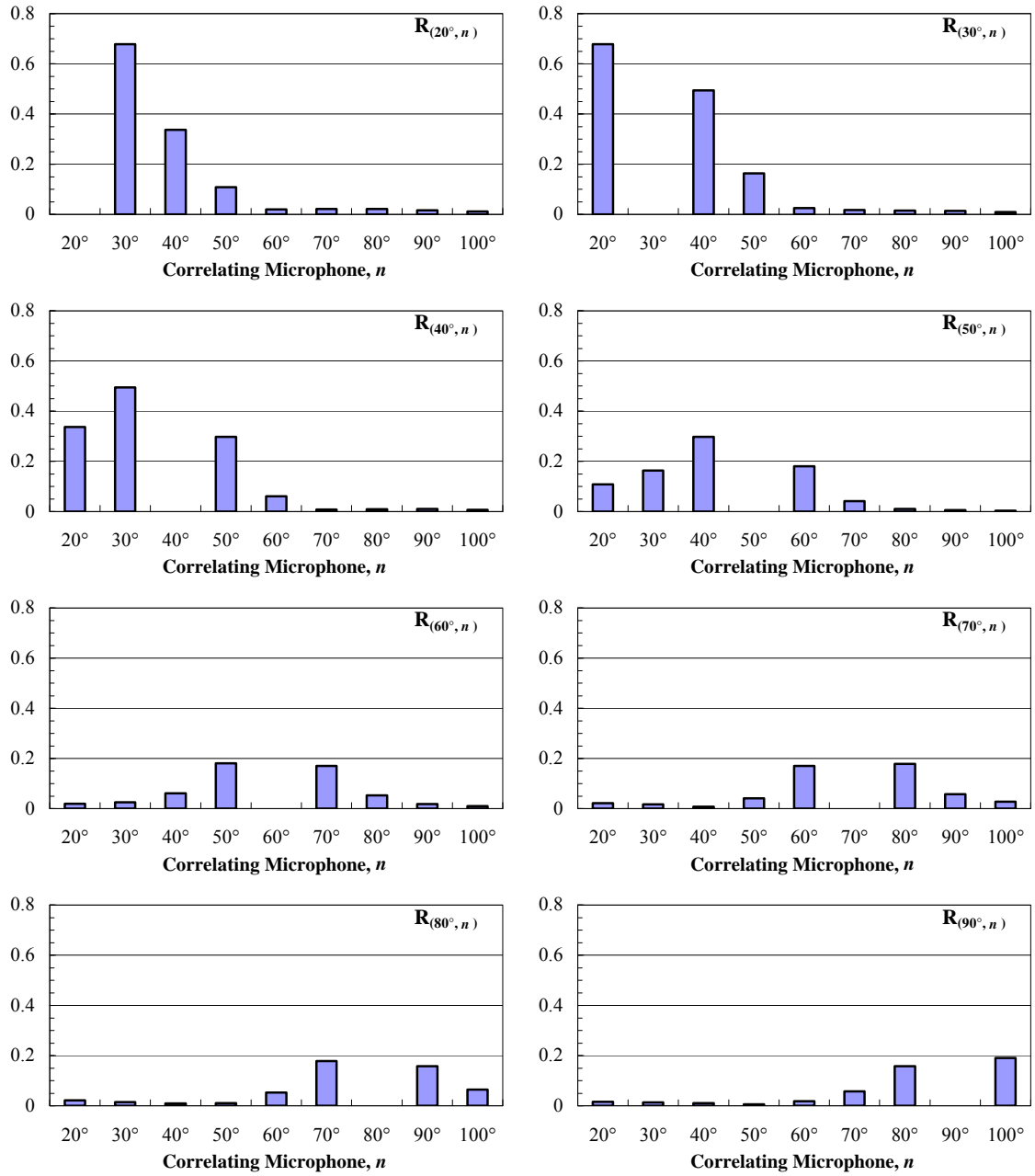


Figure 4.8 Maximum cross-correlation R_{mn} for a Mach 0.8 jet.

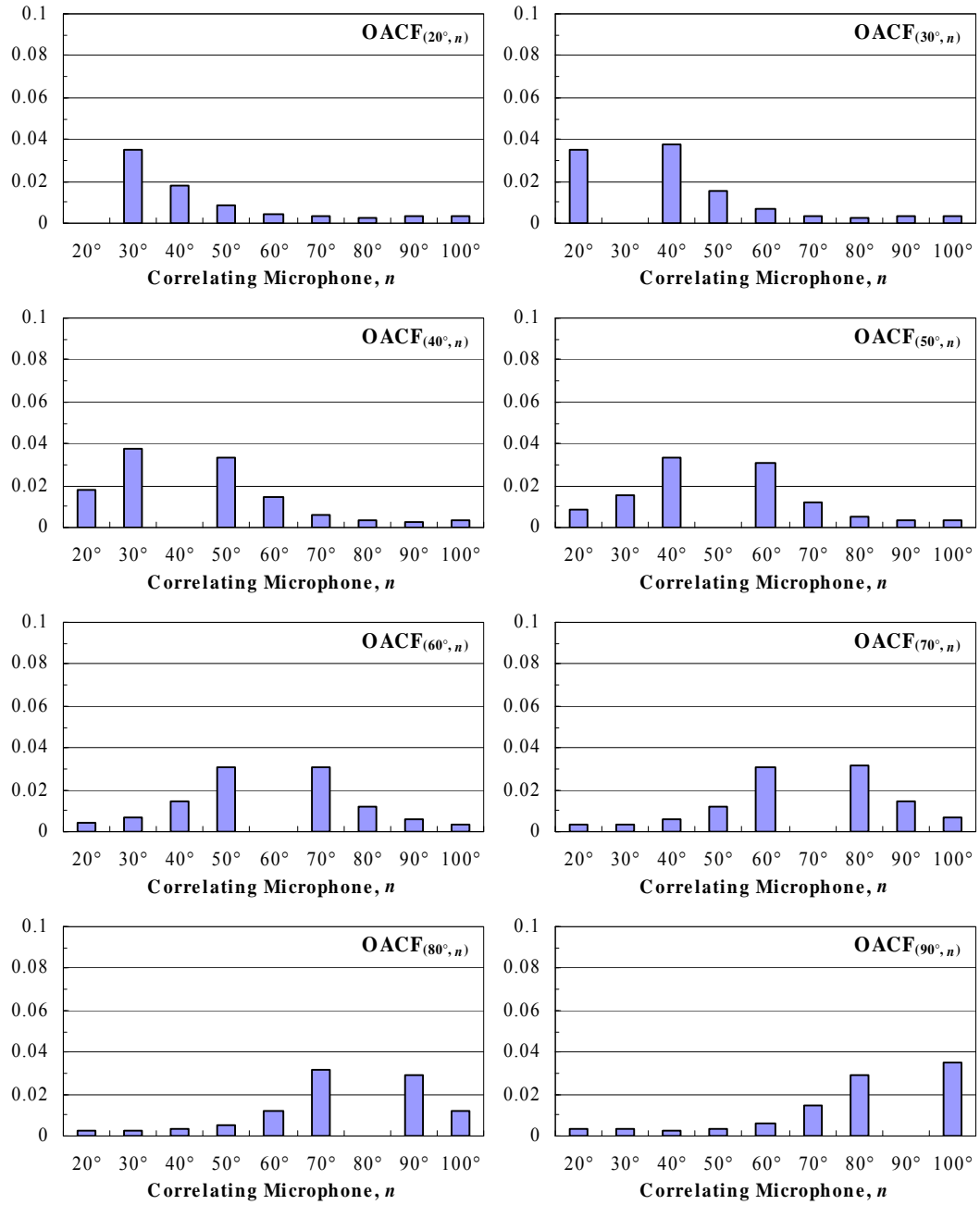


Figure 4.9 Overall coherence $OACF_{mn}$ for a Mach 0.2 jet.

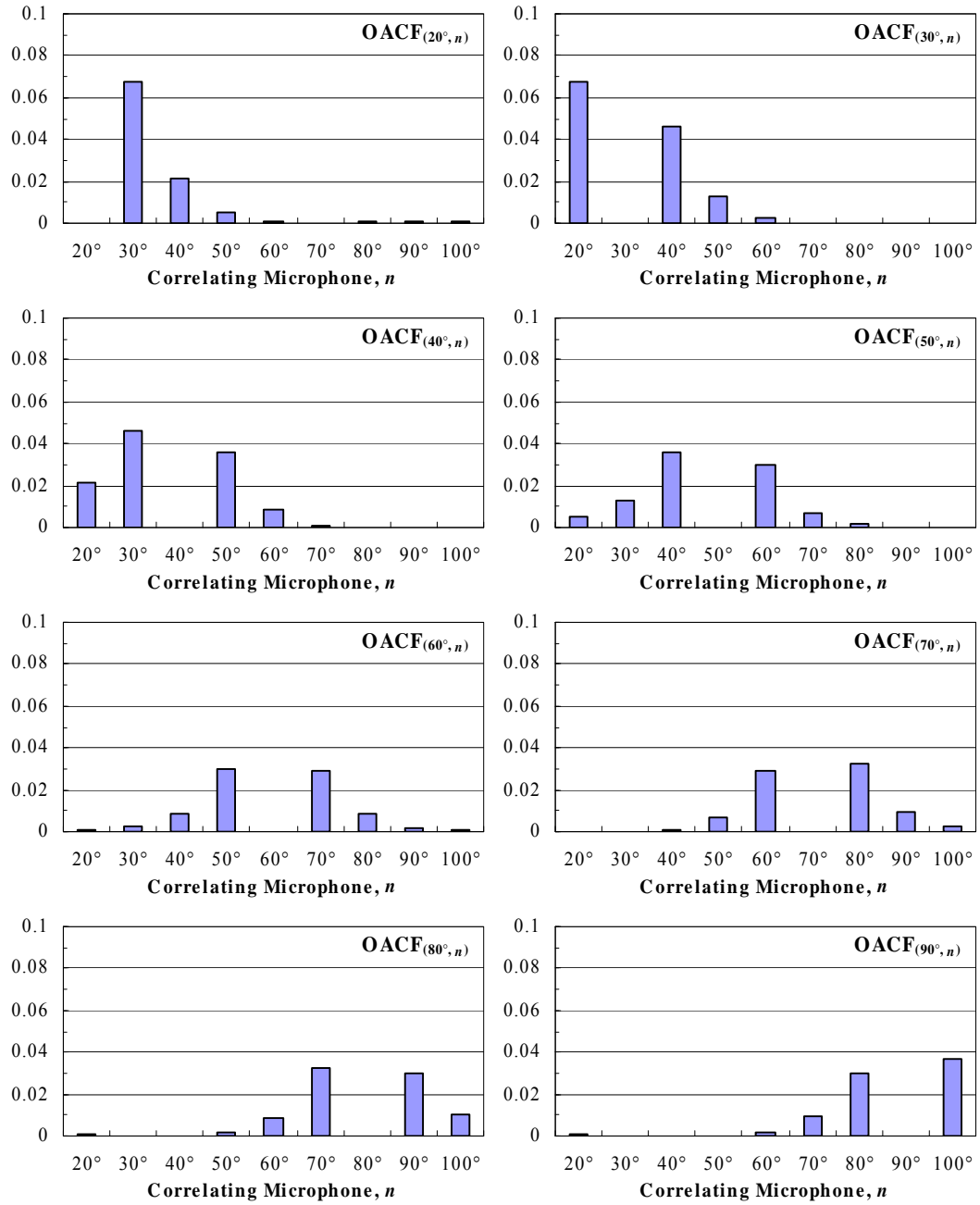


Figure 4.10 Overall coherence $OACF_{mn}$ for a Mach 0.4 jet.

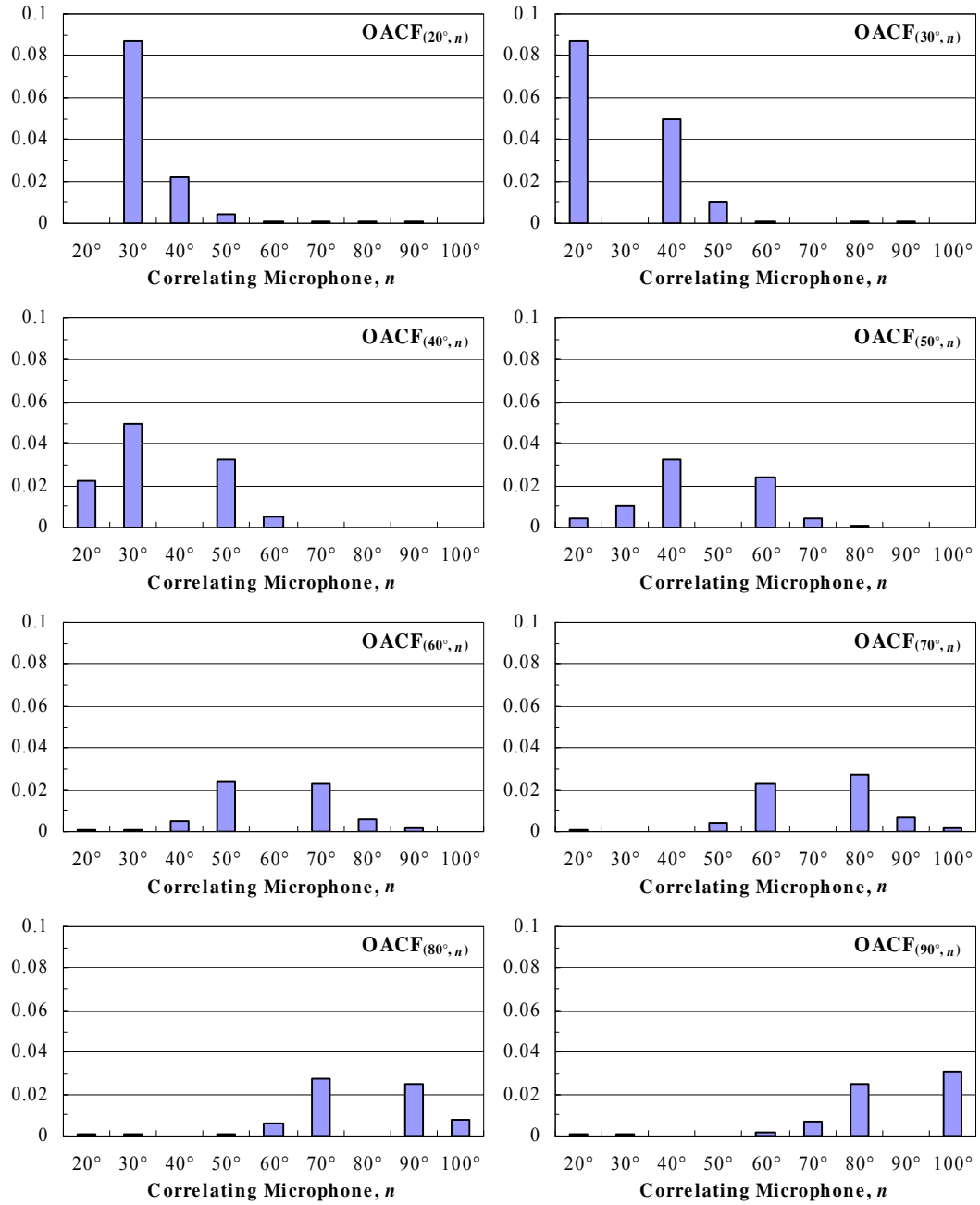


Figure 4.11 Overall coherence $OACF_{mn}$ for a Mach 0.6 jet.

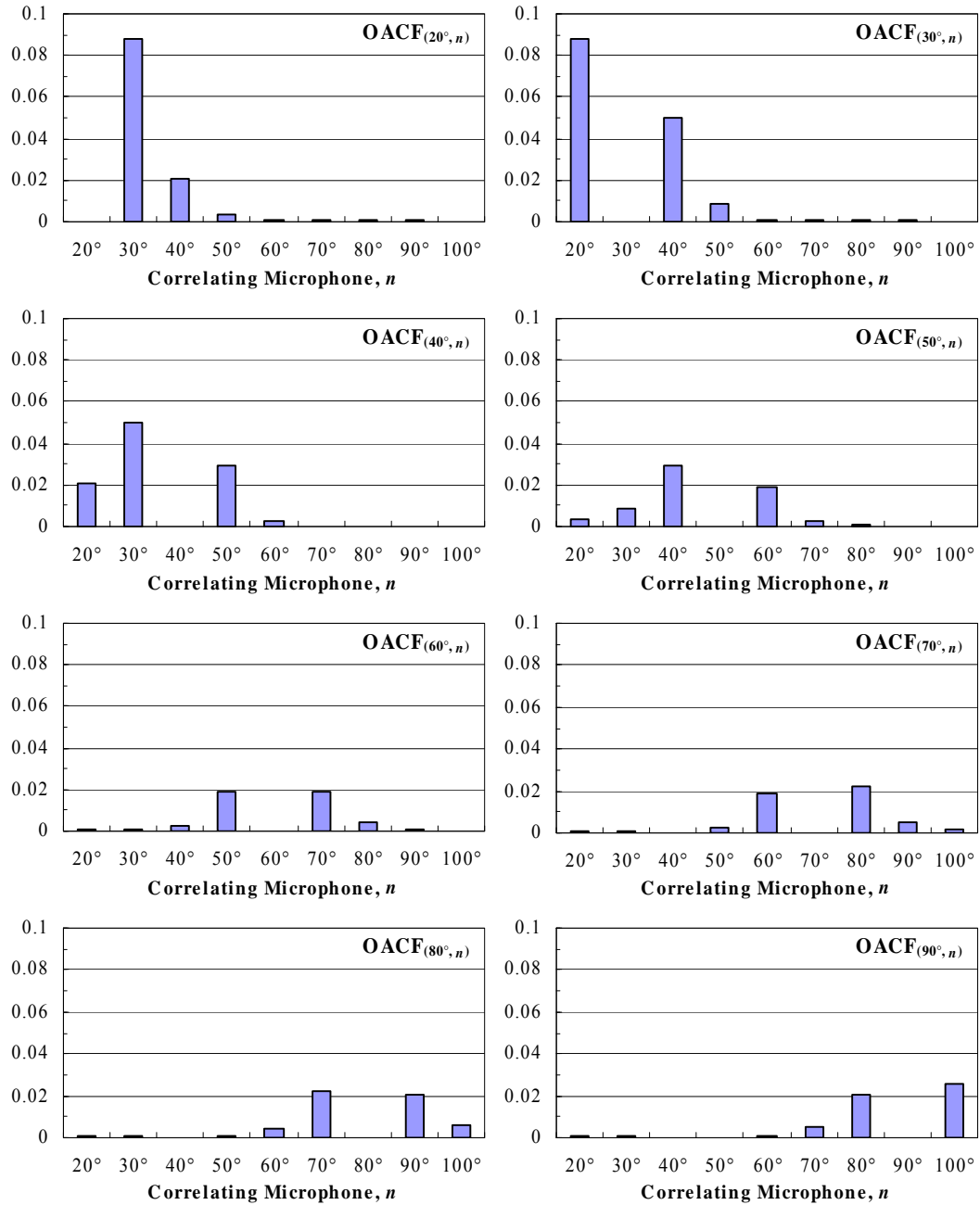


Figure 4.12 Overall coherence $OACF_{mn}$ for a Mach 0.8 jet.

Even though the basic trend in the figures above remains unchanged for all Mach numbers equal to 0.4 and larger, the quantitative levels of correlation are different as the Mach number changes. Figure 4.13 further illustrates these differences as function of jet

Mach number and measurement position relative to the downstream jet axis. Comparing the relative level of the maximum cross-correlation values for pair (30°, 20°) and pair (30°, 40°) across all Mach numbers gives some indication as how the jet velocity affects the directionality of the coherent noise radiated from the large-scale turbulence. In all instances the correlation is highest at pair (30°, 20°) and next highest at pair (30°, 40°). In fact, the maximum correlation value remains very near 0.7 for pair (30°, 20°) for all Mach numbers 0.4 and larger. This is not the case for pair (30°, 40°). As the jet velocity is increased the maximum level of $R_{(30^\circ, 40^\circ)}$ is reduced from 0.58 at Mach 0.4 to 0.48 at Mach 0.9. Thus, it can be said that as the jet velocity is increased the relative difference in the correlation level of these pairs is increased. Furthermore, for any given microphone pair positioned beyond 30° (excluding those where the correlation is extremely low) the correlation decreases with increasing Mach number. For clarification, consider pairs (40°, 50°) and (50°, 60°), as the Mach number is increased from 0.4 to 0.9, the maximum value of $R_{(40^\circ, 50^\circ)}$ is decreased from roughly 0.46 to 0.27, while $R_{(50^\circ, 60^\circ)}$ is reduced from approximately 0.37 to 0.15. The comparisons made above are shown in Figure 4.13 in the form of maximum normalized cross-correlations. The same argument can be made for the overall coherence data shown in Figure 4.4 and Figure 4.10 through Figure 4.12. These results are indicative of a reduction of the Mach wave radiation cone angle that occurs with increasing jet velocity. As the jet velocity is increased the directivity of the radiated coherent noise from the large-scale structures becomes more downstream (i.e., as the jet velocity is increased the Mach wave radiation cone angle becomes smaller and thus the noise is directed more in the downstream direction nearer the jet axis).

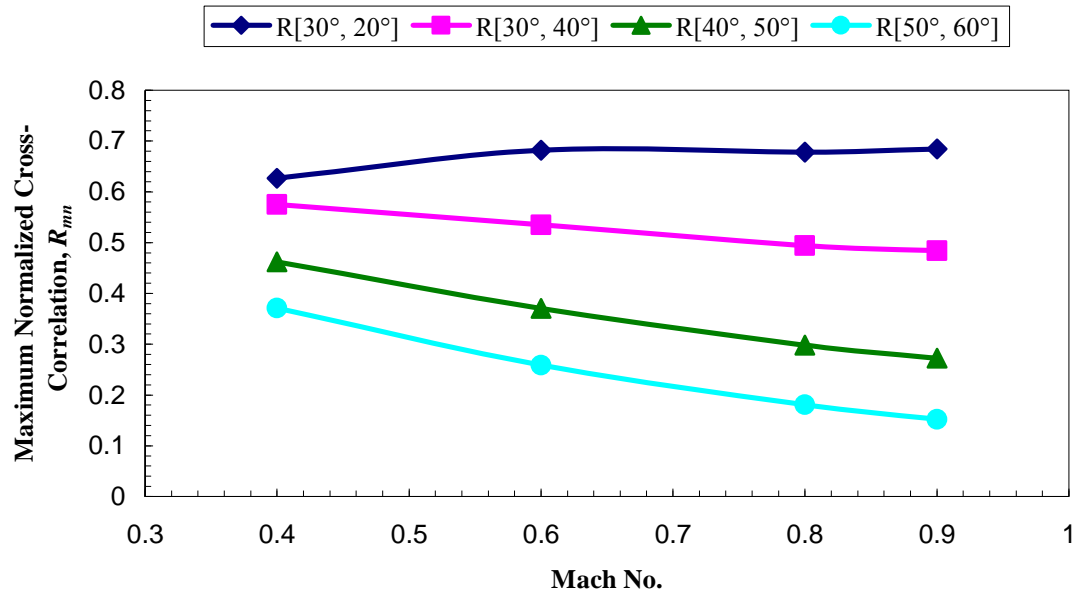


Figure 4.13 Maximum cross-correlation as a function of Mach number and position.

4.1.2 Effect of Nozzle Geometry in Subsonic Jets

In addition to the corroboratory evidence in support of the two-noise source model reported in the previous section for the 1.6-inch conical round nozzle, cross-correlation and coherence data were measured for a number of other nozzle geometries. The study of multiple nozzle configurations allows for the assessment of the validity of the two-noise source model for jets with differing physical characteristics. Specifically, the implications of a thinned boundary layer, an axisymmetric instability structure, and mixing enhancement are studied. The expected impact of each nozzle on turbulence scales and the subsequent finding from the use of each are discussed in the following sections.

The nozzle geometries studied include a pair of tabbed conical round nozzle configurations, a rectangular nozzle, and an additional smaller-diameter conical round

nozzle. The 1.6-inch diameter conical round nozzle used to generate the results in the previous section was fitted with two and four tabs. In two-tab configuration, the tabs were spaced 180° apart along the circumference of the exit plane of the nozzle. In the four-tab configuration, the tabs were positioned at 90° increments. The rectangular nozzle used in these experiments has an aspect ratio of eight. The major axis of the nozzle exit measures 4 inches, and the minor axis measures 0.5 inches. The equivalent exit diameter of the rectangular nozzle matches that of the 1.6-inch diameter conical round nozzle. The additional round nozzle has an exit diameter of 0.75 inches. Photographs of the nozzle configurations are provided in Figure 3.4 through Figure 3.8.

The overall coherence results for each nozzle operated at Mach 0.9 are reported below. In the followings sections the results for the additional nozzles are compared those of the 1.6-inch diameter round nozzle. First the findings for the 0.75-inch diameter round nozzle are compared with those of the 1.6-inch nozzle. Next the results from the rectangular nozzle are examined. Lastly, the results from the tabbed nozzles are compared to the un-tabbed case. For each comparison the overall coherence is calculated from the measured coherence spectra with the reference microphones positioned at 30° , 60° , and 90° . The overall coherence for microphone pairs consisting of the specified reference microphone and all other microphones within the polar arc (as depicted in Figure 3.3) are reported for all nozzle geometries. Each microphone was positioned at a radius of 10 feet from center of the jet exit.

4.1.2.1 Effect of Nozzle Diameter

In comparing the smaller-diameter conical round nozzle to the larger-diameter conical round nozzle, essentially the difference lies in the thickness of the jet boundary layer. The jet boundary layer thickness is directly dependent upon the Reynolds number, which in turn is directly proportional to the diameter of the nozzle. Furthermore, since the nozzles were tested under essentially identical conditions and they are assumed to have approximately the same surface roughness, the thickness of the jet boundary layer in each case is assumed to be primarily dependent upon the diameter of the nozzle. With this one can conclude a reduction in nozzle diameter thins the jet boundary layer. Ahuja et al.⁵⁰ and Lepicovsky et al.^{51,52} indicated that the large-scale instability waves have a higher growth rate if the boundary layer is thin. Thus, larger, more dominant large-scales turbulence structures are expected in the 0.75-inch diameter case as compared to the 1.6-inch diameter case. This is confirmed by the results present in the figures below. Figure 4.14 illustrates the overall coherence measured when correlating with the 30-degree microphone as the reference. In all instances where significant correlation exists, the 0.75-inch nozzle exhibits far more coherence than the 1.6-inch nozzle. The same can be said for Figure 4.15 and Figure 4.16, which show the overall coherence when correlating with reference microphones positioned at 60° and 90°, respectively. The results for the smaller-diameter jet indicate a more significant presence of large-scale structures in the smaller diameter case, and most importantly, they offer further confirmation of the two-noise source model.

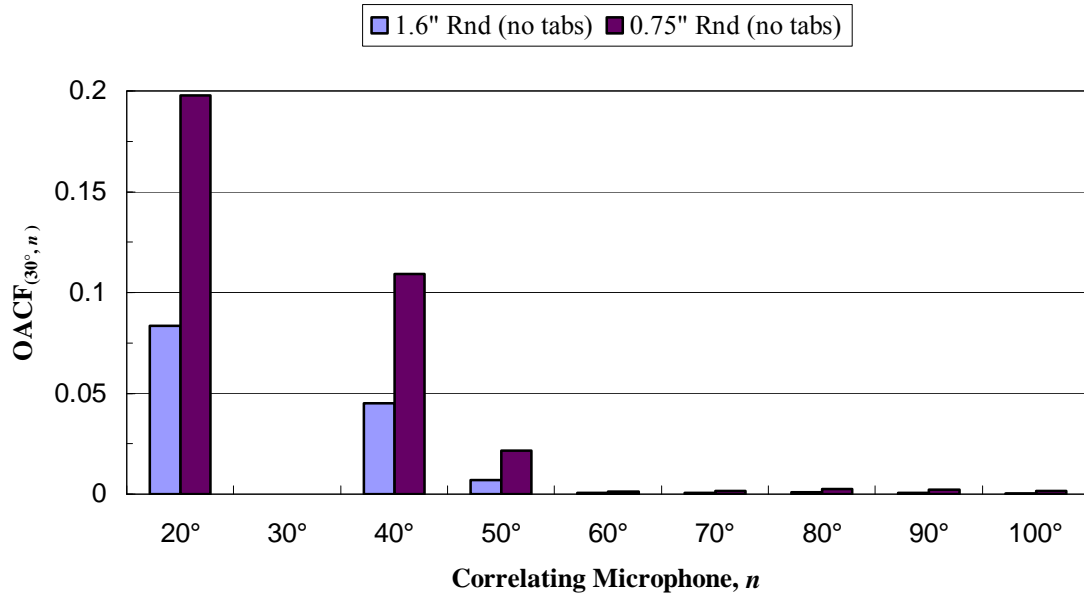


Figure 4.14 Overall coherence $OACF_{(30^\circ, n)}$ for nozzle geometries operated at Mach 0.9.

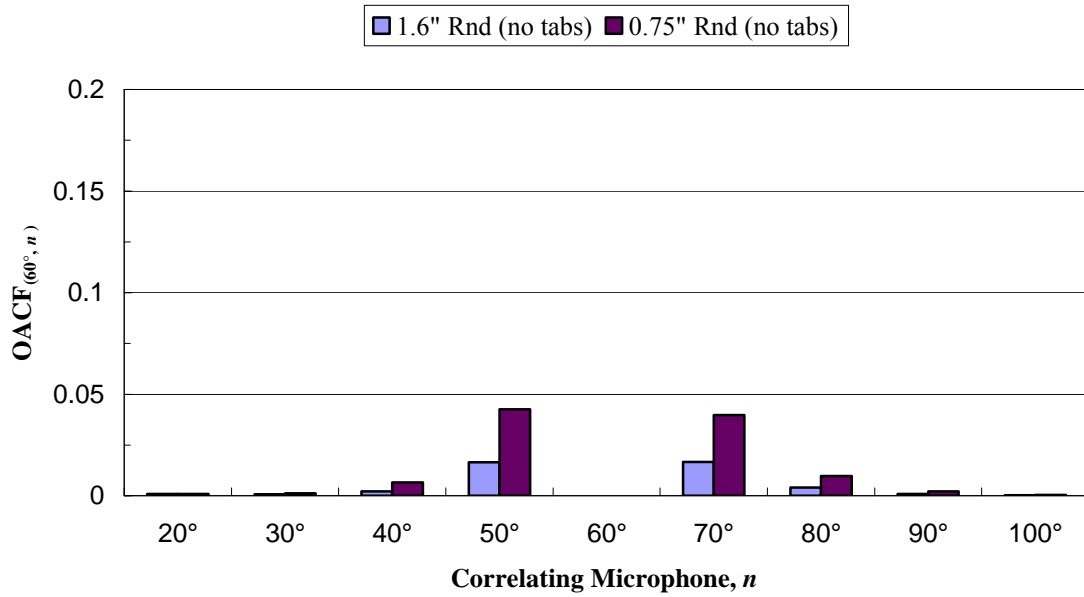


Figure 4.15 Overall coherence $OACF_{(60^\circ, n)}$ for nozzle geometries operated at Mach 0.9.

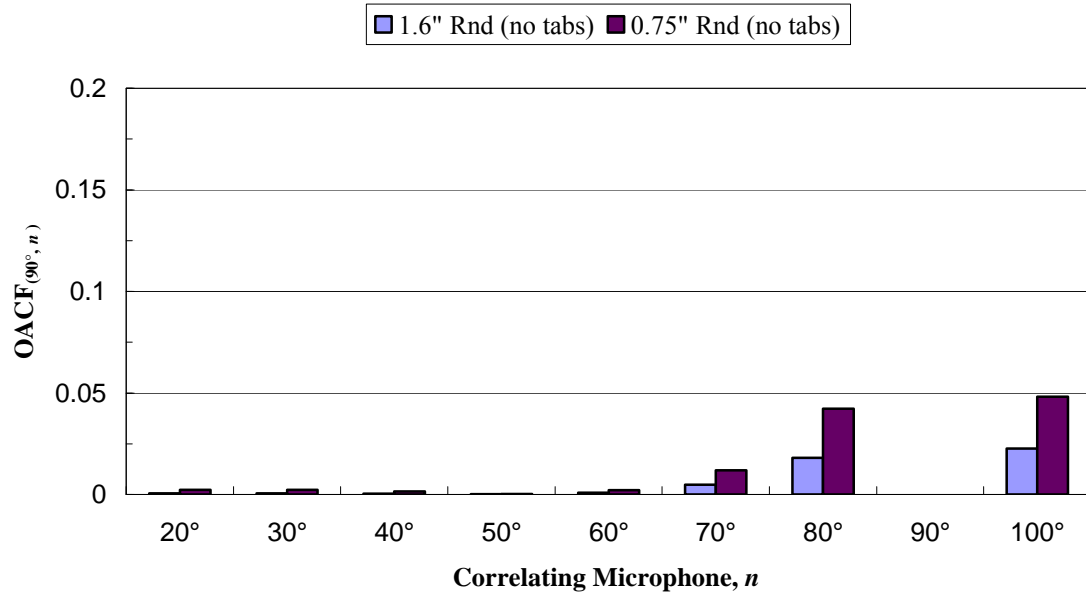


Figure 4.16 Overall coherence $OACF_{(90^\circ, n)}$ for nozzle geometries operated at Mach 0.9.

4.1.2.2 Axisymmetric Jet v. Non-Axisymmetric Jet

As mentioned earlier, the rectangular nozzle and the 1.6-inch diameter conical round nozzle have identical exit areas. Though the boundary layers at the exits of the two nozzles were not measured, it is expected that they were of different thicknesses; and in all likelihood, the rectangular nozzle has a much thinner boundary layer. The flapping instability from the rectangular jet with a thinner boundary layer (in comparison to the 1.6-inch round nozzle) is expected to have a stronger growth rate^{50,51,52}. This may be the reason for the larger coherence exhibited by the rectangular nozzle (compared to the 1.6-inch round nozzle) in Figure 4.17 through Figure 4.19. Figure 4.17 illustrates the overall coherence measured when correlating with the 30-degree microphone as the reference. In all instances where significant correlation is present, the rectangular nozzle exhibits more coherence than the 1.6-inch nozzle. The same can be said for Figure 4.18 and Figure 4.19, which show the overall coherence when correlating with reference

microphones positioned as 60° and 90°, respectively. Like the findings of the previous section, the findings for the non-axisymmetric rectangular jet are also in agreement with the two-noise source model.

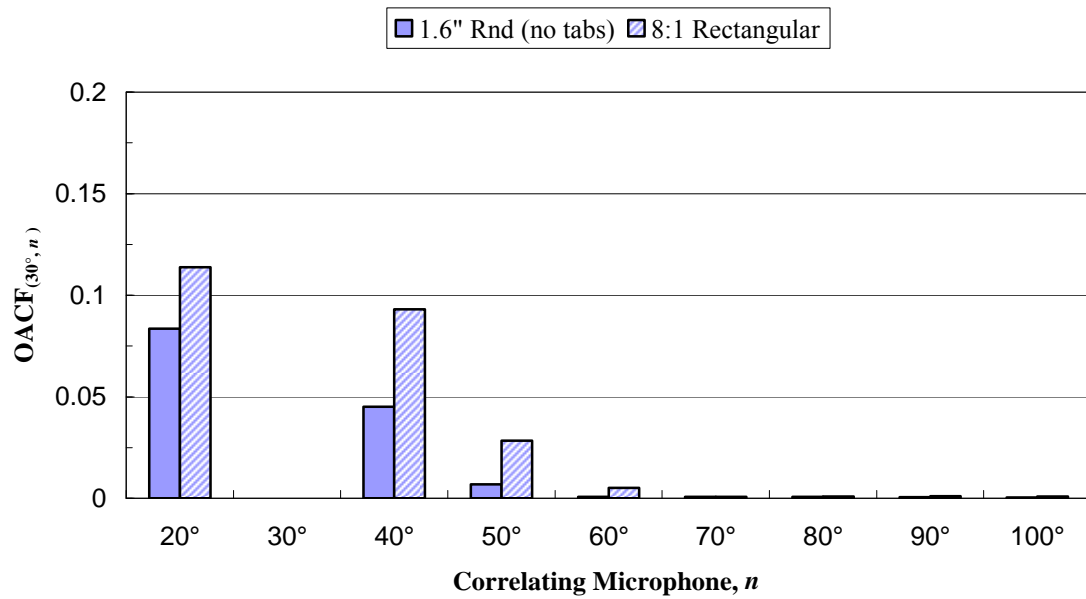


Figure 4.17 Overall coherence $OACF_{(30^\circ, n)}$ for nozzle geometries operated at Mach 0.9.

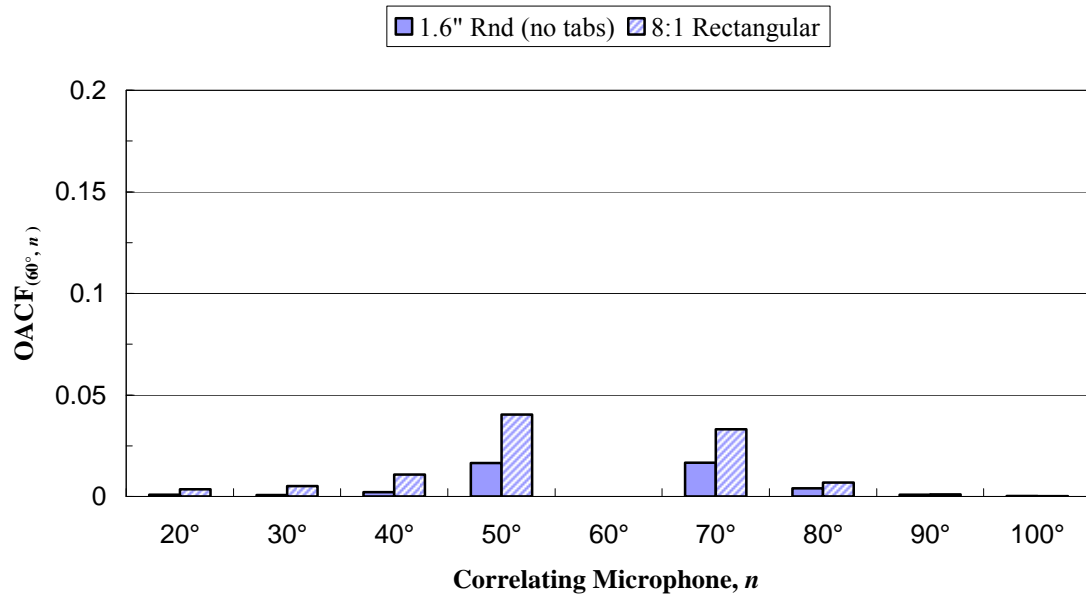


Figure 4.18 Overall coherence $OACF_{(60^\circ, n)}$ for nozzle geometries operated at Mach 0.9.

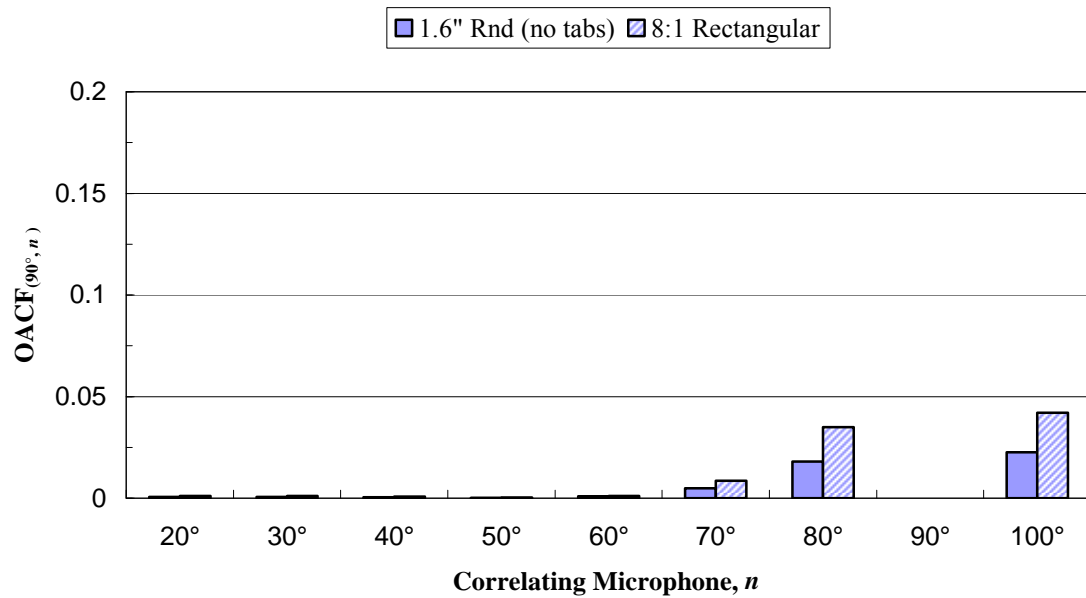


Figure 4.19 Overall coherence $OACF_{(90^\circ, n)}$ for nozzle geometries operated at Mach 0.9.

4.1.2.3 Jets with Enhanced Mixing

It is well known that the addition of tabs enhances the jet mixing and modifies the radiated noise level^{49,53}. The tabs generate longitudinal vortices leading to rapid mixing of the jet. Due to this mixing enhancement, the large-scale structures tend to experience more growth. Thus, one would expect the large-scale structures to be more dominant and thus more coherent when tabs are used to excite the jet. This is evident in the figures below. Figure 4.20 depicts the overall coherence results when correlating with the 30-degree microphone as reference. For all microphone pairs that exhibit significant coherence, the addition of tabs tends to elevate the level of the coherence. The same can be said for the 60° and 90° reference cases shown in Figure 4.21 and Figure 4.22, respectively. Just as with the previous comparisons, the results for the tabbed nozzle configurations also support the two-noise source model.

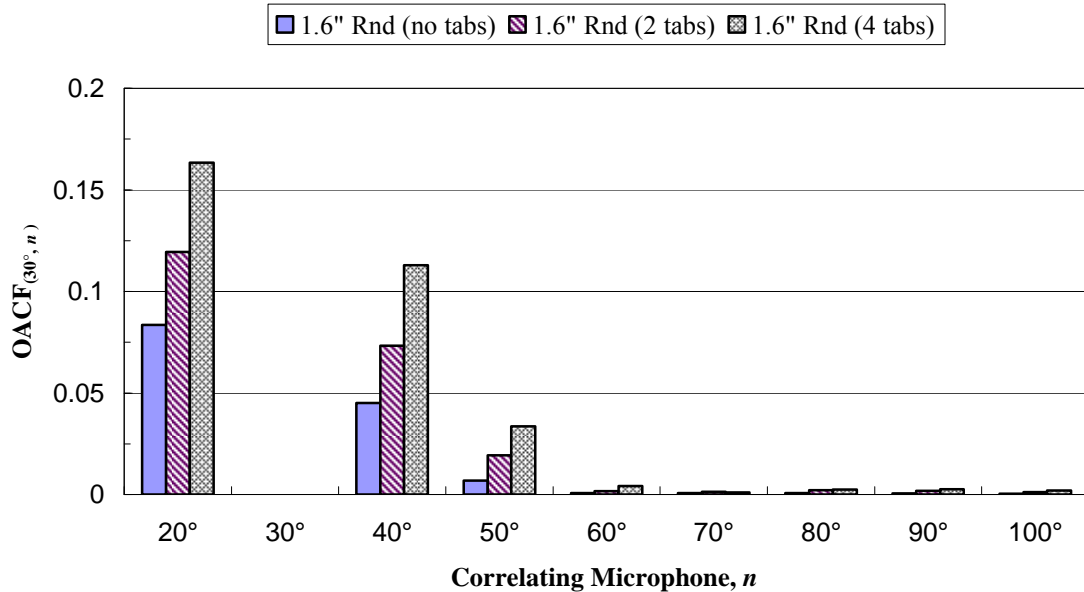


Figure 4.20 Overall coherence $OACF_{(30^\circ, n)}$ for nozzle geometries operated at Mach 0.9.

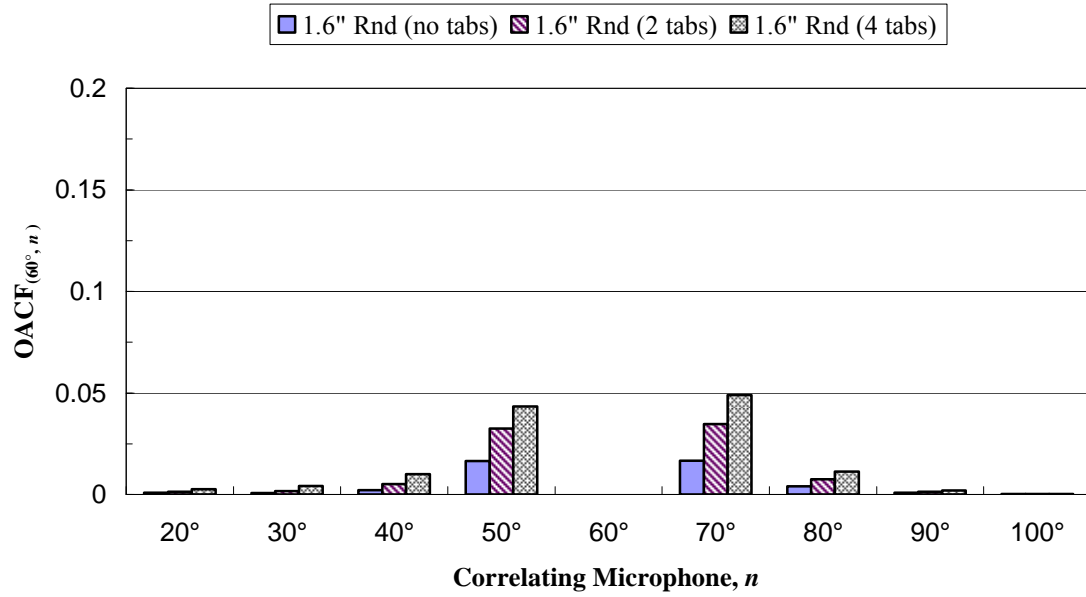


Figure 4.21 Overall coherence $OACF_{(60^\circ, n)}$ for nozzle geometries operated at Mach 0.9.

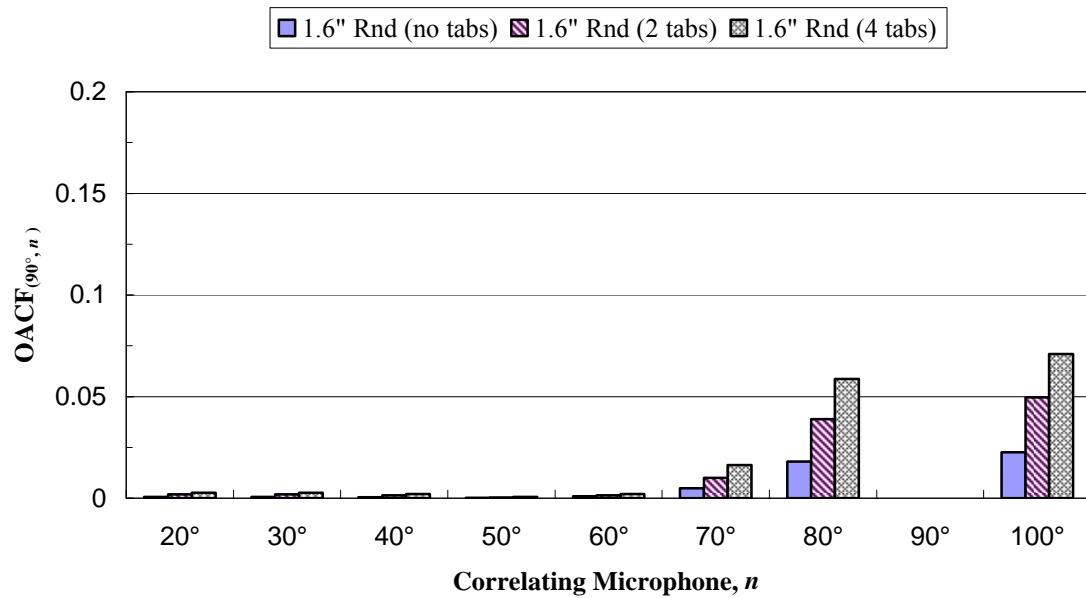


Figure 4.22 Overall coherence $OACF_{(90^\circ, n)}$ for nozzle geometries operated at Mach 0.9.

The results in the figures above indicate that the coherence spectra for a Mach 0.9 jet follow the same basic pattern independent of nozzle geometry. For all nozzle geometries,

the magnitude of the overall coherence is largest for pairs where both microphones are positioned within the Mach wave radiation cone (i.e., those pairs positioned in the extreme downstream on-axis direction). Outside of this region, the coherence tends to decrease significantly even at the smallest interval (e.g., 10°). At larger spacing intervals, the coherence is reduced to extremely low values; in some cases, these values lie near or within the noise floor of the facility. Similar results were obtained for all nozzle configurations at lower subsonic Mach numbers ranging from 0.4 – 0.8.

4.1.3 A Fully-Expanded Supersonic Jet

Microphone cross-correlation and coherence data were measured for a Mach 1.67 perfectly expanded jet exhausting from converging-diverging round nozzle with an exit diameter of 2.0 inches. As with the subsonic experiments described above, microphones were placed in polar arc positioned at a radius of 10 feet from the nozzle exit. The microphones were spaced evenly in 10° increments ranging from 20° to 100° (as shown in Figure 3.3). Data sampling parameters identical to that of the subsonic cases were used. The cross-correlation results are again reported in the form of the normalized cross-correlation coefficient, $R_{mm}(\tau)$. The measured normalized cross-correlation $R_{(30^\circ, n)}$, $n = 20^\circ, 40^\circ, 50^\circ, \dots, 100^\circ$ as a function of delay time τ for the perfectly-expanded Mach 1.67 jet is shown in Figure 4.23. Like the subsonic jet findings, the results for the Mach 1.67 jet show a fair amount of correlation within the Mach wave radiation cone. Additionally, the findings indicate a lack of correlation when the second microphone is outside the Mach wave radiation cone depicted in Figure 2.2. These observations are further confirmed by analyzing the correlations between the 30-degree microphone and

the other microphones in the frequency domain. Coherence spectra for such measurements are shown in Figure 4.24. This figure clearly shows that as the second microphone is moved away from the 30-degree microphone, increasing the angular separation, the coherence becomes almost non-existent. These observations are consistent with the two-noise source model.

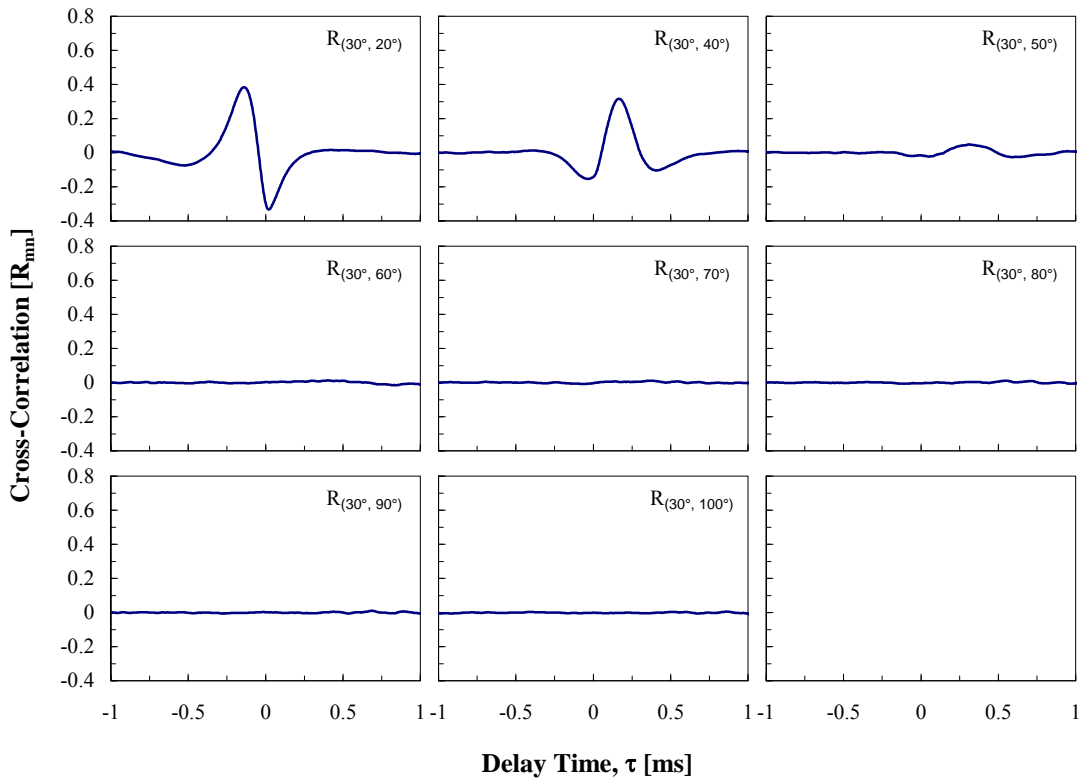


Figure 4.23 Cross-correlation with reference microphone at $\theta = 30^\circ$, fully-expanded Mach 1.67 jet.

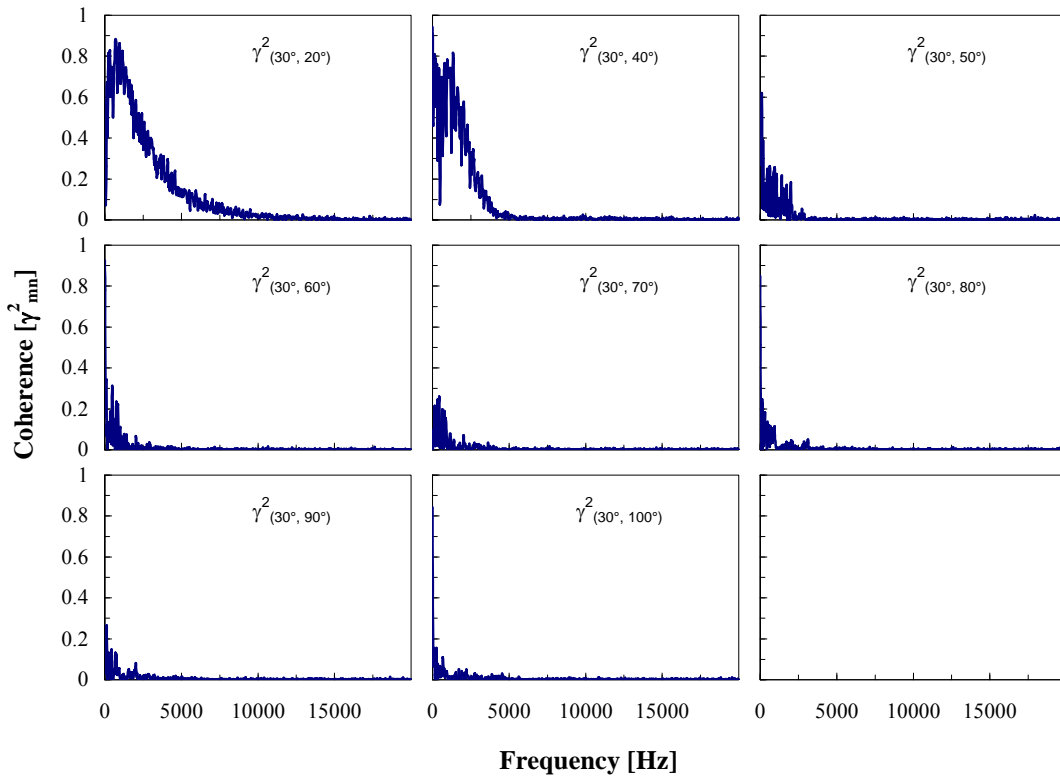


Figure 4.24 Coherence spectra with reference microphone at $\theta = 30^\circ$, fully-expanded Mach 1.67 jet.

Once again the maximum value of the normalized cross-correlation and the overall coherence function are used as indicators of the level of coherence within the measured sound field. The results are shown in Figure 4.25 and Figure 4.26 as bar charts. As shown in Figure 4.25, the maximum normalized cross-correlation reaches nearly 0.4 when both microphones are positioned within the Mach wave radiation cone. When one or both microphones are positioned outside of this region, the correlation is significantly reduced. The same can be said for the overall coherence shown in Figure 4.26. Its value is as high as roughly 0.032 when correlating between immediately adjacent microphones in the extreme downstream direction and reduces to levels that are within or near the

noise floor of the facility when correlating between microphones positioned outside of the Mach wave radiation cone.

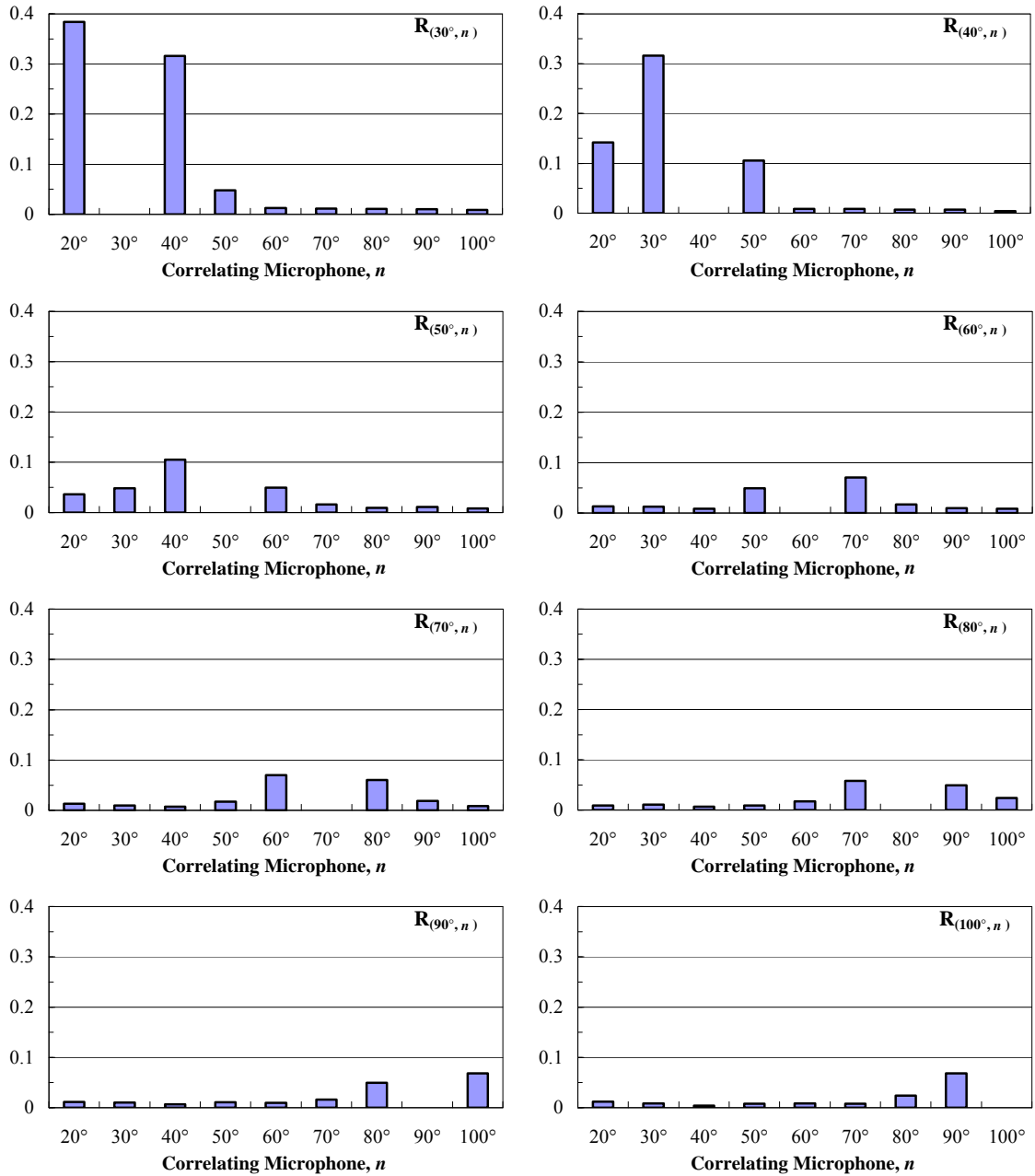


Figure 4.25 Maximum cross-correlation R_{mn} for a fully-expanded Mach 1.67 jet.

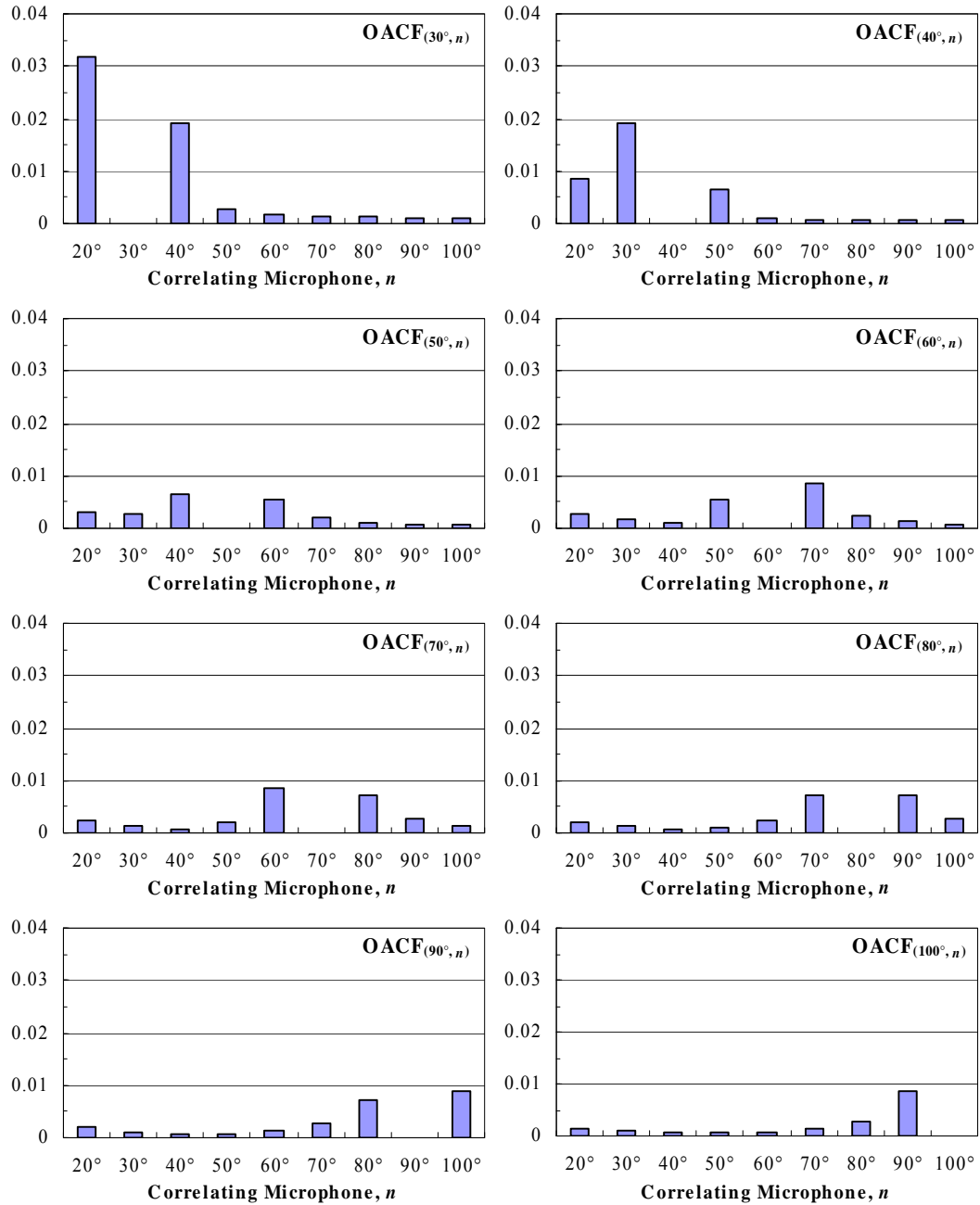


Figure 4.26 Overall coherence $OACF_{mn}$ for a fully-expanded Mach 1.67 jet.

The above maximum cross-correlation and overall coherence results indicate that on a spherical surface in the acoustic far-field, there is significant correlation of the noise field along the polar direction within the Mach wave radiation cone. However, outside this

cone, the noise field has very limited spatial correlation along the polar angle directions. These experimental observations are consistent and supportive of the two-noise source model and indicate the power of coherence-based diagnostic methods.

4.2 Separation of the Turbulence Scale Contributions in the Far-Field

In addition to the cross-correlation and coherence measurements described above, data was gathered with the premise of utilizing the three-microphone method to separate the correlated and uncorrelated portions of the radiated sound field. Specifically, the objective is to separate the contributions of the large-scale and small-scale turbulence structures at far-field measurement positions. This separation is new and provides the most significant evidence in support of the two-noise source model since the development of the two similarity spectra discussed in Chapter 2.

The results of the previous sections indicate that the large-scale turbulence structures radiate highly directional coherent noise to the far-field in the downstream direction within the Mach wave radiation cone. Additionally, the findings indicate that uncorrelated portion of the sound field are due primarily to the production of radiated noise via the random small-scale turbulent eddies. This component dominates in the sideline direction. Because of these findings and their consistency with the two-noise source model, one would expect the three-microphone method, which—as described in Chapter 2—is capable of separating correlated and uncorrelated noise sources at far-field microphones, to be useful in separating the contributions of the two turbulence scales in the far-field. Findings from such experimentation are shown in the figures below. The data reported below is for a Mach 0.9 jet exhausting from the 1.6-inch diameter conical

round nozzle shown in Figure 3.4. The jet was monitored by the eight-microphone polar arc setup depicted in Figure 3.9. Sampling parameters of 24 Hz bandwidth, 1024 averages, 25% overlap, and a span of 76.8 kHz were used in the acquisition of this data. In the figures below, the total measured auto-spectra are represented by the solid black line, the three-microphone method correlated (i.e., those labeled *Est. large-scale*) and uncorrelated (i.e., those labeled *Est. small-scale*) results are shown using blue squares and green plus symbols, respectively. The similarity spectra of Tam et al.³³ are indicated by the broken curves. The peaky or F-spectrum is indicated by the dashed red line, and the broad or G-spectrum is shown by the dash-dot orange line.

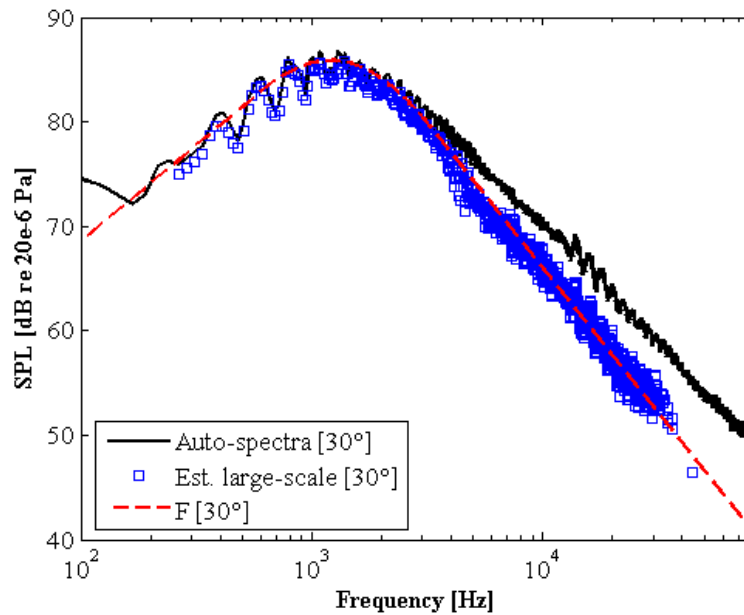


Figure 4.27 Three-microphone method (using microphones at 30, 35, and 40 degrees) findings at $\theta = 30^\circ$, Mach 0.9 jet exhausting from a 1.6-inch diameter conical round nozzle.

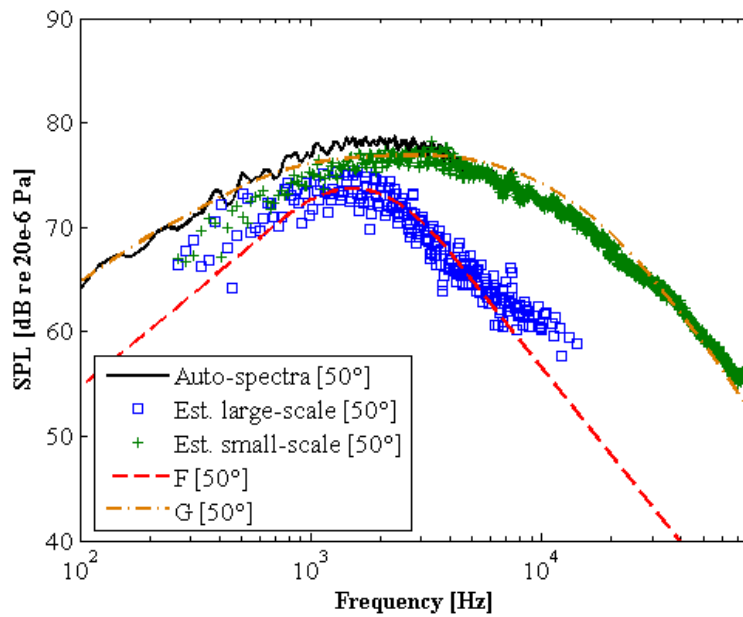


Figure 4.28 Three-microphone method (using microphones at 30, 40, and 50 degrees) findings at $\theta = 50^\circ$, Mach 0.9 jet exhausting from a 1.6-inch diameter conical round nozzle.

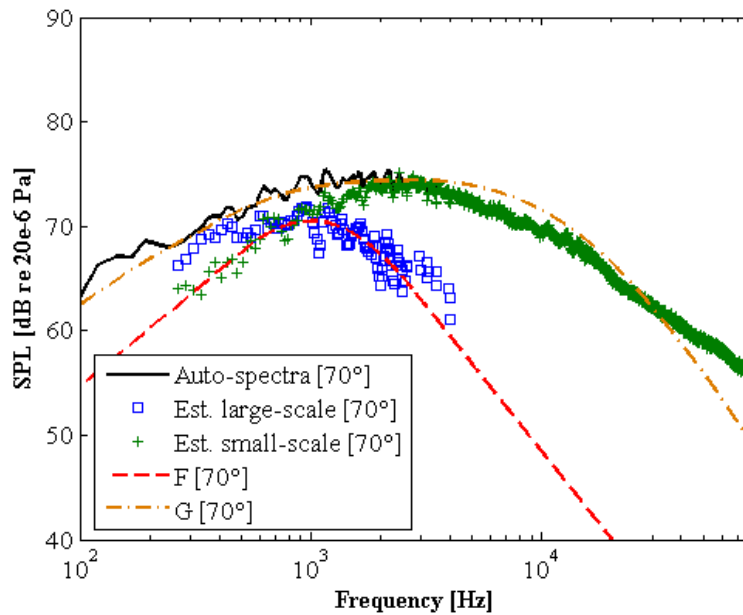


Figure 4.29 Three-microphone method (using microphones at 70, 80, and 90 degrees) findings at $\theta = 70^\circ$, Mach 0.9 jet exhausting from a 1.6-inch diameter conical round nozzle.

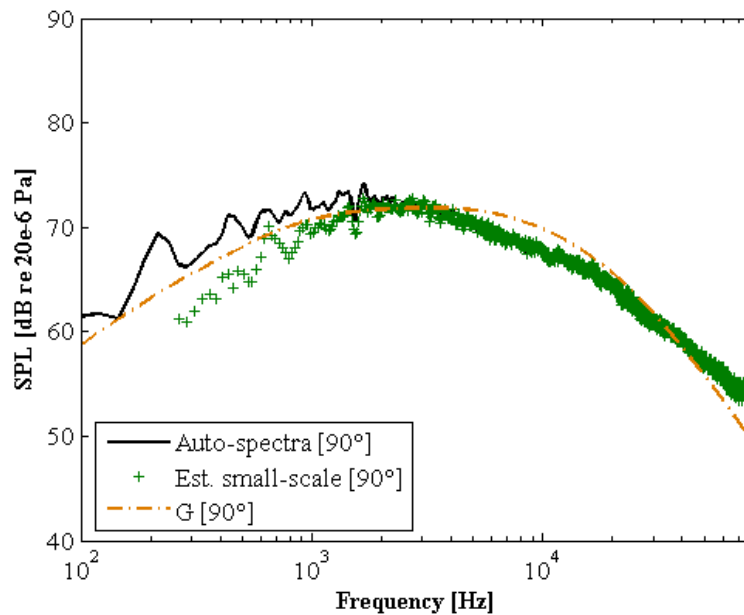


Figure 4.30 Three-microphone method (using microphones at 70, 80, and 90 degrees) findings at $\theta = 90^\circ$, Mach 0.9 jet exhausting from a 1.6-inch diameter conical round nozzle.

In Figure 4.27, the results at the 30-degree microphone are shown. The implementation of the three-microphone method at this microphone required the use of auto-power spectra and coherence data gathered at the 30, 35, and 40 degree positions. This allowed for proper characterization of the field within the Mach wave radiation cone of the Mach 0.9 jet. The 30-degree microphone is positioned in the extreme downstream direction; thus the only the correlated portion of the three-microphone results are relevant. Here the peaky similarity spectrum matches well with the calculated results indicating that the large-scale turbulence structures do indeed radiate coherent noise in this direction as predicted by the two-noise source model. Furthermore, as indicated by the two-noise source model, the contribution of large-scale turbulence structures to the far-field is shown dominant at the 30-degree microphone.

Figure 4.28 illustrates the results at the 50-degree microphone. The implementation of the three-microphone method at this microphone required the use of auto-power spectra and coherence data gathered at the 30, 40, and 50 degree positions. At the 50-degree microphone both the correlated and uncorrelated results are shown. This is done because near this angle the sound field begins to transition from a large-scale coherent noise dominated field to a random small-scale incoherent noise dominated field. Here the peaky and broad similarity spectra fit the correlated and uncorrelated three-microphone method results well at frequencies above their peaks. Even though both the correlated and uncorrelated sources are evident at the 50° angle, the correlated contribution tends to be significant especially at lower frequencies. This is due the radiation characteristics of the turbulence structures as defined by the two-noise source model and the positioning of the 50-degree microphone very near the Mach wave radiation cone of the Mach 0.9 jet. Like the results at the 30-degree microphone, these results are also in agreement with the two-noise source model.

In Figure 4.29 and Figure 4.30, measured and calculated data at the 70° and 90° angles, respectively, are illustrated. The implementation of the three-microphone method at these microphones required the use of auto-spectra and coherence data gathered at the 70, 80, and 90 degree positions. Similar to the 50-degree microphone, the 70-degree microphone is positioned within the transition region. Hence the both the uncorrelated and correlated results are indicated. In contrast to the 50-degree microphone, the 70-degree microphone is positioned nearer the sideline off-axis direction; thus, the sound field is primarily due to the uncorrelated noise. Once again this is due the radiation characteristics of the turbulence scales. The incoherent small-scale turbulence dominates

the radiated sound field in the sideline direction. Hence the contribution of the uncorrelated portion should be greater than that of the correlated portion at the 70° angle. Excluding the spectral region below 1 kHz, this is indeed the case for the 70-degree microphone data presented in Figure 4.29. Below 1 kHz, cross-over in the calculated three-microphone method levels is present. It is believed that this is due the fairly high coherence levels measured between the three microphones used within the framework of the three-microphone method. These elevated coherence levels are not believed to be a direct physical result of the jet-mixing region, but rather they may be attributed to potential internal noise (upstream of the nozzle exit) or lip noise⁶. In both instances—internal and lip noise, the noise radiated from such sources is fairly coherent at low frequencies. Thus, if internal or lip noise is present, measured coherence between the 70, 80, and 90 degree microphones (i.e., those used to generate the three-microphone method results in Figure 4.29) would indeed exhibit a fair amount of correlation as indicated above.

At the 90-degree microphone only the calculated uncorrelated results are shown. The broad spectrum matches well with the estimated small-scale contribution in the spectral region above the peak frequency. The 90-degree microphone is positioned in what is referred to as the extreme sideline direction. In this direction, the two-noise source model predicts that the sound field will be dominated by uncorrelated random small-scale turbulence eddies. The results in Figure 4.30 confirm this prediction above 1 kHz. Once again, the results below 1 kHz are believed to be contaminated by potential internal or lip noise as explained above.

The three-microphone method is not only able to separate the contributions of the turbulence scale for a 1.6-inch diameter conical round nozzle; the method is able to do so for other nozzle configurations. As shown in the figures below similar results were obtained for all other nozzle configurations tested—a 0.75-inch diameter conical round, two and four tabbed configurations fitted to the 1.6-inch diameter round nozzle, and an 8:1 rectangular nozzle. Once again the setup shown in Figure 3.9 was used to monitor a Mach 0.9 jet exhausting from the specified nozzle configuration. The sampling parameters remained unchanged from the 1.6-inch round nozzle case. The results at the 30-degree microphone as calculated via the three-microphone method using microphones positioned at 30°, 35°, and 40° are shown in the upper left-hand plot of each figure below. The findings at the 50-degree microphone as calculated using data gathered at the 30, 40, and 50 degree microphones is depicted in the upper right-hand plot of each figure. The lower plots of each figure represent results at angles of 70° (lower left-hand plot) and 90° (lower right-hand plot) calculated using the 70, 80, and 90 degree microphones.

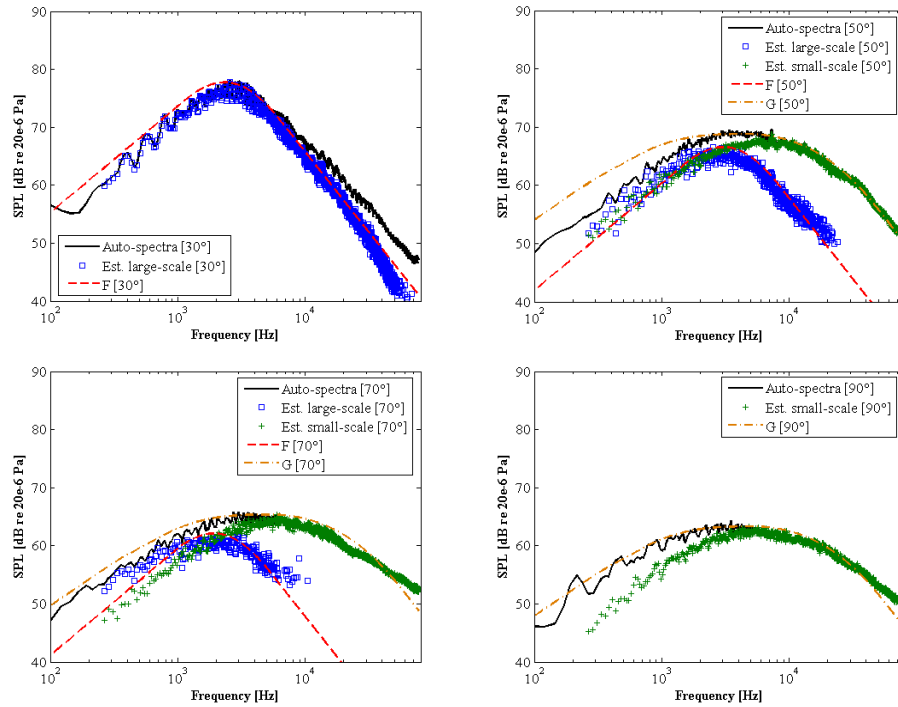


Figure 4.31 Three-microphone method results for the 0.75-inch diameter conical round nozzle at $\theta = 30^\circ, 50^\circ, 70^\circ$ and 90° , Mach 0.9 jet.

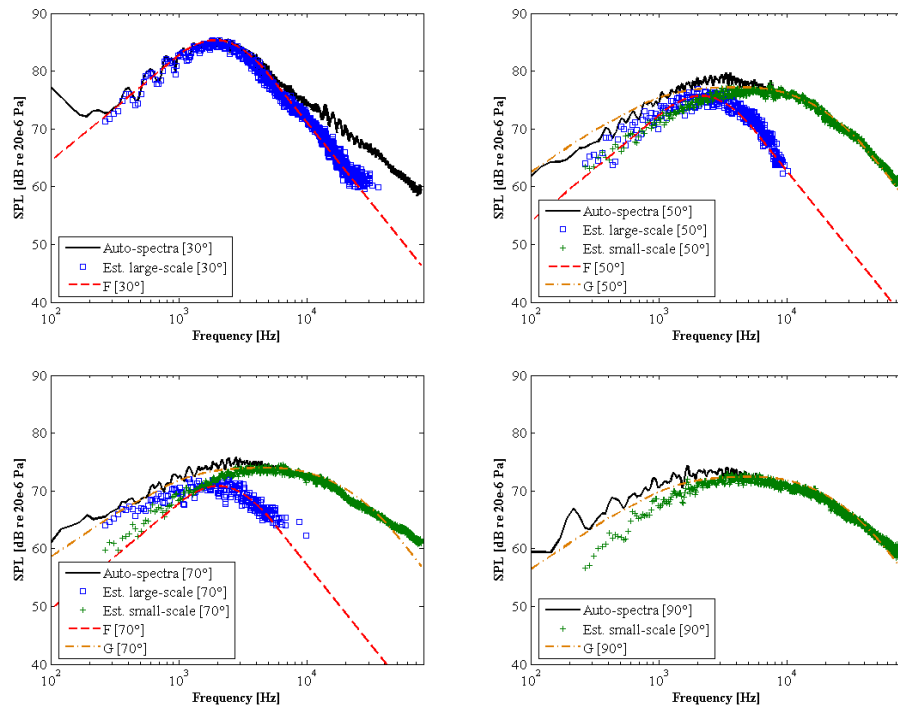


Figure 4.32 Three-microphone method results for the 1.6-inch diameter conical round nozzle with two tabs at $\theta = 30^\circ, 50^\circ, 70^\circ$ and 90° , Mach 0.9 jet.

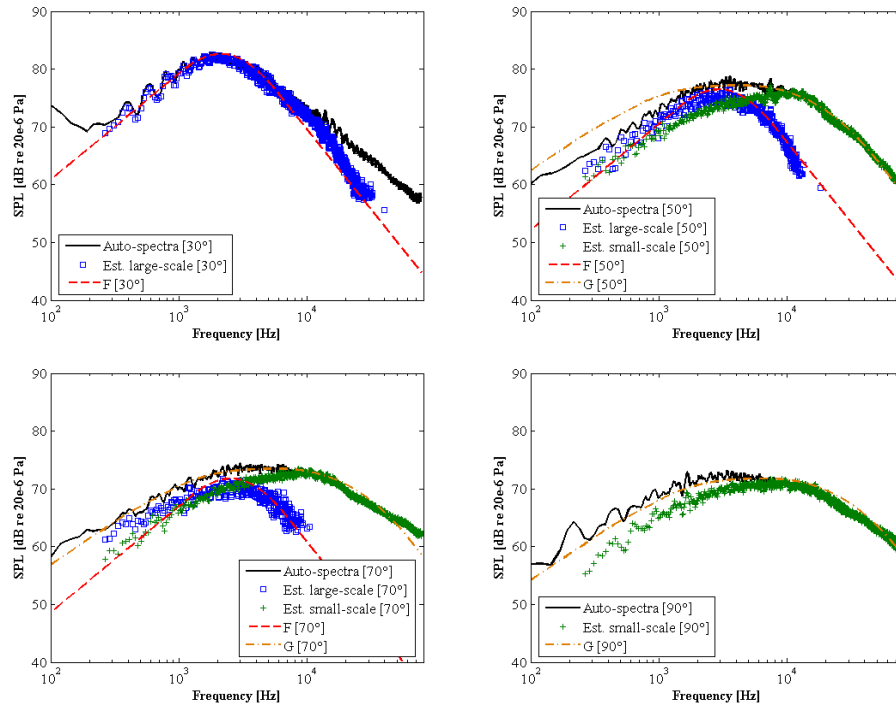


Figure 4.33 Three-microphone method results for the 1.6-inch diameter conical round nozzle with four tabs at $\theta = 30^\circ, 50^\circ, 70^\circ$ and 90° , Mach 0.9 jet.

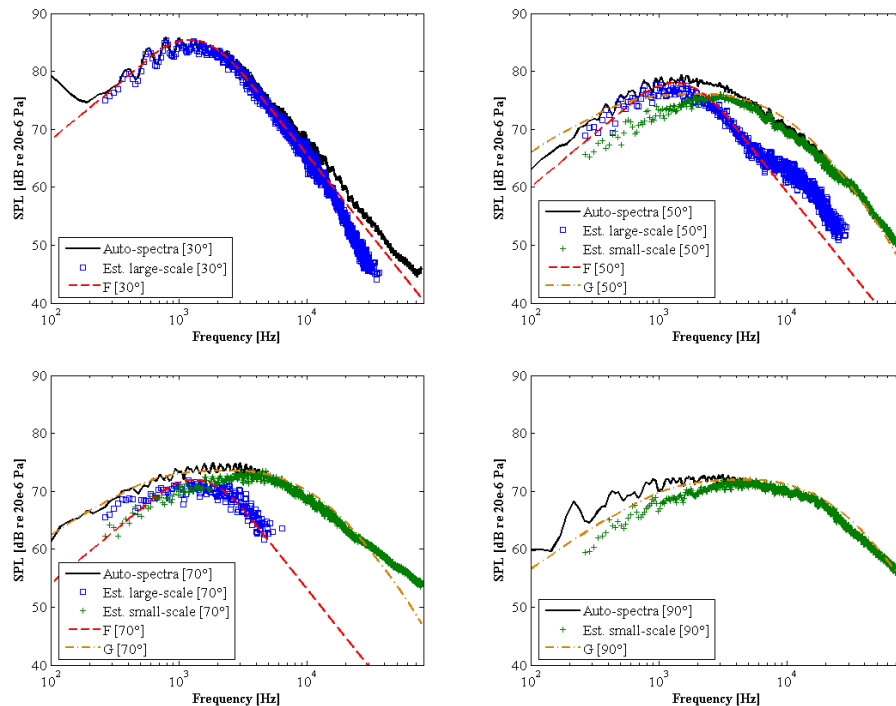


Figure 4.34 Three-microphone method results for the 8:1 rectangular nozzle at $\theta = 30^\circ, 50^\circ, 70^\circ$ and 90° , Mach 0.9 jet.

The large-scale structures are said to be the dominant noise generation entity in the downstream direction, and the small-scale turbulence eddies are said to become dominate within the sound field as the observation position is moved from the downstream direction toward the sideline direction. These phenomena are evident by comparing results in the figures above. In each of the figures above, the calculated correlated three-microphone method indicate that the sound field is dominated by the coherent large-scale turbulence structures at the extreme downstream angle of 30°. As the measurement position is moved toward the sideline direction, the contribution of the calculated correlated portion to the total measured sound pressure level becomes less substantial (excluding the spectral region below 1 kHz). This is evident when comparing the results calculated at the at the 50° and 70° positions. Below 1 kHz, cross-over in the calculated three-microphone method levels is evident. As discussed earlier, it is believed that this is due the fairly high coherence measured levels potentially due to internal noise (upstream of the nozzle exit) or lip noise. Once the observation position reaches the extreme sideline direction, the 90° position, the sound field is almost entirely due to the calculated uncorrelated portion.

The three-microphone method has been used to separate the contribution of the coherent large-scale structures from that of the uncorrelated random small-scale turbulence at multiple polar angles within the radiated sound field. Furthermore, the results from the implementation of the three-microphone method as shown in the figures above are in agreement with the two-noise source model across all observation angles at frequencies above the peaks of the *F* and *G* spectra. Moreover, the calculated correlated three-microphone method results (*Est. large-scale*) match well with the peaky spectrum across

all frequencies at the extreme downstream angle of 30° . In the 50, 70, and 90 degree plots the spectra fit— F or G —and the calculated three-microphone method results—*Est. large-scale* or *Est. small-scale*—tend to deviate from one another below their peak frequency, f_L for the large-scale/ F -spectrum fit and f_G for the large-scale/ G -spectrum fit.

CHAPTER 5

JET NOISE INCOHERENCE APPLICABILITY

The multi-microphone, coherence-based signal processing techniques discussed in Chapter 2 all rely on the measured coherence between selected pairs of microphones positioned within the radiated sound field. Specifically, the methods of Chung³, Hsu and Ahuja⁵ and Minami and Ahuja⁷ rely on the assumption that jet noise measured at selected far-field microphones spaced some distance apart can be considered incoherent at the frequencies of interest. Hsu and Ahuja⁵ and Ahuja⁶ have used the assumption that jet noise is incoherent at microphones spaced some distance apart. They verified this assumption for a round jet operated at a few limited Mach numbers. In the present investigation, the nature of jet noise has been examined through a series of experiments designed to study jet noise coherence across a variety of nozzle geometries and jet Mach numbers ranging from subsonic to supersonic. It was shown in Chapter 4 that the jet-mixing noise associated with the small-scale turbulence is incoherent for small angular separations between any two microphones. The large-scale turbulence noise, on the other hand, was found to be coherent between two microphones only in the downstream direction. What is needed is to determine the largest angular separation between any two microphones so that the coherence between them is negligible. This is required so that coherence-based, multiple-microphone techniques can be used to separate internal noise from jet-mixing noise. Some experiments discussed in this chapter are designed to determine this angular separation. All experiments discussed in this chapter have

provided further understanding about the nature of the radiated sound field of jet-mixing noise and helped in the further development of engine noise diagnostics using coherence-based signal enhancement techniques.

5.1 Establishment of a Coherence Threshold

The establishment of a minimum measurable coherence and corresponding minimum educable sound pressure level was paramount in producing accurate results using coherence-based signal processing techniques. According to Carter⁵⁴, the theoretical threshold on the measurable coherence is dependent upon the number of ensemble averages used in data acquisition. He shows that this threshold is given by

$$\left(\gamma^2\right)_{floor} = 1 - (1 - P)^{1/(n_d - 1)} \quad (5.1)$$

where n_d is the number of disjoint ensemble averages and P is the percentage of the measured coherence values (of two completely independent signals) which are greater than the coherence threshold. Further manipulation of the coherence threshold leads the establishment of a minimum educable buried sound pressure level based on the level of the total measured auto-spectrum of the signal. The difference in the total sound pressure level and the minimum educable level is given by

$$\Delta SPL_{floor} = 10 \log_{10} \left(\sqrt{\left(\gamma^2\right)_{floor}} \right) \quad (5.2)$$

Since, by definition, the theoretical coherence threshold is always less than one, ΔSPL_{floor} will be less than zero. Hence, the minimum educable buried sound pressure level at a given frequency is defined by

$$SPL_{floor}(f) = SPL_{total}(f) + \Delta SPL_{floor} = SPL_{total}(f) + 10 \log_{10} \left(\sqrt{(\gamma^2)_{floor}} \right) \quad (5.3)$$

A simple test was performed to offer verification of the analytical coherence floor for the signal analyzer used in the current research. The results are shown in Figure 5.1 and Figure 5.2. Two completely independent uncorrelated electronic signals were input into two separate signal analyzer channels. Signal processing parameters of 1024 averages and 25% overlap were used over a 76.8 kHz span with bandwidth of 6 Hz. The coherence between the two signals was measured and recorded. Two signal combinations of equal amplitude ([800 mV, 800 mV] and [400 mV, 400 mV]) and a combination (800 mV, 400 mV) of differing amplitudes were studied. Irrespective of the input signal amplitudes, the results from each cross-correlation were quite similar as indicated in Figure 5.1.

As indicated in Figure 5.2, 99.9% of the measured data is below a coherence of 0.01. This implies that when measuring coherence between two signals that have some relationship between them, measured coherence values greater than 0.01 can be used with 99.9% confidence, and those below 0.01 can be assumed to be zero. Using equation (5.3), a coherence floor of 0.01 corresponds to a minimum educable level that is 10 dB less than the total sound pressure level (e.g., $SPL_{floor}(f) = SPL_{total}(f) - 10dB$). Similarly,

at 95% confidence, a coherence of 0.002925 gives an SPL reduction of 12.7 dB (e.g., $SPL_{floor}(f) = SPL_{total}(f) - 12.7dB$) and at 90% confidence a coherence of 0.002262 yields a reduction of 13.2 dB (e.g., $SPL_{floor}(f) = SPL_{total}(f) - 13.2dB$). Throughout the experimental program utilized in this work the 99.9% confidence threshold was utilized. Thus, any measured coherence values less than 0.01 were assumed to be zero when analyzing the measured data.

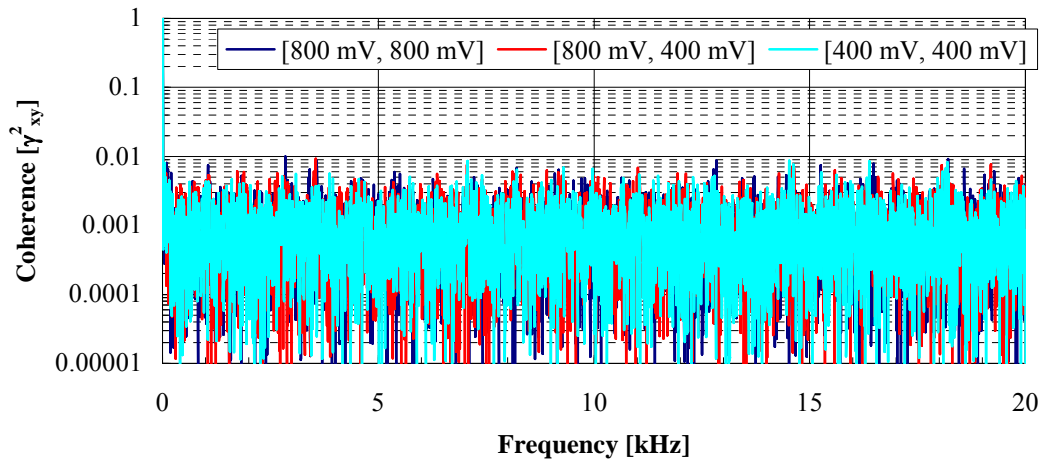


Figure 5.1 Measured coherence values between two completely independent signals.

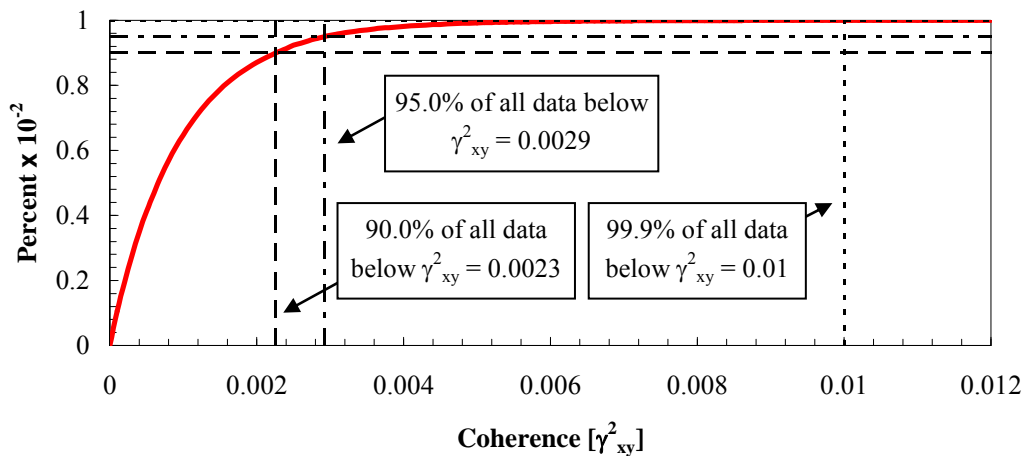


Figure 5.2 Percent of measured coherence values between two completely independent signals across all frequencies below a given coherence level.

5.2 Some Questions Answered

Prior to the detailed testing of the all nozzle geometries, tests were completed with a 1.6-inch diameter conical round nozzle. This testing was done to optimize the data sampling parameters, specifically the number of averages needed for accurate measurement of coherence. A typical example of such measured coherence data is provided in Figure 5.3.

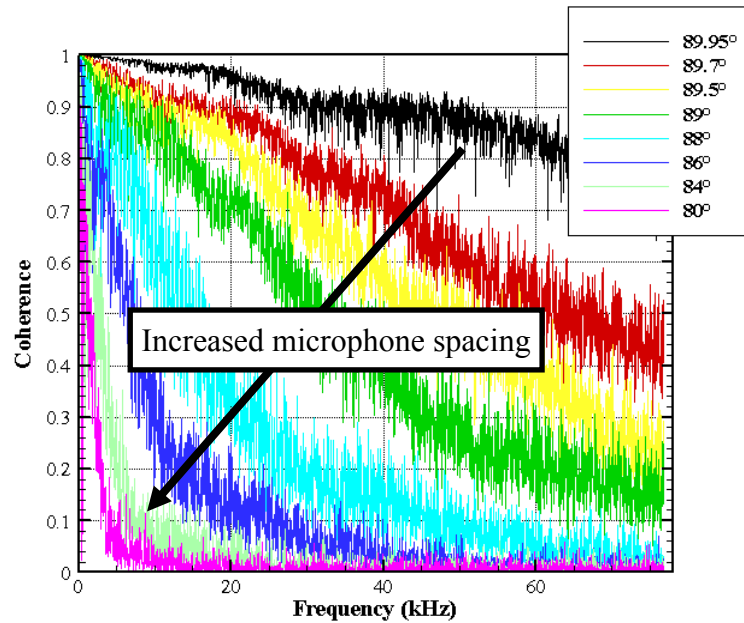


Figure 5.3 Reduction in coherence of jet noise between two far-field microphones with increasing separation between them (reference microphone positioned at 90° relative to the jet exit).

Pure subsonic jet-mixing noise typically becomes incoherent at any two microphones as the angular microphone separation is increased. This is clearly seen in the Figure 5.3. Here microphones located in a polar arc positioned at a distance of 60 diameters ($D_e = 1.6''$) from the nozzle exit were used to make coherence measurements. The coherence between a reference microphone located at 90° with respect to the downstream jet axis and another microphone almost touching it was first acquired. The second microphone

was then separated from the 90° microphone in small polar angle intervals such that the angular microphone separation gradually reached ten degrees. When the two microphones were almost touching each other the estimated angle of the second microphone was 89.95°. As the separation between the two microphones is increased, the coherence tends to zero at most frequencies. If the two microphones were co-located, the coherence would have been unity across all frequencies. Results similar to those presented above were obtained by Ahuja⁶. The spatial characteristics of jet noise are discussed in more detail later in this chapter, but first the large frequency-to-frequency fluctuations in the measured data shown in the figure above must be addressed.

The data shown in Figure 5.3 was gathered with a data acquisition setting of 128 averages. The coherence spectra display large fluctuations from frequency to frequency. This feature is typically indicative of an inadequate number of averages for acquiring the final coherence spectra. In order to clean up the coherence plots and help improve the accuracy of data measurements, a simple study was conducted to determine the optimum number of averages. In this study, jet noise measurements were taken with varying average settings at microphones located at 90, 89.95, and 89.5 degrees with respect to the downstream jet axis. Selected results for this study are depicted in Figure 5.4. Results for four separate average settings—namely, 128, 512, 1024, and 8192—are shown in Figure 5.4 (a) through (d), respectively. Each figure shows two sets of coherence spectra. The upper curve is the coherence between the 90- and 89.95-degree microphones, whereas the lower curve is the coherence between the 90- and 89.5- degree microphones. For both curves, increasing the number of averages reduces the frequency-to-frequency fluctuations, rendering a cleaner coherence spectrum. It should also be noted that these

results indicate that an additional angular separation of only 0.5° can reduce the coherence by a large factor.

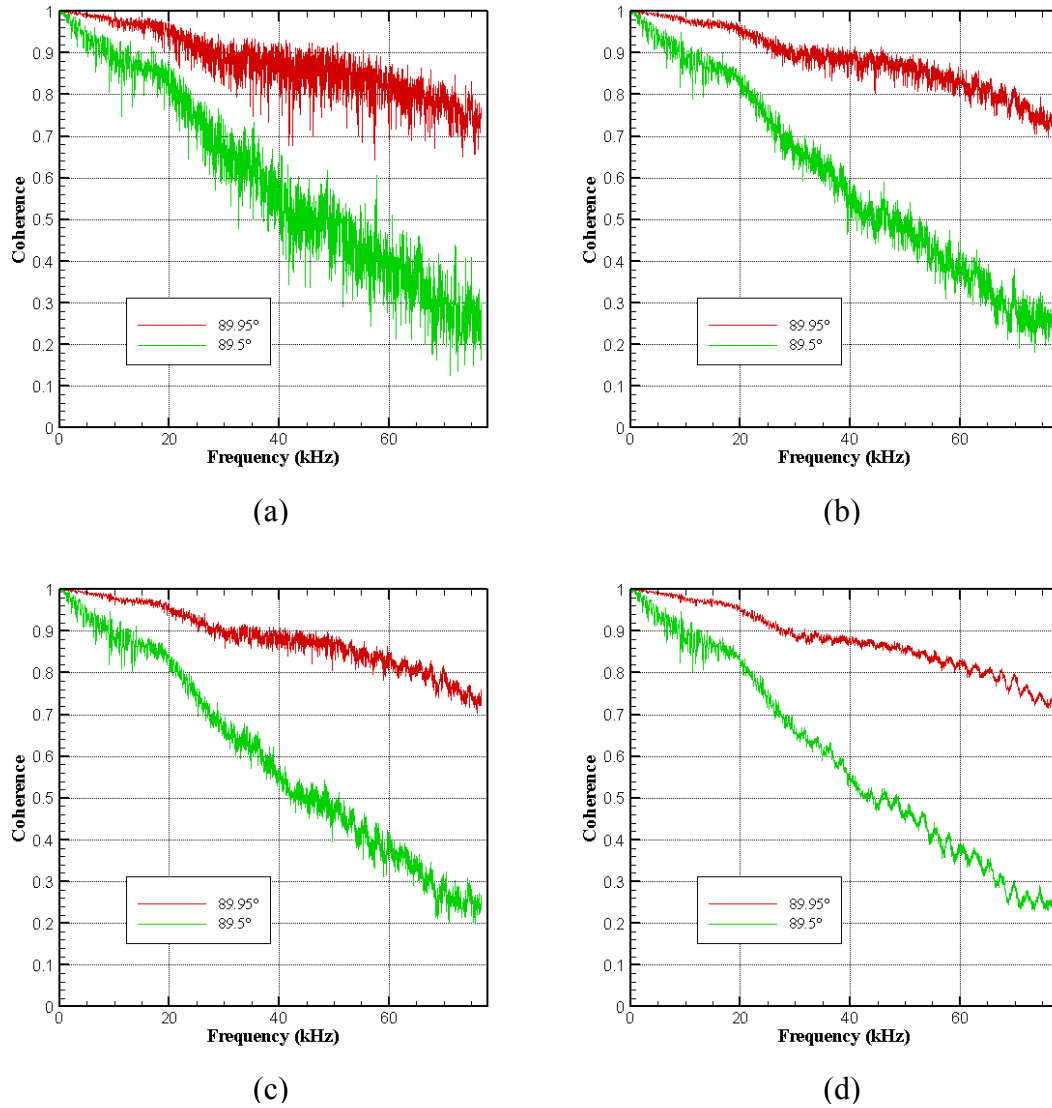


Figure 5.4 Effect of number of averages on coherence values: (a) 128 averages, (b) 512 averages, (c) 1024 averages, and (d) 8195 averages, Mach 0.8 jet, 25% Overlap.

Due to the significant increase in the amount of time required to take large numbers of averages (which with the DAC system used in the current work is not entirely dependant

upon the sampling parameters) and the fact that only negligible improvements in the cleanliness of the data were obtained after 1024 averages, a data acquisition average setting of 1024 ensemble averages was select for the remainder of the experimental tests. Further sampling parameters include a 24 Hz bandwidth, 25% overlap, and a span of 76.8 kHz.

5.3 Far-Field Coherence Measurements

Jet noise coherence studies as a function microphone arrangement (polar versus linear), adjacent microphone spacing, radial microphone positioning, jet Mach number, and nozzle geometry were carried out to determine the most advantageous microphone setup for future jet and engine noise diagnostics. In these experiments, the jet was produced by a conical round nozzle with a diameter of 1.6 inches operated at a jet Mach number of 0.8. The basic setup and placement of the microphones are shown in Figure 3.10. All variations in the setup are noted and discussed in appropriate section below. The data is plotted as a function of Strouhal number (fD/U). Results from these coherence studies are discussed in the following sections.

5.3.1 Microphone Arrangement: Polar v. Linear

The spatial coherence characteristics of jet noise were investigated with both a polar microphone arc and a linear microphone array. As expected, findings show that the level of measured coherence between adjacent microphones is highly dependent on their angular separation irrespective of whether the microphones are aligned linearly or positioned within a polar arc. Furthermore, no matter whether the microphone arrangement is linear or polar, so long as the angular separation between the microphone

pair remains consistent the coherence will remain identical. As shown below, varying the linear separation does indeed change the measured coherence, but as explained below that change is due entirely to the subsequent change in angular separation.

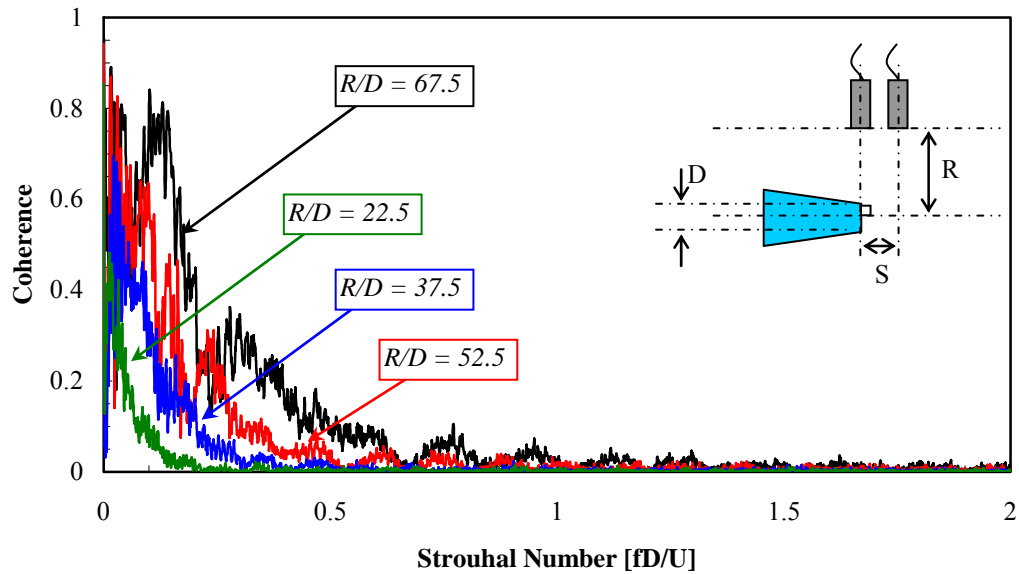


Figure 5.5 Measured jet noise coherence as function of distance from nozzle centerline, fixed linear separation of 22.5 diameters, 1.6-inch nozzle, Mach 0.8 jet.

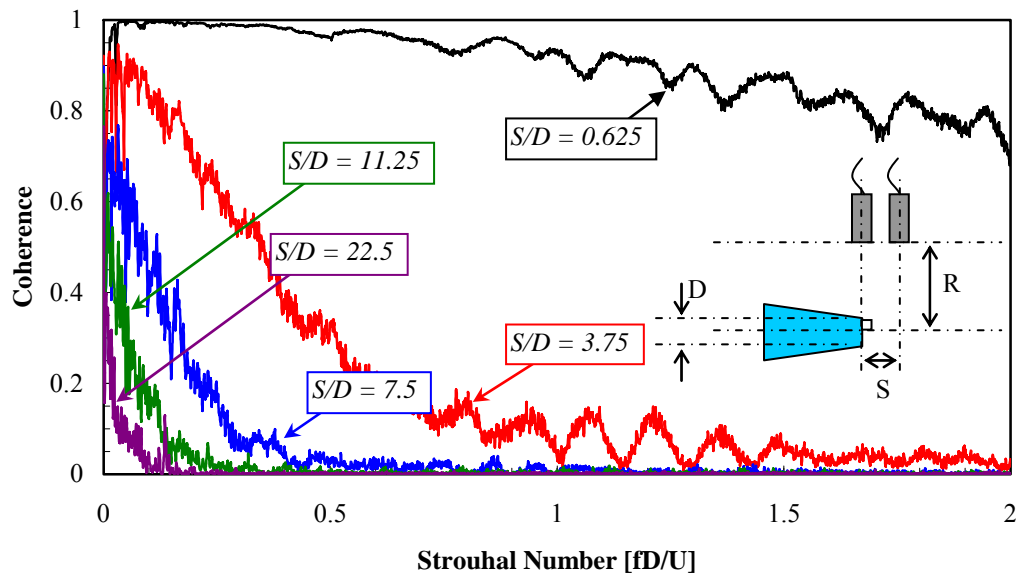


Figure 5.6 Measured jet noise coherence as function of linear microphone spacing, fixed distance from nozzle centerline of 22.5 diameters, 1.6-inch nozzle, Mach 0.8 jet.

In Figure 5.5 and Figure 5.6, the coherence is measured as a function of microphone distance from the nozzle centerline and linear microphone spacing, respectively. The data in Figure 5.5 was gathered with constant linear separation between the two microphones ($S/D = 22.5$). Conversely, the distance from the nozzle centerline to the face of the microphone pair was increased from 22.5 to 67.5 diameters. The jet noise becomes more and more coherent between the microphone positions as the microphone pair is moved away from the jet centerline. Hence, the movement of the microphone pair farther and farther away from the jet centerline while maintaining the linear separation significantly affects the measured coherence. Moreover, as the microphone pair is moved away from the nozzle exit the angular separation between the microphones is decreased and the coherence is increased.

As for the data shown in Figure 5.6, it was gathered with constant positioning of the microphone pair with respect to the jet centerline ($R/D = 22.5$). The microphone separation was increased from 0.625 to 22.5 diameters. Here the jet noise becomes less coherent as the linear separation is increased, which in turn increases the angular separation. An important side note that requires discussion here is that at the smallest S/D values (0.625 and 3.75) the coherence curves exhibit a noisy behavior beyond a Strouhal number of one. Since at such small S/D the microphones are located sufficiently close to one another, this is believed to be the result of reflections either from the microphones themselves or their supports.

These results show that the measured coherence is highly dependant upon the angular spacing of the two microphones. This is true of all acoustic systems where jet noise is prevalent. As the microphone pair was moved away from the centerline of the jet with constant linear spacing, the angular separation between the two microphones was decreased from 45 to 18 degrees. Similarly, as the linear spacing was increased at constant distance from the jet centerline, the angular separation was increased from approximately 2 to 45 degrees. In both instances, the larger angular separation yielded lower measured coherence while the smaller angular spacing provided higher measured coherence. These findings indicate that whether a linear array of microphones or polar microphone arc is used, large angular separation between the microphones provides negligible coherence for jet noise, even for the noise associated with the large-scale turbulence structures. Furthermore, they also lend themselves to the conclusion that due to the sizing limitations of the GTRI anechoic chambers (Figure 3.1 and Figure 3.2) and the extremely large linear separation distances that would be needed to maintain

sufficient angular separation for a multiple microphone system (i.e., a system composed of more than two microphones) a polar arc arrangement of microphones is more useful. The radial positioning of the polar arc with respect to the nozzle exit plane is the focus of the next section.

5.3.2 Radial Microphone Arc Positioning

Because the jet noise sources are distributed along the length of the jet, it is not immediately obvious as to where microphone arc should be placed radially for the jet noise to appear least coherent between two far-field microphones with a given angular separation. Thus, the issue of the radial positioning of the polar arc with respect to the nozzle exit is addressed in this section. Coherence data were measured between two microphones placed in the sideline direction at 90 and 80 degrees relative to the nozzle exit. The coherence spectrum between the two microphones was measured as a function of radial distance relative to the nozzle exit. The angular separation was maintained throughout the entire span of radial positions. The results are shown in Figure 5.7. Excluding the data labeled $R/D = 160$, all data reported is for a Mach 0.8 jet exhausting from a 1.6-inch conical round nozzle. To obtain an R/D of 160 a smaller diameter nozzle was used. The diameter of this nozzle measures 0.75 inches. As shown in Figure 5.7, the jet noise tends to be less coherent as the microphone pair is moved away from the nozzle exit. Moreover, after approximately 50 diameters, the reduction in the measured jet noise coherence becomes negligible. At Strouhal numbers larger than 0.5, the coherence levels approach their minimum. At the lower Strouhal numbers, the coherence levels remain reasonably high although they decrease with R/D and reach an asymptote at an R/D slightly larger than 50.

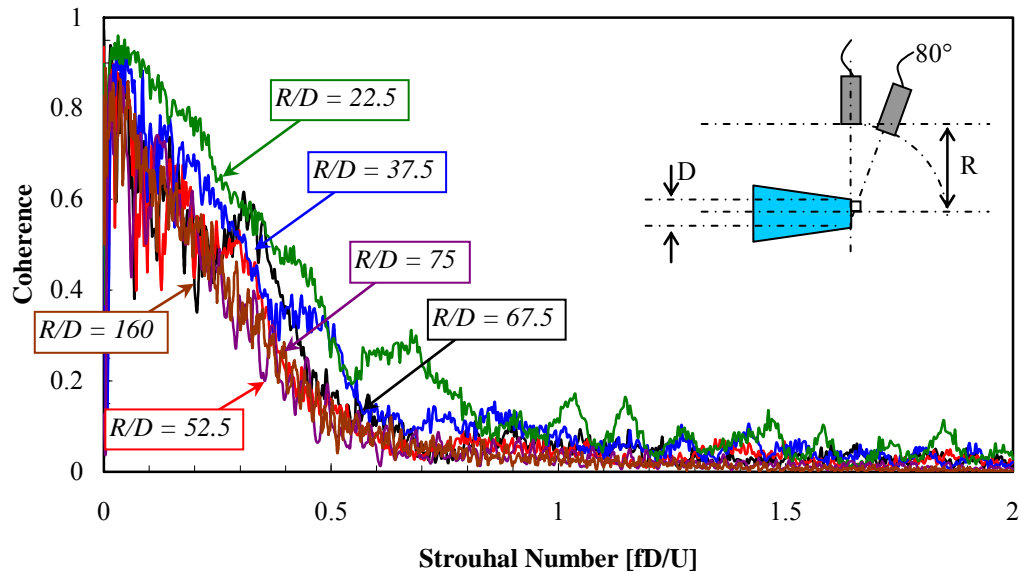


Figure 5.7 Measured jet noise coherence as function of radial distance from nozzle exit, fixed angular separation of 10 degrees, 1.6-inch nozzle, Mach 0.8 jet.

5.3.3 Microphone Separation

In the previous sections it is established that a polar arc arrangement of microphones positioned more than 50 diameters radially away from the nozzle exit is most practical for assurance of jet noise incoherence over a large range of frequencies. In most signal processing techniques used to educe a buried signal and/or eliminate signal contamination, multiple microphones are required. Furthermore, in the vast majority of the engine noise diagnostic techniques, not only are multiple microphones used, but the assumption of jet noise incoherence amongst these microphones is necessary for successful application of multiple-microphone diagnostic techniques. It is well established that widely spaced microphones exhibit sufficient jet noise incoherence^{5,6}, but the question remains as to what extent the noise generation mechanisms prescribed in the

framework of the two-noise source model affect this assumption. For these reasons, the proper angular separation of the microphones within the polar arc has been investigated.

As stated earlier, the two-noise source model implies that the noise generation mechanisms of jet noise that radiate sound in the downstream and sideline directions are physically different; hence, the jet noise coherence measured at microphone pairs in the downstream direction should differ from that measured at microphone pairs in the sideline direction. According to the model, the random small-scale turbulence radiates incoherently in all directions while the coherent large-scale structures radiate sound primarily in the downstream direction. Thus, one would expect the coherence measured between two microphones positioned in the downstream direction to show greater coherence than a pair with equivalent spacing positioned in the sideline direction. These claims were investigated through a series of measured coherence spectra of a Mach 0.8 jet exhausting from a 1.6-inch conical round nozzle. A schematic of the experimental setup is shown in Figure 3.10 (polar arc only). The findings are presented below in Figure 5.8. In Figure 5.8, the coherence spectra are shown for microphone pairs spaced 10 degrees apart along a polar arc at a radius of 75 diameters from the nozzle exit. Microphone pairs positioned in the downstream, transition, and sideline directions are included. The extreme downstream microphone pair (20° , 30°) exhibits the most coherence throughout the spectra. As the measurement position is moved more toward the sideline direction, the measured coherence is decreased. At sideline positions beyond 50° , changes in the measured coherence spectra at 10-degree polar intervals are negligible. Additional data taken with 20- and 30-degree spacing intervals are shown in Figure 5.9 and Figure 5.10. At the larger microphone spacing intervals, the coherence is

significantly reduced even when both microphones are positioned in the downstream direction, e.g., $\gamma^2_{(20^\circ, 40^\circ)}$ and $\gamma^2_{(20^\circ, 50^\circ)}$. This indicates that the dominate source in the extreme downstream direction is highly directional. Furthermore, microphones spaced roughly 20 to 30 degrees apart in the downstream direction will be sufficient when the assumption of jet noise incoherence is necessary.

The primary implication of the phenomenon illustrated in the figures below, as it applies to jet and engine noise diagnostics using multi-microphone signal processing, is the need for variable microphone spacing throughout the area encompassed by the polar arc to ensure jet noise incoherence among all microphones. Adjacent microphones should be spaced according to their location relative to the nozzle exit and the dominate jet noise radiation entity within that region. In general, to ensure jet noise incoherence between correlating microphones in the downstream on-axis direction, larger microphone separations (i.e., 20° to 30° for most applications) are needed. In the sideline direction, smaller (e.g., 10°) spacing should suffice. The specific application of this phenomenon for the model- and full-scale problems is discussed in Chapter 7.

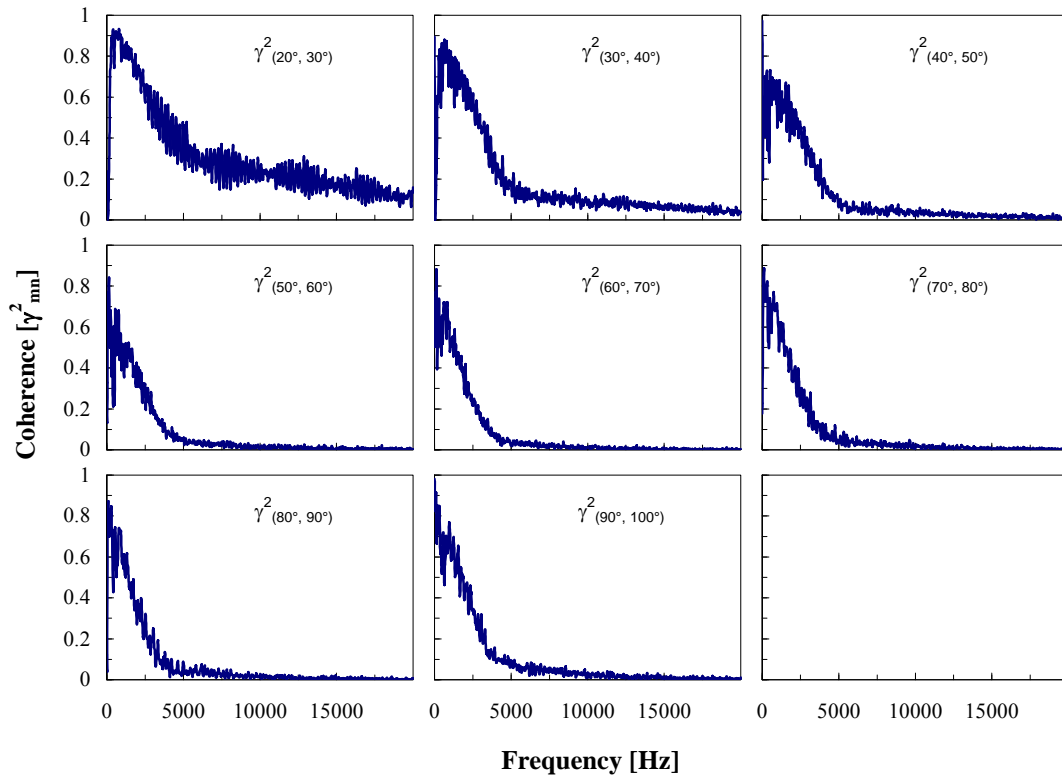


Figure 5.8 Coherence spectra for microphone pairs spaced at 10 degrees, 1.6-inch nozzle, Mach 0.8 jet.

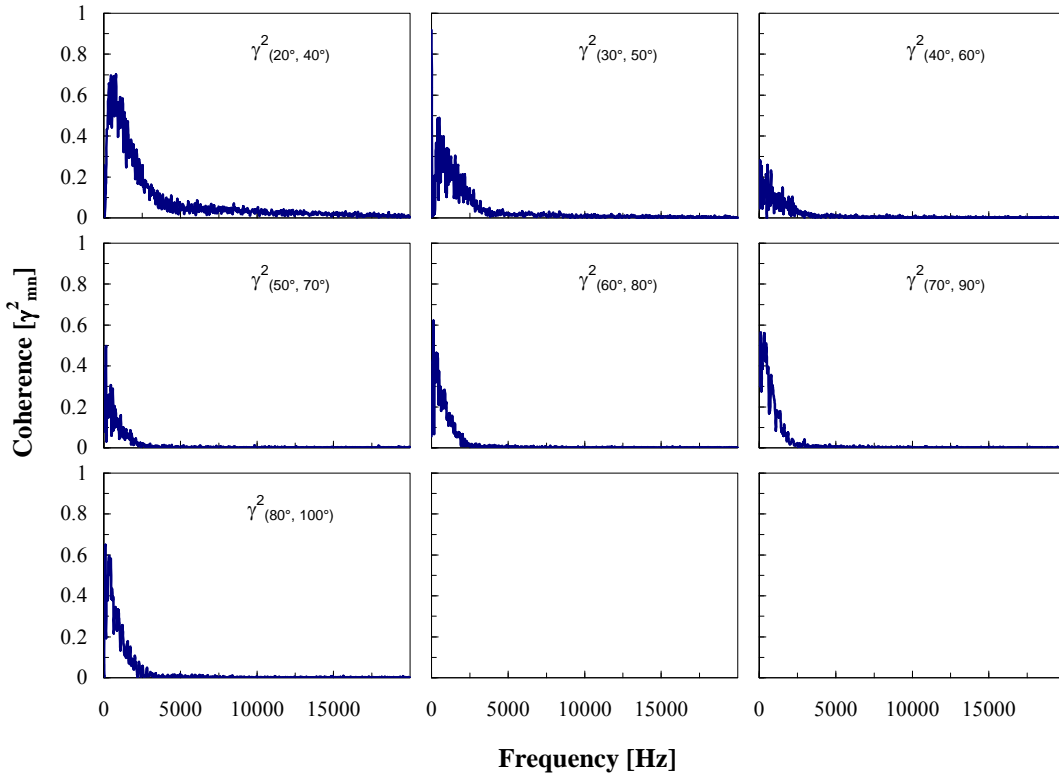


Figure 5.9 Coherence spectra for microphone pairs spaced at 20 degrees, 1.6-inch nozzle, Mach 0.8 jet.

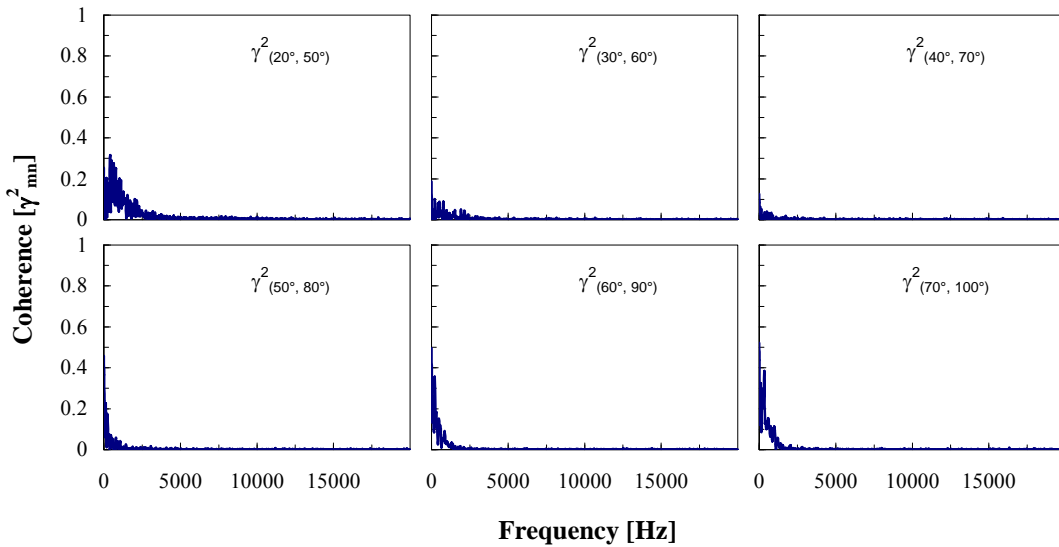


Figure 5.10 Coherence spectra for microphone pairs spaced at 30 degrees, 1.6-inch nozzle, Mach 0.8 jet.

5.3.4 Nozzle Geometry

In the previous sections, it has been shown that the assumption of jet noise incoherence is valid for a polar arc of properly positioned microphones. These microphones are to be placed at least 50 diameters radially from the nozzle exit and spaced approximately 20 to 30 degrees apart in the downstream direction and 10 degrees apart in the sideline direction. The findings of the previous sections were gathered using a 1.6-inch conical round nozzle. Additional experiments have been conducted to determine if these findings concerning the jet noise incoherence assumption are consistent over a range of nozzle geometries. In doing so, a 0.75-inch conical round nozzle, an 8:1 rectangular nozzle, and a pair of tabbed round nozzle configurations were tested. The tabbed nozzle configurations consist of a two- and a four-tab configuration with the tabs placed along the diameter of a 1.6-inch round nozzle. Photographs of all nozzles tested are shown in Chapter 3. The setup shown in Figure 3.10 (polar arc only) was used during this testing. The findings of these tests are shown the figures below.

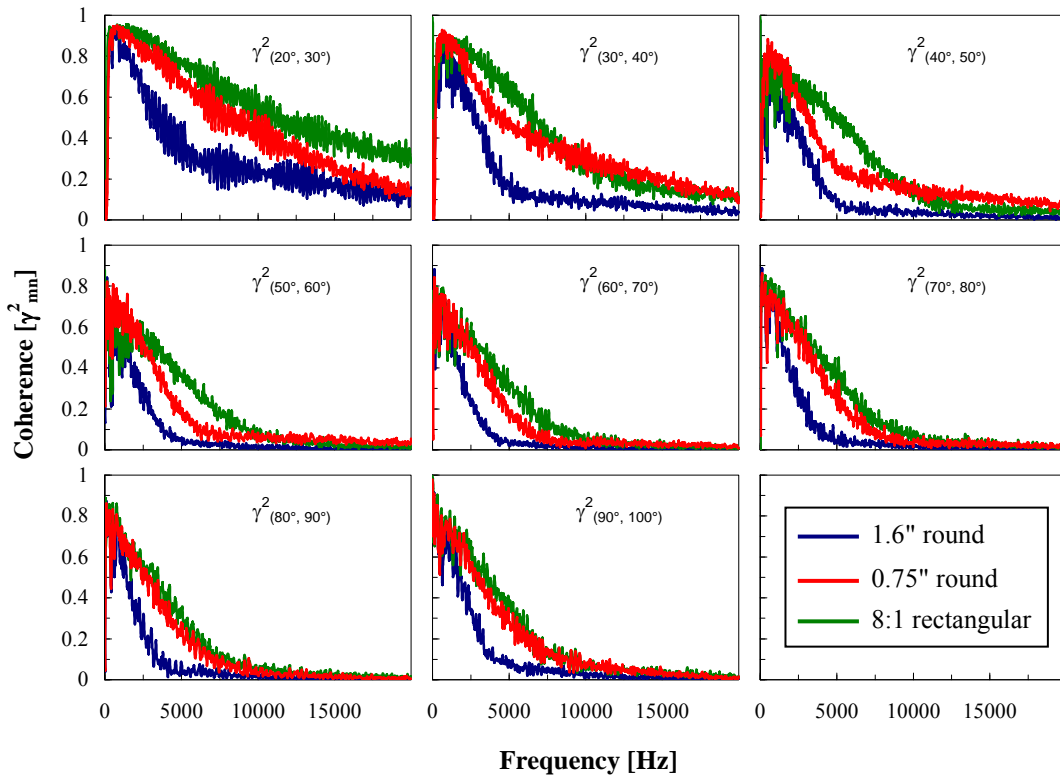


Figure 5.11 Coherence spectra for microphone pairs spaced at 10 degrees; 1.6-inch round, 0.75-inch round, and 8:1 rectangular nozzles; Mach 0.8 jet.

In Figure 5.11, coherence spectra are shown for microphone pairs spaced 10 degrees apart along a polar arc at a radius of ten feet from the nozzle exit. Nozzle geometries illustrated here include a 0.75-inch conical round nozzle, a rectangular nozzle with an aspect ratio of eight and an equivalent exit diameter of 1.6 inches, and for comparison sake, the baseline 1.6-inch conical round nozzle (same data as in Figure 5.8). The blue curve represents data for the 1.6-inch round nozzle, while the red and green curves illustrate the measurements for the 0.75-inch round and 8:1 rectangular nozzles, respectively. Once again, microphone pairs positioned in the downstream, transition, and sideline directions are included. The extreme downstream microphone pair (20°, 30°) exhibits the most coherence throughout the spectra for all nozzle geometries. As the

measurement position is moved toward the sideline direction, the measured coherence is decreased. At sideline positions beyond 50 degrees, changes in the measured coherence spectra at 10-degree polar intervals are negligible.

Another way of varying the nozzle geometry is through the addition of tabs. The inclusion of tabs is said to promote mixing of the jet fluid and reduce the radiated noise³⁵.

The effect of tabs on the measured coherence spectra is shown in Figure 5.12.

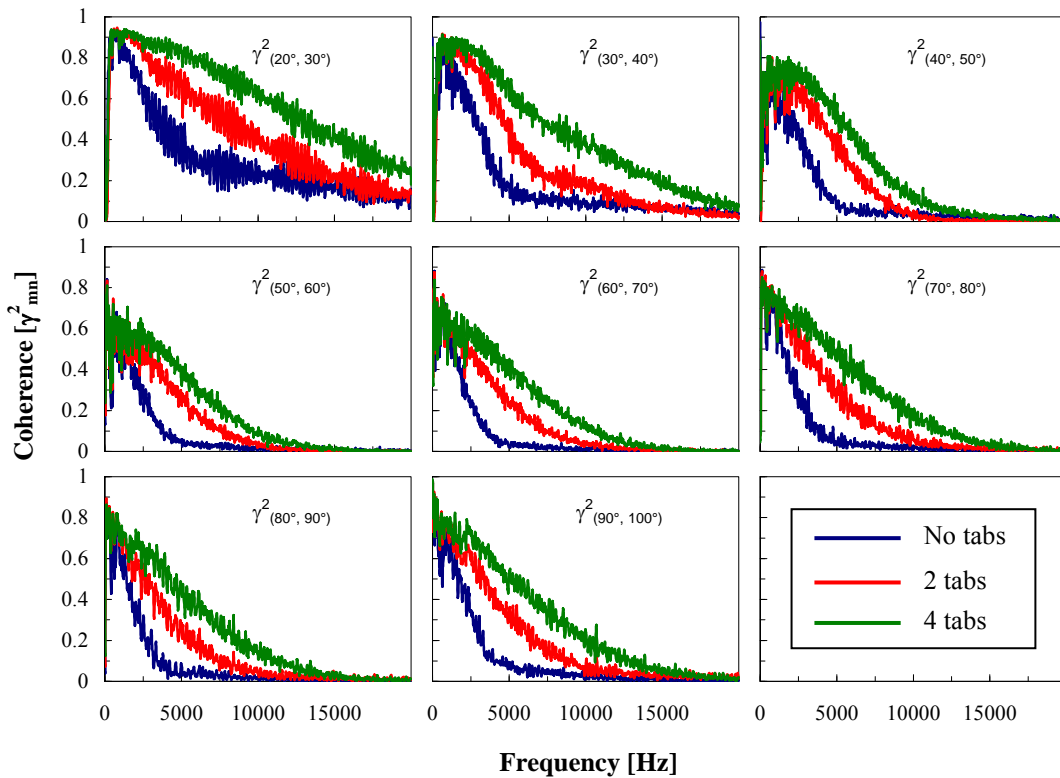


Figure 5.12 Coherence spectra for microphone pairs spaced at 10 degrees; 1.6-inch nozzle with no, two, and four tabs; Mach 0.8 jet.

In Figure 5.12, data for the two- and four-tab 1.6-inch round nozzle configurations are illustrated. For comparison, coherence spectra for the baseline (no tabs) 1.6-inch round

nozzle is also included in Figure 5.12. The data for no tabs is represented by the blue colored plot line, while the red and green curves show data for the two- and four-tab configurations, respectively. An angular microphone separation of 10 degrees was utilized. As with all previously discussed nozzle geometries, microphone pairs positioned in the downstream, transition, and sideline directions are included. The extreme downstream microphone pair (20° , 30°) exhibits the most coherence throughout the spectra for all nozzle configurations. The measured coherence is decreased as the measurement position is moved toward the sideline direction. Changes in the measured coherence spectra at 10-degree polar angle separations become negligible beyond the 50-degree position. Similar to the data taken at 10-degree intervals, additional coherence data taken for all nozzle geometries and configurations at larger angular separations are shown in the figures below. The data in Figure 5.13 through Figure 5.15 are presented in the form of calculated overall coherence (discussed in Chapter 4).

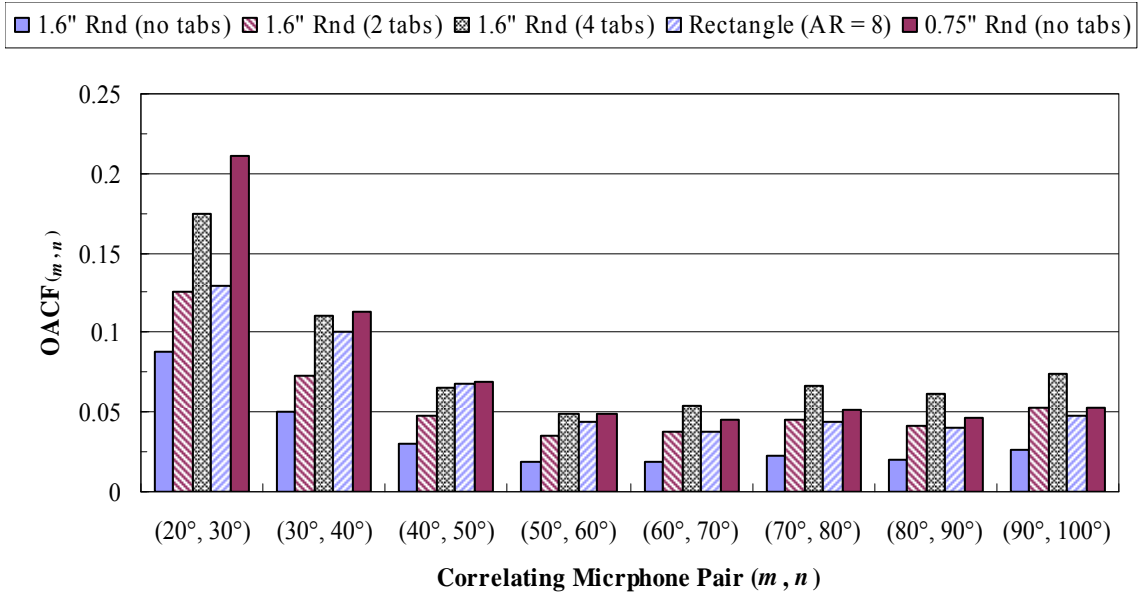


Figure 5.13 Overall coherence $OACF_{(m, m+20^\circ)}$, for multiple nozzle geometries operated at Mach 0.8.

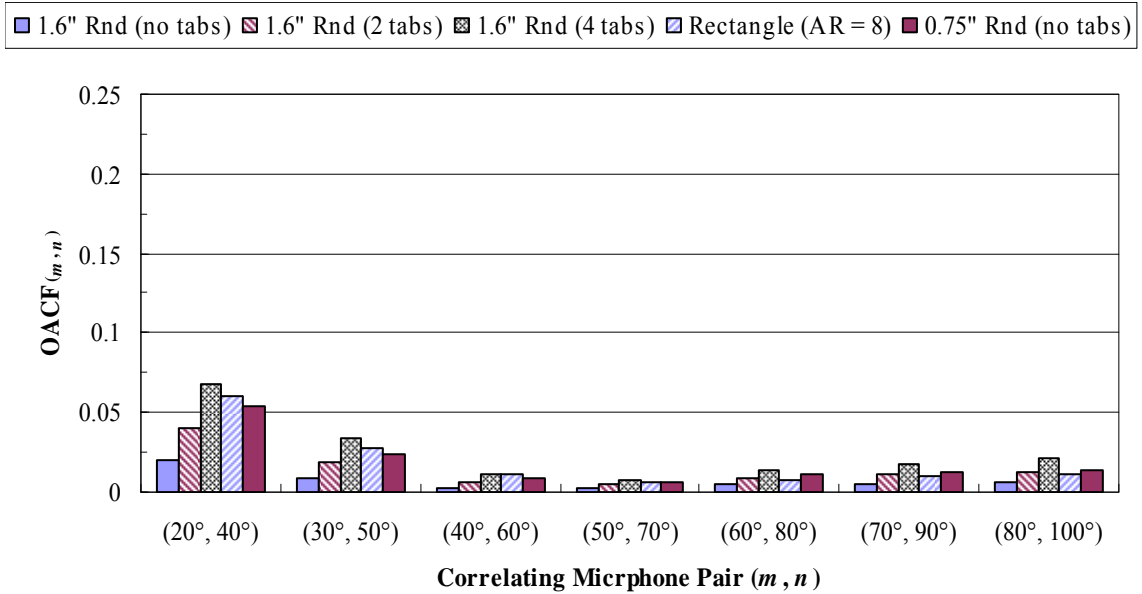


Figure 5.14 Overall coherence $OACF_{(m, m+20^\circ)}$, for multiple nozzle geometries operated at Mach 0.8.

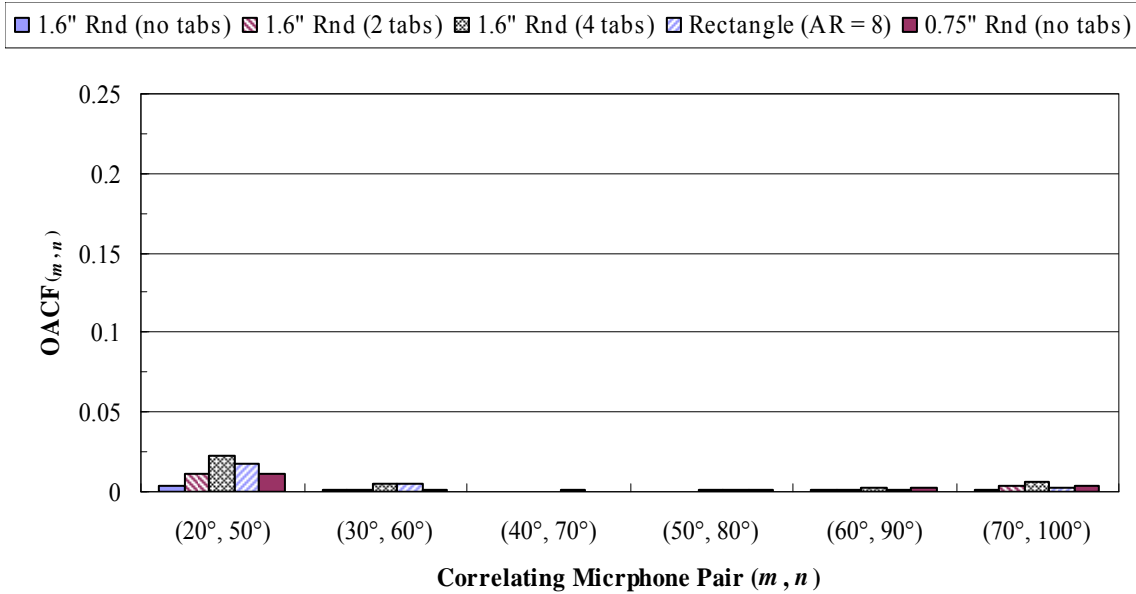


Figure 5.15 Overall coherence $OACF_{(m, m+30^\circ)}$, for multiple nozzle geometries operated at Mach 0.8.

As shown above, the coherence is significantly reduced at larger microphone spacing intervals even when both microphones are positioned in the downstream direction, e.g., $\gamma^2_{(20^\circ, 40^\circ)}$ and $\gamma^2_{(20^\circ, 50^\circ)}$. While a microphone spacing of 10° is acceptable in the sideline direction, the above figures indicate that microphone spacing of roughly 20 to 30 degrees is necessary in the downstream direction when the assumption of jet noise incoherence is used. The findings for all nozzle configurations—0.75-inch round, 8:1 rectangular, 1.6-inch round with two tabs, and 1.6-inch round with four tabs—are consistent with the results for the baseline un-tabbed 1.6-inch round nozzle.

The findings presented above in Figure 5.8 – Figure 5.15 are for a Mach 0.8 jet. Additional measurements were made for all nozzle geometries at subsonic Mach numbers ranging from 0.2 to 0.9. Results similar to those shown above were obtained across the

entire subsonic testing range for all nozzle geometries. Regardless of the consistency of the coherence measurements in the subsonic regime, the question still remains as to how the coherence spectra will behave at supersonic jet Mach numbers. Answering this question is the focus of the next section.

5.3.5 Supersonic Jet Mach Numbers

The findings in the previous sections have shown that the jet noise incoherence assumption is valid for a range of subsonic jets exhausting from a variety of nozzle geometries so long as the microphone pairs are spaced at suitable angular separations. The focus of this section is to address the validity of this assumption for supersonic jets—both fully-expanded and non-fully-expanded. The data presented in the figures below are for measured coherence between microphones placed in a polar arc positioned ten feet radially from the exit of a round converging-diverging nozzle with a design Mach number of 1.67. The CD nozzle is shown in Figure 3.8. The setup shown in Figure 3.10 (polar arc only) was used during this testing. First, the findings from the fully-expanded case are presented in Figure 5.16 and discussed below.

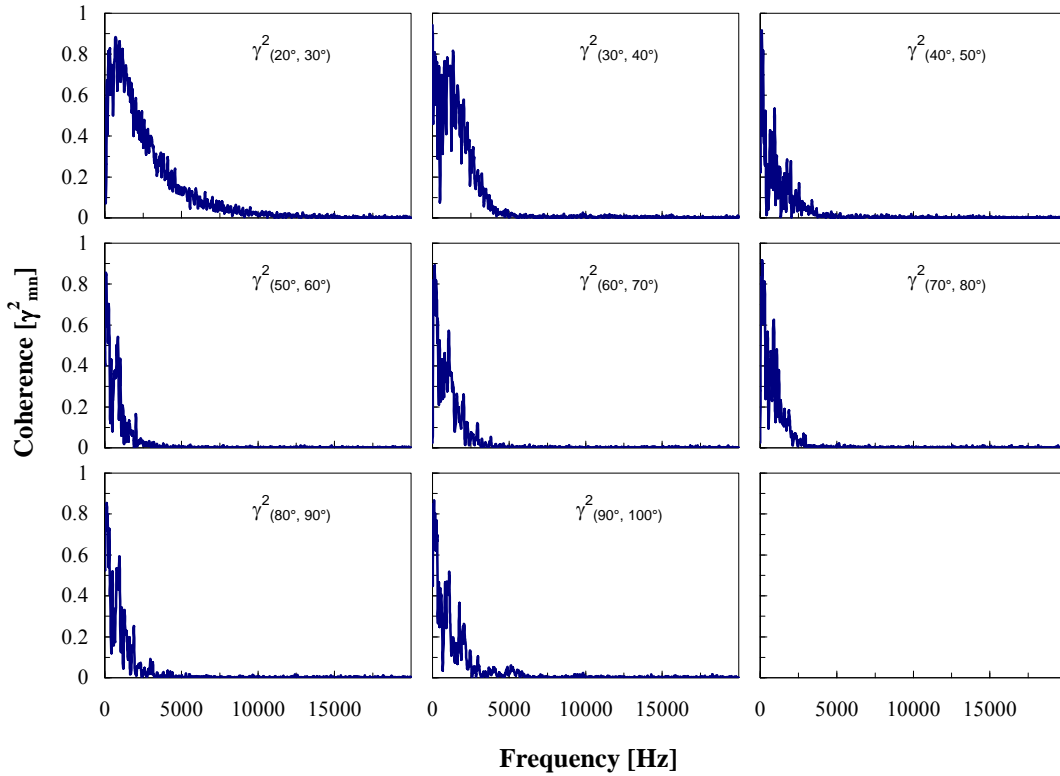


Figure 5.16 Coherence spectra for microphone pairs spaced at 10 degrees, Mach 1.67 CD nozzle with exit diameter of 2.0 inches, Mach1.67 jet.

The measured coherence spectra presented in Figure 5.16 for the Mach 1.67 CD nozzle operated at its design condition display behavior much like that of a subsonic jets (e.g., see Figure 5.8). At 10-degree spacing intervals, the coherence is largest for pairs positioned in the extreme downstream direction and smallest for pairs located in the sideline direction. At positions beyond 50° , changes in the measured coherence spectra at 10-degree polar intervals are negligible. Since it has been established that fully-expanded supersonic jets exhibit coherence behavior similar to that of subsonic jets, the next logical step is to determine if the same is true for non-fully-expanded supersonic jets. Such results are presented in Figure 5.17 and Figure 5.18 and the discussion of these results follow below.

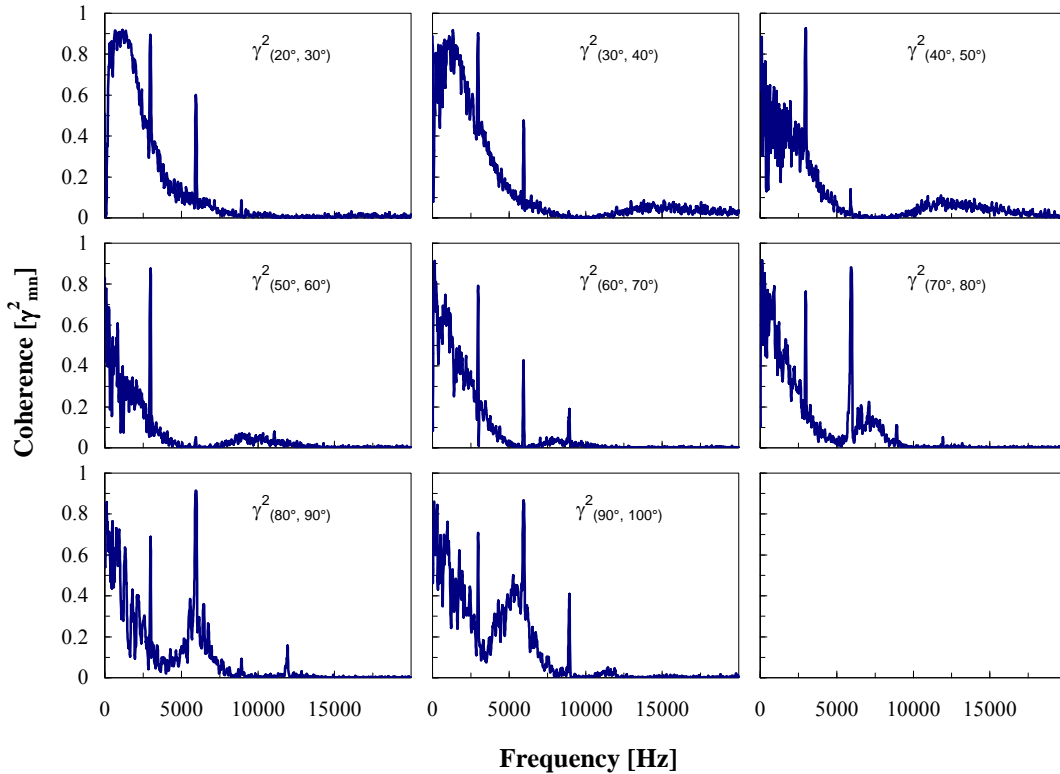


Figure 5.17 Coherence spectra for microphone pairs spaced at 10 degrees, Mach 1.67 CD nozzle with exit diameter of 2.0 inches, Mach 1.4 jet.

In Figure 5.17, a Mach 1.67 CD nozzle is operated at an over-expanded jet Mach number of 1.4. Due to the manifestation of a shock structure when operating at such an over-expanded condition, screech and broadband shock associated noise are expected. The screech is clearly evident by the spike in coherence near 3 kHz. Along with the fundamental spike, harmonics of the screech tone are evident. At positions near and beyond 70 degrees, the broadband shock associated noise induces broadband amplification of the measured coherence at frequencies between five and 10 kHz. Excluding the amplification of the measured coherence by the screech tone and broadband shock associated noise, the results are quite similar to those for the perfectly expanded case when the two microphones are spaced 10 degrees apart. The coherence is

again greatest between the extreme downstream microphones, and it decreases as the measurement position is moved toward the sideline direction.

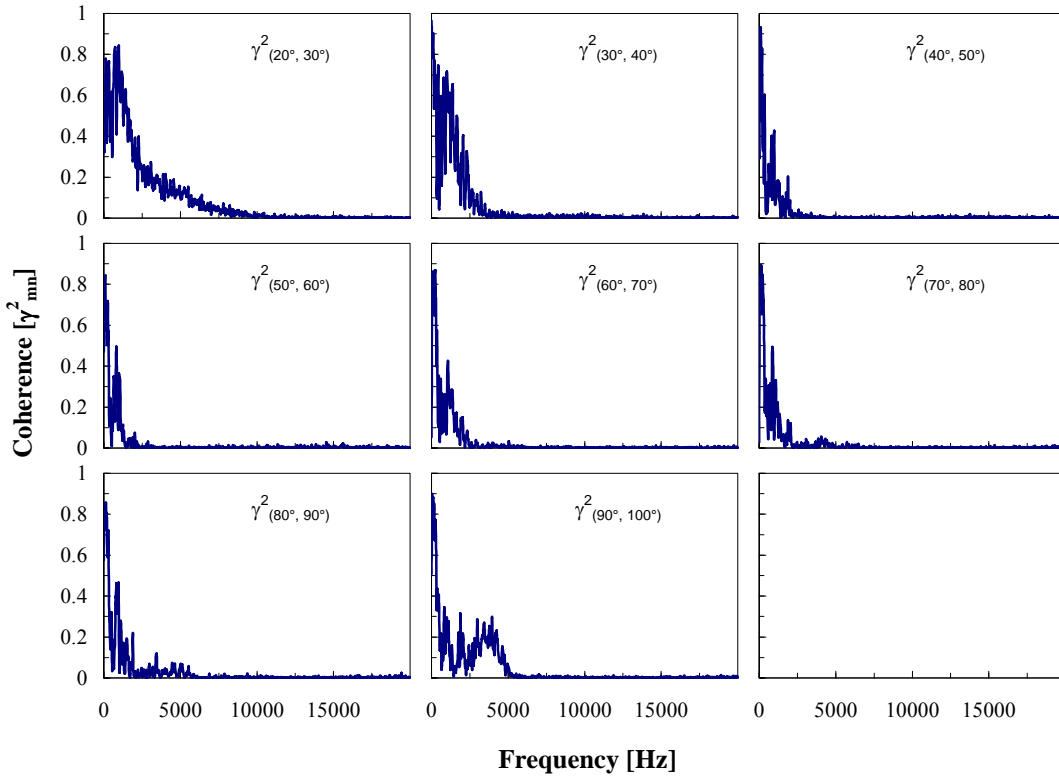


Figure 5.18 Coherence spectra for microphone pairs spaced at 10 degrees, Mach 1.67 CD nozzle with exit diameter of 2.0 inches, Mach 1.9 jet.

The data in Figure 5.18 was gathered with microphones spaced 10° apart monitoring a Mach 1.9 jet exhausting from a CD nozzle with a design Mach number of 1.67. Such operation falls within the under-expanded regime. Much like the perfectly expanded case, the coherence tends to be the largest in the downstream direction and smallest in the sideline direction. Additional overall coherence data gathered at Mach numbers of 1.4, 1.67, and 1.9 for larger microphone separation intervals of 20 and 30 degrees are shown in the figures below. The data in Figure 5.19 and Figure 5.20 are presented in the form of

calculated overall coherence. As shown in Figure 5.19 and Figure 5.20, the coherence is significantly reduced at larger microphone spacing intervals even when both microphones are positioned in the downstream direction, e.g., $\gamma^2_{(20^\circ, 40^\circ)}$ and $\gamma^2_{(20^\circ, 50^\circ)}$. The figures below indicate that microphone spacing of approximately 20 to 30 degrees is necessary in the downstream direction when the assumption of jet noise incoherence is required. In the downstream direction, the findings for all supersonic jets are consistent with the findings presented in the previous section for subsonic Mach numbers. Furthermore, the findings for the fully-expanded supersonic jet are consistent with those of subsonic jets in all directions. However, in the sideline direction, microphone separations larger than those required in the subsonic and fully-expanded supersonic cases may be necessary to ensure jet noise incoherence for shock-containing jets. Results similar to those shown below were obtained across the entire supersonic testing range (1.0 – 2.0).

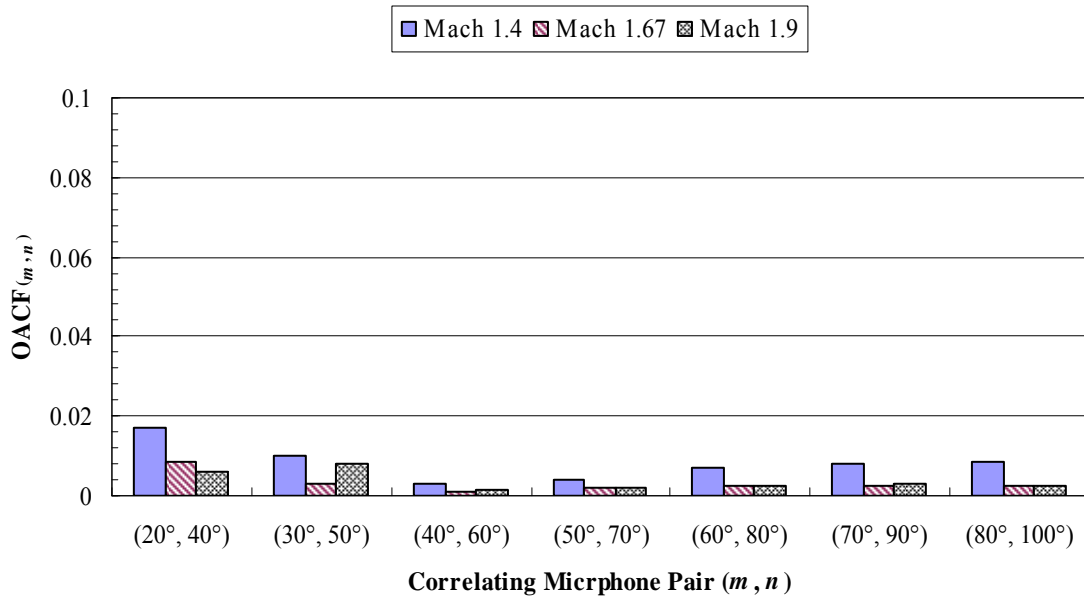


Figure 5.19 Bar chart showing the overall coherence $OACF_{(m, m+20^\circ)}$ for fully-expanded and non-fully-expanded cases, Mach 1.67 CD nozzle.

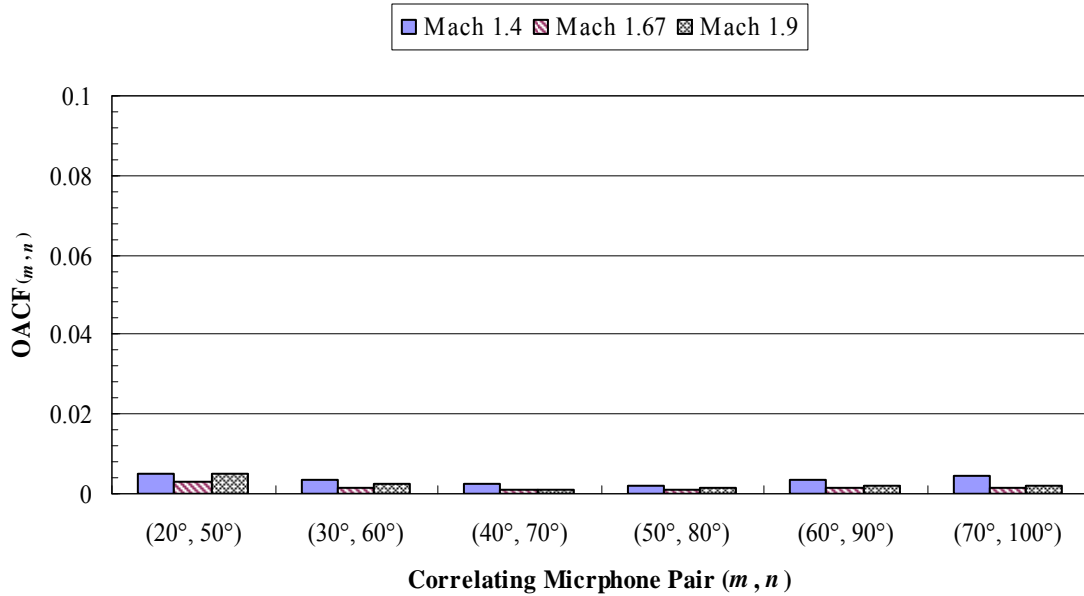


Figure 5.20 Bar chart showing the overall coherence $OACF_{(m, m+30^\circ)}$ for fully-expanded and non-fully-expanded cases, Mach 1.67 CD nozzle

In summary, the validity of the assumption of jet noise incoherence has been investigated for a wide range of microphone observation arrangements and conditions, at Mach numbers ranging from subsonic to supersonic, and for a variety of nozzle geometries. The measured coherence has been shown to be dependant upon the angular microphone separation. Due to the large linear microphone separations needed to obtain proper angular separation of adjacent microphones when using a linear array of microphones, a polar arc microphone arrangement has been found to be more advantageous when implementing coherence-based signal processing techniques that require jet noise incoherence amongst all microphones. Furthermore, it has been established that this polar microphone arc should be placed beyond 50 diameters from the nozzle exit to provide the most practical assurance of jet noise incoherence. When implementing multi-microphone signal enhancement techniques for model- and full-scale jet noise problems

the assumption of jet noise incoherence is necessary. Due to this and the findings concerning the spatial coherence characteristics of jet noise shown and discussed above, variable microphone spacing is required. Microphones should be spaced according to their location relative to downstream jet axis and the dominate jet noise radiation entity within that region. Typically, to ensure jet noise incoherence between correlating microphones in the downstream on-axis direction, larger microphone separations (i.e., 20° to 30° for most applications) are needed. In the sideline direction, smaller spacing (e.g., 10°) will suffice for subsonic and fully-expanded supersonic jets. However, for non-fully expanded supersonic jets, sideline microphone separations larger than ten degrees may be necessary. The findings for the subsonic Mach numbers are consistent over the entire range of nozzle geometries tested. The application of these findings for the model- and full-scale problems is discussed in Chapter 7.

CHAPTER 6

LIMITATIONS OF THE THREE-MICROPHONE METHOD

As discussed in Chapter 2, the three-microphone method makes use of coherence-function relations between simultaneous pressure measurements at three microphones positioned in the acoustic field and educes from the flow-noise background the auto-power spectrum of the signal in question as received at each microphone. The theory allows for an arbitrary arrangement of the microphones within the acoustic field when a single source is buried in extraneous flow noise. Regardless of the system, any extraneous flow noise that might be present must be mutually uncorrelated amongst all microphones.

The focus of this chapter is to investigate the limitations of the three-microphone method in instances where the underlying assumptions of the methodology are violated. This may happen in any variety of manners. Most notably, the assumptions are violated for systems where multiple self-coherent but mutually incoherent sources are present. For such a system, Minami and Ahuja⁷ have shown numerically that errors in the use of the three-microphone technique can be significant if noise from multiple self-correlated sources reach the far-field microphones. The predicted error that is introduced when the three-microphone technique is applied to a system that has two correlated sources buried under extraneous noise is shown in Figure 2.7. This error is a function of the relative amplitudes of the sound pressure level from the two correlated sources at a given

observation position. Since Minami and Ahuja did not to verify this experimentally, it has been done as a part of this work. The findings are reported and discussed below. Further limitations of the three-microphone method discovered via numerical simulation and confirmed via experimental testing during this work are discussed below.

6.1 Verification of the Minami/Ahuja Three-Microphone Method Error

With the use of numerical simulation, Minami and Ahuja⁷ showed that errors in the use of the three-microphone technique can be significant if noise from multiple self-correlated sources reach the far-field microphones. Their findings are shown in Figure 6.1. SPL_A and SPL_B are the measured sound pressure levels of the self-correlated but mutually uncorrelated sources A and B, respectively. The figure clearly shows that if one source is much stronger than the other, the error in using the three-microphone method to determine the contribution of that stronger source is less than ± 1 dB. If the sources are of comparable strength substantial errors may exist. In fact, if the source strengths are within five decibels of each other the error can be as large as ± 10 dB.

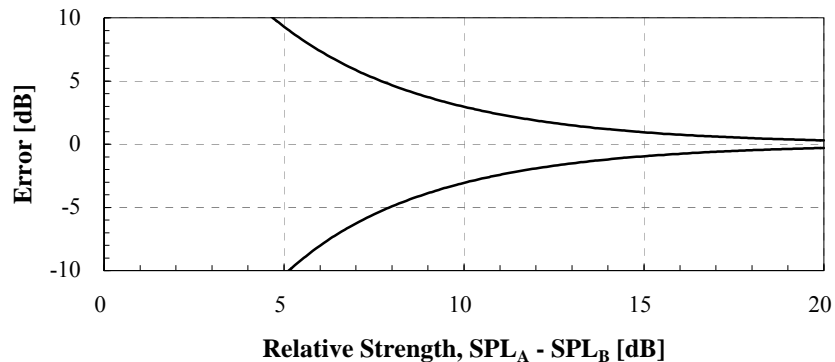


Figure 6.1 Range of error of auto-spectrum when the three-microphone technique is applied to a system that contains two correlated sources (from Minami and Ahuja⁷).

The experimental setup shown in Figure 6.2 was used to generate the results in Figure 6.3. The test configuration depicted in Figure 6.2 consisted of a single jet and two self-correlated but mutually uncorrelated electro-acoustic noise sources indicated as *A* and *B* in the photograph. The sources were supplied broadband signals from separate signal generators and the signals were feed through separate amplifiers to ensure that sources *A* and *B* would be correlated with themselves yet uncorrelated with each other (and the jet noise) in the far-field. The spacing of drivers *A* and *B* was 48 inches during this testing. The microphones were spaced from 20° to 100° (relative to the downstream jet axis) at 10-degree intervals along a polar arc positioned 10 feet from the nozzle exit plane. In Figure 6.3, the triangles represent the calculated three-microphone method correlated values. The red dashed line indicates the measured SPL with only source *A* operational, while the green dash-dot line shows SPL data measured with only source *B* operational. The solid black curve represents the measured far-field auto-spectra when all sources (*A* + *B* + jet noise) were active. Data gathered or calculated at 60-degree microphone is shown in plots of Figure 6.3. The relative level of sources *A* and *B* is varied (on average; note the frequency to frequency variation for each source) from roughly 20 dB in (a) to 0 dB in (d). In plots (b) and (c), the average relative levels are approximately 10 and five decibels, respectively.

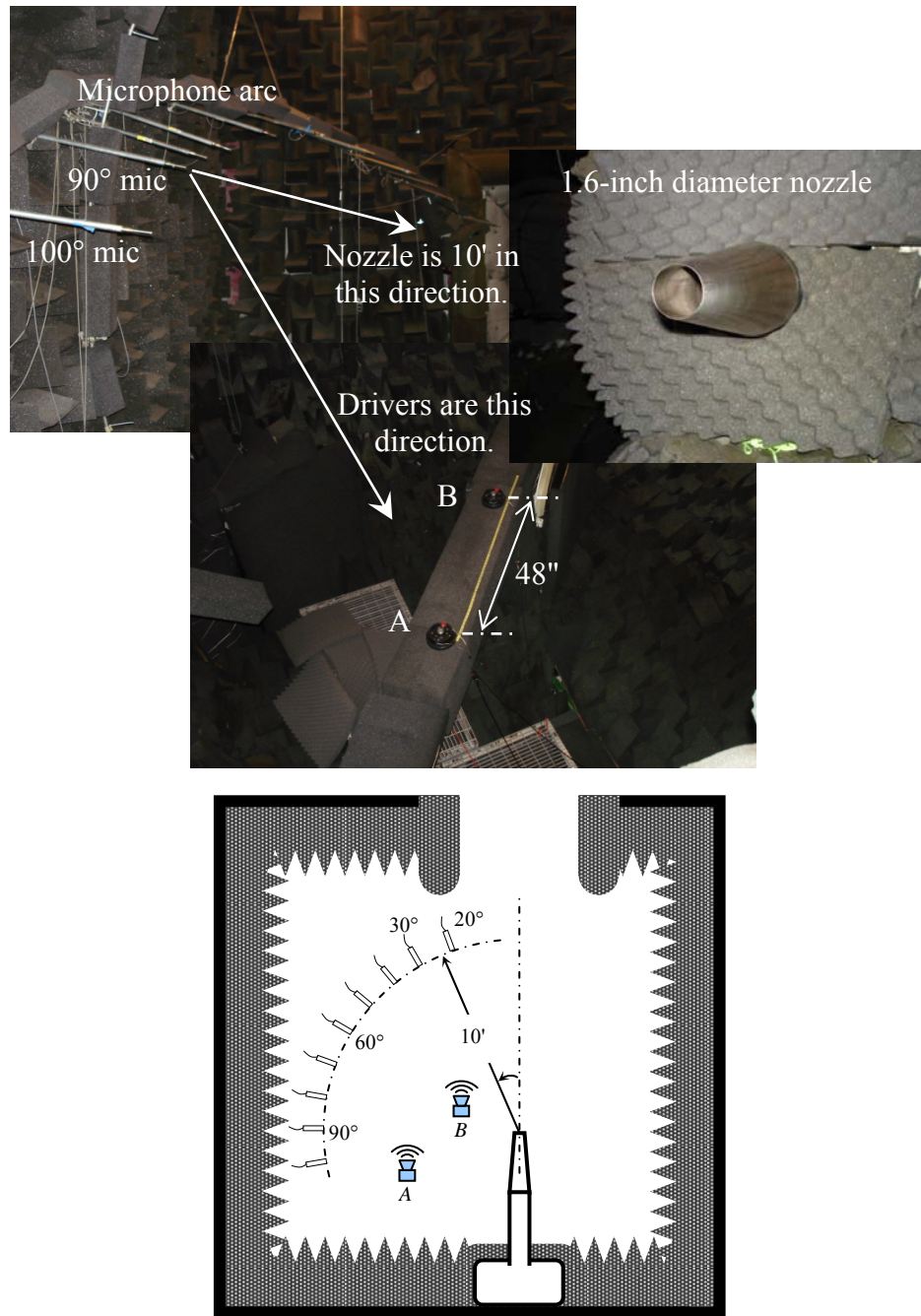


Figure 6.2 Photograph collage and top-view sketch of experimental setup used in the Minami/Ahuja three-microphone method error verification.

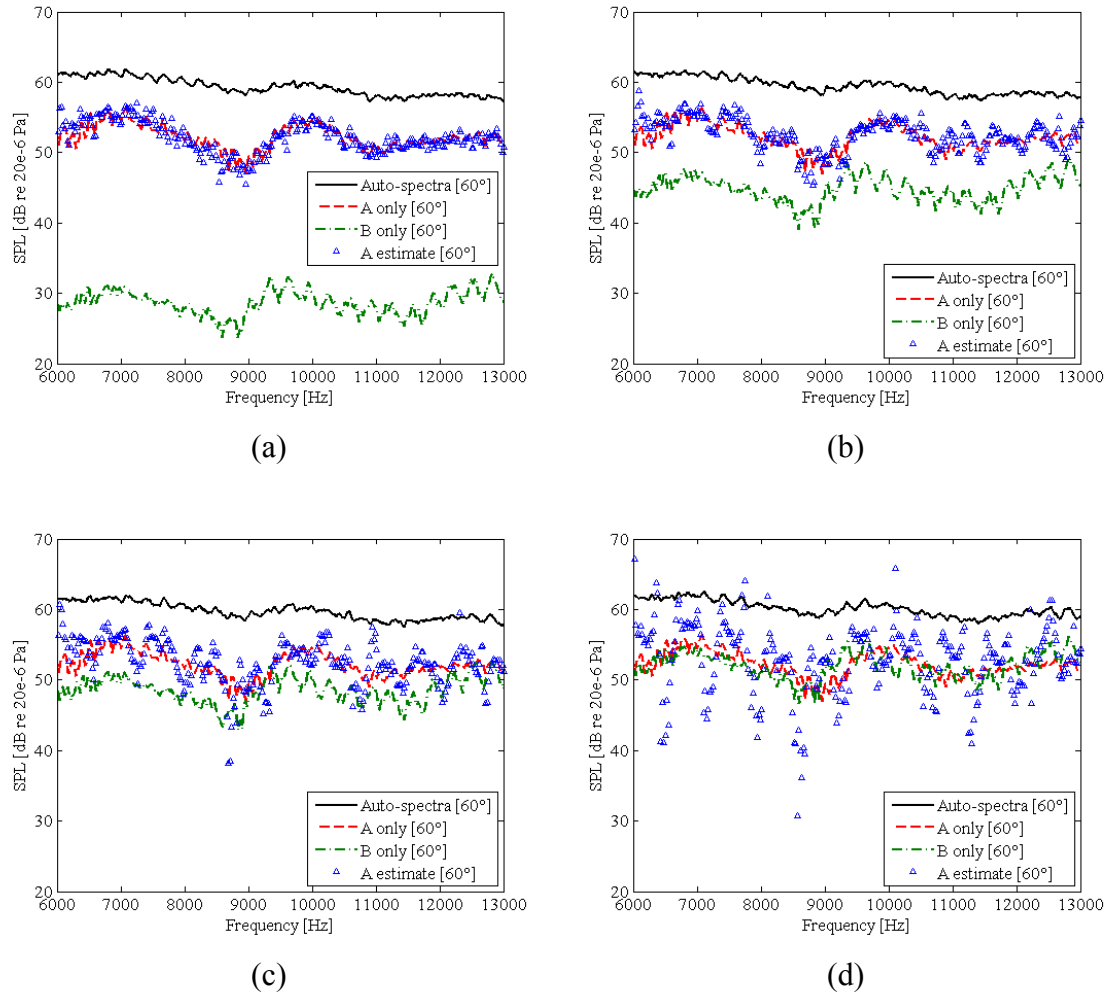


Figure 6.3 Three-microphone method results at the 60-degree microphone for drivers *A* and *B* with relative levels of (a) 20 dB, (b) 10 dB, (c) 5 dB and (d) 0 dB.

In varying the relative levels, the level of source *A* was held constant while the level of *B* was gradually increased from an average level that is nearly 20 dB less than *A* to a level roughly equivalent to that of *A*. There are very little variation in the data labeled *A estimate* and that labeled *A only* in plot (a); thus, it can be said the three-microphone method is implemented with minimal error when one correlated source is roughly 20 dB louder than the other. As the level of source *B* is increased to the value shown in (b), the calculated correlated results (i.e., those labeled *A estimate*) begin to show more frequency

to frequency variations and fall farther from the measured level of source *A* at most frequencies. These frequency to frequency variations are further increased in (c), and even more increased in (d); thus, the error tends to increase just as Minami and Ahuja predicted. It is clear that as the average relative level of the two correlated sources approaches zero the error in using the three-microphone method becomes quite significant. As shown in Figure 6.4, the experimental results (i.e., those taken from the data shown Figure 6.3 at individual frequencies) fall within the maximum and minimum error bands of Minami and Ahuja⁷ for most relative source levels. When driver *A* is over roughly 15 dB louder than *B*, the experimental results show more error than of the Minami and Ahuja simulation findings. This can be attributed to errors in the calculations involved in the three-microphone method due to measurement uncertainties as discussed in Chapter 9.

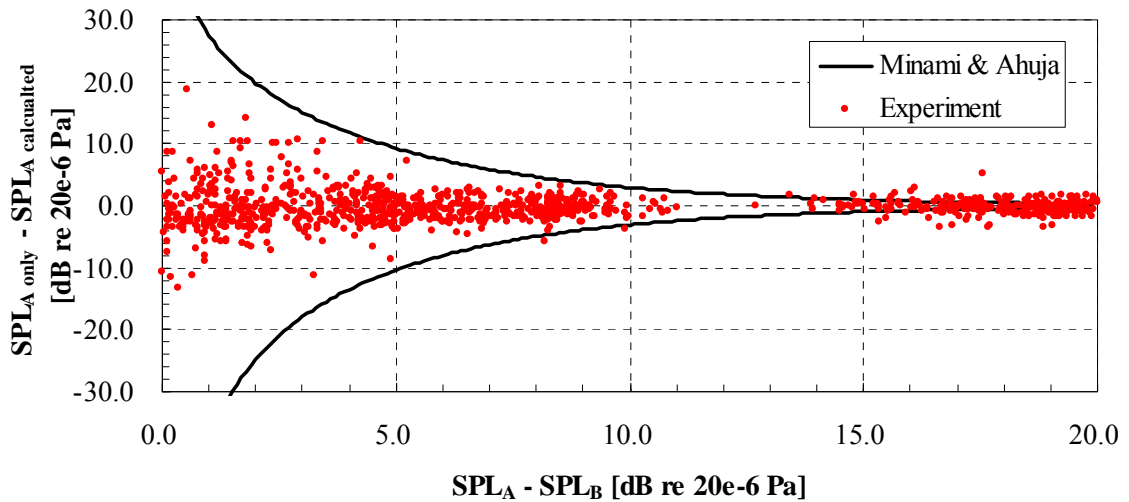


Figure 6.4 Comparison of the Minami and Ahuja⁷ prediction to experimental results.

6.2 Numerical Simulations

The numerical simulation configuration depicted in Figure 6.5 has been used to determine further limitations of the three-microphone method. This simulation is similar to that used by Minami and Ahuja⁷. The simulation allows for any of the five sources to be operated alone or in combination with any number of the remaining sources. In each simulation described below, the uncorrelated noise source is operational. The original simulation of Minami and Ahuja with two active correlated sources (*A* and *B*) operational has been repeated in order to validate the computational solution procedure employed in this work. The results have been duplicated and are shown in Figure 6.7 in the following section. The values labeled *Correlated* and *Uncorrelated* were calculated using the three-microphone method with microphones 1, 2, and 3, and the designation *Sim* indicates simulated values. This is true for all simulation plots below. Since the focus of this section is to investigate the results of the three-microphone method when its assumptions are not fully satisfied, the physical significance of the three-microphone method results are not explicitly indicated by the labels within this section. The numerical simulations within this section were used to determine exactly what information the three-microphone method returns under less than ideal conditions. Those results labeled *Correlated* were determined using equation (2.6), while those labeled *Uncorrelated* were determined using equation (2.9). Numerical simulations designed to study the influence of the presence of multiple correlated sources and the affect of microphone spacing d (as shown in Figure 6.5) have been conducted.

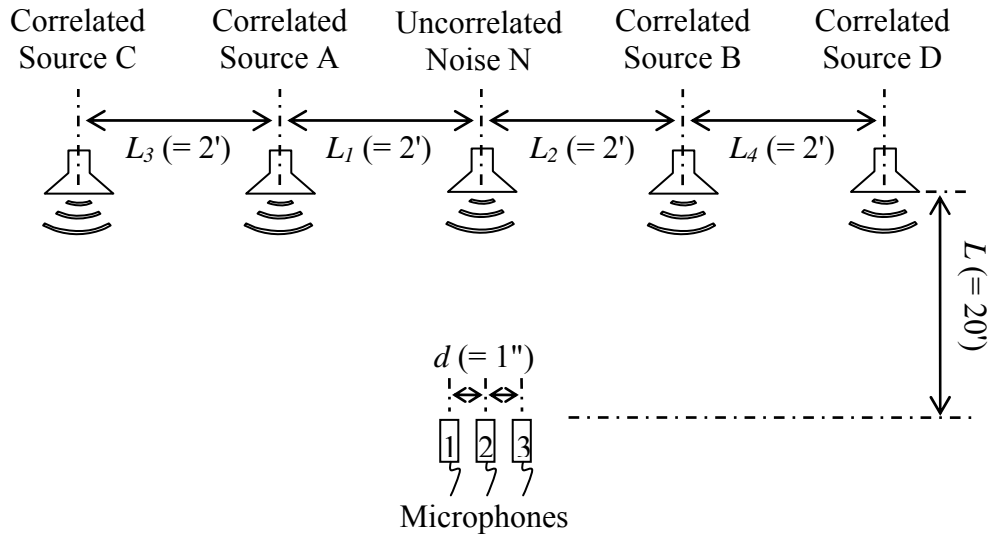


Figure 6.5 Schematic of the numerical simulation.

6.2.1 Effect of Multiple Correlated Sources

The usefulness of the three-microphone method for systems with multiple correlated sources is of keen interest. In many real-world signal processing applications, multiple indistinguishable correlated sources are present; thus leading to the investigation of the validity of the three-microphone method in such instances. The term “correlated” in this case implies that the noise from that source if operated alone will provide a coherence of unity at any two microphones in the acoustic field of that source, and the term “multiple indistinguishable” implies that there may be more than one such source which may have similar spectrum shape but these sources are totally uncorrelated with one another. The experiment depicted in Figure 6.5 is simulated with one (*A*), two (*A* and *B*), three (*A*, *B*, and *C*), and four (*A*, *B*, *C*, and *D*) correlated sources buried in uncorrelated noise (*N*). The results from those simulations are shown in figures below.

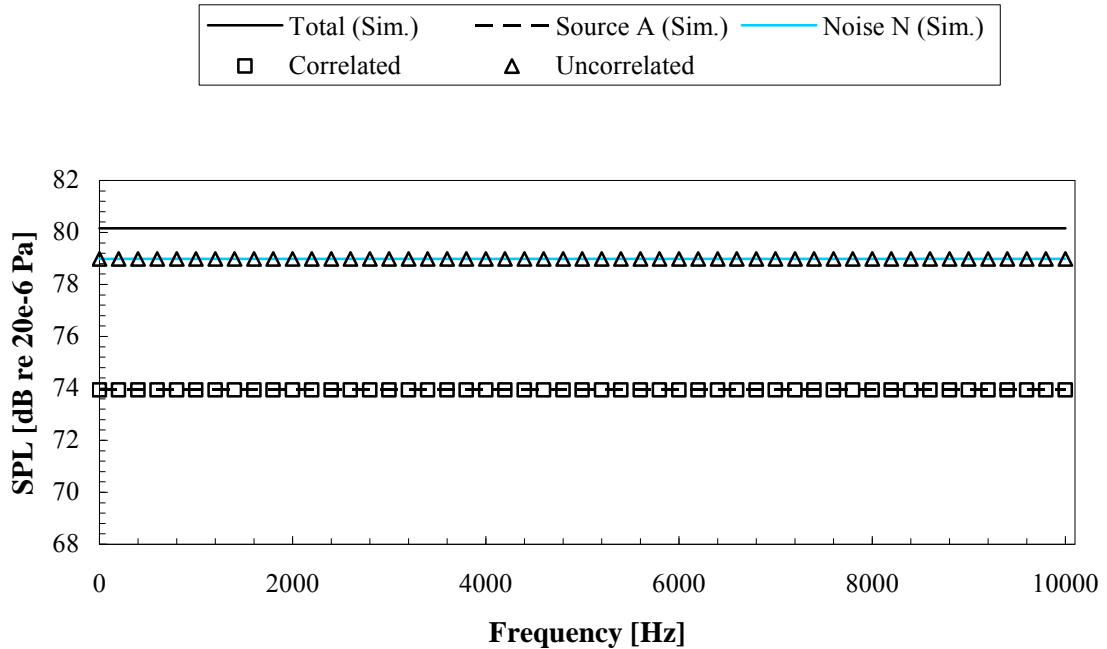


Figure 6.6 Auto-spectra of microphone 2 with one active correlated source buried in uncorrelated noise ($d = 1''$, $\Delta f = 200$ Hz).

With only one correlated source buried in uncorrelated noise, the signals are separated precisely with the three-microphone method (Figure 6.6). The solid black line represents total simulated sound pressure level ($A + N$); while the black dashed line indicates the simulated level of A . The simulated uncorrelated noise N is illustrated by the solid blue line. The calculated three-microphone method results are shown as symbols. The squares represent correlated results, and the triangles indicate uncorrelated results. This simulation strictly follows the assumptions of the three-microphone methodology; thus, the high precision of the solution is to be expected. However, the question remains as to how the three-microphone solution is affected when those assumptions are violated.

The assumptions of the three-microphone methodology are violated as more buried correlated sources are added. This of course leads to solution inaccuracies which are

easily seen in the figures below. The short-comings of the three-microphone methodology are thus illustrated, and the need for a multi-microphone method for separating more than one correlated source buried in uncorrelated noise is evident.

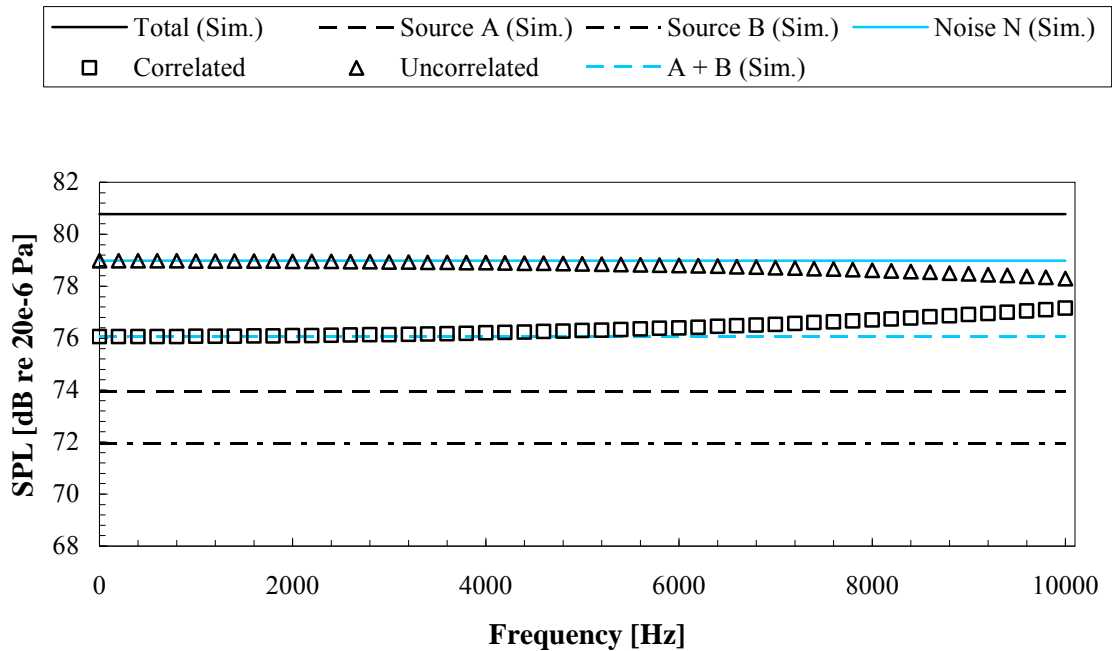


Figure 6.7 Auto-spectra of microphone 2 with two active correlated sources buried in uncorrelated noise ($d = 1''$, $\Delta f = 200$ Hz).

In Figure 6.7, the simulated and calculated auto-spectra for microphone 2 of Figure 6.5 are shown. The simulated values are illustrated with continuous curves. The solid black line represents the total simulated sound pressure level ($A + B + N$), while the dashed and dash-dot lines indicate simulated levels for sources A and B , respectively. The simulated uncorrelated noise N is illustrated by the solid line, and the dashed blue line represents the sum of the simulated correlated signals ($A + B$). The calculated three-microphone method results are shown as symbols. The squares represent correlated results, and the triangles indicate uncorrelated results. With one-inch microphone spacing and sources A ,

B , and N active, the three-microphone method is not able to separate either of the buried correlated signals (A or B) individually; however, their sum is adequately deduced at frequencies below roughly 6.0 kHz.

Due to the underlying assumption of the three-microphone methodology that states that the system must consist of only a single correlated source and uncorrelated extraneous noise, one would expect the addition of another correlated source to further skew the three-microphone method results. As shown below in Figure 6.8, this is indeed the case. The simulated and calculated auto-spectra for microphone 2 of Figure 6.5 are shown below. The total simulated SPL ($A + B + C + N$) is illustrated by the solid black line. The simulated levels of self-coherent sources A , B , and C are represented by the black dashed, dash-dot, and dash-dot-dot lines respectively. The sum of the correlated signals is represented by the blue dashed line, and the incoherent noise N is shown as a solid blue line. The squares and triangles represent correlated and uncorrelated results calculated using the three-microphone method. The three-microphone method is not able to deduce any of the buried correlated signals (A , B , or C) individually; however, their sum is adequately deduced for frequencies below approximately 4.4 kHz. Compared to the results for two buried correlated sources, this upper frequency limit is slightly reduced by the addition of a third correlated source. The spectral region in which the three-microphone method results accurately predict the combined level of the correlated sources is reduced by the addition of a third correlated source. Hence, the addition of a third correlated source does indeed lead to greater error in the results of the three-microphone method.

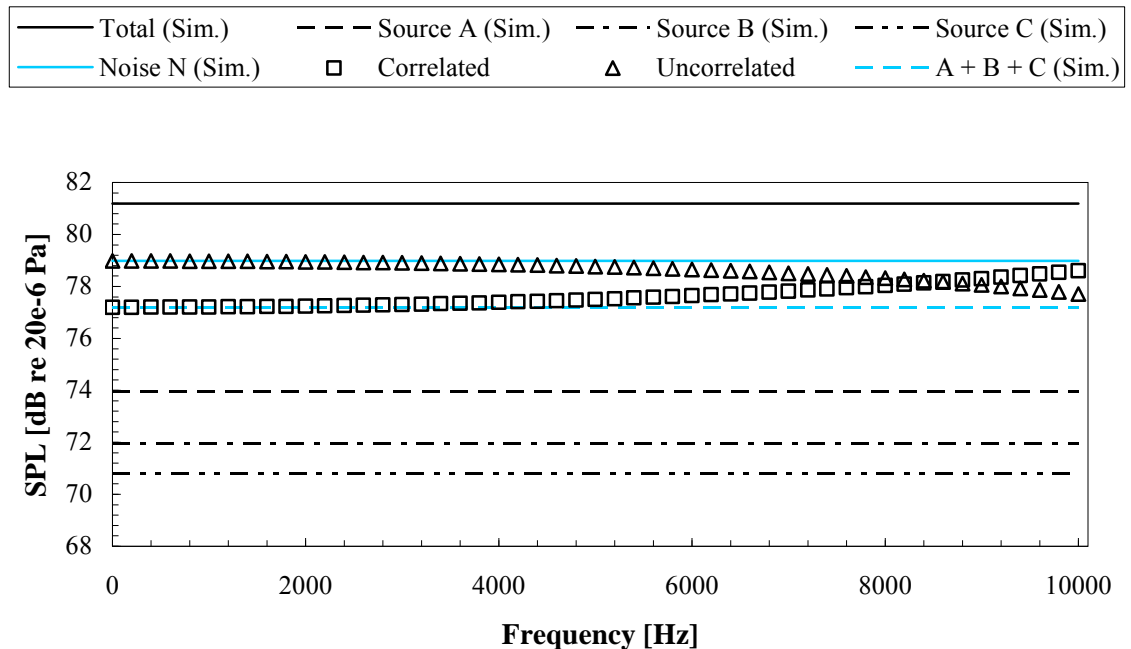


Figure 6.8 Auto-spectra of microphone 2 with three active correlated sources buried in uncorrelated noise ($d = 1''$, $\Delta f = 200$ Hz).

The effect on the three-microphone method results due to the addition of a fourth correlated source is shown in Figure 6.9. The simulated levels for the total SPL and signals A , B , C , and N are represented by lines identical to those indicated in the previous figures. The black dotted line illustrates the simulated level of the fourth correlated source D . Again, the sum of the correlated signals is represented by the blue dashed line, and the calculated correlated and uncorrelated results are indicated by squares and triangles respectively. The individual correlated sources are not separable by the three-microphone method. The sum of the correlated signals is effectively reduced below 3.6 kHz. The addition of a fourth correlated source reduces the spectral region in which the three-microphone method results accurately predict the combined level of the correlated sources. Thus, the addition of a fourth correlated source further reduces the accuracy of the results.

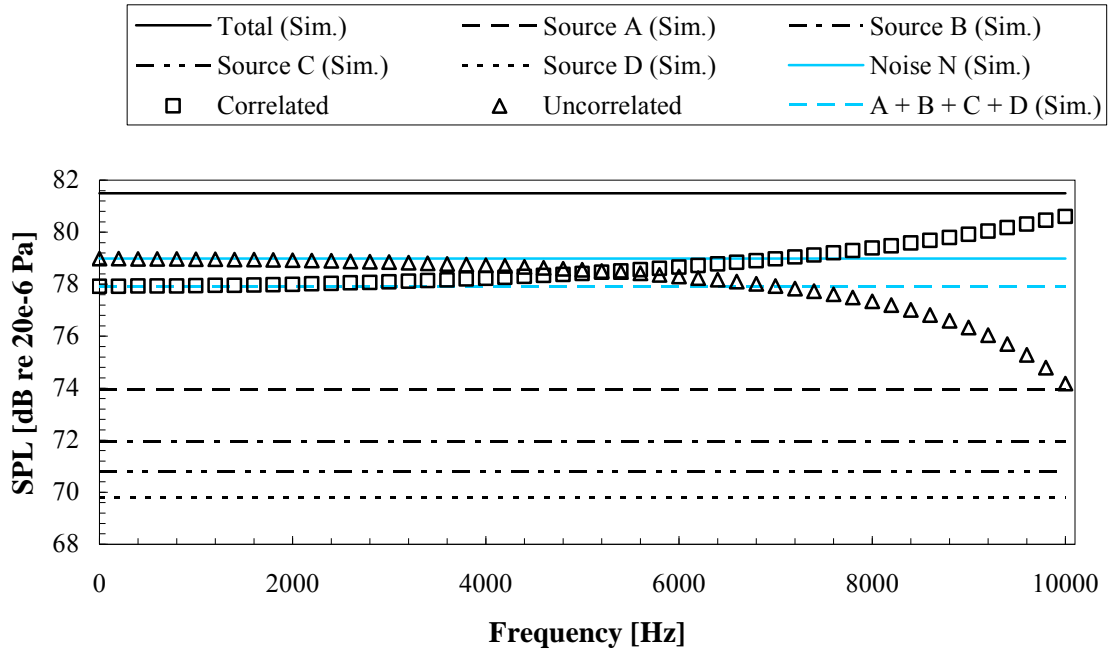


Figure 6.9 Auto-spectra of microphone 2 with four active correlated sources buried in uncorrelated noise ($d = 1''$, $\Delta f = 200$ Hz).

Due to the limiting assumptions and physical nature of sound, the three-microphone methodology is not capable of individually educing more than one correlated source buried in uncorrelated noise; however, the method accurately predicts the combined level of the correlated sources in some cases. As illustrated in the figures above the collective level of the correlated sources is predicted by the three-microphone methodology for lower frequencies. The highest frequency that shows acceptable accuracy for the prediction of the combined level of the correlated sources tends to decrease as the number of active correlated sources is increased. By way of the underlying assumptions of the three-microphone methodology, these findings indicate that the correlated sources are received by the microphones as a single combined correlated source at lower frequencies. In other words, they suggest that the correlated sources are “heard” by the microphones as a single combined source at lower frequencies. Since these errors are frequency

dependent, it seems that the ratio of the characteristic wavelength to the microphone spacing must also play a role in controlling the lowest frequency at which the three microphone method can provide an estimate of the combined sum of the correlated sources seen above. The effect of microphone separation in such simulations is the topic of the following section.

6.2.2 Effect of Microphone Spacing

The microphone spacing was set at one inch in the numerical simulations used to generate the results shown in the previous section. Additional simulations (with two correlated sources, A and B , buried in uncorrelated noise N) were run with microphone spacing intervals of two, four, eight, and 16 inches. Results from those simulations are shown below. In Figure 6.10 through Figure 6.13, the simulated values are illustrated with continuous curves. The solid black line represents the total simulated sound pressure level ($A + B + N$), while the black dashed and dash-dot lines indicate simulated levels for sources A and B respectively. The simulated uncorrelated noise N is illustrated by the solid blue line, and the dashed blue line represents the sum of the simulated correlated signals ($A + B$). The calculated three-microphone method results are shown as symbols. The squares represent correlated results, and the triangles indicate uncorrelated results.

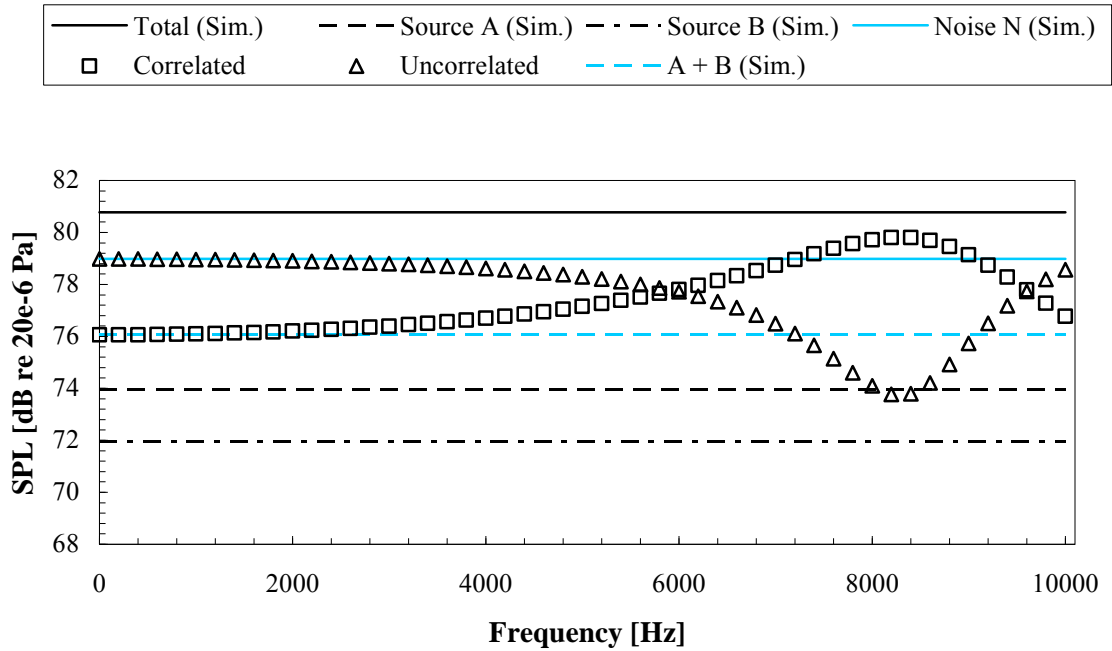


Figure 6.10 Auto-spectra of microphone 2 with two active correlated sources buried in uncorrelated noise with two-inch microphone spacing ($d = 2''$, $\Delta f = 200$ Hz).

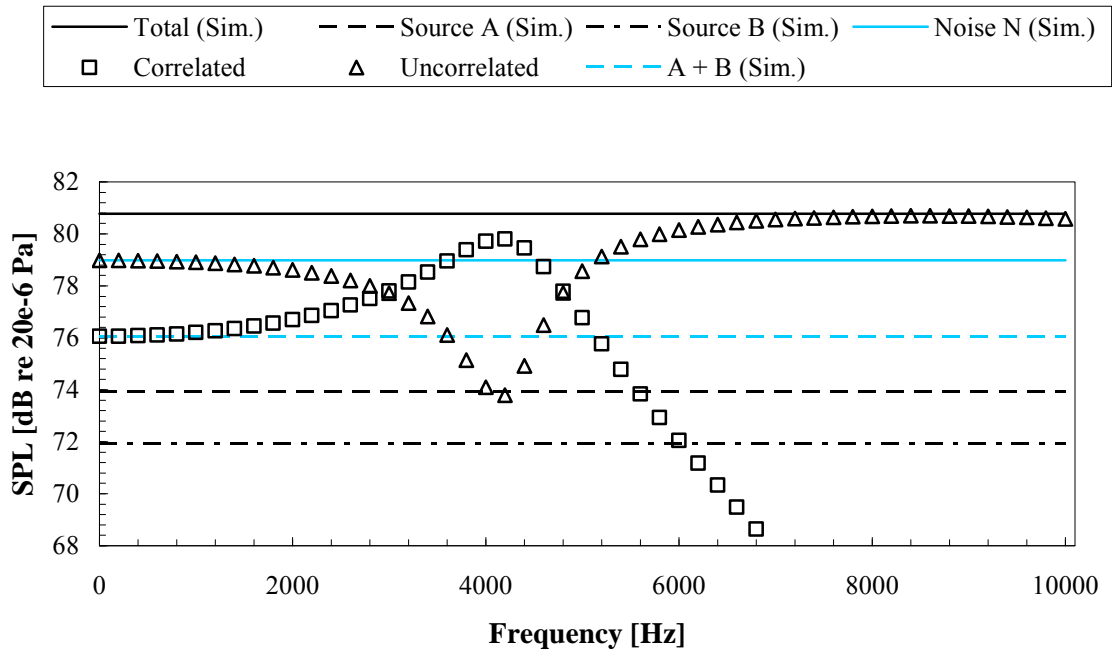


Figure 6.11 Auto-spectra of microphone 2 with two active correlated sources buried in uncorrelated noise with four-inch microphone spacing ($d = 4''$, $\Delta f = 200$ Hz).

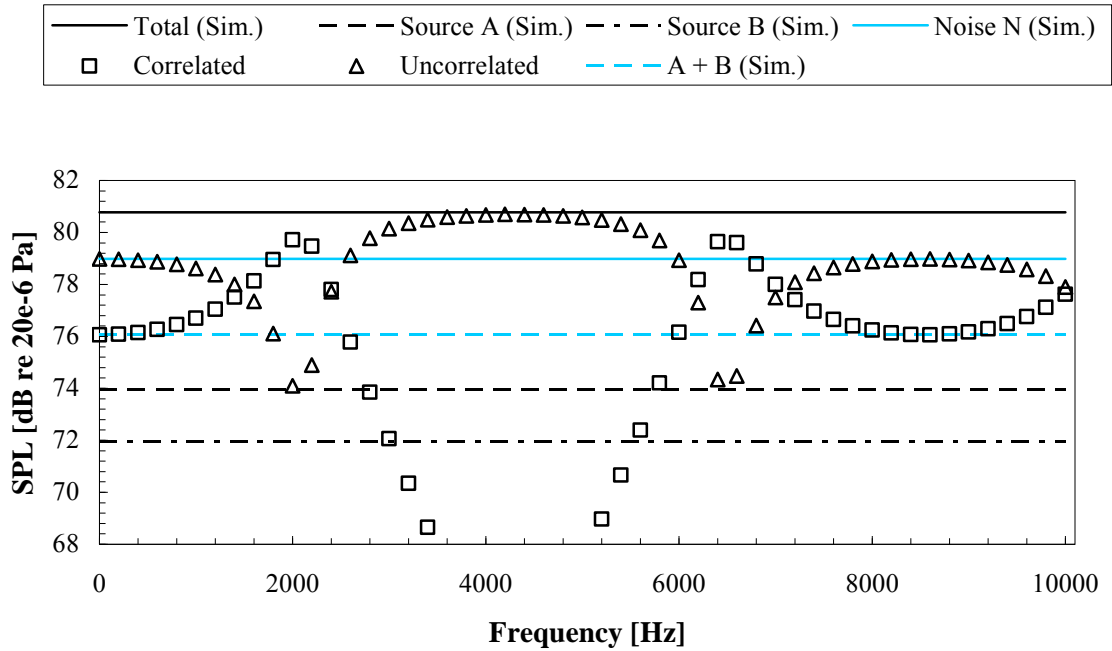


Figure 6.12 Auto-spectra of microphone 2 with two active correlated sources buried in uncorrelated noise with eight-inch microphone spacing ($d = 8''$, $\Delta f = 200$ Hz).

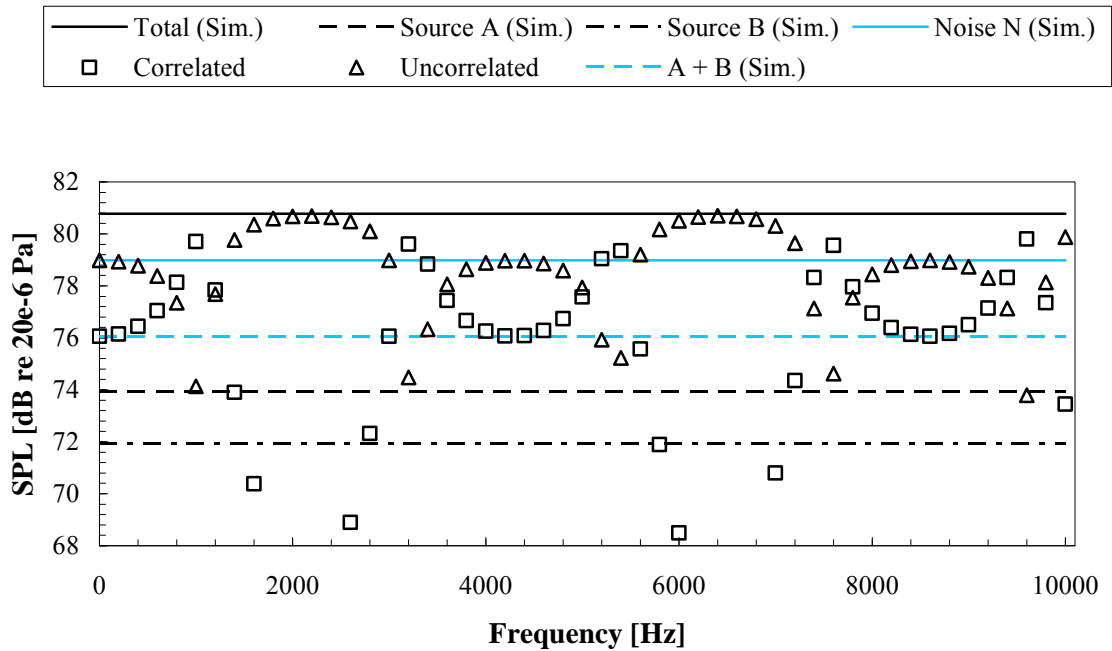


Figure 6.13 Auto-spectra of microphone 2 with two active correlated sources buried in uncorrelated noise with 16-inch microphone spacing ($d = 16''$, $\Delta f = 200$ Hz).

Recall from Figure 6.7, with one-inch microphone spacing and sources A , B , and N active, the three-microphone method is not able to separate either of the buried correlated signals (A or B) individually; however, their sum is adequately deduced at lower frequencies. The same holds true in the series of figures shown above. Moreover, they show that the highest frequency of acceptable accuracy for the prediction of the combined level of the correlated sources further decreases when the microphone spacing within the array is increased (by a factor of two in these simulations). Therefore, the usefulness of the three-microphone method solution for the simulation degrades as the spacing between the microphones is increased. In addition to these solution inaccuracies, the complexity of the behavior of the three-microphone method results increases with increased microphone spacing. In all instances where the microphone separation between adjacent microphones is larger than one inch, the three-microphone method results display cross-over. This cross-over tends to become more predominate as the microphone separation is increased once again indicating the growth of error with increased microphone separation. Like the findings presented in Section 6.2.1, these findings indicate that the correlated sources are received by the microphones as a single combined source at lower frequencies.

Upon further examination of the data shown above, a significant pattern concerning the upper frequency limit of acceptable accuracy has been established. The upper frequency limit might better be described as the lowest frequency where the calculated correlated results differ from the sum of the simulated correlated levels by some prescribed decibel amount. By choosing this difference arbitrarily to be 0.5 dB, upper limits of 7.2, 3.6, 1.8, 0.9, and 0.45 kHz have been established for microphone separation intervals of one, two,

four, eight, and 16 inches within the two-correlated, one-uncorrelated source system. Assuming omni-directional propagation of sound waves within this system, the maximum propagation time between all microphones (i.e., the maximum time it takes a wave originating from any of the active sources to reach all microphones minus the minimum time it took said wave to reach the first microphone) is determined. The corresponding maximum propagation distance is then equal to the maximum propagation time multiplied by the local speed of sound. For clarification consider the wave front propagation shown in Figure 6.14.

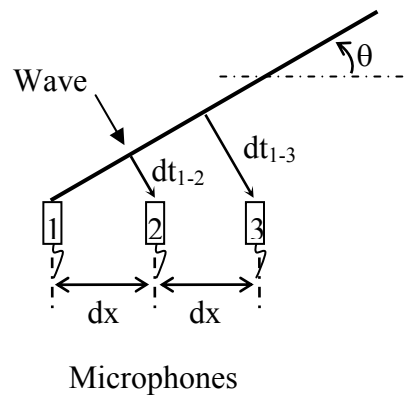


Figure 6.14 Wave front propagation.

Denoting the local speed of sound by c , the wave front propagation time between microphones 1 and 2, dt_{1-2} , is calculated as

$$dt_{1-2} = \frac{dx \sin \theta}{c} \quad (6.1)$$

while the propagation time between microphone 1 and 3 is

$$dt_{2-3} = \frac{2dx \sin \theta}{c} = 2dt_{1-2} \quad (6.2)$$

Thus the maximum propagation time amongst all microphones is dt_{2-3} . This translates into a maximum propagation distance of

$$dx_{\max} = cdt_{2-3} = 2cdt_{1-2} \quad (6.3)$$

For all microphone spacing intervals used in the numerical simulations shown above, it can be shown that the ratio of the wavelength of the sound wave at the upper frequency limit to the maximum propagation distance amongst all microphones is roughly 9.5. That is, for frequencies where $\lambda/dx_{\max} \geq 9.5$ the three-microphone method predicts the combined level of the two buried correlated source within 0.5 dB. At lower frequencies (or large wavelengths) where this condition holds, there is very little spatial variation in the wave from microphone to microphone. Hence, essentially the same region of the radiated sound wave reaches each microphone almost simultaneously. Furthermore, when multiple self coherent waves are present (as is the case here) the waves are “heard” as a single coherent entity, and no assumption of the three-microphone method is violated. This is the reasoning behind the seemingly accurate results shown above for the sum of the correlated signals at low frequency.

6.3 Verification via Proof-of-Concept Testing

To provide confirmation of the numerical simulation results presented in the previous section, experiments designed to mimic the simulations as closely as physically possible

were conducted. Due to the lack of an off-the-shelf uncorrelated noise producing driver, jet noise generated by a 1.6-inch diameter conical round nozzle operated at Mach 0.62 was used as the uncorrelated noise (denoted as N) in experimental verification of the numerical simulation findings discussed in Section 6.2. Two independently driven electro-acoustic drivers were utilized as correlated noise sources A and B . Ideally, the dimensions of the numerical simulations described above would have been duplicated; however, the spatial nature of jet noise as discussed earlier does not allow for this duplication. The actual experimental setup only varies slightly from that shown in Figure 6.2. For this testing the separation between sources A and B was set at seven inches rather than 48 inches (as indicated above).

Results from proof-of-concept testing in the GTRI/CCRF static anechoic facility are presented below. The triangles and squares show data calculated at the 60-degree microphone using the three-microphone method with microphones positioned at 20, 60, and 90 degrees with respect to the downstream jet axis. The triangles represent the calculated correlated values, and the squares illustrate the calculated uncorrelated results. The red dashed line indicates the measured SPL with only source A operational, while the green dash-dot line shows SPL data measured with only source B operational. Where needed, the cyan dotted line illustrates SPL data taken with both correlated sources operational ($A + B$). The solid black curve represents the measured far-field auto-spectra when the jet and either one (Figure 6.15) or both (Figure 6.16) of the correlated sources are active.

The three-microphone method has been successfully implemented when only one correlated source is buried in uncorrelated jet noise. In plots (a) and (b) of Figure 6.15, the correlated signal is accurately deduced for most frequencies. Furthermore, the uncorrelated jet noise is sufficiently predicted by the uncorrelated findings from the three-microphone method. These results provide solid experimental verification of the numerical simulation results shown above in Figure 6.6.

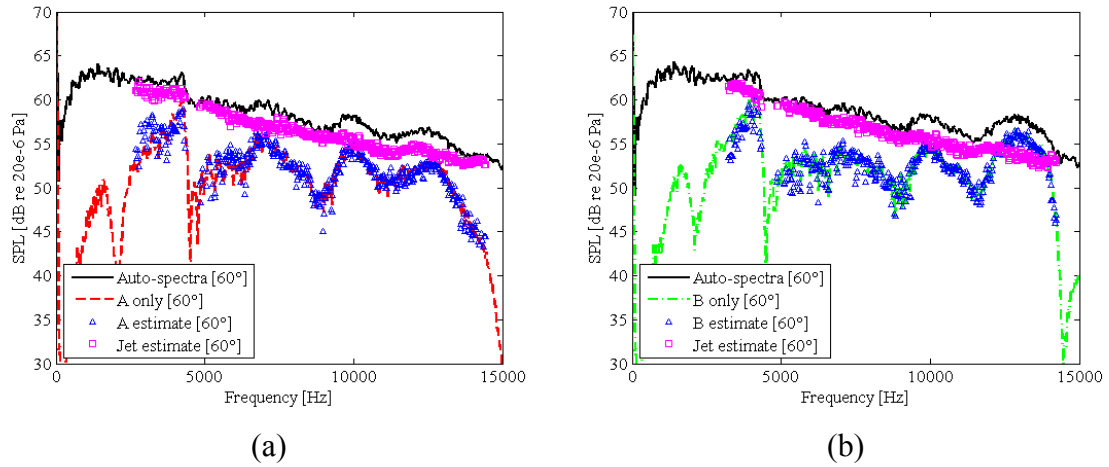


Figure 6.15 Three microphone method results at the 60-degree microphone for (a) source *A* and (b) source *B* buried in uncorrelated jet noise.

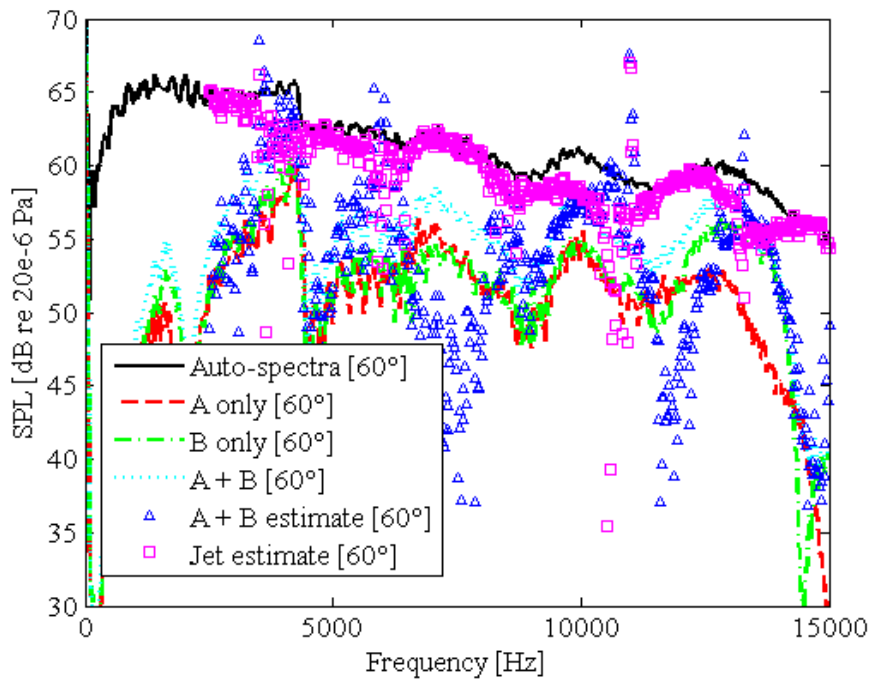


Figure 6.16 Three microphone method results at the 60-degree microphone with two correlated sources buried in uncorrelated jet noise.

Figure 6.16 illustrates three-microphone method findings when two correlated sources are buried in uncorrelated jet noise. Just as in the numerical simulations the three-microphone method is not able to reduce the noise of the correlated sources over the entire frequency span where all sources are operating at comparable levels. Over some small intermediate frequency regions (e.g., 9 to 10 kHz) the method accurately predicts the combined level of the correlated sources, but the inconsistency of these results leads to the conclusion that the three-microphone method is not reliable when attempting to reduce two buried correlated signals of similar spectral shape. The three-microphone method results shown in Figure 6.16 were calculated using the 30, 60, and 90-degree microphones as shown in Figure 3.11. Since data was actually gathered at all observation

positions indicated in Figure 3.11, this allows for a study much like that of the Section 6.2.2 where the effect of microphone spacing was investigated.

The experiments represented below are quite similar to the numerical simulations used to generate the results in Figure 6.10 through Figure 6.13. The primary difference lies in the range of microphone spacing intervals that are physically possible. As shown in Chapter 5, widely spaced microphones are needed to ensure jet noise incoherence amongst all microphones. The spacing intervals used in the numerical simulations are much too small for such assurance; hence, such small intervals could not be repeated experimentally. In this study, angular separation intervals of 10, 20, 30, and 40 degrees were used. The results from this experimentation are shown in Figure 6.17.

In Figure 6.17, the calculated three-microphone method results are indicated by symbols. The triangles represent the calculated correlated values, and the squares illustrate the calculated uncorrelated results. The red dashed line indicates the measured SPL with only source *A* operational, while the green dash-dot line shows SPL data measured with only source *B* operational. The cyan dotted line illustrates SPL data taken with both correlated sources operational ($A + B$). The solid black curve represents the measured far-field auto-spectra when all sources ($A + B + \text{jet noise}$) were active. Data gathered or calculated at 60-degree microphone is shown in all plots. To investigate the effect of microphone separation, the three-microphone method was implemented with microphone sets consisting of (a) the 50-, 60-, and 70-degree microphones; (b) the 40-, 60-, and 80-degree microphones; (c) the 30-, 60-, and 60-degree microphones; and (d) the 20-, 60-, and 100- degree microphones. The behavior of the calculated results within the

frequency range where both drivers are operational is much like that shown for such simulations in the previous section (Figure 6.10 through Figure 6.13). In both cases, the calculated results appear to asymptotically approach large errors at certain frequencies. These similarities provide sufficient validation of the conclusions drawn earlier based on the numerical simulation results.

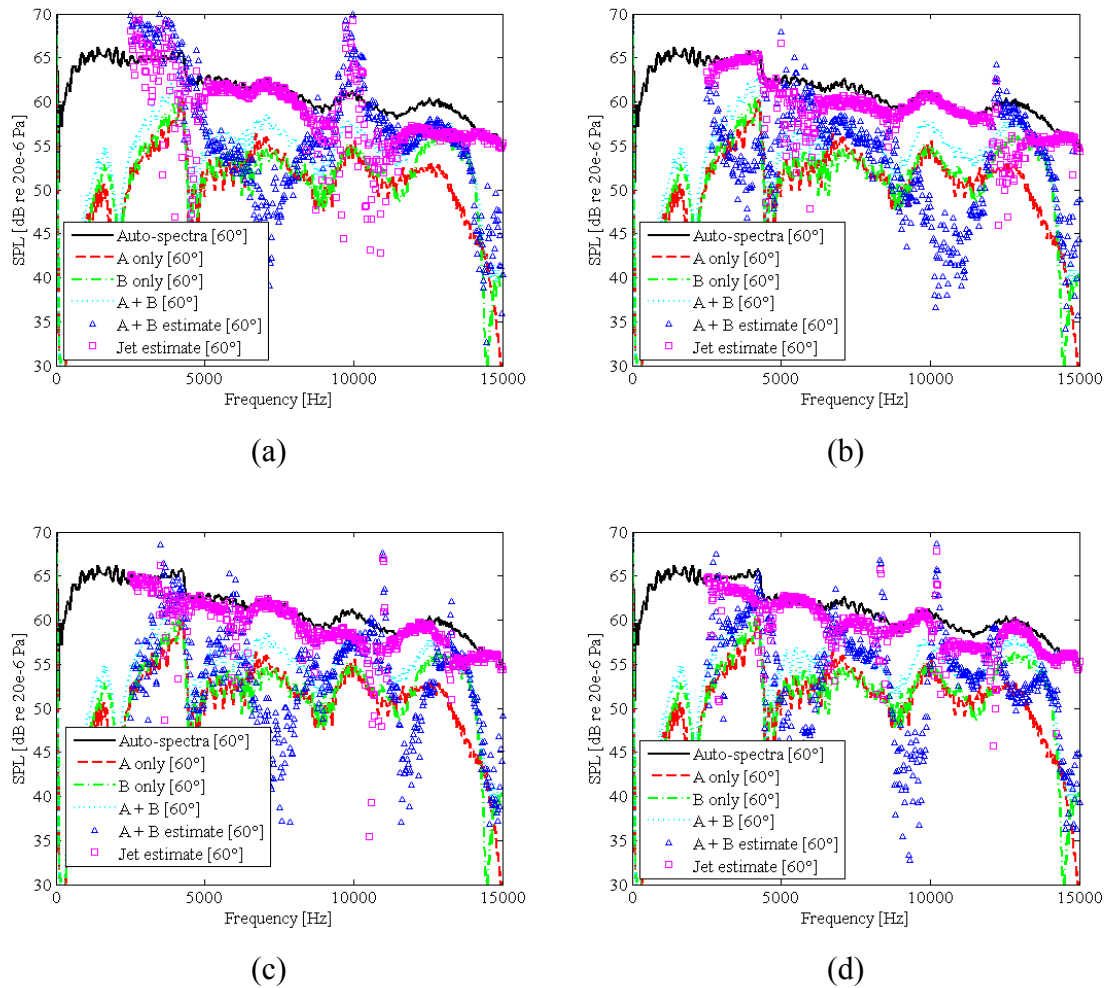


Figure 6.17 Three-microphone method results at the 60-degree microphone for sources *A* and *B* buried in uncorrelated jet noise with microphone spacing of (a) 10°, (b) 20°, (c) 30° and (d) 40°.

The shortcomings of the three-microphone method when educing multiple correlated sources buried in extraneous uncorrelated noise have been examined and discussed in previous sections. The three-microphone method has been numerically shown to be capable of educing the sum of multiple correlated signals at far-field microphones only at low frequencies. It is shown that at higher frequencies, significant errors in educing the sum of the correlated signals using the three-microphone method have been displayed. These errors are magnified as more and more correlated sources are introduced within the system and as the microphone spacing is increased. Both instances lead to increased variation in the signals received by each microphone; thus, reducing the spectral similarity of the received signals. Furthermore, this reduced spectral similarity results in signals that are less than fully coherent with each other at each microphone, and thus the underlying assumptions of the three-microphone method are violated. Thus, the underlying assumptions of the three-microphone method have been shown to limit its use to systems where a single correlated source or group of seemingly coherent sources is buried in uncorrelated noise. The so-called five microphone methodology developed by Minami and Ahuja⁷ may allow future researchers to overcome the limitations of three-microphone method when educing two correlated sources with coinciding frequency content buried in uncorrelated noise. This method has been studied and the findings of this investigation are discussed in the Chapter 8.

CHAPTER 7

APPLICATION OF FINDINGS

In the previous chapters, findings concerning implementation of coherence-based multiple microphone signal enhancement techniques to aeroacoustic systems where some correlated source(s) of interest are buried in uncorrelated jet noise have been discussed. It has been established—for both subsonic and supersonic jets—that the sources that radiate noise to the far-field in the downstream and sideline directions are different. Due to the spatial characteristics of these noise generation mechanisms and their directivities, variable microphone spacing is necessary when applying multiple-microphone noise diagnostic techniques to systems where jet noise is prevalent. Adjacent microphones positioned in the downstream on-axis direction should be spaced roughly 20 to 30 degrees apart to ensure jet noise incoherence, while in the sideline off-axis direction a separation of only 10 degrees will suffice. Furthermore, it has been shown that a polar arc arrangement of microphones positioned beyond 50 nozzle diameters measured radially from the nozzle exit is most advantageous when using coherence-based multi-microphone techniques. The underlying assumptions of the three-microphone method have been shown to limit its use to systems where a single correlated source or a group of seemingly coherent sources is buried in uncorrelated noise. Specifically, when attempting to separate two correlated sources buried in jet noise, the three-microphone method is not capable of educating the individual contribution of either source in frequency regions where the levels of each source are comparable. The combined sum of the two

correlated sources is predicted by the three-microphone method only at low frequencies. The primary focus of this chapter is the application of these findings to model-scale jet noise and full-scale engine noise diagnostics.

7.1 Model-Scale Application

The findings of the previous chapters have been applied to the model-scale jet noise problem. In doing so, two experimental setups were utilized. These configurations are briefly discussed in the Chapter 3 and termed the external- and internal-source configurations. Both setups consisted of an unheated jet exhausting from a 1.6-inch diameter conical round nozzle (which produces mutually uncorrelated jet noise at widely spaced microphones) and a pair of independently driven self-correlated acoustic drivers. In the internal-source configuration, the drivers are mounted within the jet-supply duct upstream of the nozzle exit; while in the external configuration they are positioned in the open. All noise radiation elements were controlled independently. This allowed for simultaneously operation of all sources, as well as independent operation of each and collective operation of the drivers alone. Basic schematic diagrams of each configuration are shown in Chapter 3; however, for clarity, more detailed schematics are shown below in Figure 7.1. In both setups, extra microphones are placed near enough to either of the drivers such that the signal at each microphone is dominated by the nearest driver. This was done in preparation for using the coherent output power and partial coherence methods discussed in Chapter 2. The far-field microphones were placed with the use of the three-microphone and partial coherence methods in mind.

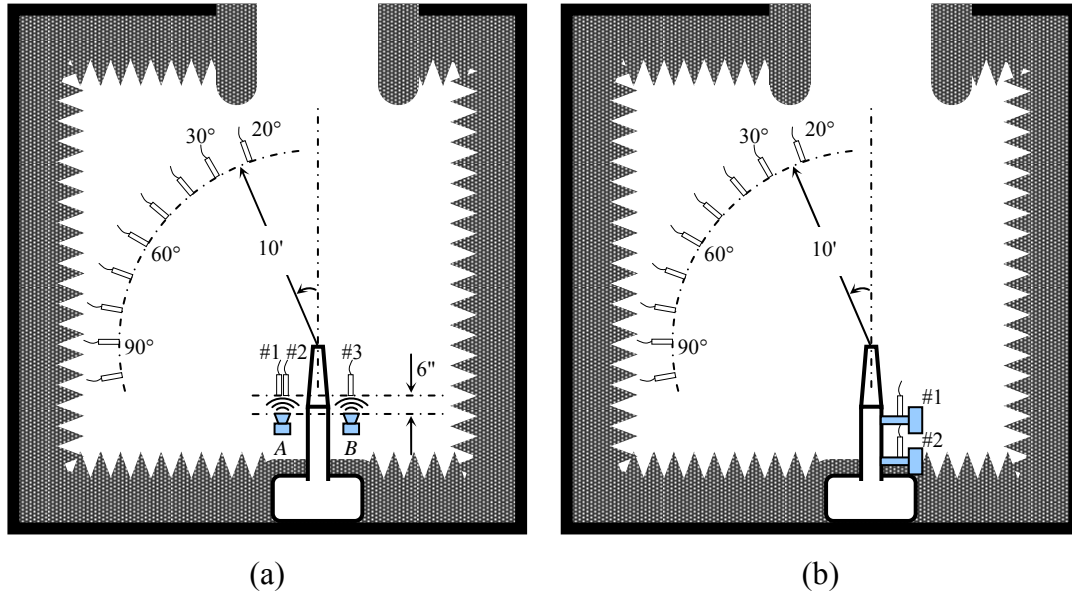


Figure 7.1 Schematic diagram of (a) external- and (b) internal-source configurations.

7.1.1 External-Source Configuration Results

Data gathered using the external-source configuration was analyzed using the three-microphone method, the coherent output power spectrum, and the partial coherence method. In all instances, some correlated source(s) was (were) buried in uncorrelated jet noise. For the single driver cases, it was found that the three-microphone method most accurately deduced the buried correlated signal produced by a single driver. With two correlated sources of similar spectral shape buried in uncorrelated noise, none of the noise reduction methods produced results of sufficient accuracy. The findings from each coherence-based technique and the perceived reasons for these findings are detailed in the following sections.

7.1.1.1 Three-Microphone Method Results

Typical three-microphone method results for the external-source configuration are depicted in Figure 7.2. The solid black line in each of the plots represents auto-spectra data as measured by the 60-degree microphone when either (a) the jet and driver *A* only, (b) the jet and driver *B* only, or (c) the jet and both drivers are operational. The red dashed line represents SPL data measured at the 60-degree microphone with only driver *A* operational, and the green dash-dot line shows auto-spectra data measured at the 60-degree microphone with only driver *B* operational. The blue triangles indicate calculated correlated three-microphone method values using microphones located at 20, 60, and 90 degrees; while the pink squares represent calculated uncorrelated three-microphone method data using the same three microphones. The dotted cyan line in (c) shows the SPL measured at the 60-degree microphone with drivers *A* and *B* simultaneously active.

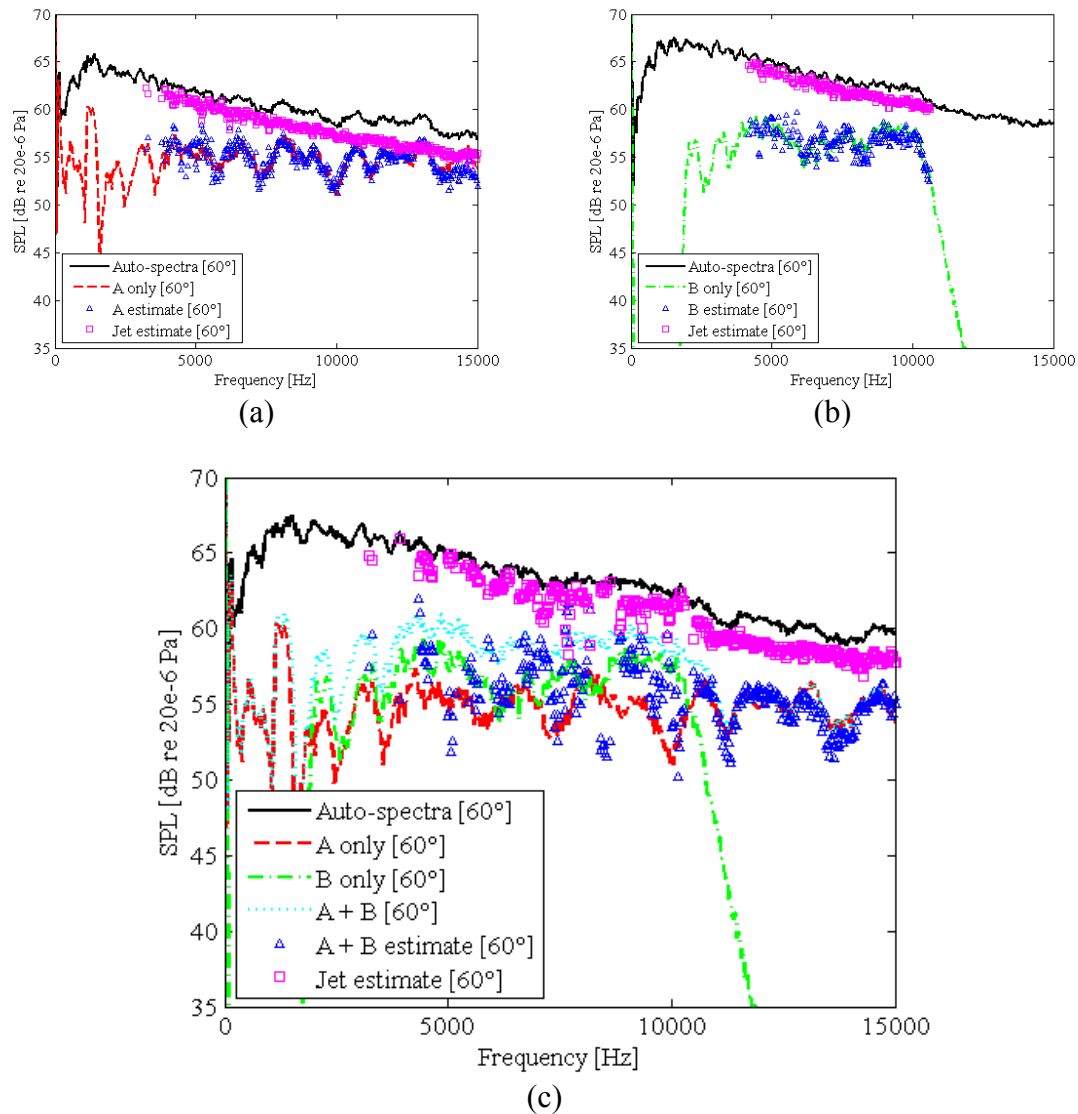


Figure 7.2 Three-microphone method results for tests where drivers were operated individually and collectively, (a) Mach 0.68 jet + *A*, (b) Mach 0.68 jet + *B*, (c) Mach 0.68 jet + *A* + *B* (external-source configuration).

The three-microphone method findings shown above are very similar to those presented in the previous chapter. In (a) and (b), only one driver—either *A* or *B*—is operational along with the jet. In these instances, the three-microphone method is able to reduce the single buried correlated source at most frequencies. In (c), both drivers are operational along with the jet. In this case, the three-microphone method results are not accurate.

The method is not able to reduce the signals of driver *A* only, driver *B* only, nor the combined sum of the two in frequency regions where the self-correlated drivers produce comparable sound pressure levels. However, in (c) the level of driver *B* is significantly reduced beyond 10 kHz, in this region the three-microphone method works quite well. The level of driver *A* is predicted with sufficient accuracy, just as in (a). Thus, for systems composed of multiple correlated sources that radiate sound within overlapping frequency regions, the three-microphone method seems to work well in regions where one of the sources is dominant. As shown below, these results are consistent with that of full-scale engine noise experimentation.

7.1.1.2 Coherent Output Power Spectrum Results

Typical coherent output power method results for the external-source configuration are depicted in Figure 7.3. The labeling conventions for all measured data (i.e., results plotted as lines) are analogous to those used in the previous figure. As for calculated data (i.e., the symbols in the figure below), the blue triangles indicate the calculated coherent output power using microphones labeled 60° and #1 in Figure 7.1(a); while the pink squares represent the calculated coherent output power for microphones 60° and #3. Consistent with the presentation of the three-microphone method results above, plots (a) and (b) of Figure 7.3 illustrate comparisons of the measured and calculated level of a single correlated source buried in uncorrelated noise, and plot (c) compares measured and calculated data for the case where all noise sources are active. The measured data shown in Figure 7.3 is identical to that of Figure 7.2.

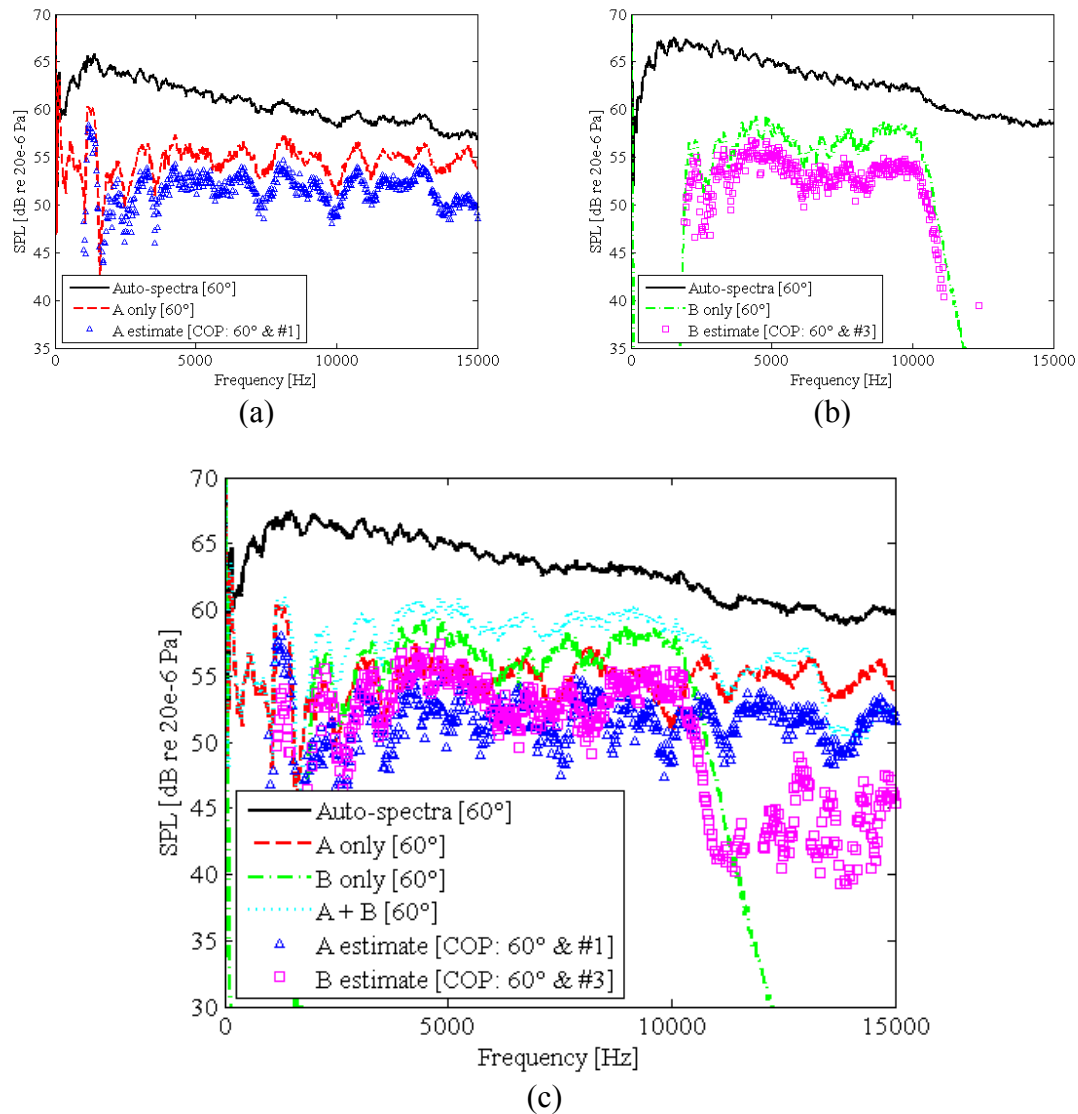


Figure 7.3 Coherent output power method results for tests where drivers were operated individually and collectively, (a) Mach 0.68 jet + *A*, (b) Mach 0.68 jet + *B*, (c) Mach 0.68 jet + *A* + *B* (external-source configuration).

As shown in Figure 7.3, the coherent output power method tends to underestimate the true levels in all testing cases—(a) jet + *A*, (b) jet + *B*, and (c) jet + *A* + *B*. The coherent output power method is said to accurately predict the level of the source(s) of interest (*A* and/or *B* as indicated in Figure 7.1) if the assumption of a linear system can be made and the microphone(s) used to characterize the source(s) of interest is free from extraneous

noise⁴. In order for a system to be classified as linear, the radiated sound must propagate linearly to all microphones (i.e., the propagation must obey the inverse square law). For such a system composed of a single correlated source alone, the coherence between any two microphones placed arbitrarily throughout the sound field should be unity. This is not the case for the data shown above. Figure 7.4 illustrates the measured coherence between the 60-degree microphone and those positioned near the drivers (as shown in Figure 3.12). The curve labeled $[60^\circ, \#1]$ is the measured coherence for driver *A* alone, while the curve labeled $[60^\circ, \#3]$ is for driver *B* alone. In both instances the measured coherence is less than unity; thus, the wave propagation between the microphones positioned near the drivers and the 60-degree microphone is not fully linear. Two possible reasons for the non-fully coherent measurement between the 60-degree far-field microphone and those positioned near the drivers are (1) the microphones positioned near the drivers experience near-field effects from the drivers; thus, the far-field microphone and those positioned near the drivers measure physically different sound fields and (2) the microphones positioned near the drivers measure elevated amplitudes; hence, the far-field microphone and those positioned near the drivers experience waves with physically different spectral content. Since the coherence measured between the microphones positioned near the drivers and the 60-degree microphone is less than unity when a single correlated source is operated alone, the linear assumption is not valid. This is likely the reason for the discrepancies in the measured and calculated levels indicated in Figure 7.3.

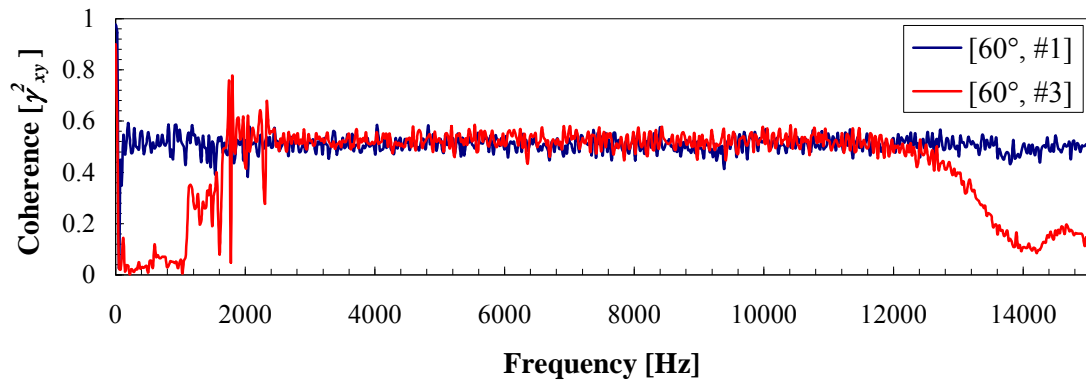


Figure 7.4 Measured coherence for a single driver (A: $\gamma^2_{(60^\circ, \#1)}$ and B: $\gamma^2_{(60^\circ, \#3)}$, external-source configuration).

7.1.1.3 Partial Coherence Method Results

Representative results from the partial coherence method analysis of the external-source configuration are shown in Figure 7.5. The measured and calculated data for the case where all noise sources are active is compared. The labeling conventions for all measured data (i.e., results plotted as lines) are analogous to those used previously. As for the calculated data (i.e., the symbols), the blue triangles indicate data calculated using equation (2.15), while the orange squares represent that calculated using equation (2.12). Microphone signals used in the partial coherence method analysis were 20° , 60° , 90° , #1, and #2 as shown in Figure 3.12(a). According the partial coherence methodology and the placement of these sensors, the results labeled *PCM: SPL_k* should follow the measured data labeled *B only*, and those labeled *PCM: SPL_u* should match the measured *A only* data. This is not the case for either set of calculated data shown in the Figure 7.5. The results labeled *PCM: SPL_k* exhibit significant error across all frequencies. Much like the coherent output power spectrum, the partial coherence method results labeled *PCM:*

SPLu underestimate the true levels. This is attributable to non-linear wave propagation as discussed above.

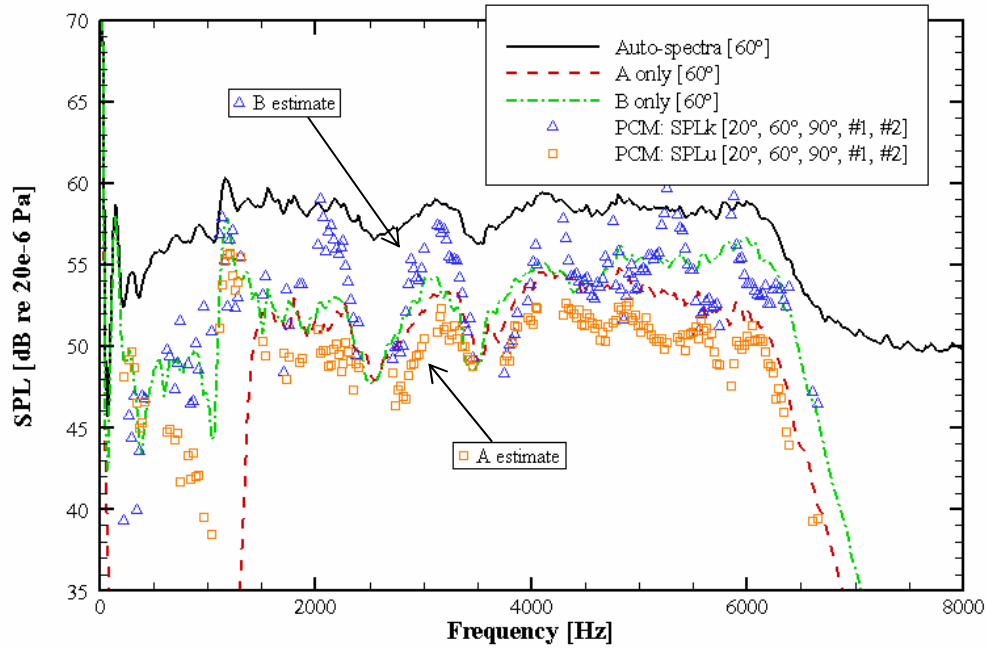


Figure 7.5 Partial coherence method results, Mach 0.5 jet + *A* + *B* (external-source configuration).

7.1.2 Internal-Source Configuration

The three-microphone method and the coherent output power spectrum was utilized to analyze data gathered using the internal-source configuration. In all instances, some correlated source(s) was (were) buried in uncorrelated jet noise. For the single driver cases, it was found that the three-microphone method most accurately predicted the buried correlated signal. When two correlated sources were active, neither the three-microphone method nor the coherent output power spectrum produced sufficient results. The findings from each are discussed below.

7.1.2.1 Three-Microphone Method Results

Figure 7.6 depicts typical three-microphone method results for the internal-source configuration. The findings shown below are for the 60-degree microphone as calculated using data gathered by the microphones located at the 20, 60, and 90-degree positions. The line and symbol conventions explained for the previous three-microphone figures remain consistent for Figure 7.6. Plots (a) and (b) show data gathered and calculated for internal-configuration for systems where a single correlated source is buried in uncorrelated jet noise produced by a Mach 0.46 jet exhausting from a 1.6-inch conical round nozzle. Plot (c) illustrates the results derived using the three-microphone method for a case where both acoustic drivers and a Mach 0.46 jet are operational. In Figure 7.6(a) and (b), the measured values of the noise of each source *A* and *B* were obtained with no flow whereas and calculated values were obtained with the flow on. The less than exact agreement between the measured and calculated values of plots (a) and (b) in Figure 7.6 can be attributed to flow-induced changes in the response of the drivers. These flow-induced changes are due to flow-acoustic interaction at the at the termination of the short tube connecting the driver and the jet supply duct⁵⁵. Impedance changes due to this flow-acoustic interaction cause flow-induced changes in the response of the drivers. Due to these response variations caused by the introduction of flow through the jet supply duct and the high precision of the three-microphone method in the single-driver external configuration testing (see Figure 7.2), it is believed that the flow-induced driver response variations are responsible for the less than exact agreement between the measured and calculated values of plots (a) and (b) below in Figure 7.6.

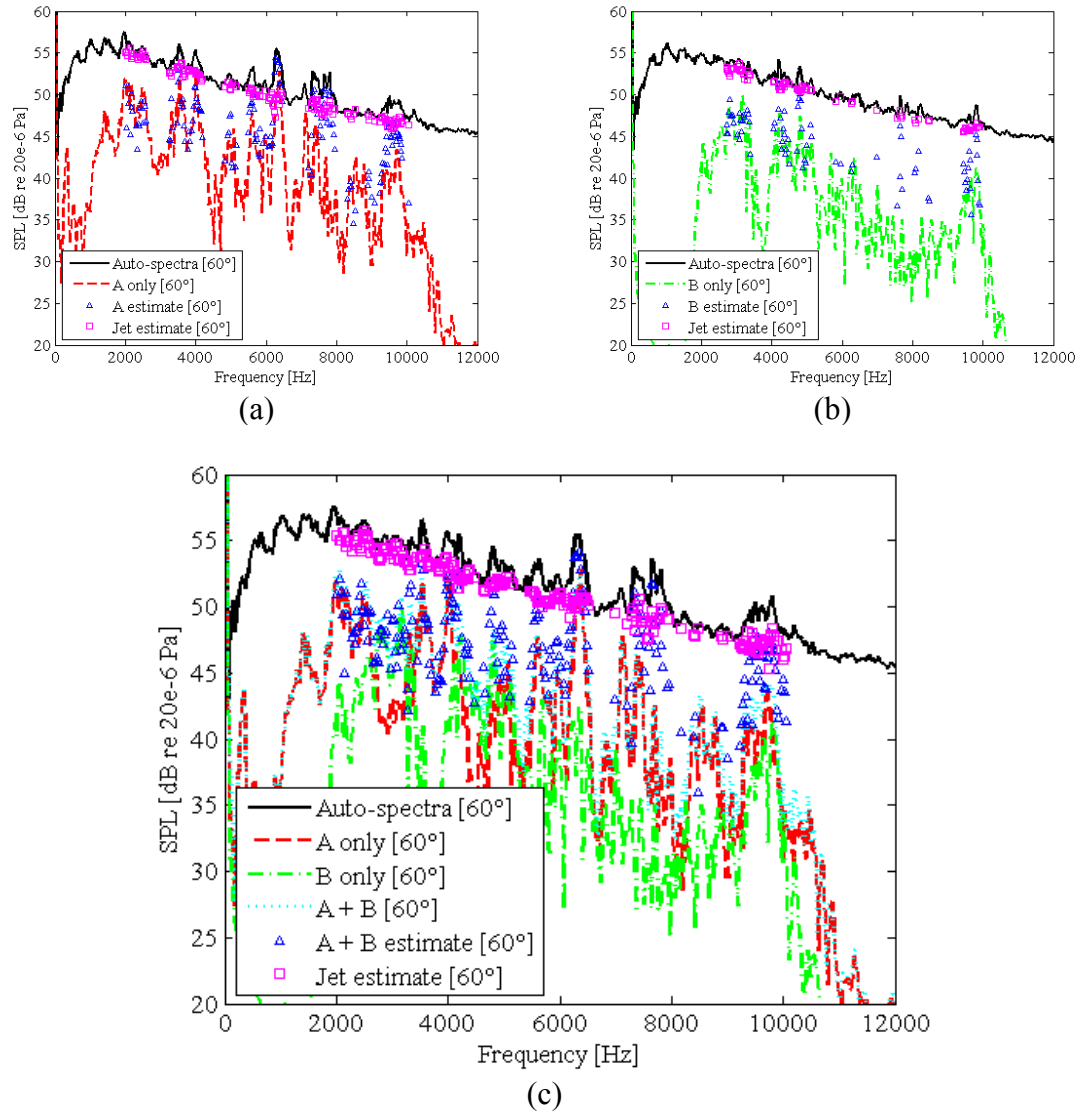


Figure 7.6 Three-microphone method results for tests where drivers were operated individually and collectively, (a) Mach 0.46 jet + *A*, (b) Mach 0.46 jet + *B*, (c) Mach 0.46 jet + *A* + *B* (internal-source configuration).

7.1.2.2 Coherent Output Power Spectrum Results

The microphone arrangement and measurement system used to generate the results shown in the figure above allow for further manipulation of the data using the coherent output power spectrum. Typical results from the coherent output power spectrum analysis of the data for the internal-source configuration are shown in Figure 7.7. The

coherent output power spectrum is calculated at the 60-degree microphone while correlating with #1 and #2. Microphones #1 and #2 are positioned near sources *A* and *B*, respectively. The labeling conventions for all measured data (i.e., results plotted as lines) are analogous to those used in the previous figure. As for calculated data (i.e., the symbols in the figure below), the blue triangles indicate the calculated coherent output power using microphones labeled 60° and #1 in Figure 7.1(b); while the pink squares represent the calculated coherent output power for microphones 60° and #2. Consistent with the presentation of the three-microphone method results above, plots (a) and (b) of Figure 7.7 illustrate comparisons of the measured and calculated level of a single correlated source buried in uncorrelated noise. The measured data shown in Figure 7.7 is identical to that of Figure 7.6.

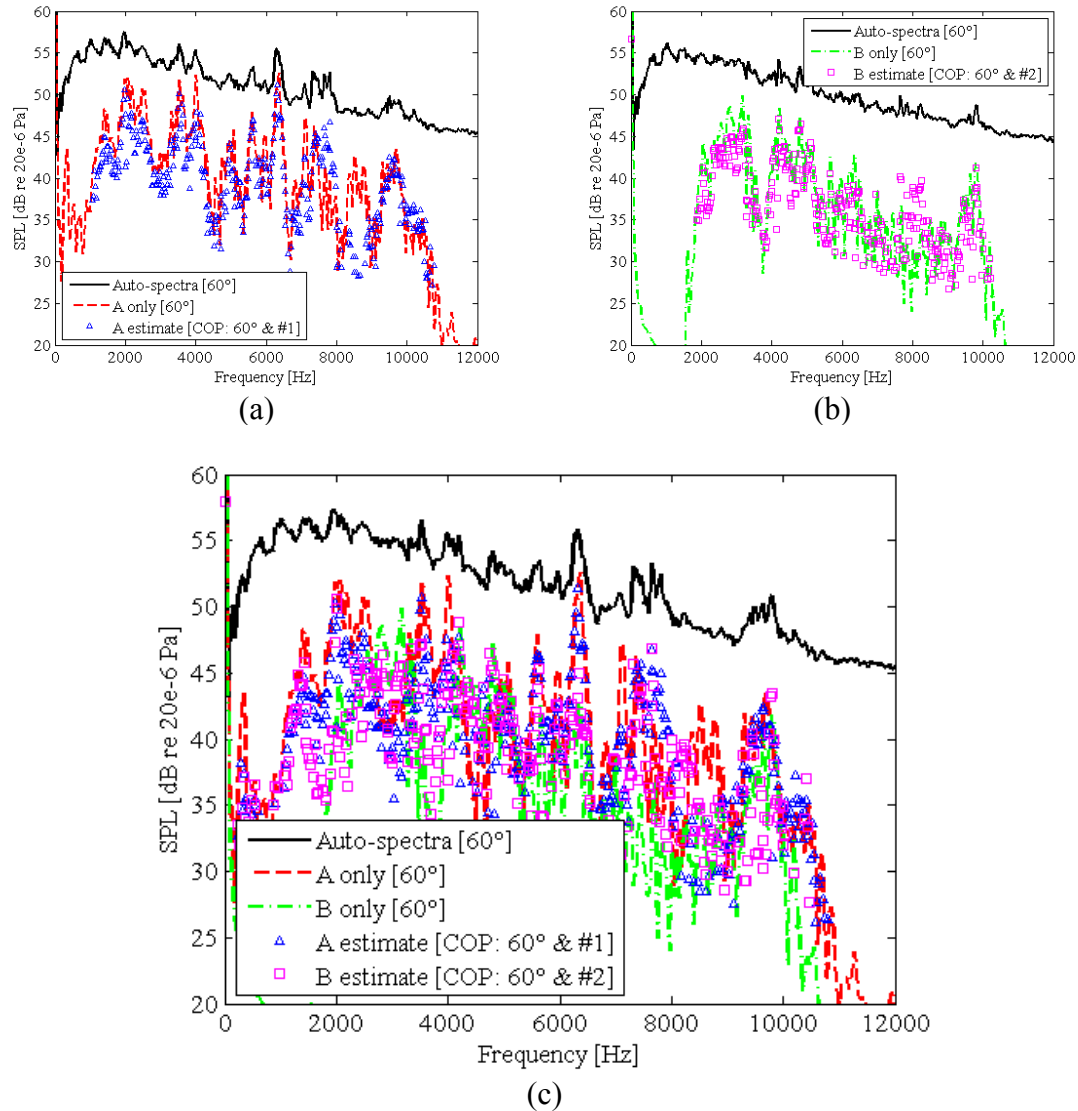


Figure 7.7 Coherent output power method results for tests where drivers were operated individually and collectively, (a) Mach 0.46 jet + A, (b) Mach 0.46 jet + B, (c) Mach 0.46 jet + A + B (internal-source configuration).

In Figure 7.7, the coherent output power method seems to predict the level of the measured driver(s) fairly well. However, this result is somewhat misleading. Upon comparing the coherent output power results with that of three-microphone method for the single driver systems, discrepancies are noticed between the spectral predictions as illustrated in Figure 7.8. Plots (a) and (b) of Figure 7.8 show comparisons of the

correlated three-microphone method results and the coherent output power spectrum results for systems where driver *A* and driver *B*, respectively, are buried in uncorrelated jet noise. That is, Figure 7.8(a) compares data from Figure 7.6(a) and Figure 7.7(a), and similarly Figure 7.8(b) compares data from Figure 7.6(b) and Figure 7.7(b). If the three-microphone results are considered to be most accurate—which is expected to be the case here due the high precision displayed in the external-driver configuration where no flow-induced variations in driver response are present since the drivers are not located in the flow carrying interior of the duct, then it can be said the coherent output power spectrum under-predicts the true correlated contribution at the 60-degree far-field microphone in all instances. This is consistent with results presented earlier for the external-source configuration. Figure 7.9 illustrates the measured coherence between the 60-degree microphone and the microphones positioned near the drivers (as shown in Figure 7.1). The curve labeled $[60^\circ, \#1]$ is the measured coherence for driver *A* alone, while the curve labeled $[60^\circ, \#2]$ is for driver *B* alone. In both instances the measured coherence is less than unity. This is similar to the external-source configuration where the wave propagation between the microphones positioned near the drivers and far-field is found to be somewhat non-linear.

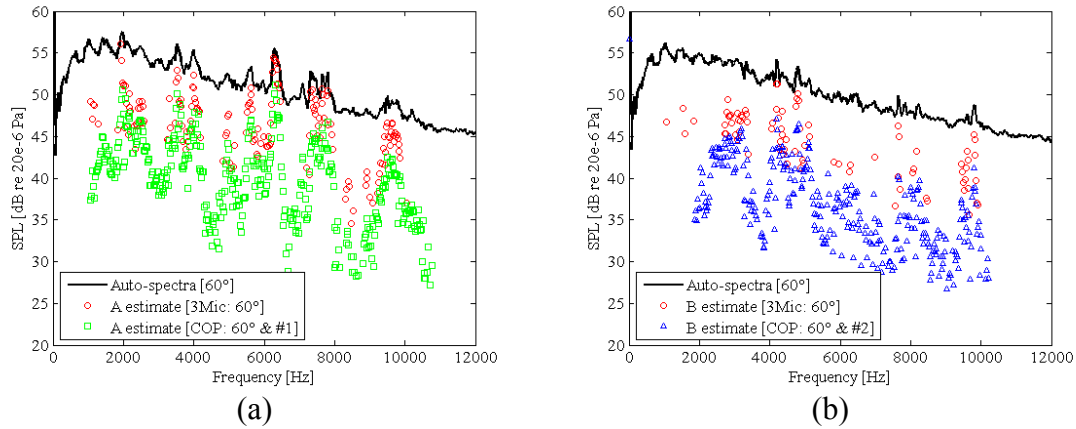


Figure 7.8 Comparison of three-microphone and coherent output power spectrum findings for (a) Mach 0.46 jet + A, (b) Mach 0.46 jet + B (internal-source configuration).

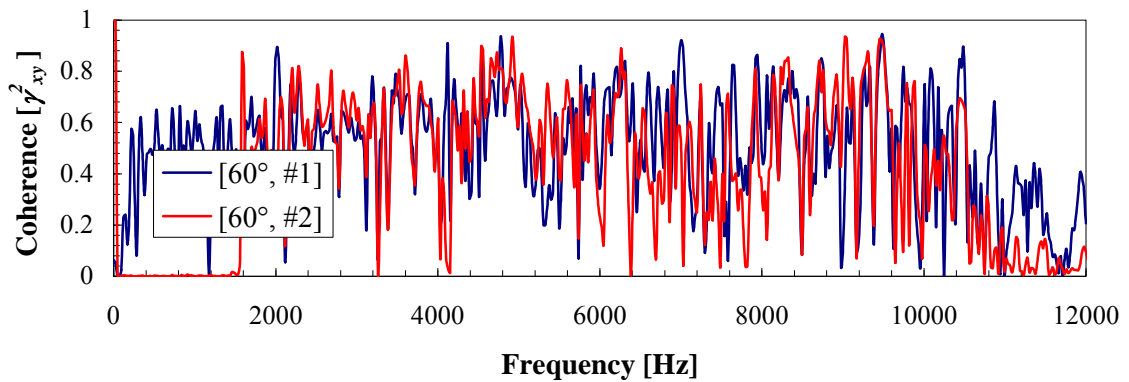


Figure 7.9 Measured coherence for a single driver (A: $\gamma^2_{(60^\circ, \#1)}$ and B: $\gamma^2_{(60^\circ, \#2)}$, internal-source configuration).

The salient conclusion from the model-scale testing is that when attempting to educe a single correlated source buried in uncorrelated jet noise the three-microphone method works well at all frequencies. Furthermore, when two correlated sources are operational, the three-microphone method works well in any frequency region where one of the correlated sources is dominant. If the two sources are comparable in level, the calculated levels show considerable error. The coherent output power spectrum and the partial

coherence method were found to be unsuccessful when attempting to educe a single correlated signal or a pair of correlated signals buried in uncorrelated noise due to the non-linear wave propagation within the model-scale systems.

7.2 Application of the Lessons Learned to Full-Scale Engine Noise Measurements

Based upon the results of the previous chapters and the findings from the model-scale implementation of said coherence-based techniques, the system requirements needed to provide useful data for manipulation via the three-microphone, coherent output power spectrum, and partial coherence methods have been determined for full-scale engine diagnostics. Specifically, the far-field microphone layout and data acquisition requirements are of highest importance. In addition to the far-field microphones, the coherent output power spectrum and partial coherence methods require internal sensors. The data acquisition system used in the full-scale testing and the subsequent results are summarized below.

7.2.1 Far-field Microphone Layout

As discussed in Chapter 5, when implementing coherence-based single processing techniques, a polar microphone arc should be placed beyond 50 diameters from the nozzle exit to provide the most practical assurance of jet noise incoherence. Variable microphone spacing within the arc is required. Microphones should be spaced according to their location relative to downstream jet axis and the dominate noise radiation entity within that region. To ensure jet noise incoherence between all correlating microphone pairs during a Honeywell full-scale engine test far-field microphones were placed at the

20, 50, 70, 90, 110, 130, 150, and 170-degree locations in a polar arc positioned roughly 50 diameters from the nozzle exit, as shown in Figure 7.10.

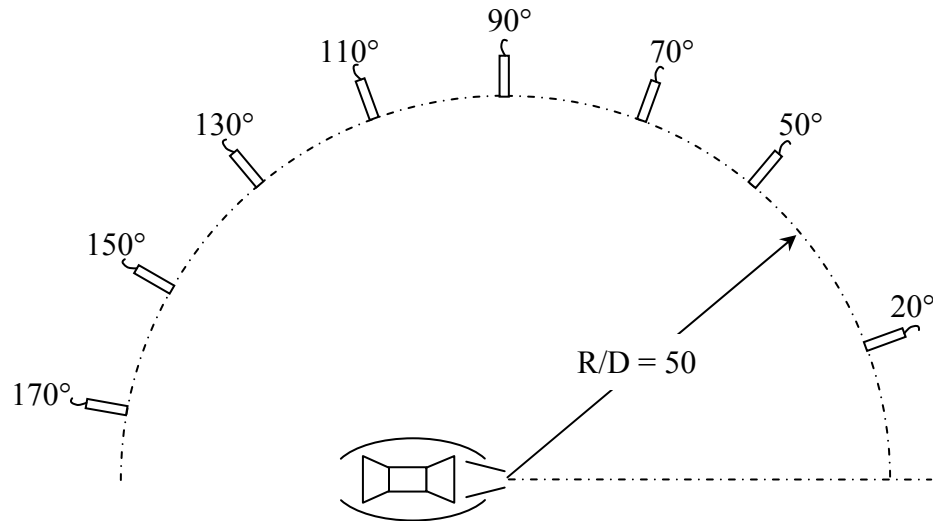


Figure 7.10 Far-field microphone arc used in the full-scale engine tests.

7.2.2 Internal Sensors

The internal sensors should be placed in manner such that normal operation of the engine will be least affected. In a Honeywell program where the recommendations outlined here were implanted, a single sensor was used to characterize the combustion noise; while two sensors were used within the turbine exit region. In the subsequent results discussed below, the combustor sensor is label *CI*, and the turbine sensors are labeled *T1* and *T2*.

7.2.3 Data Acquisition Requirements

The pre-existing full-scale engine data acquisition system utilized in this work maintains a sampling rate of 65 kHz. Narrow band data with a bandwidth of 8 Hz was required by the sponsor; thus, a sampling duration of roughly 100 seconds was needed to provide

1024 ensemble averages with 25% overlap (i.e., the 100 second time history data was analyzed with a bandwidth of 8 Hz, 1024 averages, and 25% overlap). Hanning windowing was used in the FFT (fast Fourier transform) analyzer.

7.2.4 Coherence Threshold

The establishment of a minimum measurable coherence and corresponding minimum educable level in the model-scale experimentation lent itself to a similar analysis of this property for the Honeywell full-scale testing mentioned above. This was done according to the aligned/unaligned coherence procedure outlined by Miles⁵⁶. In essence, this technique calls for the addition of a time delay to one of the correlating signals. The delayed signal at one microphone is then correlated with another microphone signal that is not delayed. When the applied time delay exceeds the sample record length, the coherence measured between the two signals is that of two independent random signals. Thus, an unaligned coherence is attained. When implementing this technique in this work, time histories for each microphone pair were unaligned and then an FFT analyzer was used to determine the coherence between all microphone pairs. An examination of the baseline engine data was carried out via this procedure. A minimum measurable coherence threshold of 0.01 was found. The aligned and unaligned coherence between a single pair of microphones are compared in Figure 7.11. Note that in the frequency range of up to about 5 kHz, where there is plenty of acoustic energy, the coherence is more substantial, being the highest in the tonal regions. The unaligned coherence reduces to 0.01 or less in the broadband region. Unaligning the data is said not to affect the tonal components of the spectrum⁵⁶. This is evident by comparing plots (a) and (b) of Figure

7.11. Similar results were found for all microphone pairs and power settings, and thus a coherence threshold of 0.01 was used in all analysis.

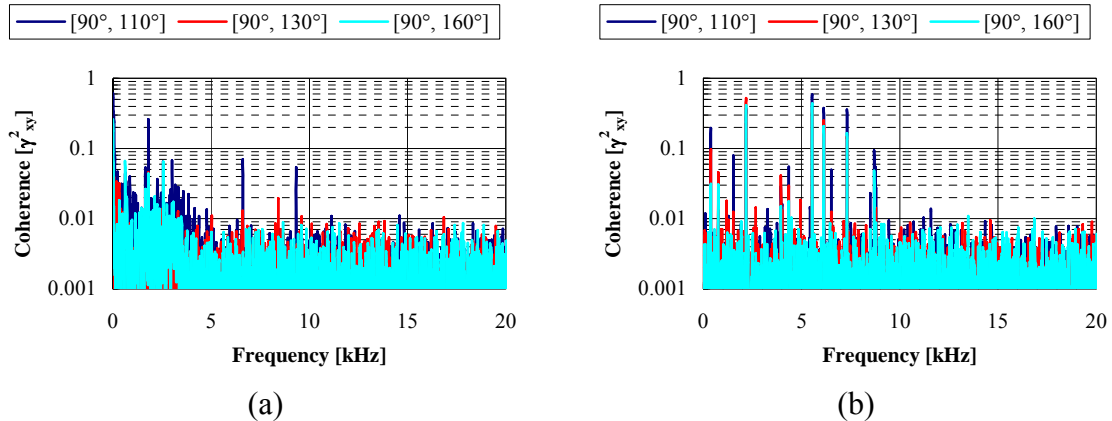


Figure 7.11 Typical results from full-scale engine (a) aligned versus (b) unaligned coherence study, 60% power.

7.2.5 Full-Scale Engine Results

Time history data was acquired with tarmac microphones located at the 20, 50, 70, 90, 110, 130, 150, and 170-degree positions and internal sensors placed in the combustor and turbine exit. Data acquisition was performed simultaneously at each microphone allowing for the time delay calculations between the far-field microphones and internal sensors. An average time delay of 100 milliseconds was applied to the far-field time histories to account for internal to far-field wave propagation. The analysis of the processed data has been carried out via the three-microphone, coherent output power, and partial coherence methods. Representative results are depicted below. In the figures below, the microphones used in the three-microphone analysis were the 20, 50, and 70-degree far-field microphones. The results labeled *Three-mic [50°]* represent three-microphone method calculated correlated findings and the 50-degree far-field

microphone. They are shown as cyan filled squares. In Figure 7.12, the coherent output power results generated using 50-degree far-field microphone and the specified internal sensors—combustor-mounted *CI* or turbine-mounted *TI*—are shown. Data represented as red circles are for the former and those shown as blue triangles are for the latter. The 20, 50, and 70-degree far-field microphones along with the two internally mounted turbine microphones (i.e., those with designations *TI* and *T2*) were used in the partial coherence method analysis. The green diamonds in Figure 7.12 represent results calculated with equation (7.1), and the orange plus symbols represent results from equation (7.2).

$$G_{k_2k_2} = \frac{\left| G_{12} - \frac{G_{14}G_{52}}{G_{54}} \right| \left| G_{23} - \frac{G_{24}G_{53}}{G_{54}} \right|}{\left| G_{13} - \frac{G_{14}G_{53}}{G_{54}} \right|} \quad (7.1)$$

$$G_{u_2u_2} = \frac{|G_{24}| |G_{25}|}{|G_{45}|} \quad (7.2)$$

The subscripts 1, 2, 3, 4, and 5 represent the transducers located at positions 20°, 50°, 70°, *TI*, and *T2*, respectively. The coherent output power and partial coherence findings are compared to those for the three-microphone method in Figure 7.12 and Figure 7.13, respectively.

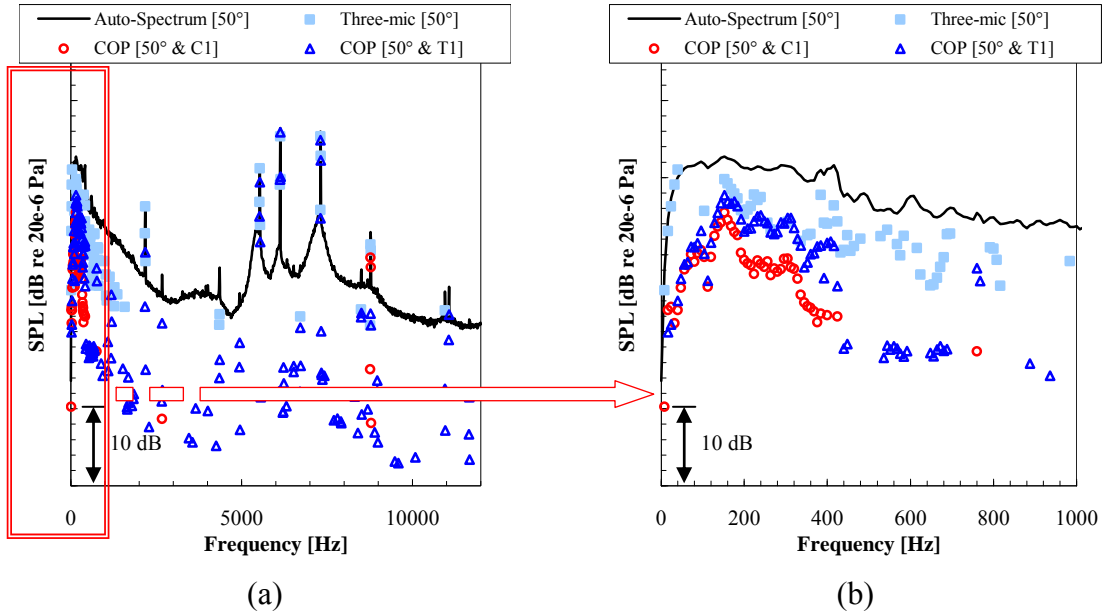


Figure 7.12 Educued results—(a) full frequency span and (b) concentrated frequency span below 1 kHz—via the three-microphone and coherent output power spectrum methods at the 50-degree far-field microphone, 60% power.

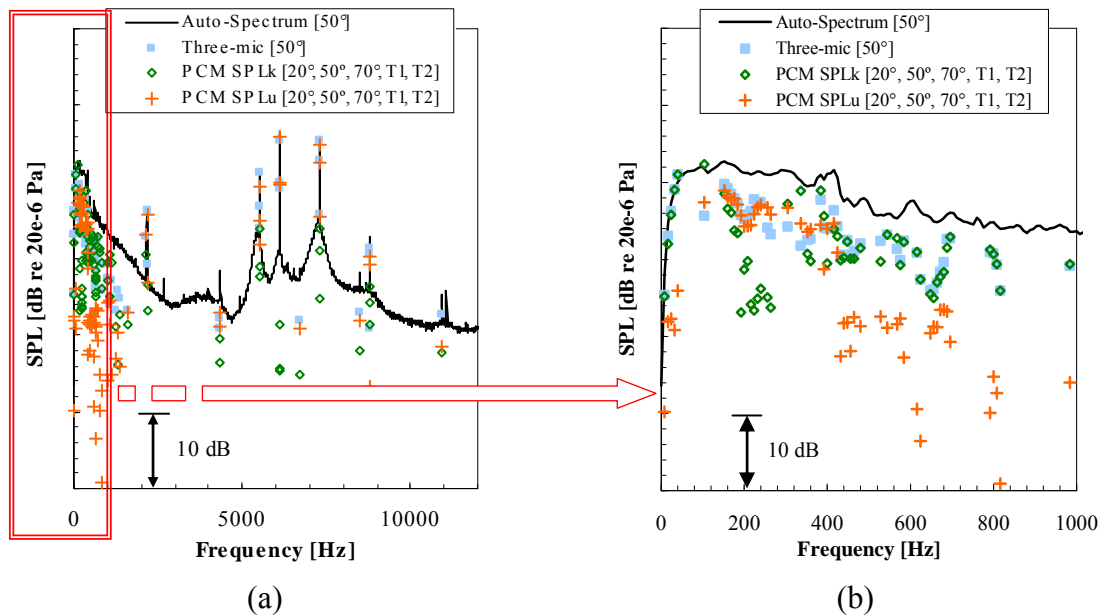


Figure 7.13 Educued results—(a) full frequency span and (b) concentrated frequency span below 1 kHz—via the three-microphone and partial coherence methods at the 50-degree far-field microphone, 60% power.

Consistent with the findings of the model-scale testing, the findings above for the full-scale engine indicate that the coherent output power spectrum results tends to predict levels that fall well below that of the correlated three-microphone calculations, except at some tonal components. It is believed that the discrepancies are a result of the fact that the internal microphone signal is contaminated by hydrodynamic noise. The presence of such contamination violates a key assumption of the coherent output power spectrum, where the method assumes that the internal microphone is measuring nothing but the acoustic signal from the turbine in this case. The fact that most tonal components, which are much higher in amplitude compared to the hydrodynamic noise, are accurately predicted by the coherent output power spectrum further solidifies this belief. These results lead to the conclusion that the coherent output power method is not a completely satisfactory method when determining the contribution of internal sources to microphones located in the far-field at all frequencies.

As for the partial coherence results presented above, they show good agreement with those of the correlated three-microphone method calculations across all frequencies. In the partial coherence method, the hydrodynamic noise is cancelled. The agreement between the partial coherence method and the three-microphone results across all frequencies leads to the conclusion that the three-microphone method can be used to reduce internal noise from jet mixing noise for a full-scale engine at those frequencies where one knows in advance that any two self-correlated internal sources definitely produce noise at different frequencies. The preliminary predictions from the manufacturer suggest that the combustor and turbine noise overlap only within a small frequency span; thus, the signals have indeed been accurately reduced within their

respective frequency regions using the three-microphone method. Furthermore, the level within the overlap region is more than 10 dB below the total noise; consequently, the signals are uneducable by coherence-based methods under the current testing conditions. The three-microphone methodology does not work well in the spectral region where the combustion noise and the turbine noise spectrum overlap. If predictions are needed for this region, the best thing to do is to extrapolate the skirts of the spectrum of each source as determined by the scheme used here.

CHAPTER 8

SOLVING THE FIVE-MICROPHONE PROBLEM

This chapter deals with solving the five-microphone methodology equations laid out earlier for separating two coherent signals buried in uncorrelated noise using measured data. Attempts have been made to solve the non-linear system of equations resulting from the implementation of the five-microphone method; however, all have failed to give solutions of sufficient accuracy in proof-of-concept experimentation. The original solution procedure employed by Minami and Ahuja⁷ and its caveats are discussed below, along with a summary of the solution schemes attempted during the present work and the failures of each. This effort is documented here as a means of providing future researchers with a starting point for a possible solution to this potentially extremely useful coherence-based signal enhancement technique.

8.1 Minami and Ahuja Solution Routine

When first solving the five-microphone problem for the simulation outlined in their paper, Minami and Ahuja⁷ algebraically reduced the system of 55 equations with 55 unknowns outlined earlier to a system consisting of only 8 equations with 8 unknowns. The reduced 8-equation system was solved using the Newton-Raphson method. This solution procedure required an initial guess of the unknown variables. It appears that the work of Minami and Ahuja⁷ required an initial guess with an accuracy that is physically unattainable in experiments where the unknown variables are not numerically pre-

defined. Thus, their solution procedure is unacceptable for real-world experimentation. This established the need for further code development in order to utilize the five-microphone methodology in the present work.

8.2 Physics-Based Initial Guess/Bounds

Before reporting further, the issue of the physics-based initial guess or bounds for the unknown variables must be addressed—their origin as well as their significance to data processing. In the numerical simulation, these physics-based bounds were chosen based on the masking rule of acoustics that requires a buried signal to be within 12 dB of the loudest level in order to meaningfully contribute to the total sound pressure level. Thus, the lower bounds placed on the unknown auto-spectra and cross-spectra magnitudes were determined by simply subtracting 12 dB from simulated levels of the total auto-spectrum and cross-spectrum magnitude at any given microphone or pair of microphones respectively. The upper bounds were set at the total simulated levels. The phases were allowed to vary over the entire numerical space, $[-\pi, \pi]$.

The determination of the physical bounds of the system for proof-of-concept experimentation is based on the existence of a theoretical threshold on the lowest measurable coherence (as reported in Chapter 5). Because the five-microphone problem is extremely sensitive to even minor discrepancies in the measured value of coherence, a coherence threshold of 0.01 was used, thus, leading to lower bounds of 10 dB less than the measured levels of the auto-spectrum and cross-spectrum magnitude and upper bounds equal to the total measured levels. As in the numerical simulation, the phases were allowed to vary over the entire numerical space, $[-\pi, \pi]$.

8.3 Numerical Schemes Employed

A total of 11 trials have been completed in an attempt to solve the five-microphone problem. These attempts are listed below in Table 8.1. The outcome for each attempt is further explained below in the following sections. Trials 1 – 5 in Table 8.1 refer to attempts made in order to solve the numerical simulation of Minami and Ahuja⁷. The remaining trials refer to attempts made to solve the five-microphone problem resulting from proof-of-concept testing using the external-source configuration discussed earlier. The trial numbers are further alluded to in the text below to provide the reader with knowledge of which attempt is being discussed. Solution tools including the third-party, Newton-Rhaphson based Polymath 6.0, the MATLAB® *fminsearch* function, and a genetic algorithm (i.e., the MATLAB® *ga* function) were utilized in this effort.

Table 8.1 Summary of five-microphone problem solution routines.

Trial no.	Configuration	Scheme tried	Initial guess or bounds	Special constraints	Findings
1	Miami/Ahuja simulation	Newton-Raphson based Polymath 6.0 solving 55 non-linear equations	$[G_{yy} - 12\text{dB}, G_{yy}]$ for auto-spectra levels; $[G_{xy} - 12\text{dB}, G_{xy}]$ for cross-spectra magnitudes; $[-\pi, \pi]$ for cross-spectra phase	none	non-physical solution (imaginary numbers introduced)
2	Miami/Ahuja simulation	Newton-Raphson based Polymath 6.0 solving 8 non-linear equations	$[G_{yy} - 12\text{dB}, G_{yy}]$ for auto-spectra levels; $[G_{xy} - 12\text{dB}, G_{xy}]$ for cross-spectra magnitudes; $[-\pi, \pi]$ for cross-spectra phase	none	non-physical solution (imaginary numbers introduced)
3	Miami/Ahuja simulation	MATLAB® <i>fminsearch</i> function	initial guess within $\pm 2\%$ of actual solution	none	results within $\pm 1\text{dB}$
4	Miami/Ahuja simulation	MATLAB® <i>fminsearch</i> function	$[G_{yy} - 12\text{dB}, G_{yy}]$ for auto-spectra levels; $[G_{xy} - 12\text{dB}, G_{xy}]$ for cross-spectra magnitudes; $[-\pi, \pi]$ for cross-spectra phase	none	results off by as much as $\pm 30\text{dB}$
5	Miami/Ahuja simulation	MATLAB® <i>ga</i> function + MATLAB® <i>fminsearch</i> function	$[G_{yy} - 12\text{dB}, G_{yy}]$ for auto-spectra levels; $[G_{xy} - 12\text{dB}, G_{xy}]$ for cross-spectra magnitudes; $[-\pi, \pi]$ for cross-spectra phase	none	results within $\pm 1\text{dB}$ at all frequencies
6	External-source configuration, $M_j = 0.7$	MATLAB® <i>ga</i> function + MATLAB® <i>fminsearch</i> function	$\pm 3\text{dB}$ for auto- and cross-spectra levels; $[-\pi, \pi]$ for phase	$\gamma^2(f) \geq 0.01$	results within $\pm 2.6\text{dB}$ at selected frequencies
7	External-source configuration, $M_j = 0.7$	MATLAB® <i>ga</i> function + MATLAB® <i>fminsearch</i> function	$\pm 5\text{dB}$ for auto- and cross-spectra levels; $[-\pi, \pi]$ for phase	$\gamma^2(f) \geq 0.01$	results within $\pm 4.7\text{dB}$ at selected frequencies
8	External-source configuration, $M_j = 0.7$	MATLAB® <i>ga</i> function + MATLAB® <i>fminsearch</i> function	$\pm 10\text{dB}$ for auto- and cross-spectra levels; $[-\pi, \pi]$ for phase	$\gamma^2(f) \geq 0.01$	ran for days and did not find a solution
9	External-source configuration, $M_j = 0.7$	MATLAB® <i>ga</i> function + MATLAB® <i>fminsearch</i> function	$[G_{yy} - 10\text{dB}, G_{yy}]$ for auto-spectra levels; $[G_{xy} - 10\text{dB}, G_{xy}]$ for cross-spectra magnitudes; $[-\pi, \pi]$ for cross-spectra phase	$\gamma^2(f) \geq 0.01$	results within $\pm 8\text{dB}$ at selected frequencies
10	External-source configuration, $M_j = 0.7$	MATLAB® <i>ga</i> function + MATLAB® <i>fminsearch</i> function	$[G_{yy} - 10\text{dB}, G_{yy}]$ for auto-spectra levels; $[G_{xy} - 10\text{dB}, G_{xy}]$ for cross-spectra magnitudes; $[-\pi, \pi]$ for cross-spectra phase	$\gamma^2(f) \geq 0.01$; jet noise level at each mic calculated from 3-mic method	results within $\pm 5\text{dB}$ at all frequencies
11	External-source configuration, $M_j = 0.5$	MATLAB® <i>ga</i> function + MATLAB® <i>fminsearch</i> function	$[G_{yy} - 10\text{dB}, G_{yy}]$ for auto-spectra levels; $[G_{xy} - 10\text{dB}, G_{xy}]$ for cross-spectra magnitudes; $[-\pi, \pi]$ for cross-spectra phase	$\gamma^2(f) \geq 0.01$; jet noise level at each mic calculated from 3-mic method	results within $\pm 5\text{dB}$ at all frequencies

8.3.1 Using the Netwon-Rhapson Based Polymath 6.0

In the initial attempts made by the author to solve the five-microphone problem resulting from the numerical simulation outlined in Minami and Ahuja⁷, a third-party Netwon-Rhapson based software, *Polymath 6.0*, was implemented. This software required an initial guess for each unknown value. When using the initial guess prescribed by Minami and Ahuja for their numerical simulation, results of sufficient accuracy were attained. However, the findings resulting from these early attempts at solving both the original 55-equation system and the reduced 8-equation system were quite poor—non-physical imaginary solutions were obtained—when using physics-based initial values for the unknowns (i.e., real-world initial values). The attempt at solving the 55-equation system is noted by trial number 1 in Table 8.1, and the attempt at solving the 8-equation system is noted by trial number 2.

8.3.2 Using MATLAB *fminsearch*

The use of the MATLAB® *fminsearch* function to solve the original 55-equation system was then attempted (denoted as trials 3 and 4 in Table 8.1). This built-in function locally optimizes a scalar function of several variables by searching for function minima starting with an initial estimate of each variable. Specifics of the algorithm used are in the MATLAB® Help Documentation⁵⁷. Since the *fminsearch* function requires a single scalar function for optimization, the 55-equation system was reduced to one equation by subtracting the right-hand side of each equation from both the left- and right-hand sides of that equation. For example, take

$$G_{y_i y_i} = G_{u_i u_i} + G_{v_i v_i} + G_{n_i n_i} \quad (i = 1, 2, \dots, 5) \quad (8.1)$$

Subtracting the RHS from both itself and the LHS gives

$$G_{y_i y_i} - (G_{u_i u_i} + G_{v_i v_i} + G_{n_i n_i}) = 0 \quad (i = 1, 2, \dots, 5) \quad (8.2)$$

This was done for each of the 55 equations, and then the equations were squared and summed. The result of this process was one scalar function of all variables that is equal to zero when minimized. Just as with the solution procedure employed by Minami and Ahuja, an initial guess of each unknown variable was required. In trial number 3, when utilizing the *fminsearch* function, results within ± 1 dB of the actual solution were obtained using initial values within $\pm 2\%$ of the actual solution (very similar to the initial guess employed by Minami and Ahuja). However, initial guesses with that type of accuracy are unrealistic (i.e., there is no guarantee that the values of auto-spectra and cross-spectra can ever be known in an acoustic environment within $\pm 2\%$ accuracy). In fact, if the unknown power-spectra values were known within $\pm 2\%$, there would be no need to use any signal enhancement technique because the sound pressure levels would be within roughly ± 0.09 dB of the actual value (e.g., $10 \log_{10}(1.02) = 0.09$ and $10 \log_{10}(0.98) = -0.09$), which is far more accurate than any coherence-based method developed to date. Thus, a physics-based initial guess as discussed in Section 8.2 was then utilized. For this case (denoted as trial number 4), results were off by as much as 30 dB. An alternate method was then explored.

8.3.3 Using MATLAB *fminsearch* and *ga*

8.3.3.1 Solving the Minami and Ahuja Simulation

Upon the suggestion of researchers Mike Jones and Dr. Willie Watson of the NASA Langley Research Center, the use of genetic algorithms was explored. The built-in genetic algorithm within MATLAB®, *ga*, was utilized along with the *fminsearch* function. The *ga* function provides a means by which the single scalar function described above can be minimized globally. The specifics of the algorithm used by the *ga* function are in the MATLAB® Help Documentation⁵⁷. By pairing the genetic algorithm with the *fminsearch*, the need of an initial guess is eliminated. The solution to the *ga* function is used as the initial guess for the *fminsearch* function. Thus, the scalar function is first minimized globally, and then the solution is refined locally. The *ga* function does allow for a set of bounds to be prescribed for the unknown variables. Doing so limits the search space and reduces the computation time. By defining these bounds based on the realistic physical constraints of the Minami and Ahuja simulated system, results within ± 1 dB of the actual solution were obtained at all frequencies with the paired *ga* and *fminsearch* routine (trial number 5 in Table 8.1). At this point, a solution of Minami and Ahuja simulation of acceptable accuracy was attainable via the paired routine with physics-based bounds placed on the unknown variables. Attention then turned to solving the five-microphone problem for proof-of-concept experimentation.

8.3.3.2 Solving the Five-Microphone Problem for Model-Scale Testing

Prior to the implementation of the paired *ga* and *fminsearch* routine with physics-based bounds in proof-of-concept experimentation, the paired routine with bounds of

unattainable accuracy was used (trial numbers 6, 7, and 8 in Table 8.1). These bounds were determined from the auto-spectra and cross-spectra magnitude of the buried correlated signals described in the external-source configuration testing of the previous chapter. As mentioned earlier, experiments were run with each driver operating alone, the jet operating alone, and all operating collectively. Testing in this manner provided knowledge of the levels and phases of the buried correlated sources beforehand. Thus, bounds of ± 3 dB, ± 5 dB, and ± 10 dB of the actual solution for the auto-spectra and cross-spectra magnitudes were used. When using bounds of ± 3 dB and ± 5 dB, the accuracy of the results at selected frequencies was ± 2.6 dB and ± 4.7 dB, respectively. These accuracies are only slightly better than that of the bounds. In the case of the ± 10 dB bounds, the code ran for days without reaching a solution indicating that the search space was far too large. The paired routine with physics-based bounds as described in Section 8.2 for proof-of-concept testing was then attempted.

Experiments performed using the external-source configuration depicted in Figure 3.12 were examined at selected frequencies using the paired routine with the physical bounds described earlier. In this case (denoted as trial number 8), results within ± 8 dB of the actual solution were found at selected frequencies. Thus, only a slight improvement had been made. The use of an alternative approach to further limit the search space of the *ga* algorithm was then investigated.

This solution space limiting approach (noted as trials 10 and 11 in Table 8.1) utilized the three-microphone method solution of the system at each microphone. The three-microphone method was used to find the uncorrelated portion of the total signal at each

far-field microphone. The three-microphone solution was used to provide a limited search space for the uncorrelated portion by setting the bounds of the uncorrelated noise auto-spectra in the five-microphone problem to values only slightly less than and greater than the values obtained via the three-microphone method. The bounds of the remaining unknown auto-spectra and the unknown cross-spectra magnitudes were determined using coherence threshold approach and the unknown cross-spectra phases were once again allowed to vary over the entire numerical space. After changing the many options within the MATLAB® *ga* function numerous times, the best results for the experimental data were merely within ± 5 dB of actual solution. Thus, a solution procedure of sufficient accuracy has not been obtained.

In summary, the paired *ga* and *fminsearch* routine with physics-based bounds placed on the unknown variables provides a solution of sufficient accuracy for the numerical simulation outlined in Minami and Ahuja. The physics-based bounds rely on the physical constraints of the radiated sound field and signal analyzer. This method along with many permutations of it has not been successful in solving the five-microphone problem in proof-of-concept testing. A dedicated effort by an expert in the area of solving large systems of non-linear algebraic equations will be required to solve the five-microphone problem.

CHAPTER 9

UNCERTAINTY ANALYSIS

The focus of this chapter is to provide an accurate estimation of the uncertainty involved in predicting sound pressure levels using the three-microphone, coherent output power spectrum, and partial coherence methods. The approach outlined in Coleman and Steele⁵⁸, which is consistent with that outlined in the ANSI/ASME Standard⁵⁹ and the AIAA Standard⁶⁰, is followed in order to gain further understanding regarding the level of confidence in using coherence-based signal processing techniques. In this uncertainty approach, the details of the systematic and random errors in each measured variable are considered and their propagation throughout the experimental results is investigated separately. A brief overview of the procedure is provided below.

Consider the following general data reduction equation

$$r = r(X_1, X_2, \dots, X_J) \quad (9.1)$$

where r is the experimental result determined from J measured variables, X_i , the 95% confidence large sample uncertainty analysis equation is

$$U_r^2 = B_r^2 + R_r^2 \quad (9.2)$$

where

$$B_r^2 = \sum_{i=1}^J \theta_i^2 B_i^2 + 2 \sum_{i=1}^{J-1} \sum_{k=i+1}^J \theta_i \theta_k B_{ik} \quad (9.3)$$

and

$$R_r^2 = \sum_{i=1}^J \theta_i^2 R_i^2 \quad (9.4)$$

In the above equations U_r , B_r , and P_r are the overall uncertainty, systematic uncertainty, and random uncertainty, respectively, for the experimental result, r . B_i and R_i are the systematic uncertainty and random uncertainty, respectively, of the measured variables, X_i . B_{ik} is the covariance estimator for the systematic errors in X_i and X_k , and θ_i is the partial derivative of the experimental result with respect to measured variable X_i .

$$\theta_i = \frac{\partial r}{\partial X_i} \quad (9.5)$$

Before the application of this procedure to the three-microphone method, the coherent output power spectrum, and the partial coherence method is discussed, the systematic and random uncertainties of each measured variable involved is discussed in the next section.

9.1 Uncertainty Involved in Coherence-Based Signal Enhancement Techniques

Table 9.1 provides a list of the systematic and random uncertainty estimates for measured variables used in the three-microphone method, coherent output power spectrum, and partial coherence method. The uncertainty is given for the auto-power spectrum, cross-power spectrum magnitude and coherence estimation; however, since the cross-power spectrum phase can be zero, the associated uncertainty is not normalized. The cross-power spectrum phase standard deviation is utilized in the uncertainty analysis. The function of each of these measured variables and their uncertainty as applied to each of the previously mentioned coherence-based signal processing techniques is discussed in the following sections. In Table 9.1, n_d is the number of ensemble averages and B_{SPL} is the uncertainty as provided by the microphone manufacturer in decibels.

Table 9.1 Uncertainty involved in using coherence-based techniques.

Measured variable, X_i	Systematic uncertainty, B_i	Random uncertainty, R_i
Auto-power spectrum, G_{xx}	$\frac{G_{xx} \ln(10)}{10} B_{SPL}$	$\frac{G_{xx}}{\sqrt{n_d}}$
Cross-power spectrum magnitude, $ G_{xy} $	$\sqrt{\frac{ G_{xy} ^2}{4} \left[\left(\frac{1-\gamma_{xy}^2}{n_d \gamma_{xy}^2} \right)^2 + 2 \left(\frac{\ln(10)}{10} B_{SPL} \right)^2 \right]}$	$\frac{ G_{xy} }{\sqrt{n_d \gamma_{xy}^2}}$
Cross-power spectrum phase, ϕ_{xy}	0; microphones are assumed to be perfectly phase matched	$s.d. = \sqrt{\frac{1-\gamma_{xy}^2}{2n_d \gamma_{xy}^2}}$
Coherence, γ_{xy}^2	$\frac{(1-\gamma_{xy}^2)^2}{n_d}$	$\sqrt{\frac{2\gamma_{xy}^2}{n_d} (1-\gamma_{xy}^2)}$

Before proceeding further, consider the degree of uncertainty in the estimation of the measured variables indicated in Table 9.1. The uncertainty of the auto-power spectra,

cross-power spectra magnitude, and coherence and the standard deviation of the cross-power spectra are plotted in the figures below. The findings illustrated in the figures below are discussed in the following sections.

9.1.1 Auto-Power Spectrum Uncertainty

The normalized systematic and random uncertainties in the auto-power spectra estimates— $B[G_{xx}]/G_{xx}$ and $R[G_{xx}]/G_{xx}$ —are shown as a function of the number of ensemble averages in Figure 9.1. Based on the typical manufacturer statistics for the microphones used in this work, a nominal value of 0.2 dB was used for B_{SPL} . The normalized systematic uncertainty remains constant at a value of 0.046; while the normalized random uncertainty decreases from 0.1 at 100 averages to 0.01 at 10000 averages.

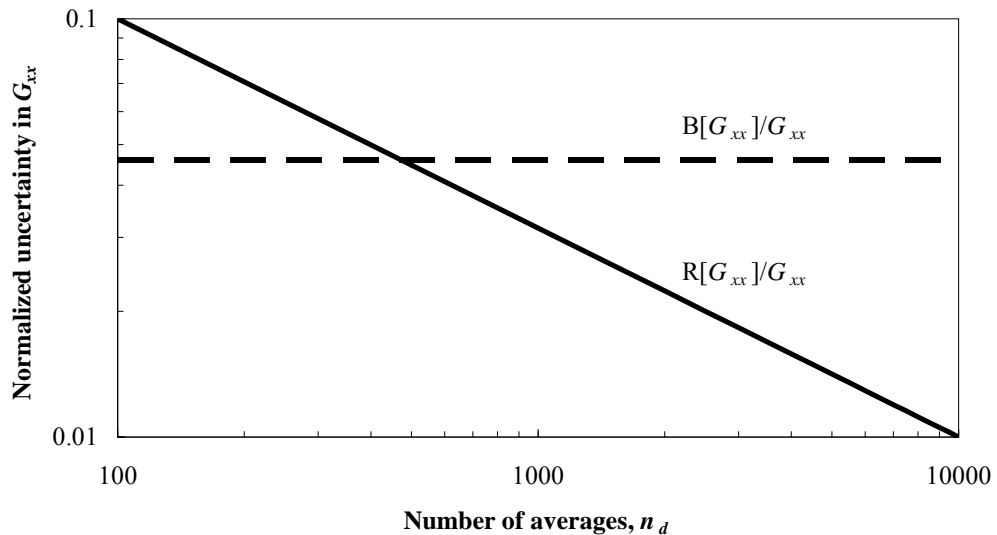


Figure 9.1 Normalized uncertainty of auto-power spectra estimates versus number of averages.

9.1.2 Cross-Power Spectrum Magnitude Uncertainty

In Figure 9.2 and Figure 9.3, the systematic and random uncertainties in the cross-power spectra magnitude measurements are shown, respectively. The uncertainties are calculated for coherence estimates of 0.01, 0.1, 0.4, and 0.8. As the number of averages is increased, the systematic uncertainty in the cross-power spectra magnitude asymptotically approaches a value of 0.065 for all coherence estimates shown in Figure 9.2. The random uncertainty decreases with increased averaging for all coherence function estimates. The uncertainty—both systematic and random—in the cross-power spectra magnitude measurement is increased as the actual measured value of the coherence is decreased.

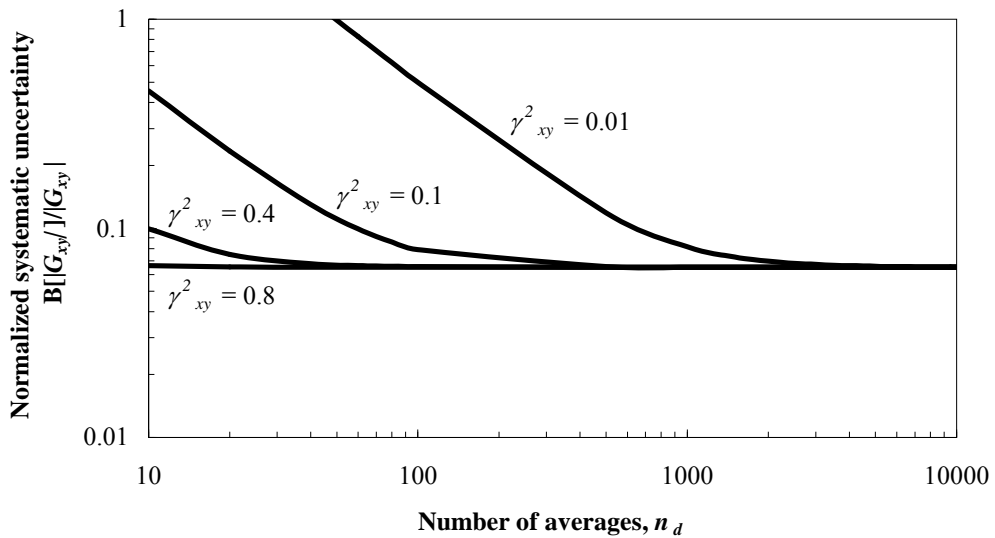


Figure 9.2 Normalized systematic uncertainty of cross-power spectra magnitude estimates versus number of averages.

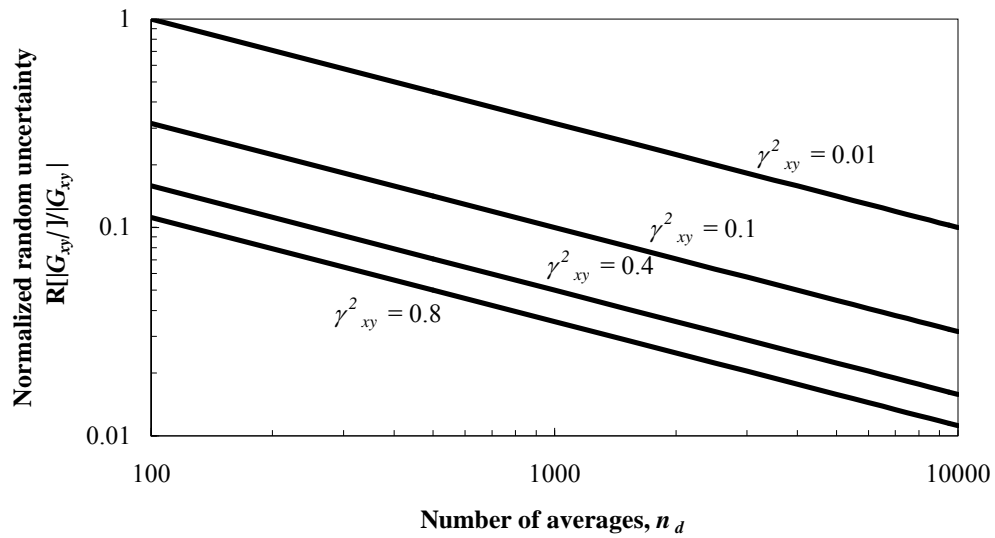


Figure 9.3 Normalized random uncertainty of cross-power spectra magnitude estimates versus number of averages.

9.1.3 Cross-Power Spectrum Phase Uncertainty

The random uncertainty in the cross-power spectra phase measurement is depicted in Figure 9.4. The uncertainty is calculated for coherence estimates of 0.01, 0.1, 0.4, and 0.8. As with the cross-power spectra magnitude, the uncertainty in the cross-power spectra phase decreases with increased averaging, and the uncertainty is most for $\gamma_{xy}^2 = 0.01$ and least for $\gamma_{xy}^2 = 0.8$. Since the microphones are assumed to be phase matched, the systematic uncertainty in the cross-power spectra phase measurement is assumed to be zero.

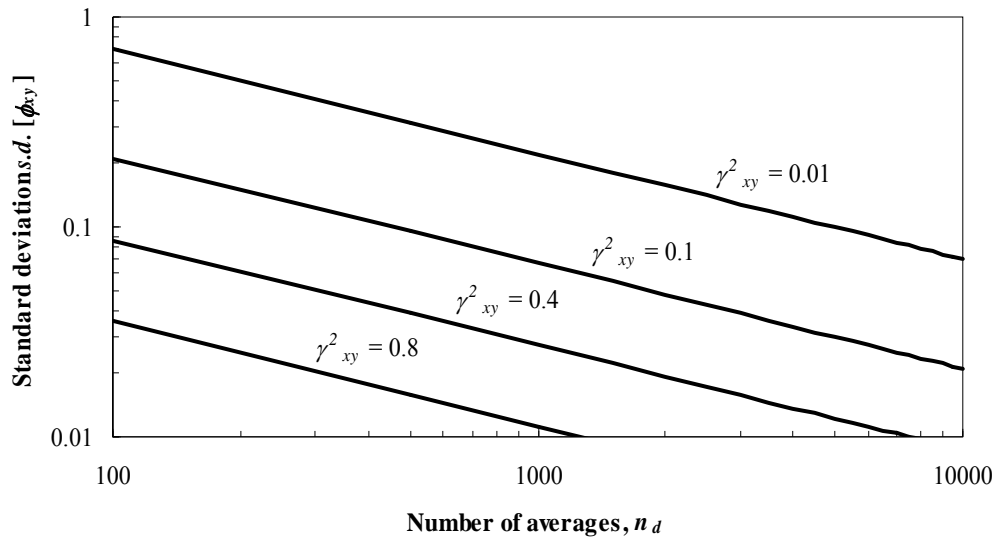


Figure 9.4 Random uncertainty of cross-power spectra phase estimates versus number of averages.

9.1.4 Coherence Estimation Uncertainty

In Figure 9.5 and Figure 9.6, the systematic and random uncertainties in the coherence function estimate are shown, respectively. The uncertainties are calculated for coherence estimates of 0.01, 0.1, 0.4, and 0.8. The uncertainty is most for $\gamma_{xy}^2 = 0.01$ and least when $\gamma_{xy}^2 = 0.8$. The uncertainty—both systematic and random—in the coherence estimation decreases with increased averaging for all values of coherence.

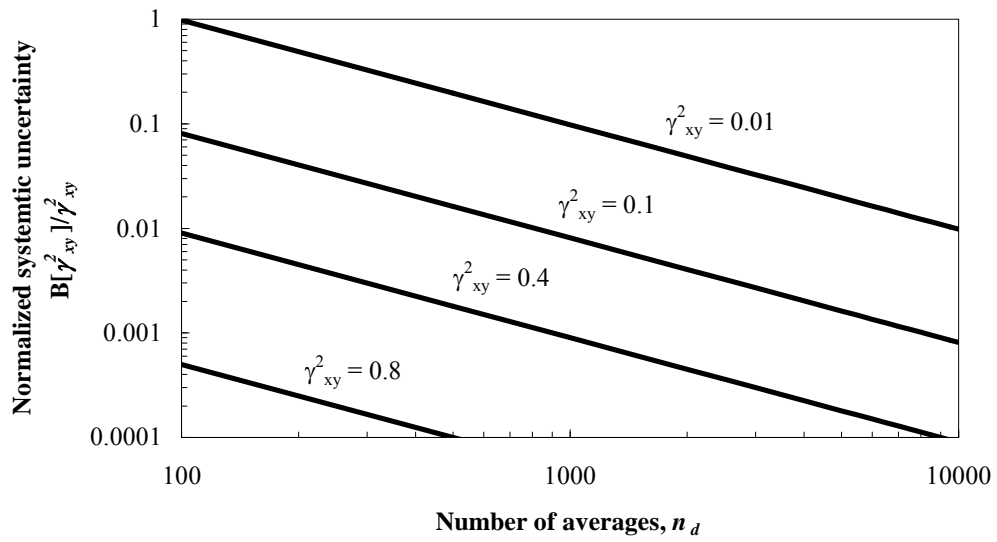


Figure 9.5 Normalized systematic uncertainty of coherence function estimates versus number of averages.

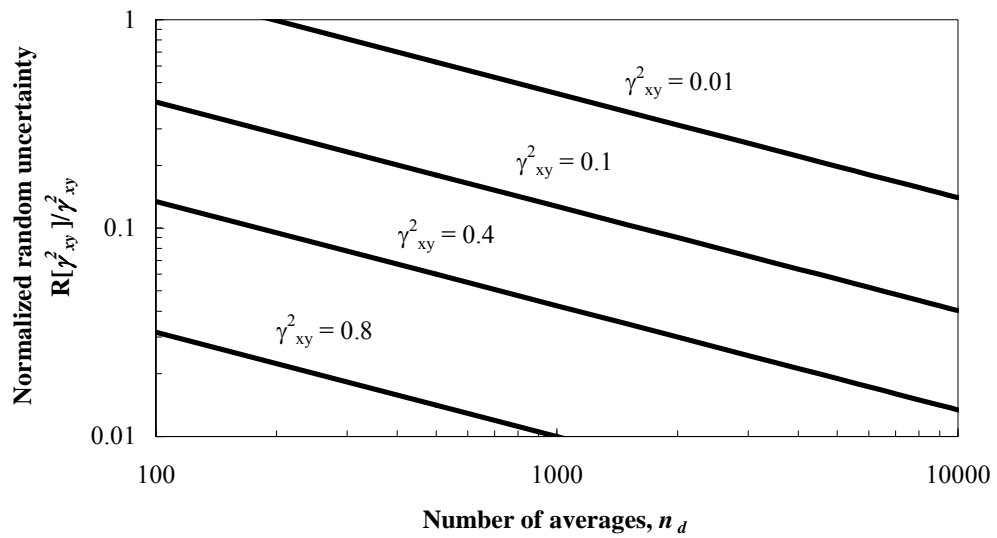


Figure 9.6 Normalized random uncertainty of coherence function estimates versus number of averages.

In the following, sections the uncertainties indicated in the Table 9.1 are applied to the three-microphone method, the coherent output power spectrum, and the partial coherence method. The uncertainty is tracked through each signal enhancement method, and 95% confidence bounds are established for the predicted sound pressure level values at any given frequency.

9.2 Three-Microphone Method Uncertainty

The primary focus of this section is to determine the uncertainty involved in using the three-microphone method to predict correlated and uncorrelated levels within an acoustic system. As discussed in Chapter 2, the three-microphone method utilizes auto-power spectra measured with three far-field microphones along with the coherence between each unique microphone pair to separate the correlated and uncorrelated contributions at each microphone. Consider the diagram of the three-microphone system shown Figure 2.5. Microphones 1, 2, and 3 are assumed to be positioned in the far-field of the radiated sound field, which consists of a single correlated source buried in extraneous uncorrelated noise. The normalized uncertainty in the calculated correlated auto-power spectrum for microphone 1 is given by

$$\frac{U_{G_{u1u1}}}{G_{u1u1}} = \left[\left(\frac{B_{G_{u1u1}}}{G_{u1u1}} \right)^2 + \left(\frac{R_{G_{u1u1}}}{G_{u1u1}} \right)^2 \right]^{0.5} \quad (9.6)$$

Likewise, the normalized random uncertainty in the calculated auto-power spectrum for microphone 1 is given by

$$\frac{U_{G_{nl}nl}}{G_{nl}nl} = \left[\left(\frac{B_{G_{y1y1}}}{G_{y1y1}} \right)^2 + \left(\frac{R_{G_{y1y1}}}{G_{y1y1}} \right)^2 + \left(\frac{U_{G_{ul}ul}}{G_{ul}ul} \right)^2 \right]^{0.5} \quad (9.7)$$

The values on the RHS of the two previous equations are defined by

$$\begin{aligned} B_{G_{ul}ul}^2 &= \theta_{G_{y1y1}}^2 B_{G_{y1y1}}^2 + \theta_{\gamma_{12}}^2 B_{\gamma_{12}}^2 + \theta_{\gamma_{13}}^2 B_{\gamma_{13}}^2 + \theta_{\gamma_{23}}^2 B_{\gamma_{23}}^2 \\ &+ 2 \left(\theta_{G_{y1y1}} \theta_{\gamma_{12}} B_{G_{y1y1}} B_{\gamma_{12}} + \theta_{G_{y1y1}} \theta_{\gamma_{13}} B_{G_{y1y1}} B_{\gamma_{13}} \right) \\ &+ 2 \left(\theta_{\gamma_{12}} \theta_{\gamma_{13}} B_{\gamma_{12}} B_{\gamma_{13}} + \theta_{\gamma_{12}} \theta_{\gamma_{23}} B_{\gamma_{12}} B_{\gamma_{23}} + \theta_{\gamma_{13}} \theta_{\gamma_{23}} B_{\gamma_{13}} B_{\gamma_{23}} \right) \end{aligned} \quad (9.8)$$

$$R_{G_{ul}ul}^2 = \theta_{G_{y1y1}}^2 R_{G_{y1y1}}^2 + \theta_{\gamma_{12}}^2 R_{\gamma_{12}}^2 + \theta_{\gamma_{13}}^2 R_{\gamma_{13}}^2 + \theta_{\gamma_{23}}^2 R_{\gamma_{23}}^2 \quad (9.9)$$

$$\theta_{G_{y1y1}} = \left[\frac{\gamma_{12}^2 \gamma_{13}^2}{\gamma_{23}^2} \right]^{0.5} \quad (9.10)$$

$$\theta_{\gamma_{12}} = \frac{G_{y1y1}}{2} \left[\frac{\gamma_{13}^2}{\gamma_{23}^2 \gamma_{12}^2} \right]^{0.5} \quad (9.11)$$

$$\theta_{\gamma_{13}} = \frac{G_{y1y1}}{2} \left[\frac{\gamma_{12}^2}{\gamma_{23}^2 \gamma_{13}^2} \right]^{0.5} \quad (9.12)$$

and

$$\theta_{\gamma_{23}} = \frac{-G_{y1y1}}{2\gamma_{23}^2} \left[\frac{\gamma_{12}^2 \gamma_{13}^2}{\gamma_{23}^2} \right]^{0.5} \quad (9.13)$$

After substituting the necessary estimates from Table 9.1 into the series of equations above and normalizing, the normalized uncertainty for calculated correlated and uncorrelated auto-power spectrum for microphone I is given by

$$\frac{U_{G_{ulul}}}{G_{ulul}} = \left[\left(\frac{B_{G_{ulul}}}{G_{ulul}} \right)^2 + \left(\frac{R_{G_{ulul}}}{G_{ulul}} \right)^2 \right]^{0.5} \quad (9.14)$$

and

$$\frac{U_{G_{nlnl}}}{G_{nlnl}} = \left[\left(\frac{G_{ylyl}}{G_{nlnl}} \right)^2 \left(\left(\frac{\ln(10)}{10} B_{SPL} \right)^2 + \frac{1}{n_d} \right) + \left(\frac{G_{ulul}}{G_{nlnl}} \right) \left(\frac{U_{G_{ulul}}}{G_{ulul}} \right)^2 \right]^{0.5} \quad (9.15)$$

where

$$\left(\frac{B_{G_{ulul}}}{G_{ulul}} \right)^2 = \left(\frac{\ln(10)}{10} B_{SPL} \right)^2 + \frac{1}{4} \cdot \begin{bmatrix} \left(\frac{1-\gamma_{12}^2}{n_d \gamma_{12}^2} \right)^2 \\ \left(\frac{1-\gamma_{13}^2}{n_d \gamma_{13}^2} \right)^2 \\ \left(\frac{1-\gamma_{23}^2}{n_d \gamma_{23}^2} \right)^2 \end{bmatrix} + \frac{1}{2} \cdot \begin{bmatrix} \left(\frac{(1-\gamma_{12}^2)^2}{n_d \gamma_{12}^2} \right) \left(\frac{(1-\gamma_{13}^2)^2}{n_d \gamma_{13}^2} \right) \\ - \left(\frac{(1-\gamma_{12}^2)^2}{n_d \gamma_{12}^2} \right) \left(\frac{(1-\gamma_{23}^2)^2}{n_d \gamma_{23}^2} \right) \\ - \left(\frac{(1-\gamma_{13}^2)^2}{n_d \gamma_{13}^2} \right) \left(\frac{(1-\gamma_{23}^2)^2}{n_d \gamma_{23}^2} \right) \end{bmatrix} + \left(\frac{\ln(10)}{10} B_{SPL} \right) \cdot \begin{bmatrix} \left(\frac{(1-\gamma_{12}^2)^2}{n_d \gamma_{12}^2} \right) \\ \left(\frac{(1-\gamma_{13}^2)^2}{n_d \gamma_{13}^2} \right) \end{bmatrix} \quad (9.16)$$

$$\left(\frac{R_{G_{ulul}}}{G_{ulul}} \right)^2 = \left(\frac{1}{\sqrt{n_d}} \right)^2 + \frac{1}{4} \left(\left(\frac{\sqrt{2}(1-\gamma_{12}^2)}{\sqrt{n_d} \gamma_{12}^2} \right)^2 + \left(\frac{\sqrt{2}(1-\gamma_{13}^2)}{\sqrt{n_d} \gamma_{13}^2} \right)^2 + \left(\frac{\sqrt{2}(1-\gamma_{23}^2)}{\sqrt{n_d} \gamma_{23}^2} \right)^2 \right) \quad (9.17)$$

$$\frac{G_{ylyl}}{G_{nlnl}} = \frac{1}{1-10^{\log_{10} \left(\frac{1}{1+10^{\frac{\Delta dB}{10}}} \right)}} \quad (9.18)$$

$$\frac{G_{ulul}}{G_{nlnl}} = 10^{\frac{-\Delta dB}{10}} \quad (9.19)$$

and ΔdB is the difference in the uncorrelated and correlated sound pressure levels as calculated by

$$\Delta dB_1 = SPL_{n1n1}(\text{in dB}) - SPL_{u1u1}(\text{in dB}) \quad (9.20)$$

Similarly, for microphones 2 and 3 the normalized uncertainty in the calculated correlated and uncorrelated results are given by

$$\frac{U_{G_{u2u2}}}{G_{u2u2}} = \left[\left(\frac{B_{G_{u2u2}}}{G_{u2u2}} \right)^2 + \left(\frac{R_{G_{u2u2}}}{G_{u2u2}} \right)^2 \right]^{0.5} \quad (9.21)$$

$$\frac{U_{G_{n2n2}}}{G_{n2n2}} = \left[\left(\frac{G_{y2y2}}{G_{n2n2}} \right)^2 \left(\left(\frac{\ln(10)}{10} B_{SPL} \right)^2 + \frac{1}{n_d} \right) + \left(\frac{G_{u2u2}}{G_{n2n2}} \right) \left(\frac{U_{G_{u2u2}}}{G_{u2u2}} \right)^2 \right]^{0.5} \quad (9.22)$$

$$\frac{U_{G_{u3u3}}}{G_{u3u3}} = \left[\left(\frac{B_{G_{u3u3}}}{G_{u3u3}} \right)^2 + \left(\frac{R_{G_{u3u3}}}{G_{u3u3}} \right)^2 \right]^{0.5} \quad (9.23)$$

and

$$\frac{U_{G_{n3n3}}}{G_{n3n3}} = \left[\left(\frac{G_{y3y3}}{G_{n3n3}} \right)^2 \left(\left(\frac{\ln(10)}{10} B_{SPL} \right)^2 + \frac{1}{n_d} \right) + \left(\frac{G_{u3u3}}{G_{n3n3}} \right) \left(\frac{U_{G_{u3u3}}}{G_{u3u3}} \right)^2 \right]^{0.5} \quad (9.24)$$

where

$$\left(\frac{B_{G_{u2u2}}}{G_{u2u2}} \right)^2 = \left(\frac{\ln(10)}{10} B_{SPL} \right)^2 + \frac{1}{4} \cdot \begin{bmatrix} \left(\frac{1-\gamma_{12}^2}{n_d \gamma_{12}^2} \right)^2 \\ \left(\frac{1-\gamma_{13}^2}{n_d \gamma_{13}^2} \right)^2 \\ \left(\frac{1-\gamma_{23}^2}{n_d \gamma_{23}^2} \right)^2 \end{bmatrix} + \frac{1}{2} \cdot \begin{bmatrix} - \left(\frac{1-\gamma_{12}^2}{n_d \gamma_{12}^2} \right) \left(\frac{1-\gamma_{13}^2}{n_d \gamma_{13}^2} \right) \\ \left(\frac{1-\gamma_{12}^2}{n_d \gamma_{12}^2} \right) \left(\frac{1-\gamma_{23}^2}{n_d \gamma_{23}^2} \right) \\ - \left(\frac{1-\gamma_{13}^2}{n_d \gamma_{13}^2} \right) \left(\frac{1-\gamma_{23}^2}{n_d \gamma_{23}^2} \right) \end{bmatrix} + \left(\frac{\ln(10)}{10} B_{SPL} \right) \cdot \left[\frac{(1-\gamma_{12}^2)^2}{n_d \gamma_{12}^2} \right] \quad (9.25)$$

$$\left(\frac{B_{G_{u3u3}}}{G_{u3u3}}\right)^2 = \left(\frac{\ln(10)}{10} B_{SPL}\right)^2 + \frac{1}{4} \bullet \left[\begin{array}{c} \left(\frac{1-\gamma_{12}^2}{n_d \gamma_{12}^2}\right)^2 \\ \left(\frac{1-\gamma_{13}^2}{n_d \gamma_{13}^2}\right)^2 \\ \left(\frac{1-\gamma_{23}^2}{n_d \gamma_{23}^2}\right)^2 \end{array} \right] + \frac{1}{2} \bullet \left[\begin{array}{c} -\left(\frac{(1-\gamma_{12}^2)^2}{n_d \gamma_{12}^2}\right) \left(\frac{(1-\gamma_{13}^2)^2}{n_d \gamma_{13}^2}\right) \\ -\left(\frac{(1-\gamma_{12}^2)^2}{n_d \gamma_{12}^2}\right) \left(\frac{(1-\gamma_{23}^2)^2}{n_d \gamma_{23}^2}\right) \\ -\left(\frac{(1-\gamma_{13}^2)^2}{n_d \gamma_{13}^2}\right) \left(\frac{(1-\gamma_{23}^2)^2}{n_d \gamma_{23}^2}\right) \end{array} \right] + \left(\frac{\ln(10)}{10} B_{SPL}\right) \bullet \left[\begin{array}{c} \left(\frac{(1-\gamma_{13}^2)^2}{n_d \gamma_{13}^2}\right) \\ \left(\frac{(1-\gamma_{23}^2)^2}{n_d \gamma_{23}^2}\right) \end{array} \right] \quad (9.26)$$

$$\left(\frac{R_{G_{u2u2}}}{G_{u2u2}}\right)^2 = \left(\frac{R_{G_{u3u3}}}{G_{u3u3}}\right)^2 = \left(\frac{R_{G_{u1u1}}}{G_{u1u1}}\right)^2 = \left(\frac{1}{\sqrt{n_d}}\right)^2 + \frac{1}{4} \left(\left(\frac{\sqrt{2}(1-\gamma_{12}^2)}{\sqrt{n_d} \gamma_{12}^2}\right)^2 + \left(\frac{\sqrt{2}(1-\gamma_{13}^2)}{\sqrt{n_d} \gamma_{13}^2}\right)^2 + \left(\frac{\sqrt{2}(1-\gamma_{23}^2)}{\sqrt{n_d} \gamma_{23}^2}\right)^2 \right) \quad (9.27)$$

$$\frac{G_{y2y2}}{G_{n2n2}} = \frac{1}{1-10^{\log_{10}\left(\frac{1}{1+10^{\frac{\Delta dB_2}{10}}}\right)}} \quad (9.28)$$

$$\frac{G_{y3y3}}{G_{n3n3}} = \frac{1}{1-10^{\log_{10}\left(\frac{1}{1+10^{\frac{\Delta dB_3}{10}}}\right)}} \quad (9.29)$$

$$\frac{G_{u2u2}}{G_{n2n2}} = 10^{\frac{-\Delta dB_2}{10}} \quad (9.30)$$

$$\frac{G_{u3u3}}{G_{n3n3}} = 10^{\frac{-\Delta dB_3}{10}} \quad (9.31)$$

ΔdB_1 and ΔdB_2 are the difference in the uncorrelated and correlated sound pressure levels as calculated by

$$\Delta dB_2 = SPL_{n2n2}(\text{in } dB) - SPL_{u2u2}(\text{in } dB) \quad (9.32)$$

and

$$\Delta dB_3 = SPL_{n3n3}(\text{in } dB) - SPL_{u3u3}(\text{in } dB) \quad (9.33)$$

The upper and lower uncertainty bounds of 95% confidence for data processed using the three-microphone method is given via the following equations

$$SPL_{upper} = 10 \log_{10}(1 + \bar{U}) \quad (9.34)$$

and

$$SPL_{lower} = 10 \log_{10}(1 - \bar{U}) \quad (9.35)$$

where \bar{U} is the normalized uncertainty as calculated via the procedure outlined above. The findings from this uncertainty analysis are reported below.

Once again consider the diagram of the three-microphone system shown Figure 2.5. Microphones 1, 2, and 3 are assumed to be located in the far-field at adjacent positions separated by some arbitrary distance. The microphone separation is assumed constant; thus the separation between microphones 1 and 2 and microphones 2 and 3 are equal and one-half of that between microphones 1 and 3. Based on typical coherence values found in jet noise experiments conducted as a part of this investigation, typical values for coherences $\gamma^2_{(1, 2)}$, $\gamma^2_{(1, 3)}$, and $\gamma^2_{(2, 3)}$ are assumed to vary between 0.01 and 1.0. The error in the calculation of the correlated sound pressure level at each of the three microphones is determined as a function of the measured coherence between the microphone pair with the largest spacing, $\gamma^2_{(1, 3)}$. The role of the relative coherence levels between all microphone pairs and the effect of the relative sound pressure level of the correlated and uncorrelated signals are investigated. From this point forward, the notation [1, 2], [1, 3],

and [2, 3] will be used when referring to microphone pairs 1 and 2, 1 and 3, and 2 and 3, respectively.

9.2.1 Effect of Relative Coherence Levels

The findings from the study on the effect of relative coherence levels between all microphone pairs indicate that the error in using the three-microphone method can be large if the measured coherence between microphones 1 and 3 is substantially less than that measured at pairs [1, 2] and [2, 3]. Such instances occur at extremely low values of coherence measured at pair [1, 3]. Furthermore, the error remains nearly constant for coherence values at pair [1, 3] that are larger than 0.1. This nearly constant error decreases as the coherence for pairs [1, 2] and [2, 3] increases from 0.01 to 0.9. Also, the results at microphones 1 and 3 are identical; thus, the results shown in Figure 9.7 (a) and (c) are representative of both microphones.

The multiple curves of the Figure 9.7 are formed by assuming the coherence for microphone pairs [1, 2] and [2, 3] varies between 0.01 and 0.9. Arbitrary values of 0.01, 0.1, 0.3, 0.5, and 0.9 are shown in Figure 9.7. As described above the microphones are spaced equally apart; thus, the coherence values at microphone pairs [1, 2] and [2, 3] are assumed to be equal. This will be exactly correct if the noise generation mechanism acts as a point source. However, in most experiments the point source assumption is not entirely accurate, but for the purposes of assigning value to the coherence at pairs [1, 2] and [2, 3] in this uncertainty analysis the point source assumption is acceptable. Since the primary interest of this work is educating a buried correlated signal using the three-microphone method, the uncorrelated noise is arbitrarily assumed to be 3 dB louder than

the correlated noise at each microphone. As indicated above the uncertainty relation for the correlated value has no mention of ΔdB ; thus, the choice of 3 dB has no effect on the correlated uncertainty; it only affects the uncorrelated uncertainty.

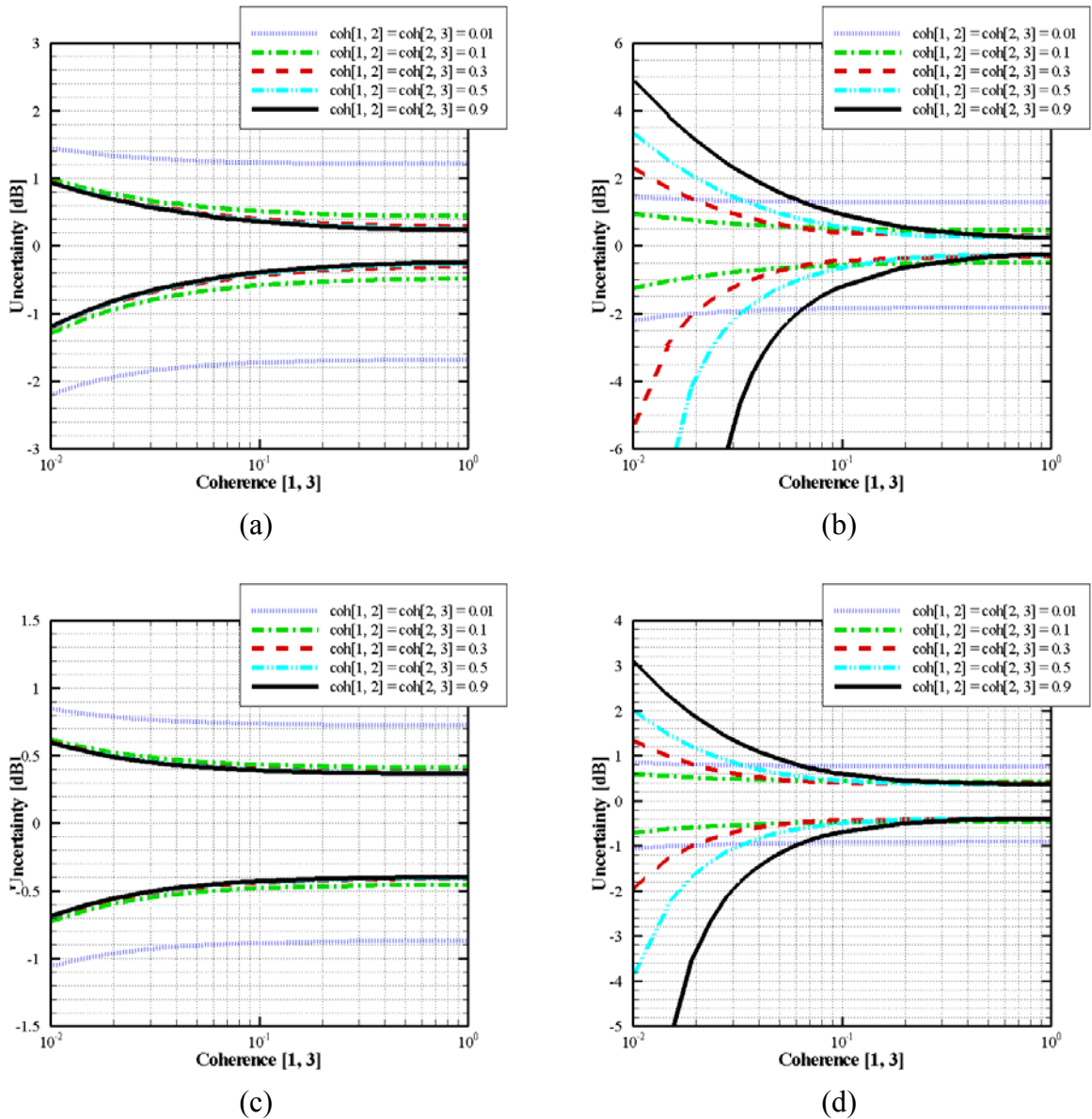


Figure 9.7 Uncertainty in the calculated correlated results obtained using the three-microphone method at (a) microphones 1 and 3 and (b) microphone 2 and uncertainty in the calculated uncorrelated results at (c) microphones 1 and 3 and (d) microphone 2 respective to $\gamma_{(1,3)}^2$.

To examine the uncertainty in the correlated plots—Figure 9.7 (a) and (b)—more closely, first consider the portions where the measured coherence between microphones 1 and 3 is greater than 0.1 (i.e., the regions where the curves are almost horizontal). For all microphones, the most widely spaced error bands result from the lowest measured coherence between microphone pairs [1, 2] and [2, 3]— $\gamma^2_{(1,2)} = \gamma^2_{(2,3)} = 0.01$. The upper bound of the error is approximately 1.3 dB, while the lower bound is nearly -1.9 dB. Such a case where $\gamma^2_{(1,3)} = 0.1$ and $\gamma^2_{(1,2)} = \gamma^2_{(2,3)} = 0.01$ is not likely to occur in full-scale engine testing due to the physical nature of the radiated sound. Since microphones 1 and 3 are assumed to be the largest spaced pair, signals measured at [1, 3] are expected to exhibit less coherence than that measured at microphone pairs [1, 2] and [2, 3]. Thus the points on the plots where $\gamma^2_{(1,3)} > \gamma^2_{(1,2)} = \gamma^2_{(2,3)}$ are physically unlikely to occur in actual testing. The same argument can be applied to the remaining curves. Nonetheless, the error tends to decrease as the measured coherence at microphone pairs [1, 2] and [2, 3] is increased. The most closely spaced set of bounds for results calculated at microphones 1 and 3 occurs when $\gamma^2_{(1,2)} = \gamma^2_{(2,3)} = 0.9$. The bounds are approximately ± 0.4 dB at $\gamma^2_{(1,3)} = 0.1$, and they narrow to ± 0.25 dB at $\gamma^2_{(1,3)} = 0.9$. The value of coherence at pairs [1, 2] and [2, 3] that results in smallest error for the data calculated at microphone 2 varies depending upon the value of the coherence at pair [1, 3]. At $\gamma^2_{(1,3)} = 0.1$, the minimum error is ± 0.45 dB, which results from $\gamma^2_{(1,2)} = \gamma^2_{(2,3)} = 0.3$. The minimum error at $\gamma^2_{(1,3)} = 0.9$ occurs when $\gamma^2_{(1,2)} = \gamma^2_{(2,3)} = 0.9$. This error is ± 0.25 dB.

Now consider the portions where $\gamma^2_{(1,3)} < 0.1$. In this region, the results at microphones 1 and 3 differ dramatically from those at microphone 2. For microphones 1 and 3, in all

instances the error is the largest as the coherence for pair [1, 3] approaches 0.01. The largest error occurs when $\gamma^2_{(1,2)} = \gamma^2_{(2,3)} = 0.01$; the upper bound is 1.5 dB, and the lower bound is -2.2 dB. For microphone 2, the maximum positive error occurs when $\gamma^2_{(1,2)} = \gamma^2_{(2,3)} = 0.9$. As for the largest negative error, it occurs when $\gamma^2_{(1,2)} = \gamma^2_{(2,3)} > 0.3$; this error asymptotically approaches negative infinity at a given value of the measured coherence for pair [1, 3]. The asymptote lies at increasingly larger values of $\gamma^2_{(1,3)}$ as $\gamma^2_{(1,2)} = \gamma^2_{(2,3)}$ is increased. The ratio of the coherence at pairs [1, 2] (recall that $\gamma^2_{(1,2)} = \gamma^2_{(2,3)}$) and [1, 3] is approximately 42 at each asymptote where the negative error bound approaches minus infinity. This indicates that given a three-microphone system where the ratio of the coherence of the closest spaced microphones to that of the largest spaced microphones exceeds 42 the three-microphone method results can be extremely erroneous. In fact to maintain error bounds of ± 1 dB for microphone 2, this ratio should be less than 8.

Results following similar patterns were obtained for the calculated uncorrelated sound pressure level at each microphone—Figure 9.7 (c) and (d). In all instances excluding those where the error in the calculated correlated level tends to minus infinity, the error in the calculated uncorrelated level is within ± 1.1 dB. This leads to the conclusion that errors in the calculated uncorrelated levels are less substantial than those of the calculated correlated levels. The uncertainty in the uncorrelated results in the region where $\gamma^2_{(1,3)} < 0.1$ follows patterns much like that of the correlated uncertainty. This error approaches minus infinity for $\gamma^2_{(1,2)} = \gamma^2_{(2,3)} > 0.5$.

9.2.2 Effect of Relative Sound Pressure Levels

As stated earlier, the uncertainty in calculated correlated sound pressure level is unchanged at all microphones by varying the relative level between the correlated and uncorrelated signals. Once again, the results at microphones 1 and 3 are identical; thus, the plot (a) of Figure 9.8 is representative of both. The results depicted in Figure 9.8 were generated by fixing the measured coherence $\gamma^2_{(1,2)}$ and $\gamma^2_{(2,3)}$ at values of 0.5. In choosing 0.5, the results depicted in Figure 9.7 were considered. Since the error is large for $\gamma^2_{(1,2)} = \gamma^2_{(2,3)} = 0.01$ and a coherence of 0.01 is seemingly unrealistic for values of $\gamma^2_{(1,3)} > 0.01$ in actual testing, 0.5 was arbitrarily chosen from the remaining values. The difference in the uncorrelated and correlated signal levels were allowed to vary from 0 dB to 10 dB.

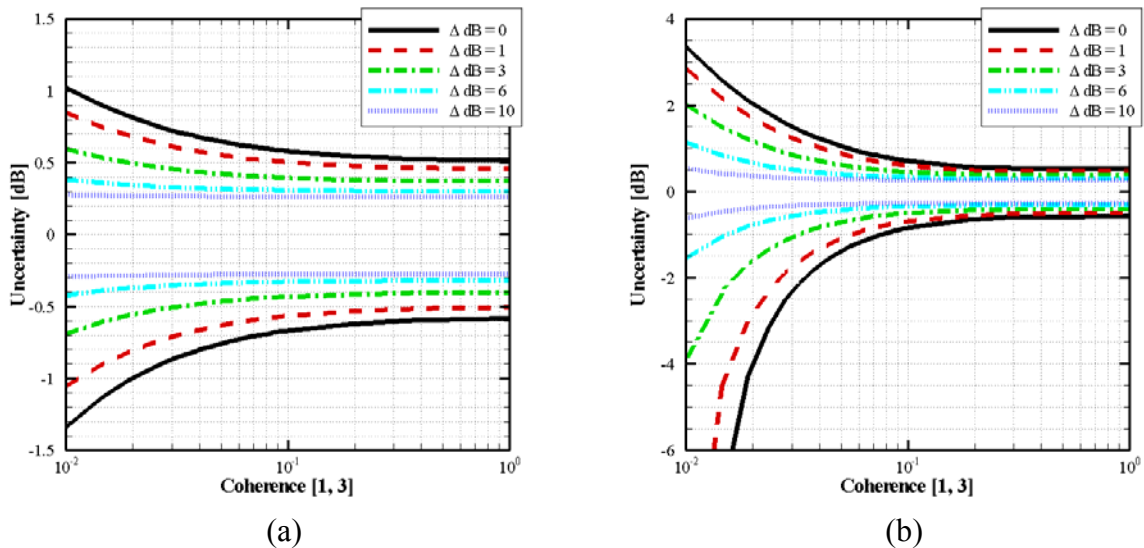


Figure 9.8 Calculated uncorrelated uncertainty at (a) microphones 1 and 3 and (b) microphone 2 relative to $\gamma^2_{(1,3)}$.

In Figure 9.8, the uncertainty in the uncorrelated results exhibits dependency upon the relative sound pressure level of the correlated and uncorrelated signals. As the relative SPL difference between the signals (ΔdB) is increased the uncertainty tends to decrease for all values of $\gamma^2_{(1, 3)}$. The smallest uncertainty in the uncorrelated results at all microphones occurs at $\Delta dB = 10$; while the largest uncertainty occurs when the correlated and uncorrelated levels are equivalent. The uncertainty in the calculated uncorrelated sound pressure level at microphones 1 and 3 is within ± 0.7 dB in all instances where $\gamma^2_{(1, 3)} > 0.1$. At microphone 2, results with accuracies within ± 0.9 dB can be expected for cases where $\gamma^2_{(1, 3)} > 0.1$. For $\Delta dB < 3$, the uncorrelated uncertainty at microphone 2 asymptotically tends to minus infinity as the coherence between pair [1, 3] approaches its minimum value. Results consistent with those reported above were obtained for the remaining coherence values.

The results shown in the previous sections indicate that the uncertainty in calculated correlated sound pressure levels is entirely dependent upon the relative coherence levels between each microphone pair. In all instances, the uncertainty becomes more significant as the measured coherence between the largest spaced microphone pair approaches its minimum value. In some cases, the lower error bound for the calculated results approaches minus infinity. In the following section, this uncertainty analysis is applied to previously reported three-microphone method results in order to provide further validation of the accuracy of the results.

9.2.3 Uncertainty Applied to Three-Microphone Method Experiments

In Chapters 6 and 7, the three-microphone method was applied to aeroacoustic systems consisting one and two correlated source(s) buried in uncorrelated jet noise. The results of this experimentation and analysis indicate the three-microphone method works well when a single correlated source is present at a given frequency within the spectra. However, when two correlated sources are present the method fails to adequately reduce the sources either source. The results of this experimentation are duplicated below with the addition of error bars generated via the procedures outline above. Plots (a) and (b) of Figure 9.9 illustrate three-microphone findings at the 60-degree microphone for systems consisting of a single correlated source buried in uncorrelated jet noise produced by a 1.6-inch conical round nozzle operated at Mach 0.62. In both plots the measured driver level (*A only* or *B only*) lies within the 95% confidence interval for all calculated correlated data. Thus, one can be fairly confident in the accuracy of the three-microphone method when utilized under such circumstances.

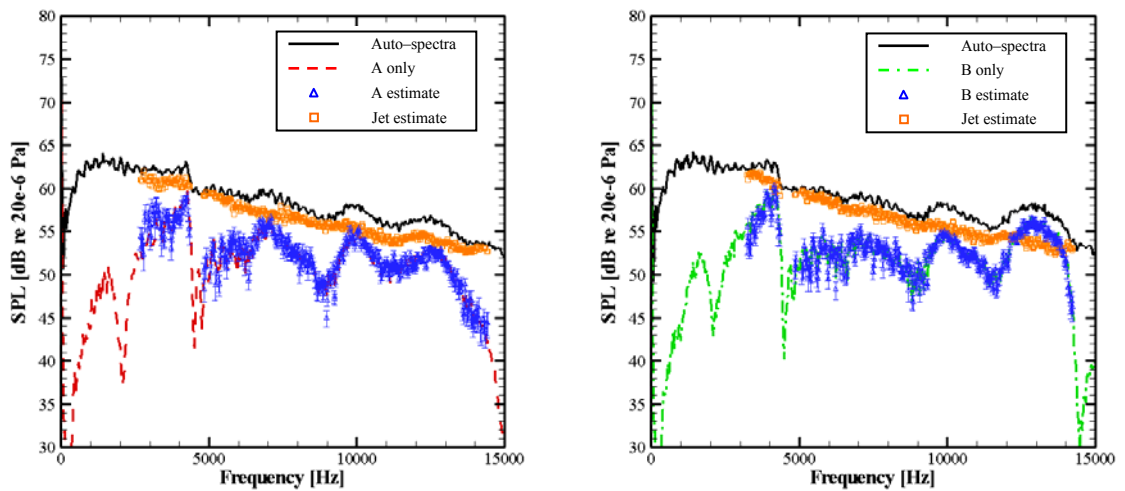


Figure 9.9 Typical three-microphone method results (a single correlated source) with 95% confidence interval uncertainty bars applied.

In Figure 9.10, the results depict three-microphone method results at the 60-degree microphone for a system with two correlated sources buried uncorrelated jet noise produced and 1.6-inch conical round nozzle operated at Mach 0.62. The 95% confidence uncertainty intervals are quite large in the frequency regions where the sources are operated at comparable levels. Furthermore, in some spectral regions the measured levels lie completely outside of the uncertainty intervals. Hence, the lack of confidence indicated in Chapters 6 and 7 concerning these results is once again exhibited

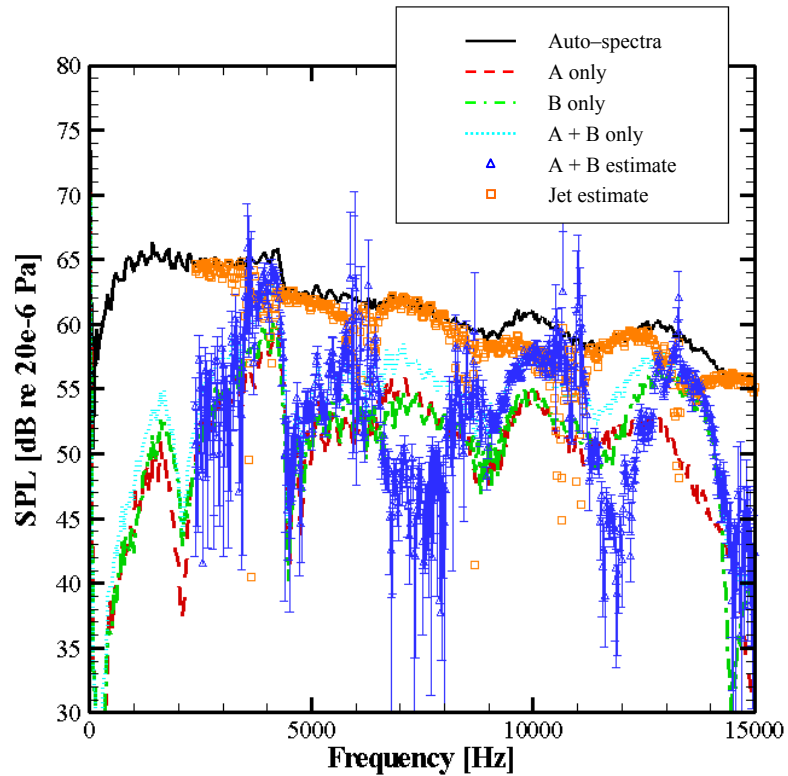


Figure 9.10 Typical three-microphone method results (two correlated sources) with 95% confidence interval uncertainty bars applied.

9.3 Coherent Output Power Spectrum

As discussed in Chapter 2, the coherent output power spectrum utilizes at least two microphones—one in the far-field and another positioned such that its signal is dominated by the correlated source of interest. The coherent output power at the far-field microphone is the product measured far-field auto-power spectrum and the measured coherence between the microphone pair. Consider the diagram shown in Figure 2.4. Microphone 1 is assumed to be positioned in the far-field, and microphone 2 is assumed to be positioned near the source of interest. The normalized uncertainty in the predicted coherent output power spectrum and microphone 1 is given by

$$\frac{U_{COP}}{G_{COP}} = \left[\left(\frac{B_{G_{y1y1}}}{G_{y1y1}} \right)^2 + \left(\frac{R_{G_{y1y1}}}{G_{y1y1}} \right)^2 + \left(\frac{B_{\gamma_{12}^2}}{\gamma_{12}^2} \right)^2 + \left(\frac{R_{\gamma_{12}^2}}{\gamma_{12}^2} \right)^2 \right]^{0.5} \quad (9.36)$$

Upon substituting the appropriate values from Table 9.1 in the above equation, the uncertainty becomes

$$\frac{U_{COP}}{G_{COP}} = \left[\left(\frac{\ln(10)}{10} B_{SPL} \right)^2 + \left(\frac{1}{\sqrt{n_d}} \right)^2 + \left(\frac{(1-\gamma_{12}^2)}{n_d \gamma_{12}^2} \right)^2 + \left(\frac{\sqrt{2}(1-\gamma_{12}^2)}{\sqrt{n_d} \gamma_{12}^2} \right)^2 \right]^{0.5} \quad (9.37)$$

The upper and lower uncertainty bounds of 95% confidence for data processed using the coherent output power spectrum is given via the following equations

$$SPL_{upper} = 10 \log_{10} \left(1 + \frac{U_{COP}}{COP} \right) \quad (9.38)$$

and

$$SPL_{lower} = 10 \log_{10} \left(1 - \frac{U_{COP}}{COP} \right) \quad (9.39)$$

The findings from the uncertainty analysis of the coherent output power spectrum are illustrated in Figure 9.11. Arbitrary values of 0.01, 0.1, 0.3, 0.5, and 0.9 were assigned to $\gamma_{(1,2)}^2$, and the uncertainty in the coherent output power spectrum at microphone 1 was calculated as a function of the number of averages (n_d) for each coherence estimate.

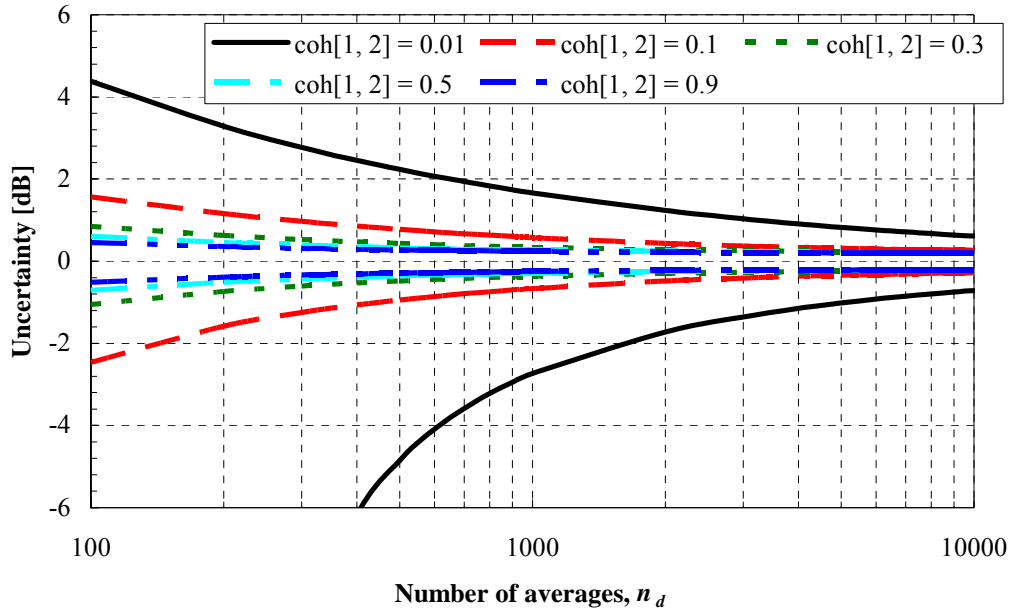


Figure 9.11 Coherent output power uncertainty versus number of averages.

In Figure 9.11, the largest error exists for $\gamma^2_{(1, 2)} = 0.01$; while the smallest uncertainty occurs when $\gamma^2_{(1, 2)} = 0.9$. The coherent output power uncertainty is highly dependent upon the level of coherence between the correlating microphones. Furthermore, since the uncertainty in the coherence estimate is largely dependent upon the number of averages, one would expect the coherent output power uncertainty to demonstrate similar dependency upon the number averages. The results shown in Figure 9.11 are consistent with the previous statements. In all instances, the coherent output power uncertainty increases with decreased averaging, which is identical to the behavior of the uncertainty in the coherence estimate. Excluding the $\gamma^2_{(1, 2)} = 0.01$ case, the uncertainty in the coherent output power spectrum lies within roughly ± 2 dB for averaging that exceeds 100. As for the $\gamma^2_{(1, 2)} = 0.01$ case, the uncertainty becomes quite large as the averaging is

decreased. In fact, it approaches minus infinity for averages less than 300. This is due to the significant uncertainty in estimated coherence with such reduced averaging.

The coherent output power spectrum uncertainty has been applied to data shown in Chapter 7. The findings of this application are reported in Figure 9.12 and Figure 9.13. Plots (a) and (b) of the former illustrate coherent output power spectrum findings at the 60-degree microphone for systems consisting of a single correlated source buried in uncorrelated jet noise produced by a 1.6-inch conical round nozzle operated at Mach 0.68. In both plots the measured driver level (*A only* or *B only*) lies above the 95% confidence interval for all calculated data. This reemphasizes the under-prediction of the true level in this particular system by the coherent output power spectrum. In Figure 9.13, the results depict coherent output power results at the 60-degree microphone for a system with two correlated sources buried within uncorrelated jet noise produced and 1.6-inch conical round nozzle operated at Mach 0.68. Similar to the single correlated driver cases of Figure 9.12, the measured driver level (*A only* or *B only*) lies above the 95% confidence interval for all calculated data in Figure 9.13.

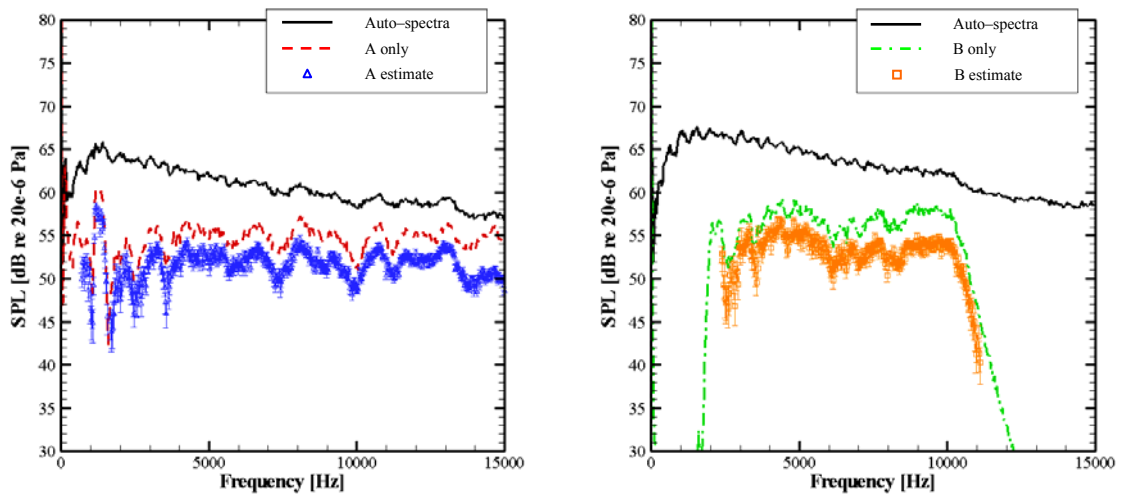


Figure 9.12 Typical coherent output power spectrum results (a single correlated source) with 95% confidence interval uncertainty bars applied.

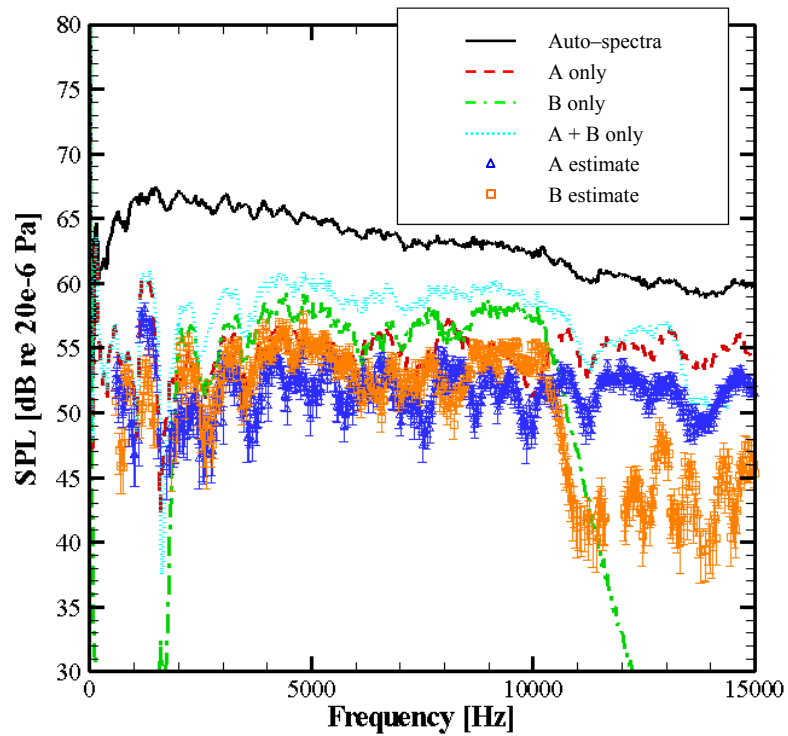


Figure 9.13 Typical coherent output power spectrum results (two correlated sources) with 95% confidence interval uncertainty bars applied.

9.4 Partial Coherence Method

The uncertainty analysis outlined in Coleman and Steele⁵⁸ was also applied the partial coherence method analysis detailed in Chapter 2. Due to the limited use of the partial coherence method in this work and the complexity of the equations involved, the details of the uncertainty analysis have been omitted. The primary goal here is not to provide a detailed explanation as to the derivation of the uncertainty results but rather to show the impact of the analysis on typical measured data. In Figure 9.14, the uncertainty analysis has been applied to representative partial coherence method findings for a system where two correlated sources are buried in uncorrelated jet noise produced by a Mach 0.5 jet exhausting from a 1.6-inch conical round nozzle. Much like the coherent output power results shown above, the 95% confidence partial coherence uncertainty intervals for the data labeled *PCM: SPL_u* all lie below the true level of the source to which microphones 1 and 2 are located nearest. The uncertainty intervals are quite large for the data labeled *PCM: SPL_k*. Furthermore, the measured levels lie completely outside of the uncertainty intervals in some spectral regions.

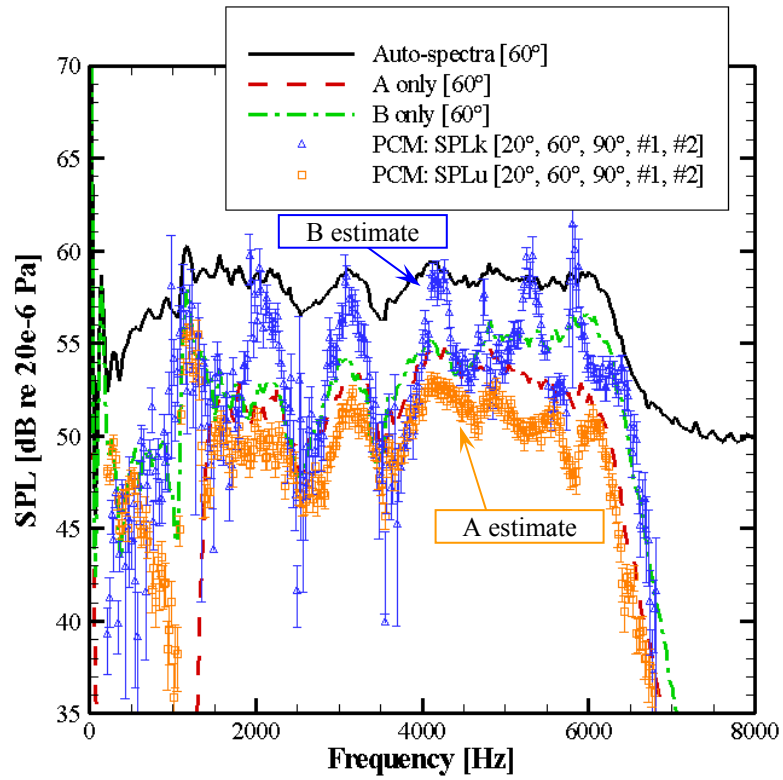


Figure 9.14 Typical partial coherence method results with 95% confidence interval uncertainty bars applied.

CHAPTER 10

CONCLUSION

The two noise source model claims that the radiated jet noise is composed of two distinct sources—one associated with the small-scale turbulence and another associated with the large-scale turbulence. The former source is claimed to radiate noise predominantly at larger angles with respect to the jet axis, whereas the large-scale turbulence radiates predominantly at the shallower angles. In this effort, significant experimental evidence in support of the two-noise source model has been shown for multiple nozzle geometries and jet exit Mach numbers ranging from low subsonic to fully-expanded supersonic using multi-microphone, coherence-based signal processing techniques. Two-point space-time correlation and coherence measurements have been utilized to display that typical jet noise spectra display considerable correlation in the downstream direction and relatively low coherence in the sideline direction, just as predicted by the two-noise source model. Upon the successful validation of the two-noise source model for jets exhausting from multiple nozzle geometries driven at Mach numbers ranging from subsonic to supersonic, a three-microphone signal enhancement technique has been employed to separate the contribution of the small-scale turbulence from that of the large-scale turbulence in the far-field. This is the first ever quantitative separation of the contributions of the two turbulence scales in far-field jet noise measurements. Furthermore, by suitable selection of far-field microphone positions, the separation of the contributions of any internal or core noise from that of the jet-mixing noise has been achieved.

In the application of coherence-based multiple-microphone signal processing techniques to separate the contributions of the small-scale turbulence, large-scale turbulence, and any internal or core noise in the far-field, research efforts focused on three techniques (1) the coherent output power spectrum method using two microphones, (2) an ordinary coherence method using the three-microphone technique, and (3) the partial-coherence method using five microphones. The assumption of jet noise incoherence between correlating microphone is included in the each of these methods. In light of the noise radiation mechanisms described within the framework of the two-noise source model and their spatial characteristics as experimentally determined in the far-field, the assumption of jet noise incoherence has been evaluated through a series of experiments designed to study jet noise coherence across a variety of nozzle geometries and jet Mach numbers ranging from subsonic to supersonic. Guidelines for the suitable selection of far-field microphone locations have been established. It has been established that equally-spaced microphone pairs in the downstream and sideline directions exhibit dramatically different coherence spectra. A microphone pair positioned in the downstream direction displays more coherence than a pair with equivalent spacing in the sideline direction. This holds for all nozzle geometries tested. It also holds for subsonic and supersonic Mach numbers. Typically, to ensure jet noise incoherence between correlating microphones in the downstream on-axis direction, larger microphone separations (i.e., 20° to 30° for most applications) are needed. In the sideline direction, smaller spacing (e.g., 10°) will suffice for subsonic and fully-expanded supersonic jets. However, in the sideline direction, microphone separations larger than those required in the subsonic and fully-expanded supersonic cases may be necessary to ensure jet noise incoherence for shock-containing

jets. Since much of the present work was concerned with fully-expanded jets, further investigation is needed to fully determine how shock-associated broadband noise modifies the far-field jet noise coherence.

A set of applicability bounds for applying coherence based multi-microphone techniques when separating core noise buried in jet mixing noise as measured in the far-field has been determined. Such bounds were developed using the coherent output power spectrum method using two microphones, an ordinary coherence method using the three-microphone technique, and the partial-coherence method using five microphones. These bounds have been applied to model-scale and full-scale jet noise measurements reported in this dissertation.

The usefulness of the five-microphone method, which claims to utilize only the far-field microphones to separate individual core noise components from jet mixing noise, has been investigated. Extensive work has been done in an attempt to solve the five-microphone problem associated with the implementation of the so-called multi-microphone method. The author encountered major difficulties in the solving the non-linear system of equations resulting from its implementation. These difficulties have been discussed, and the attempted solution routines have been documented for the use of future researchers. It has been concluded that a dedicated effort by an expert in the area of solving large systems of non-linear algebraic equations will be required to solve the five-microphone problem.

REFERENCES

- ¹ Tam, C. K. W., and Chen, P., "Turbulent Mixing Noise from Supersonic Jets," *AIAA Journal*, Vol. 32, No. 9, 1994, pp. 1774-1780.
- ² Tam, C. K. W., "Supersonic Jet Noise," *Annual Review of Fluid Mechanics*, Vol. 27, 1995, pp. 17-43.
- ³ Chung, J. Y., "Rejection of Flow Noise Using a Coherence Function Method," *Journal of the Acoustical Society of America*, Vol. 62, No. 2, Aug. 1977, pp. 388-395.
- ⁴ Halvorsen, W. G., and Bendat, J. S., "Noise Source Identification Using Coherent Output Power Spectra," *Journal of Sound and Vibration*, Vol. 8, No. 9, Aug. 1975, pp. 15, 18-24.
- ⁵ Hsu, J. S. and Ahuja, K. K., "A Coherence-Based Technique to Separate Ejector Internal Mixing Noise from Far-field Measurements," *Proceedings of the 4th AIAA/CEAS Aeroacoustics Conference*, June 2-4, 1998.
- ⁶ Ahuja, K. K., "Designing Clean Jet Noise Research Facilities and Making Accurate Jet Noise Measurements," *International Journal of Aeroacoustics*, Vol. 2, Nos. 3 & 4, 2003, pp. 371-412.
- ⁷ Minami, T., and Ahuja, K. K., "Five-Microphone Method for Separating Two Different Correlated Noise Sources from Far-field Measurements Contaminated by Extraneous Noise," *Proceedings of the 9th AIAA/CEAS Aeroacoustics Conference*, May 12-13, 2003.
- ⁸ Bendat, J. S., and Piersol, A. G., *Random Data: Analysis and Measurement Procedures*, 2nd ed., John Wiley & Sons, New York, 1971, Chaps. 5-6.
- ⁹ Lighthill, M. J., "On Sound Generated Aerodynamically: I. General Theory," *Proceedings of the Royal Society of London, Series A, Mathematical and Physical Sciences*, Vol. 211, Royal Society of London, London, 1952, pp. 564-581.

¹⁰ Lighthill, M. J., "On Sound Generated Aerodynamically: II. Turbulence as a Source of Sound," *Proceedings of the Royal Society of London, Series A, Mathematical and Physical Sciences*, Vol. 222, No. 1148, Royal Society of London, London, 1954, pp. 1-32.

¹¹ Proudman, I., "The Generation of Noise by Isotropic Turbulence," *Proceedings of the Royal Society of London, Series A, Mathematical and Physical Sciences*, Vol. 214, No. 1116, Royal Society of London, London, 1952, pp. 119-132.

¹² Ffowcs-Williams, J. E., "The Noise from Turbulence Convected at High Speed," *Philosophical Transactions for the Royal Society of London, Series A*, Vol. 255, No. 1061, Royal Society of London, London, 1963, pp. 469-503.

¹³ Lilley, G. M., "On the Noise from Air Jets," *Aeronautical Research Council Reports and Memoranda*, No. 20, 376, 1958.

¹⁴ Philips, O. M., "On the Generation of Sound by Supersonic Turbulent Shear Layer," *Journal of Fluid Mechanics*, Vol. 9, Sept. 1960, pp. 1-28.

¹⁵ Ribner, H. S., "The Generation of Sound by Turbulent Jets," *Advances in Applied Mechanics*, Vol. 8, Academic Press, New York, 1964, pp.108-182.

¹⁶ Doak, P. E., "Acoustic Radiation from a Turbulent Fluid Containing Foreign Bodies," *Proceedings of the Royal Society of London, Series A, Mathematical and Physical Sciences*, Vol. 254, No. 1276, Royal Society of London, London, 1960, pp. 129-145.

¹⁷ Goldstein, M. E., and Rosenbaum, B.M., "Effect of Anisotropic Turbulence on Aerodynamic Noise," *Journal of the Acoustical Society of America*, Vol. 54, No.3, 1973, pp.630-645.

¹⁸ Tester, B. J., and Morfey, C. L., "Development in Jet Noise Modeling – Theoretical Predictions and Comparisons with Measured Data," *Journal of Sound and Vibration*, Vol. 46, No. 1, 1976, pp.79-103.

¹⁹ Khavaran, A., Krejsa, E. A., and Kim, C. M., "of Supersonic Jet Mixing Noise from an Axisymmetric Convergent-Divergent Nozzle," *Journal of Aircraft*, Vol. 31, No. 5, 1994, pp. 603-609.

- ²⁰ Hunter, C., and Thomas, R. H., "Development of a Jet Noise Prediction Method for Installed Jet Configuration," *Proceedings of the 9th AIAA/CEAS Aeroacoustics Conference*, May 2003.
- ²¹ Morris, P. J., and Farassat F., "Acoustic Analogy and Alternative Theories of Jet Noise," *AIAA Journal*, Vol. 40, No. 4, 2002, pp. 671-680.
- ²² Goldstein, M. E., "A Generalized Acoustic Analogy," *Journal of Fluid Mechanics*, Vol. 488, 2003, pp.315-333.
- ²³ Laufer, J., Schlinker, R. H. and Kaplan, R. E., "Experiments on Supersonic Jet Noise," *AIAA Journal*, Vol. 14, No. 4, 1976, pp. 489-497.
- ²⁴ Schlinker, R. H., "Supersonic Jet Noise Experiments," Ph.D. Thesis, Department of Aerospace Engineering, University of Southern California, August, 1975.
- ²⁵ Crow, S. C., and Champagne, F. H., "Orderly Structures in Jet Turbulence," *Journal of Fluid Mechanics*, Vol. 48, 1971, pp. 547-591.
- ²⁶ Brown, G. L., and Roshko, A., "On Density Effects and Large Structures in Turbulent Mixing Layers," *Journal of Fluid Mechanics*, Vol. 64, 1974, pp. 775-816.
- ²⁷ Ahuja, K. K., Milway, S., and Hunter, N., Unpublished data on tandem nozzle flows, Work in progress as a part of URETI project, 2006.
- ²⁸ Tam, C. K. W, Ahuja, K. K., Viswanathan, K., and Panda, J., "The Sources of Jet noise: Experimental Evidence," *Proceedings of the 13th AIAA/CEAS Aeroacoustics Conference*, May 21-23, 2007.
- ²⁹ Tam, C. K. W., and Burton, D. E., "Sound Generated by Instability Waves of Supersonic Flows. Part 1. Two-Dimensional Mixing Layers," *Journal of Fluid Mechanics*, Vol. 138, 1984, pp. 249-272.
- ³⁰ Tam, C. K. W., and Burton, D. E., "Sound Generated by Instability Waves of Supersonic Flows. Part 2. Axisymmetric Jets," *Journal of Fluid Mechanics*, Vol. 138, 1984, pp. 273-295.

- ³¹ Tam, C. K. W., and Auriault, L. "Jet Mixing Noise from Fine Scale Turbulence," *AIAA Journal*, Vol. 37, No. 2, 1999, pp. 145-153.
- ³² Tam, C. K. W., and Chen, K. C., "A Statistical Model of Turbulence in Two-Dimensional Mixing Layers," *Journal of Fluid Mechanics*, Vol. 92, Pt. 2, 1979, pp. 303-326.
- ³³ Tam, C. K. W., Golebiowski, M., and Seiner, J. M., "Two Components of Turbulent Mixing Noise from Supersonic Jets," *Proceedings of the 2nd AIAA/CEAS Aeroacoustics Conference*, May 6-8 1996.
- ³⁴ Dahl, M. D., and Papamoschou, D., "Analytical Predictions and Measurements of the Noise Radiated from Supersonic Coaxial Jets," *AIAA Journal*, Vol. 38, No. 4, 2000, pp. 584-591.
- ³⁵ Tam, C. K. W., "Influence of Nozzle Geometry on the Noise of High Speed Jets," *AIAA Journal*, Vol. 36, No. 8, 1998, pp.1735-1744.
- ³⁶ Viswanathan, K., "Aeroacoustics of Hot Jets," *Journal of Fluid Mechanics*, Vol. 516, 2004, pp. 39-82.
- ³⁷ Viswanathan, K., "Analysis of the Two Similarity Components of Turbulent Mixing Noise," *AIAA Journal*, Vol. 40, No. 9, 2002, pp. 1735-1744.
- ³⁸ Tam, C. K. W., and Zaman, K. B., "Subsonic Jet Noise from Non-axisymmetric and Tabbed Nozzles," *AIAA Journal*, Vol. 38, No. 4, 2000, pp. 592-599.
- ³⁹ Munro, S., and Ahuja, K. K., "Aeroacoustics of a High Aspect-Ratio Jet," *Proceedings of the 9th AIAA/CEAS Aeroacoustics Conference and Exhibit*, May 2003.
- ⁴⁰ Panda, J., and Seasholtz, R. G., "Experimental Investigation of Density Fluctuations in High-Speed Jets and Correlation with Generated Noise," *Journal of Fluid Mechanics*, Vol. 450, 2002, pp. 97-130.
- ⁴¹ Panda, J., Seasholtz, R. G., and Elam, K. A., "Investigation of Noise Sources in High-speed Jets via Correlation Measurements," *Journal of Fluid Mechanics*, Vol. 537, 2005, pp. 349-385.

- ⁴² Hurdle, P.M., Meecham, W. C., and Hodder, B. K., "Investigation of the Aerodynamic Noise Generating Region of a Jet Engine by Means of the Simple Source Fluid Dilatation Model," *Journal of the Acoustical Society of America*, Vol. 56, No. 6, 1974, pp. 1708-1721.
- ⁴³ Schaffar, M., "Direct Measurements of the Correlation between Axial in-jet Velocity Fluctuations and far field noise near the axis of a cold jet," *Journal of Sound and Vibration*, Vol. 64, No. 1, 1979, pp. 73-83.
- ⁴⁴ Karchmer, A. M., and Reshotko, M., "Core Noise Source Diagnostics on a Turbofan Engine Using Correlation and Coherence Techniques," NASA TMX-73535, 1979.
- ⁴⁵ Karchmer, A. M., Reshotko, M. and Montegani, F. J., "Measurement of Far-field Combustion Noise from a Turbofan Engine Using Coherence Function," *Proceedings of the 4th AIAA Aeroacoustics Conference*, Oct. 3-5, 1977.
- ⁴⁶ Brooks, T. F., and Hodgson, T. H., "Trailing Edge Noise Prediction from Measured Surface Pressure," *Journal of Sound & Vibration*, Vol. 78, No. 1, Sept. 8, 1981, pp. 69-117.
- ⁴⁷ Shivashankara, B. N., "High Bypass Ratio Engine Noise Component Separation by Coherence Technique," *Proceedings of the 7th AIAA Aeroacoustics Conference*, Oct. 5-6, 1981.
- ⁴⁸ Stoker, R. W., Ahuja, K. K., and Hsu, J. S., "Separation of Wind-Tunnel Background Noise and Wind Noise from Interior Measurements," *Proceedings of the 2nd AIAA/CEAS Aeroacoustics Conference*, May 6-8, 1996.
- ⁴⁹ Ahuja, K. K., and Brown, W. H., "Shear Flow Control by Mechanical Tabs," *Proceedings of the 2nd AIAA Shear Flow Conference*, March 13-16, 1989.
- ⁵⁰ Ahuja, K. K., Lepicovsky, J., Tam, C. K. W., Morris, P. J., and Burrin, R. H., "Tone-Excited Jet: Theory and Experiments," *NASA Contractor Report*, Nov. 1982.
- ⁵¹ Lepicovsky, J., Ahuja, K. K., Brown, W. H., Salikuddin, M., and Morris, P. J., "Acoustically Excited Heated Jets: Internal Excitation," *NASA Contractor Report Part I*, June 1998.

- ⁵² Lepicovsky, J., Ahuja, K. K., Brown, W. H., Salikuddin, M., and Morris, P. J., "Acoustically Excited Heated Jets," *NASA Contractor Report Part II*, June 1998.
- ⁵³ Samimy, M., Zaman, K. B. M. Q., and Reeder, M. F., "Effect of Tabs on the Flow and Noise of an Axisymmetric Jet," *AIAA Journal*, Vol. 31, No. 4, 1993, pp 609-619.
- ⁵⁴ Carter, G. C., "Receiver Operating Characteristics for a Linearly Thresholded Coherence Estimation Detector," *IEEE Transactions on Acoustics, Speech, and Signal Processing*, Vol. 25, No. 1, 1997, pp. 90-92.
- ⁵⁵ Munjal, M. L., *Acoustics of Ducts and Mufflers*, John Wiley & Sons, New York, 1987, Chapter 5.
- ⁵⁶ Miles, J. H., "Aligned and Unaligned Coherence A New Diagnostic Tool," *Proceedings of the 44th AIAA Aerospace Sciences Meeting and Exhibit*, Jan. 2006.
- ⁵⁷ Mathsoft, MATLAB Help Documentation.
- ⁵⁸ Coleman, H. W., and Steele, W. G., *Experimentation and Uncertainty Analysis for Engineers*, 2nd ed., John Wiley & Sons, New York, 1999, Chaps. 3-5.
- ⁵⁹ American National Standards Institute/American Society of Mechanical Engineers, *Test Uncertainty*, PTC 19.1-1998, ASME, New York, 1998.
- ⁶⁰ American Institute of Aeronautics and Astronautics, *Assessment of Wind Tunnel Data Uncertainty*, AIAA Standard S-071-1995, AIAA, New York, 1995.

VITA

Donald Kirby Nance was born in Meridian, Mississippi on November 8, 1979, the son of Aubrey and Debbie Nance. He grew up in Philadelphia, Mississippi, and graduated from Neshoba Central High School in 1998. He received his Bachelor of Science in Aerospace Engineering from Mississippi State University (Mississippi State, MS) in 2002 and Masters of Science in Aerospace Engineering from Mississippi State University in 2003. Don is married to Kristin Nance, and they have one child, Norah Ann (born August 9, 2007).